PREPARATION AND OPTICAL PROPERTIES OF CRYSTALS AND FILMS OF VANADIUM OXIDES

John C. C. Fan

Harvard University
Cambridge, Massachusetts

May 1972

Office of Naval Research

Contract N00014-67-A-0298-0012 NR-017-308

ARPA Contract DAHC-15-67-C-0219

PREPARATION AND OPTICAL PROPERTIES OF CRYSTALS AND FILMS OF VANADIUM OXIDES

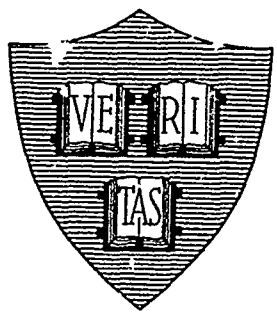

By

John C. C. Fan

May 1972

Technical Report No. HP-28

Technical Report No. ARPA-43

Division of Engineering and Applied Physics
Harvard Univerity - Cambridge, Massachusetts

Unclassified

Security Classification

DOCUMENT CONTROL DATA - R & D

Security classification of title, body of abstract and indexing annotation must be entered when the overall report is classified)

1 ORIGINATING ACTIVITY *(Corporate author)*
Division of Engineering and Applied Physics
Harvard University
Cambridge, Massachusetts

2a. REPORT SECURITY CLASSIFICATION

2b GROUP

3 REPORT TITLE

PREPARATION AND OPTICAL PROPERTIES OF CRYSTALS AND FILMS OF VANADIUM OXIDES

4. DESCRIPTIVE NOTES *(Type of report and, inclusive dates)*

Interim technical report

5 AUTHOR(S) *(First name, middle initial, last name)*

John C. C. Fan

6. REPORT DATE
May 1972

7a. TOTAL NO OF PAGES
303

7b. NO. OF REFS
221

8a. CONTRACT OR GRANT NO.
N00014-67-A-0298-0012 and ARPA

b. PROJECT NO. DAHC 15-67-C-0219

c.

d.

9a. ORIGINATOR'S REPORT NUMBER(S)
Technical Report No. HP-28
Technical Report No. ARPA-43

9b. OTHER REPORT NO(S) *(Any other numbers that may be assigned this report)*

10. DISTRIBUTION STATEMENT

Reproduction in whole or in part is permitted by the U. S. Government.
Distribution of this document is unlimited.

11 SUPPLEMENTARY NOTES

12 SPONSORING MILITARY ACTIVITY

Office of Naval Research

13 ABSTRACT

This manuscript describes mainly the preparation and optical properties of crystals and films of some of the vanadium oxides. In addition, different methods of determining the optical constants of solids are discussed and compared.

The complex vanadium-oxygen system contains several oxides which exhibit first order insulator-metal phase transition as a function of temperature. There are different models that have been suggested to explain the nature of these transitions. In practice, it is often difficult to choose an appropriate model or models to explain the meachnism of each of the phase transitions. In our work, we concentrated on the VO_2, V_2O_3 and V_2O_3-Cr_2O_3 systems, which exhibit many features of the phase transitions.

Single crystals of V_2O_3 and $(V_{1-x}Cr_x)_2O_3$ were grown by the tri-arc Czochralski technique. Using a vapor transport technique, we also prepared single crystals of V_2O_3 and films of V_2O_3 and VO_2. Sputtered V_2O_3 films, as grown, were found to exhibit no phase transition around 150° K. Upon annealing, the phase transition occurred, suggesting that if there was no change in chemical composition on annealing, critical grain sizes might be necessary for the phase transition to propagate.

Optical reflectivity measurements were made on single crystals of V_2O_3. The optical properties of V_2O_3 exhibited a free electron absorption in its metallic state, which was replaced by an optical absorption edge in its low temperature insulating state. The optical constants of V_2O_3 were evaluated from the reflectivity spectra by using both the Kramers-Kronig analysis and the oscillator fit technique.

Similarly, the optical constants of VO_2, both in its insulating state and metallic state were evaluated. In addition, the optical constants of a single crystal of $(V_{0.982}Cr_{0.018})_2O_3$ at room temperature were reported. At room temperature, the optical properties of $(V_{0.182}Cr_{0.18})_2O_3$ and V_2O_3 were found to be similar, indicating that at room temperature, the band structures of these two materials might not be too different.

The structural and electrical characteristics of our films of V_2O_3 and VO_2 indicated that the films were of poorer quality than the single crystals. Optical measurements on the films, though complementing our optical reflectivity measurements on the single crystals, were not used to evaluate the optical constants of these materials. The optical transmission measurements on these films did, however, confirm the existence of absorption edges in V_2O_3 and VO_2 in their low temperature insulating states.

From the optical data, order of magnitude values of optical effective mass and optical mobility were obtained for the conduction electrons in the metallic states of both V_2O_3 and VO_2. Our optical data were, however, not capable of indicating which mechanism or mechanism were responsible for the phase transition in these materials. The optical properties were not unusual, and could be explained in terms of a one-electron band model. The mean free paths of the conduction electrons were, however, short and thus electron correlation and/or electron phonon interaction were probably present.

The $(V_{1-x}Cr_x)_2O_3$ system was investigated mainly by optical reflectivity measurements as a function of temperature. We concentrated on the phase transition between the paramagnetic metallic state and the paramagnetic insulating state. Our measurements showed that this phase transition could be either a first order or a higher order transition, depending on the chromium doping level.

During our investigation, different methods of determining optical constants were discussed. We found that the angular dependence measurements, though often limited to a few wavelengths, offered direct and accurate measurements of n and k. The Kramers-Kronig analysis is subject to extrapolation uncertainties, and the oscillator fit technique to fitting uncertainties. By constraining at some wavelengths, the optical constants calculated from either the Kramer-Kronig analysis or the oscillator fit technique to approach those obtained from the angular dependence measurements at the same wavelengths, the above uncertainties can be greatly reduced.

DD FORM 1 NOV 65 1473 (PAGE 1)

S/N 0102-014-6700

I

Unclassified

Security Classification

D-23822

14. KEY WORDS	LINK A		LINK B		LINK C	
	ROLE	WT	ROLE	WT	ROLE	WT
Transition Metal Oxides						
Semiconductor-Metal Transitions						
Preparation of Vanadium Oxides						
Optical Properties of Vanadium Oxides						
Mott Transitions						

ACKNOWLEDGMENT

The preparation of this report was made possible by the support and cooperation of many colleagues and friends. I would like to mention some of their contributions here. First and foremost, I would like to thank my thesis advisor Professor William Paul for his advice and guidance throughout my research, from choosing the research topic to critically reviewing and helping with this final manuscript.

Professor Paul Raccah, formerly of MIT Lincoln Laboratory and now of Yeshiva University, proved to be of invaluable assistance and guidance in helping with those parts of my research that were conducted at Lincoln Laboratory. I am greatly indebted to him.

For their experienced advice, I am grateful to Doctors Larry Ladd, John Goodenough and, particularly, Tom Reed, who aided me in growing the V_2O_3-Cr_2O_3 crystals. My colleagues at Harvard, Mr. Wesley Akutagawa, who helped in growing vapor transport films and crystals, Mr. William Rosevear and Mr. Nigel Shevchik, are also gratefully acknowledged for their helpful suggestions and cooperation.

Mr. Albert Manning and the late Mr. James Inglis provided expertise in machining, and Mr. David McLeod in sample preparation. Mr. Edward Owens of Lincoln Laboratory was very helpful with the analysis of some of the samples and the discussion of analytical problems connected with this work. Mr. Carl Anderson, also of Lincoln Laboratory helped in setting up some of the optical equipment used there. My sincere thanks to them all.

Office of Naval Research

Contract N00014-67-A-0298-0012

NR - 017 - 308

PREPARATION AND OPTICAL PROPERTIES OF CRYSTALS AND FILMS OF VANADIUM OXIDES

By

John C. C. Fan

May 1972

Technical Report No. HP-28

Technical Report No. ARPA-43

The research reported in this document was made possible through support extended the Division of Engineering and Applied Physics, Harvard University, by the Office of Naval Research, under Contract N00014-67-A-0298-0012 and by the Advanced Research Projects Agency under Contract DAHC-15-67-C-0219.

Division of Engineering and Applied Physics

Harvard University · Cambridge, Massachusetts

PREPARATION AND OPTICAL PROPERTIES OF CRYSTALS AND FILMS OF VANADIUM OXIDES

By

John C. C. Fan

Division of Engineering and Applied Physics

Harvard University · Cambridge, Massachusetts

ABSTRACT

This manuscript describes mainly the preparation and optical properties of crystals and films of some of the vanadium oxides. In addition, different methods of determining the optical constants of solids are discussed and compared.

The complex vanadium-oxygen system contains several oxides which exhibit first order insulator-metal phase transition as a function of temperature. There are different models that have been suggested to explain the nature of these transitions. In practice, it is often difficult to choose an appropriate model or models to explain the mechanism of each of the phase transitions. In our work, we concentrated on the VO_2, V_2O_3 and V_2O_3-Cr_2O_3 systems, which exhibit many features of the phase transitions.

Single crystals of V_2O_3 and $(V_{1-x}Cr_x)_2O_3$ were grown by the tri-arc Czochralski technique. Using a vapor transport technique, we also prepared single crystals of V_2O_3 and films of V_2O_3 and VO_2. Sputtered V_2O_3 films, as grown, were found to exhibit no phase transition around $150^{\circ}K$. Upon annealing, the phase transition occurred, suggesting that

if there was no change in chemical composition on annealing, critical grain sizes might be necessary for the phase transition to propagate.

Optical reflectivity measurements were made on single crystals of V_2O_3. The optical properties of V_2O_3 exhibited a free electron absorption in its metallic state, which was replaced by an optical absorption edge in its low temperature insulating state. The optical constants of V_2O_3 were evaluated from the reflectivity spectra by using both the Kramers-Kronig analysis and the oscillator fit technique.

Similarly, the optical constants of VO_2, both in its insulating state and metallic state were evaluated. In addition, the optical constants of a single crystal of $(V_{0.982}Cr_{0.018})_2O_3$ at room temperature were reported. At room temperature, the optical properties of $(V_{0.982}Cr_{0.18})_2O_3$ and V_2O_3 were found to be similar, indicating that at room temperature, the band structures of these two materials might not be too different.

The structural and electrical characteristics of our films of V_2O_3 and VO_2 indicated that the films were of poorer quality than the single crystals. Optical measurements on the films, though complementing our optical reflectivity measurements on the single crystals, were not used to evaluate the optical constants of these materials. The optical transmission measurements on these films did, however, confirm the existence of absorption edges in V_2O_3 and VO_2 in their low temperature insulating states.

From the optical data, order of magnitude values of optical effective mass and optical mobility were obtained for the conduction electrons in the metallic states of both V_2O_3 and VO_2. Our optical data were, however, not capable of indicating which mechanism or mechanism were responsible

for the phase transitions in these materials. The optical properties were not unusual, and could be explained in terms of a one-electron band model. The mean free paths of the conduction electrons were, however, short and thus electron correlation and/or electron phonon interaction were probably present.

The $(V_{1-x}Cr_x)_2O_3$ system was investigated mainly by optical reflectivity measurements as a function of temperature. We concentrated on the phase transition between the paramagnetic metallic state and the paramagnetic insulating state. Our measurements showed that this phase transition could be either a first order or a higher order transition, depending on the chromium doping level.

During our investigation, different methods of determining optical constants were discussed. We found that the angular dependence measurements, though often limited to a few wavelengths, offered direct and accurate measurements of n and k. The Kramers-Kronig analysis is subject to extrapolation uncertainties, and the oscillator fit technique to fitting uncertainties. By constraining, at some wavelengths, the optical constants calculated from either the Kramers-Kronig analysis or the oscillator fit technique to approach those obtained from the angular dependence measurements at the same wavelengths, the above uncertainties can be greatly reduced.

TABLE OF CONTENTS

LIST OF FIGURES

CHAPTER I

Figure No.

CHAPTER II

Figure No.

CHAPTER III

Figure No.

CHAPTER IV

Figure No.

Figure No.

Figure No.

Figure No.

LIST OF TABLES

CHAPTER I

INTRODUCTION

Ever since F.J. Morin (1) reported, in 1959, that single crystals of VO, VO_2, V_2O_3 and Ti_2O_3 all exhibited sharp changes of electrical conductivity from metallic to semiconducting behavior at certain transition temperatures, intense efforts have been made to understand this class of materials, both experimentally and theoretically. The object of this thesis is to investigate these compounds, especially in the areas of preparation and optical properties.

First, however, a brief survey of the experimental and theoretical studies in this area is necessary to put this investigation into its proper perspective.

A. Transition Metal Compounds

The transition metals possess one to nine d electrons on each atom, in addition to the s and p electrons found on the atoms of ordinary metals. In a solid, the d orbitals overlap to form a relatively narrow d band. The next higher s band is usually wide and overlaps the entire d band. Thus, the s band is always partially full and metallic conductivity prevails in all the transition metals.

When compounds of transition metals are formed, their electrical properties vary widely from insulating to metallic behaviour. If we restrict ourselves to oxides and sulphides of the transition metals, many compounds can be classified by their electrical conductivity characteristics into three distinct classes:

(a) Insulators (resistivity of the order of $10^3 - 10^7$ Ω-cm and decreasing with increasing temperature): NiO (2), CoO (3.9), MnO (4), FeO (5), Fe_2O_3 (6), Cr_2O_3 (7), Mn_3O_4 (4), Mn_2O_3 (8), Co_3O_4 (8), MnS (10), FeS_2 (10), and MnS_2 (10).

(b) Metals (resistivity of the order of $10^{-2} - 10^{-6}$ Ω-cm at room temperature, and linearly increasing with increasing temperature): TiO (11), VO (11), CrO_2 (12), NbO (13), ReO_2 (14), ReO_3 (15), TiS (16), CoS_2 (10), and CuS_2 (10).

(c) Materials with insulator-metal transitions: V_2O_3 (1, 16), VO_2 (1, 17), V_6O_{13} (18), V_4O_7 (19), V_5O_9 (20), V_8O_{15} (21), Ti_2O_3 (1), Ti_4O_7 (22), Ti_3O_5 (22), Ti_5O_9 (22), Ti_6O_{11} (22), NbO_2 (23), Fe_3O_4 (24), NiS (25), CrS (26), and FeS (27).

Two striking features of these compounds emerge from this classification: (1) failure of the Bloch-Wilson one electron band theory in explaining the electrical conductivities of some of the insulating transition metal compounds, and (2) frequent occurrence of insulator-metal transitions in a large number of materials, especially in the oxides of vanadium and titanium.

In the next section, we will elaborate on these two points as they pertain to some of the transition metal oxides.

B. Theoretical Discussion on Transition Metal Oxides

One of the classical examples of the failure of the Bloch-Wilson theory is NiO. In NiO, as well as in many transition metal oxides, the

bonding of Ni^{++} cations with O^{--} anions is partially ionic. The O^{--} 2p states are the bonding orbitals and form a band ~ 6 eV below the anti-bonding orbitals of Ni^{++} 4s states (28). The 3d band is generally assumed to be somewhere between the 2p and 4s bands (28). In the ground state, the s band is completely empty and the p band is completely full. Therefore, only the d band is near the Fermi level and should be responsible for both the electrical and magnetic properties of NiO.

NiO has a cubic NaCl structure, and the ten-fold degenerate 3d states are split by the crystalline field into a lower six-fold degenerate t_{2g} band and an upper four-fold degenerate e_g band. Since NiO contains eight 3d electrons per unit cell, the e_g band should be partially filled and NiO should be metallic. NiO however, is a good insulator. Since NiO is antiferromagnetic below the Néel temperature T_N, its ground state can be insulating if the antiferromagnetism, which leads to doubling of the primitive cell, actually opens up a gap in the density of states in the e_g band. At temperatures above T_N, this band splitting should disappear and NiO should be metallic. This, however, is not the case. Thus, the one electron Bloch-Wilson band theory fails to explain the insulating property of NiO above T_N.

In order to modify the Bloch-Wilson band theory, one must understand the assumptions on which the theory is based, namely, the Hartree-Fock hypothesis, which reduces a many-electron problem to the description of a single electron moving in a periodic field. But this hypothesis fails

to treat adequately electron correlations and electron-phonon interactions, which, for reasons outlined below, could be important in transition metal compounds.

The properties of outer electrons in crystals can often be described by either of two theories, one the crystal field theory, and the other the one-electron band theory. Crystal field theory is adequate to describe the properties of the outer electrons in a crystal if the interaction between the neighboring atoms is so weak that each electron is essentially localized near its nucleus. On the other hand, one electron band theory is most appropriate for explaining outer electrons if they are essentially itinerant and are equally likely to be found at any site in the solid. There are, however, outer electrons which are neither sufficiently itinerant nor localized to be adequately described by either of the two above theories. The outer d-electrons in some transition metal compounds fall into this category. The following justification applies, strictly speaking, to the atomic limit only, though quantitatively, it is usually applicable even in crystals.

Outer s and p electronic wave functions usually spread far from their atomic nuclei and their properties are usually adequately described by one electron band theory. The outer 4f electrons, on the other hand, are more localized to their nuclei, and are screened from their neighboring atoms by the $5s^2$ and $5p^6$ electrons (28, 29). These electrons are then considered to be localized and their behavior can be described by the crystal field theory. The outer d electrons are, however, generally

intermediate in nature. In many transition metal compounds, such as NiO and MnO, the outer d electrons cannot be described by either of the two theories and the theories have to be modified. Here, we are interested only in modification of the one electron band theory, which then should include consideration of electron correlations and electron-phonon interactions.

Besides the failure of the one electron band theory in explaining the electrical insulating behavior of some transition metal oxides, another striking feature of the transition metal compounds is the frequent occurrence of first order phase transitions.

In 1949, Mott (30) provided an argument which not only showed the limitation of the one electron band theory, but also demonstrated how a first order phase transition could occur. Briefly, suppose we have a crystal made of atoms whose outer shell has only one s electron, and which has only one atom per unit cell. One electron band theory will predict the crystal to be metallic. If, however, the atoms are very far apart, the overlap between the orbitals from the neighboring atoms will be small, and the electronic energy levels will not be too different from the atomic energy levels. Now, if we consider a particular atomic site at which there is already an electron, a second electron of the opposite spin placed at the same site will have to have an additional energy U since a Coulomb repulsion force will have to be overcome in order to place two electrons at the same site. Thus migration of electrons in this crystal will necessitate an activation energy U. The electrons are essentially localized

to their respective atomic sites, and we have an insulator; however, as the atoms are brought together, the kinetic energy of the electrons increases as they are confined to their respective atomic sites. Eventually, the energy of the repulsion of two electrons on one atomic site becomes less than the energy required to localize the electrons in their atomic sites. The electronic wave function then spreads out reducing the kinetic energy of the electrons. The electrons become delocalized and metallic conductivity results.

In such a crystal, according to the Mott theory, the interatomic distances are crucial in determining the electrical conductivity. If the interatomic distances in the crystal are so large that its outer s electrons are essentially localized, then the crystal is an insulator, although the one electron band theory predicts that it should be a metal. If the interatomic distances are so small that the outer s electrons are delocalized, the crystal is a metal. If the interatomic distance is in between these two limits, then the properties of the s electrons are not clear. If, say, the crystal has interatomic distances sufficiently large that the outer s electrons are essentially localized, but yet small enough that the application of hydrostatic pressure on this crystal may well reduce the interatomic distances until the outer s electrons become essentially free, then the conductivity of such a crystal will increase under hydrostatic pressure. Such a transition could conceivably be either gradual or sharp. Mott further suggested that when the interatomic distances in the crystal are near the critical value, free electrons and holes may be produced.

If only one free electron and one free hole are present in the crystal, then they would attract each other by a Coulomb interaction:

$$V(r) = \frac{-e^2}{\kappa r}$$

where e = electron charge, κ = dielectric constant of the crystal and r = distance between the electron and hole. They form an exciton and therefore are bound. If the exciton concentration increases, for instance with increasing pressure, then the Coulomb interaction will be screened by the electrons and holes associated with the excitons, until, at a certain exciton concentration, the effective Coulomb interaction will be too weak to bind the electrons and holes together, and there will be an abrupt transition from a small number to a large number of free carriers. Such a transition — often referred to as the Mott transition — is then first order. One prediction of the Mott theory is the possible existence of a Mott transition in some solids under pressure, especially in transition metal compounds where the outer d electrons are in the intermediate region between being localized and itinerant. The transition should appear as a sudden drop in resistivity at a given pressure, whereas a transition due to band overlap should lead to a gradual change in resistivity. In fact, the Mott transition is hard to demonstrate unambiguously, since in practice, where abrupt insulator-metal transitions are found, other phenomena such as magnetic ordering and crystalline distortion, which can also cause first order transitions, are found simultaneously. Many attempts however, have been made to observe such a transition.

NiO had been subjected to a quasi-hydrostatic pressure of 500 kilobars (31) without a resistivity transition occurring. Recently, however, Kawai and Mochizuki (32) did observe a sharp drop in resistivity when NiO was subjected to a very high quasi-hydrostatic pressure. At a pressure larger than 2 megabars (no exact value was reported because the calibration of pressure in this range is difficult), a sharp drop in resistivity of a factor of $\sim 10^6$ was observed. No conclusion, however, can be drawn as to whether this sharp transition is indeed the Mott transition because the physical properties of NiO, such as the crystal structure, magnetic properties, etc., before and after it undergoes the transition have not been investigated.

McWhan, Rice et al. (33, 34) investigated the $(V_{1-x}Cr_x)_2O_3$ system and observed a first order insulator to metal transition with a resistivity change as large as a factor of 10^2 under hydrostatic pressure. There is no change in crystal symmetry although there is a change in the crystal volume at the transition. They suggested that this transition might be a Mott transition, but the evidence is not conclusive because other mechanisms may be involved. A more detailed discussion of the $(V_{1-x}Cr_x)_2O_3$ system will be presented in the latter part of this chapter.

VO_2, as will be discussed later, is insulating at room temperature. At 340°K, VO_2 undergoes a first order insulator-metal transition with a resistivity change as large as a factor of 10^5 and becomes a metal. Roach and Balberg argued that if VO_2 had interatomic distances near the critical interatomic distance such that its insulating state was caused by the formation of excitons, as in the Mott theory, then the generation of

free carriers — for example, by a ruby laser — would increase the screening effect on the Coulomb interaction that binds the holes and electrons together. If a certain critical free electron concentration were reached, the Coulomb interaction would no longer be able to bind the holes and electrons together, and the Mott transition would occur. They were, indeed, able to switch the films from an insulating state into a metallic state. In practice, however, the ruby laser used not only generates free carriers in VO_2 films, but also heats up the films during the process. They are, therefore, unable to distinguish whether the observed insulator-metal transition is a Mott transition, or is caused by thermally heating the VO_2 films through the transition temperature at $340^{\circ}K$.

The investigations cited above fail to demonstrate unambiguously the existence of the Mott transition. As we have discussed earlier, the main difficulty is finding a material whose insulator-metal transition property can be explained only by the Mott theory, and wherein no other mechanisms which can cause a first order phase transition, such as crystalline distortion, are present. Detailed analyses of other such mechanisms can be found in Adler's review paper (36) and Goodenough's summer lecture in Poland (37).

Here, we will discuss only some of the more important models, namely the Adler-Brooks crystalline distortion model, the homopolar bond model, and the Hubbard model, and will briefly mention some of the effects of electron-phonon interactions on the insulator-metal transition.

Only a qualitative discussion of the Adler-Brooks crystalline distortion model will be presented here since detailed quantitative analysis has been put forth by Adler and Brooks (38). This model makes use of the fact that in the narrow band limit, a metallic state can be unstable at T = 0°K and a crystalline distortion towards a lower symmetry can be favored. This arises because, for any metal, a crystalline distortion can always be envisioned which will reduce the electronic energy of just the number of states that are filled, but will raise the energy of just those states that are empty. Such a distortion always minimizes the electronic energy of the system. An insulating state will result if a real energy gap in the density of states is produced. This is more likely if the energy bands are narrow. This distortion, however, will not occur unless the free energy of the insulating state is lower than that of the metallic state. Since at T = 0°K, there are no entropy contributions to the free energy, we have only to consider the total energy of the system in both states. The distortion will occur if the decrease in the electronic energy outweighs the increase in the strain energy caused by the crystalline distortion. This, again, has been shown to be the case only if the energy bands are narrow (38). As the temperature of such a narrow band insulating material is increased from 0°K, electrons are excited thermally across the energy gap into the conduction band. The thermal excitation of carriers will increase the electronic energy of the insulating state. In addition, as the temperature is increased, the entropy contribution to the free energy also becomes important. Since the

electronic entropy of the metallic state is usually greater than that of the insulating state, as the temperature increases, the free energy of the insulating state becomes closer to that of the metallic state, until at a certain critical temperature, the free energy of the metallic state becomes lower than that of the insulating state, and a first order insulator to metal transition occurs.

The Adler-Brooks theory has an important drawback in that it neglects electron correlation effects and electron-phonon interaction in its hypothesis. In fact, it assumes that one electron band theory is still appropriate. However, if we have a narrow band material, so that we can try to apply the Adler-Brooks theory, we should also take into account electron correlation effects and the electron-phonon interaction.

If the electron-phonon interaction in a crystal is sufficiently large, an electron can polarize and, thereby distort, the lattice in its neighborhood. The polarization, in turn, acts on the electron and lowers its energy. As the electron moves through the crystal, it takes along the distortion of the lattice. The electron together with the accompanying self-consistent polarization field can be thought of as a quasi-particle, and is usually called a polaron. Its effective mass is larger than that of the Bloch electron. Polaron effects might thus explain the low conductivity of some of the transition metal oxides.

Within the limits of small polaron theory (small polarons occur if the dimension of the polaron, that is, of the electronic wave function and the self-consistent polarization field, is smaller than the lattice constant),

Holstein (39) reported that at low temperatures, polaron conductivity was due to polaron bands, and conductivity was low. Above a critical temperature (approximately at half of the Debye temperature), conduction took place by means of thermally activated polaron hopping of very low mobility. Therefore, we have a transition from a state with low conductivity to a state with even lower conductivity as temperature increases, and this is the reverse of what we observe in many transition metal oxides and sulphides except in the $(V_{1-x}Cr_x)_2O_3$ system. Accordingly, polaron effects are generally not applicable in explaining the insulator-metal transition. This is not, however, to imply that the electron-phonon interaction is not important, as its effect may be present in other forms.

Berglund and Guggenheim (40) calculated that the latent heat of VO_2 at the phase transition could not be accounted for by the change in the electronic entropy at the phase transition alone. They then suggested that most of the latent heat should be supplied by the lattice. Ladd (41) suggested that the latent heat could be supplied by lattice-vibrational mode-softening in the metallic state in VO_2.

Paul (42) and Hearn (43) suggest that since the 3d electrons in transition metal compounds, and particularly in VO_2 are intermediate in character between localized and itinerant electrons, they can be easily excited by changing the temperature or stress into higher energy states. They are, however, still sufficiently localized that these excitations may produce considerable local charge fluctuation. If the distribution of

d-electron charges near the vanadium ions is such that the lattice phonon spectrum is critically dependent on it, this local charge fluctuation may induce a strong electron-phonon interaction and lead to the softening of the phonon spectrum in the metallic phase where, by second order perturbation theory, the effect of the electron-phonon interaction is greater than in the insulating state because of the larger number of degenerate states at the Fermi level. The softening of phonon modes in the metallic state decreases its lattice free energy and eventually the total free energy becomes lower for the metallic phase than for the insulating phase, causing the insulator-metal transition.

Hearn did a one dimensional calculation for atoms along the c-axis in VO_2, using this idea, and obtained reasonable quantitative agreement with known experimental data. Mattis and Langer (44) obtained some quantitative results of the effects of phonons and band structure on the metal-insulator transition. Depending on the electron-phonon coupling coefficients and the band structures of the materials, either first order or second order phase transitions may occur. Insulator-metal transitions, therefore, should depend strongly on the crystal structures of the solids if they are driven by electron-phonon interactions. In contrast, the crystal structures may not be important in the Mott transition. The interatomic distances and the nature of valence electrons in the solid determine the possible existence of the Mott transition. In fact, in a solid, if the interatomic distances are in the critical region where the electrons can either be itinerant or localized, the Mott transition may be possible even in amorphous materials.

In 1960, Goodenough (45) suggested the possibility that for some transition metal ion arrangements, it might be favorable for some of the d orbitals of the cations to form covalent-bonded molecular orbitals, where electrons are localized. These molecular orbitals, often referred to as homopolar bonds, may be formed at a certain critical temperature. At temperatures above this critical temperature, these homopolar bonds break apart, and the electrons become delocalized (28), leading to an insulator-metal transition.

As Mott has pointed out, electron correlation can play an important role in the properties of some transition metal compounds. Hubbard in a series of papers (46, 47, 48, 49) incorporated correlation effects into band theory by introducing the Hamiltonian

$$H = \sum_{k,\sigma} \mathcal{E}(k)\, n_{k,\sigma} + U \sum_{i} n_{i\uparrow}\, n_{i\downarrow} - \left(\frac{N}{2}\right) n^2 U$$

where $\mathcal{E}(k)$ are the Bloch energies.

$n_{k,\sigma}$ are the number operators for the Bloch states,

$n_{i,\sigma}$ are the number operators for the Wannier states centered at the lattice site $\overline{R}_i$

σ represents spin

U is the intra-atomic Coulomb repulsion,

n is the number of electrons per atom,

N is the number of atoms in the crystal.

The first term in the Hamiltonian is the normal Hartree-Fock term, and the second term represents the correlation effects between

two electrons of opposite spin in the same atomic site. These correlation effects were included by an important approximation where only the intra-atomic Coulomb interaction was considered.

Hubbard applied this Hamiltonian to a half-filled s band and obtained some quantitative results. In the atomic limit, that is, when the bandwidth is zero, the above Hamiltonian can be solved exactly by means of retarded and advanced Green's function (46). The s band is found to be split into two subbands, separated by an energy gap U at T = 0. In this case, the lower band is completely filled and the upper band is empty at T = 0°K. As the ratio of the bandwidth Δ to U is increased, the energy gap decreases until it disappears at $\frac{\Delta}{U} = \frac{2}{\sqrt{3}}$ (see Fig. I-1). Since the gap decreases slowly to zero, we have only a gradual change in conductivity. A sudden first order transition cannot be predicted by the Hubbard model. However, this does not imply that the electron correlation effects cannot give rise to a first order phase transition. If we include long range Coulomb interactions, a first order insulator-metal transition might be possible. A theoretical approach to this problem is difficult and so far no solution has been presented.

Other models have also been offered which exhibit a gradual change (such as the band overlap model (50)) and sharp change (such as antiferromagnetism (51)) in the electrical conductivity.

As we have discussed before, it is usually difficult to choose the appropriate model or models to explain the mechanisms of the phase

transitions in many transition metal oxides. Many experimental observations are still incomplete, and in some compounds, more than one mechanism seems to be operating. In the next section we shall present some experimental results on the VO_2, V_2O_3, V_2O_3-Cr_2O_3 systems, which exhibit many features of the models mentioned above.

C. Experimental Results on Some Transition Metal Oxides

1. VO_2

For $T > T_t = 340^oK$, VO_2 has a structure which is a minor modification of that of rutile. There are two vanadium ions in each unit cell, and the vanadium ions, after having given electrons to satisfy the bonding requirement of the oxygen ions, have one valence electron per ion remaining in the vanadium d bands. For $T < 340^oK$, VO_2 undergoes a crystalline distortion into a monoclinic symmetry, and has its unit cell doubled. Figures I-2 and I-3 show the crystal structures above and below T_t, and the relationship between the two states.

The electrical conductivity has been measured by many investigators (1, 17, 40, 53, 54, 55), all of whom observed a sharp insulator-metal transition at $\sim 340^oK$, with a conductivity discontinuity of a factor as large as 10^5. If one defines activation energy E_a by the following equation,

$$\sigma = \sigma_o \exp(-E_a/kT)$$

where σ = conductivity at a temperature T
k = Boltzmann's constant
T = Temperature in ^oK
σ_o = conductivity at $\frac{1}{T} = O(1/^oK)$.

then in the insulating state, E_a is not constant as in most semiconductors, but varies slightly with temperature (17).

Hall measurements have been reported by several workers (56, 57, 58, 59) on ceramic samples, films and single crystals, the most recent of which were done on single crystals at Harvard by Rosevear and Paul (60). Their results showed a Hall mobility of $\sim 0.5\ cm^2/V$ sec at $T < T_t$, and $\sim 0.4\ cm^2/V$ sec at $T > T_t$ with weak temperature dependence in both phases.

Magnetic susceptibility measurements, nuclear magnetic resonance measurements, and the Mössbauer effect have revealed a small temperature-independent susceptibility of $\sim 10^{-6}$ emu/g at $T < T_t$ (40). At T_t, the susceptibility jumps by a factor of approximately 8, and remains temperature-independent for $T > T_t$ (40). There is no evidence of any long-range magnetic ordering.

Optical measurements have been performed on single crystals of VO_2 in several laboratories (17, 58, 61, 62). All have found that the reflectivity spectrum at $T > T_t$ manifests a free electron absorption region with a reflectivity minimum at ~ 1.5 eV. At $T < T_t$, the free electron absorption disappears, and an absorption edge appears at ~ 0.7eV. Ladd and Paul (17) determined the temperature dependence of the absorption edge by optical transmission measurements on thin single crystals. The absorption edge shifts from 0.74 eV at $100^{\circ}K$ to 0.61 eV at a temperature just below T_t. The size of the change of absorption edge is not inconsistent with that of the change of absorption edge in ordinary semiconductors with high Debye temperatures.

From optical reflectivity data (61), the possible bandwidths for VO_2 are ~ 1 eV wide. Photoemission measurements (63) also suggest that the 3d band is not very narrow and an energy gap in excess of 0.6 eV exists at the semiconducting state.

Although many experimental and theoretical efforts have been concentrated on VO_2, the mechanisms or mechamisms that provide the driving force for this transition are still uncertain. It is definitely not due to antiferromagnetism as no long-range magnetic ordering has ever been detected. Goodenough (28) suggested that at $T < T_t$, the single d electron associated with each V^{4+} ion forms a homopolar bond with the one associated with its nearest neighbor. This cation-cation interaction, together with an antiferroelectric distortion (caused by the tilting of the c-axis cation pairs forming more stable cation-anion bonds) permits the opening of a finite energy gap. If the Fermi energy is in the energy gap, VO_2 would become insulating. Above the transition temperature, these bonds break, causing the energy gap to disappear, and VO_2 to become metallic.

As mentioned earlier, in 1970, Paul (42) and Ladd (41) suggested that the insulator-metal transition in VO_2 might be due to phonon mode-softening as temperature increased above T_t. Paul (42) and Hearn (43) further proposed such phonon mode-softening in the metallic state could be caused by the strong electron-phonon interaction in the crystal. Theoretical calculations incorporating the electron-phonon interactions were made by Hearn (43) and Mattis and Langer (44) and their results tended to favor this hypothesis. Experimentally, Raman scattering on VO_2 crystals was

performed by Chase and Srivastava (64) which suggested strong electron phonon coupling at $T > T_t$. They also suggested a possible optical phonon mode softening at $T > T_t$. Their experiment was, however, not entirely conclusive, and more definitive experiments in this area have yet to be done.

2. $\underline{V_2O_3}$

At room temperature, V_2O_3 has the corundum structure, which has a slightly distorted hexagonal lattice. Below $\sim 150^{\circ}K$, there is a first order phase transition to monoclinic symmetry. The relationship of the monoclinic unit cell to the hexagonal cell is shown in Fig. I-4. The volume of the crystal increases about 3.5% through the transition to the low-temperature phase (65). Therefore, the Clausius-Clapeyron equation implies that hydrostatic pressure will reduce the transition temperature T_t.

Feinleib and Paul found

$$\left(\frac{dT_t}{dp}\right) = -(3.78 \pm 0.15) \times 10^{-3} {}^{o}K/bar$$

under hydrostatic pressure (16), while McWhan and Rice managed to suppress the low temperature phase entirely for hydrostatic pressure greater than 26 kbar (66).

Electrical measurements have also been made (1, 16, 67). At low temperatures, the conductivity increased exponentially with increasing temperature with an activation energy of approximately 0.15 eV. At $\sim 150^{\circ}K$, the conductivity jumped by a factor of 10^7. Above $150^{\circ}K$, the conductivity decreased linearly with temperature. A second anomaly

occurred near 550°K where the conductivity decreased by a factor of 2 over a 100° range (16).

Specific-heat data (68, 69) showed a first order phase transition near 150°K on cooling, 168°K on heating and a higher order phase change in the interval between 383°K and 533°K.

Magnetic susceptibility measurements (70) revealed an anomaly near 150°K where the susceptibility dropped by a factor of ~ 2 when V_2O_3 went from the metallic state to the antiferromagnetic insulator state. There was also another anomaly near $380^{\circ}K < T < 550^{\circ}K$ where the susceptibility vs temperature curve exhibited a shallow maximum. Mossbauer results (71) showed that V_2O_3 becomes antiferromagnetic below 150°K. This was confirmed by Moon using the neutron diffraction technique; he found an ordered magnetic moment of 1.2 μ_B per vanadium atom (72).

An optical transmission measurement was done on a thin single crystal (~ 25 microns thick) of V_2O_3 by Feinleib and Paul (16). No transmission was observed in the metallic state between 0.1 and 6 eV. In the insulating state, transmission was observed between 0.1 and 0.4 eV. At 0.4 eV, the transmission was less than 0.1%, and increased gradually to about 10% at about 0.2 eV. Since there is no sharp rise in transmission as in Ge and Si, it is difficult to decide an exact value for the energy gap.

Optical reflectivity at room temperature has been reported by Barker et al. (73) from 0.04 eV to 3 eV, and by Feinleib (74) from photon energy close to 0.0 eV to about 6 eV. All have found that the reflectivity

spectra show a free electron absorption region with a reflectivity minimum at $\sim$ 3.0 eV.

Hall effect data on single crystals were taken in the metallic state (75), showing that the charge carriers were holes with a concentration of $\sim 4 \times 10^{22}/cm^3$. The Hall mobility varied from 0.55 at 200°K to 0.40 cm^2/V sec at 300°K. Since the crystals cracked when going through the transition, no Hall data were obtained in the insulating state.

Hall effect measurements were also done on single crystals of V_2O_3 by Rosevear and Paul (60), and they obtained a Hall mobility of $\sim$ 0.9 cm^2/V sec with a hole concentration of $\sim 1.5 \times 10^{22}/cm^3/V$ sec in the metallic state.

Austin and Turner (76), likewise, reported a Hall mobility of $\sim$ 0.6 cm^2/V sec in the metallic state of single crystals of V_2O_3. However, they interpreted the charge carriers as electrons with a concentration of $\sim 3 \times 10^{22}/cm^3$. In the insulating state, no Hall signal was detected. They, then, inferred the Hall mobility should be less than 3×10^{-4} cm^2/V sec in the insulating state.

Adler-Brooks crystalline distortion theory has been applied to V_2O_3 (77). Using a transition temperature of 150°K and a semiconducting gap of 0.1 eV, their model predicted a first order insulator-metal transition. The model also predicted that

$$\frac{d\ \ell n\ T_o}{dx} = \frac{d\ \ell n\ Eg_o}{dx}$$

where T_o = the transition temperature in °K, Eg_o = energy gap at T = 0°K, x = either hydrostatic pressure or stress. The above relationship was

verified to within experimental error by Feinleib and Paul (16) by their measurements of the variation of the activation energy in the insulating state and of the transition temperature with hydrostatic pressure and with uniaxial stress in V_2O_3. However, the jump in carrier density predicted by the theory was only about two orders of magnitude, much less than the 10^7 discontinuity in the conductivity. The remaining factor of 10^5 was therefore supposed to be caused by the very much increased mobility in the metallic state resulting from the increased screening. The Austin and Turner Hall measurement, if reliable, could indeed denote a large change of mobility at T_t. Another point which should be mentioned is that the assumed semiconducting gap of 0.1 eV may also be on the low side, judging from the optical transmission spectrum reported by Feinleib and Paul (16).

In 1963, Goodenough (8) suggested that in the low temperature monoclinic phase, the atoms in the basal plane moved together to form homopolar bonds, leading to its insulating properties. At $T > T_t$, when the atoms in the basal plane moved apart, the homopolar bonds broke up, and metallic conductivity resulted. Recent x-ray measurements (34) showed that the atoms in the basal plane actually moved together as the temperature increased through T_t. Goodenough revised his hypothesis and proposed that in V_2O_3 the interaction between the neighboring cations in the basal plane was critical so that the 3d electrons could be either described as itinerant or localized. depending on the interatomic distance between the neighboring cations in the basal plane. In

the metallic phase, the interatomic distance between the cations was close enough so that the 3d electrons were essentially itinerant. At $T > T_t$, the cations in the basal plane moved apart, and the interatomic distance between neighboring cations was then large enough so that the d electrons became localized.

Goodenough suggested a possible energy band picture for V_2O_3 both in the insulating and metallic phases using this idea of critical cation-cation interaction with due consideration for both symmetry changes and ionicity of the crystal. A detailed discussion of his model can be found in his paper (78).

3. $(V_{1-x}Cr_x)_2O_3$

In 1969, McWhan, Rice and Remeika (33) reported the existence of a first order insulator-metal transition, with a change in crystal volume but without any change in crystal symmetry in the $(V_{1-x}Cr_x)_2O_3$ system. They were able to induce this transition by varying temperature, pressure and chromium concentration. They then suggested that the transition had all the qualitative features of a Mott transition, and that it was difficult to explain the transition on other grounds. Since then, many papers have been published on this system (34, 79, 80, 81, 82, 83). Figure I-5 shows a phase diagram of the system as a function of chromium concentration and pressure. There are three different phases present: a low temperature antiferromagnetic insulating phase, and two high temperature phases. The high temperature phases are separated into a paramagnetic insulating

phase and a paramagnetic metallic phase that differ in resistivities by a factor of about 10^3. They have the same corundum crystal structure, but with different lattice constants. The antiferromagnetic insulating phase has monoclinic symmetry.

McWhan et al. found that the high temperature first order phase transition changed into a higher order transition for $x < 0.005$ $(V_{1-x}Cr_x)_2O_3$, from x-ray, magnetic susceptibility, and electrical measurements (33, 79, 80). For x approximately between 0.005 and 0.016, there was a first order phase transition from a paramagnetic metallic phase into a paramagnetic insulating phase at atmospheric pressure with increasing temperature. In addition, when ~ 10 kilobar of hydrostatic pressure was applied to a $(V_{0.96}Cr_{0.04})_2O_3$ sample at room temperature, an abrupt decrease of the resistivity of a factor of $\sim 10^2$ was observed (33). There was no long-range magnetic order in either phase. In addition, magnetic susceptibility measurements as a function of temperature (80) showed anomalies in the samples where x is approximately between .005 and 0.016. These anomalies, which usually appeared as a shallow maximum in the temperature range near the high temperature transition, were interpreted as being caused by a possible onset of electron correlation as the crystals went from the paramagnetic metallic phase into the paramagnetic insulating phase (80). Optical reflectivity measurements as a function of temperature were done on one $(V_{.988}Cr_{.012})_2O_3$ sample and no sharp optical reflectivity change was observed between the two phases. Instead, the reflectivity of the sample at 8μ wavelength was found to increase slightly over a broad

temperature interval where the insulator to metal transition was to take place. X-ray measurement (34) distinctly showed an abrupt change of volume at the phase transition. Between $0.005 < x < 0.016$, in $(V_{1-x}Cr_x)_2O_3$, x-ray measurements also indicated that both the metallic and insulating phases coexisted at room temperature and atmospheric pressure. Rubinstein (83) made nuclear magnetic resonance measurements on sintered samples of $(V_{1-x}Cr_x)_2O_3$ and confirmed the phase diagram and the coexistence of both insulating and metallic phases for the appropriate chromium concentration. The interpretation that this transition is of the nature of a Mott transition is, however, not conclusive, although it does possess some features of a Mott transition, viz., it can be induced by pressure and the electrons in the paramagnetic insulating state may be highly correlated. Experimental evidence is not definitive, and theoretically, there are still no quantitative results to demonstrate that a Mott transition can be a first order phase transition.

Some other mechanisms may well give rise to a transition with similar characteristics, or other mechanisms may be present together with the mechanism that causes the Mott transition. Nonetheless, the discovery is of great interest, since, if the transition is a Mott transition, then it may be induced by lasers in the same manner as we have discussed for VO_2. Changes in the electrical conductivity in a Mott transition induced by this method could very well occur in a much shorter time than conductivity changes in phase transitions that are induced by thermal heating. Faster electrical conductivity switching times could have wide device applicability.

D. Research Objectives

Although the experimental and theoretical studies on the transition metal oxides that exhibit insulator-metal transition have been extensive, we feel some of the measurements on these materials are either incomplete or not very conclusive. In addition, the preparation of these materials has been difficult, and often not very satisfactory. Our research objectives, therefore, were focused on the preparation of thin films and single crystals of these materials by various means. From our experience, we then attempted to draw a few conclusions about some of the features and difficulties of the various methods of film and crystal growth. We concentrated only on three systems, VO_2, V_2O_3, and $(V_{1-x}Cr_x)_2O_3$, as their transition mechanisms are probably characteristic of the various models that have been proposed.

Besides some structural analysis and electrical measurements on these films and crystals, our measurements were mainly optical transmission and reflectivity. From these measurements, we obtained some optical constants for these materials in their metallic and insulating states by both Kramers-Kronig analysis and the oscillator fit method, which are presently the two frequently used methods of deriving optical constants from reflectivity spectra. Advantages and disadvantages of these two approaches were examined.

The V_2O_3-Cr_2O_3 alloy systems were investigated with emphasis on the transition between the paramagnetic metallic state and the paramagnetic insulating state, and especially on the optical reflectivity changes between these two states.

From the optical constants, we were able to obtain some understanding of the band structures of these materials, if indeed it is appropriate to describe them by a band approach. In the process of our research, we increased our knowledge of some of the properties of the various phases on both sides of the insulator-metal transition in these materials, and hence of the mechanisms responsible for these transitions.

CHAPTER I

REFERENCES

1. F.J. Morin, Phys. Rev. Lett. 3, 34 (1959).

2. Ya.M. Ksendzov, L.N. Ansel'rn, L.L. Vasil'eva and V.M. Latysheva, Soviet Phys. - Solid State (English Transl.) 5, 1116 (1963).

3. M. Roilos and P. Nagels, Solid State Comm. 2, 285 (1964).

4. V.G. Bhide and R.H. Dani, Physica 27, 832 (1961).

5. D.S. Tannhauser, J. Phys. Chem. Solids 23, 25 (1962).

6. R.F.G. Gardner, F. Swett and D.W. Tanner, J. Phys. Chem. Solids 24, 1183 (1963).

7. W.C. Hagel, J. Appl. Phys. 36, 2586 (1965).

8. J.B. Goodenough, "Magnetism and the Chemical Bond," Wiley (Interscience), New York, 1963.

9. F.J. Morin, Bell System Tech. J. 37, 1047 (1958).

10. D. Adler, Rev. Mod. Phys. 40, 714 (1968).

11. M.D. Banus and T.B. Reed, "The Chemistry of Extended Defects in Non-Metallic Solids," North-Holland Publishing Company, Amsterdam (1970).

12. D.S. Chapin, J.A. Kafalas and J.M. Honig, J. Phys. Chem. 69, 1402 (1965).

13. W. Meissner, H. Franz and H. Westerhoff, Ann. Physik 17, 593 (1933).

14. J.B. Goodenough, P. Gibart and J. Brenet, Compt. Rend. 261, 233 (1965).

15. A. Ferretti, D.B. Rogers and J.B. Goodenough, J. Phys. Chem. Solids 26, 2007 (1965).

16. J. Feinleib and W. Paul, Phys. Rev. 155, 841 (1967).

17. L. Ladd and W. Paul, Solid State Comm. 7, 425 (1969).

18. K.K. Kanazawa, Bull. Am. Phys. Soc. 12, 1120 (1967).

19. S. Kachi and T. Takada, J. Phys. Soc. Japan 28, 798 (1970).

20. H. Okinaka, K. Nagasawa, K. Kosuge, Y. Bando, S. Kachi and T. Takada, J. Phys. Soc. Japan 28, 803 (1970).

21. K. Nagasawa, Y. Bando and T. Takada, Japan J. Appl. Phys. 9, 841 (1970).

22. R.F. Bartholomew and D.R. Frankl, Phys. Rev. 187, 828 (1969).

23. R.F. Janninck and D.H. Whitmore, J. Phys. Chem. Solids 27, 1183 (1966).

24. P.A. Miles, W.B. Westphal and A. Von Hippel, Rev. Mod. Phys. 29, 279 (1957).

25. J.T. Sparks and T. Komoto, Phys. Lett. 25A, 398 (1967).

26. T. Kamigaichi, K. Masumoto and T. Hihara, J. Phys. Soc. Japan 15, 1355 (1960).

27. M. Murakami, J. Phys. Soc. Japan 16, 187 (1961).

28. J.B. Goodenough, "Progress in Solid State Chemistry," H. Reiss ed. (Pergamon), 1971 (Chapter 4).

29. A.H. Morrish, "The Physical Principles of Magnetism," p. 36, Wiley, New York (1966).

30. N.F. Mott, Proc. Phys. Soc. (London) A62, 416 (1949).

31. S. Minomura and H.G. Drickamer, J. Appl. Phys. 34, 3043 (1963).

32. N. Kawai and S.S. Mochizuki, Solid State Comm. 9, 1393 (1971).

33. D.B. McWhan and T.M. Rice, Phys. Rev. Lett. 23, 1384 (1969).

34. D.B. McWhan and J.P. Remeika, Phys. Rev. B2, 3734 (1970).

35. W.R. Roach and I. Balberg, Solid State Comm. 9, 551 (1971).

36. D. Adler, Solid State Phys. 21, 1 (1968).

37. J.B. Goodenough, Summer Lectures on "The Theory of Magnetism in Metals," Zakopane, Poland (1970).

38. D. Adler and H. Brooks, Phys. Rev. 155, 826 (1967).

39. T. Holstein, Ann. Phys. 8, 325 (1959).

40. C.N. Berglund and H.J. Guggenheim, Phys. Rev. 185, 1022 (1969).

41. L. Ladd, Tech. Report No. HP-26, Gordon McKay Laboratory, Harvard University, 1971 (unpublished).

42. W. Paul, Matl. Res. Bull. 5, 691 (1970).

43. C.J. Hearn, to be published.

44. D.C. Mattis and W.D. Langer, Phys. Rev. Lett. 25, 376 (1970).

45. J.B. Goodenough, Phys. Rev. 117, 1942 (1960).

46. J. Hubbard, Proc. Roy. Soc. (London) A276, 238 (1963).

47. J. Hubbard, Proc. Roy. Soc. (London) A277, 238 (1964).

48. J. Hubbard, Proc. Roy. Soc. (London) A281, 401 (1964).

49. J. Hubbard, Proc. Roy. Soc. (London) A285, 542 (1965).

50. B.I. Halperin and T.M. Rice, Rev. Mod. Phys. 40, 755 (1968).

51. J.C. Slater, Phys. Rev. 82, 538 (1950).

52. S. Westman, Acta. Chem. Scand. 15, 217 (1961).

53. H. Sasaki and A. Watanabe, J. Phys. Soc. Japan 19, 1748 (1964).

54. P.F. Bongers, Solid State Comm. 3, 275 (1965).

55. H. Takei and S. Kiode, J. Phys. Soc. Japan, 21, 1010 (1966).

56. I. Kitahiro, T. Ohashi and A. Watanabe, J. Phys. Soc. Japan 21, 2422 (1966).

57. D.H. Hensler, J. Appl. Phys. 39, 235 (1968).

58. A.S. Barker, H.W. Verleur and H.J. Guggenheim, Phys. Rev. Lett. 17, 1286 (1966).

59. W. Rosevear and W. Paul, Bull. Am. Phys. Soc., Series II, 15, 316 (1970).

60. W. Rosevear and W. Paul, to be published.

61. H.W. Verleur, A.S. Barker, Jr. and C.N. Berglund, Phys. Rev. 172, 788 (1968).

62. V.G. Mokerov and A.V. Rakov, FiZ. Tverd. Tela 11, 197 (1969) (Soc. Phys. - Solid State 11, 150 (1969)).

63. R.J. Powell, C.N. Berglund and W.E. Spicer, Phys. Rev. 178, 1410 (1969).

64. L.L. Chase and Ramakant Srivastava, Phys. Rev. Lett. 27, 727 (1971).

65. S. Minomura and H. Nagasaki, J. Phys. Soc. Japan 19, 131 (1964).

66. D.B. McWhan and T.M. Rice, Phys. Rev. Lett. 22, 887 (1969).

67. M. Foëx, Compt. Rend. 227, 193 (1948).

68. C.T. Anderson, J. Am. Chem. Soc. 58, 564 (1936).

69. J. Jaffrey and R. Lyand, J. des Recherches du C.N.R.S. Labs. Bellevue (Paris) 4, 249 (1952).

70. P.H. Carr and S. Foner, J. Appl. Phys. Suppl. 31, 344S (1960).

71. T. Shingo and K. Kosuge, J. Phys. Soc. Japan 21, 2622 (1966).

72. R.M. Moon, Phys. Rev. Lett. 25, 527 (1970).

73. A.S. Barker, Jr. and J.P. Remeika, Solid State Comm. 8, 1521 (1970).

74. J. Feinleib, "Electronic Structures in Solids," E. Haidemenakis ed., p. 239, Pergamon Press, New York, 1969.

75. V.P. Zhuze, A.A. Andreev and A.I. Shelykh, Soviet Phys. – Solid State 10, 2914 (1969).

76. I.G. Austin and C.E. Turner, Phil. Mag. 19, 939 (1969).

77. D. Adler, J. Feinleib, H. Brooks and W. Paul, Phys. Rev. 155, 851 (1967).

78. J.B. Goodenough, Proc. of the 10th Intl. Conf. of the Phys. of Semiconductors, 304 (1970).

79. A. Jayaraman, D.B. McWhan, J.P. Remeika and P.D. Dernier, Phys. Rev. B2, 3751 (1970).

80. A. Menth and J.P. Remeika, Phys. Rev. B2, 3756 (1970).

81. P.D. Dernier and M. Marezio, Phys. Rev. B2, 3771 (1970).

82. W.F. Brinkman and T.M. Rice, Phys. Rev. B2, 1324 (1970).

83. M. Rubinstein, Phys. Rev. B2, 4731 (1970).

84. A. Magnéli and G. Andersson, Acta. Chem. Scand. 9, 1378 (1955).

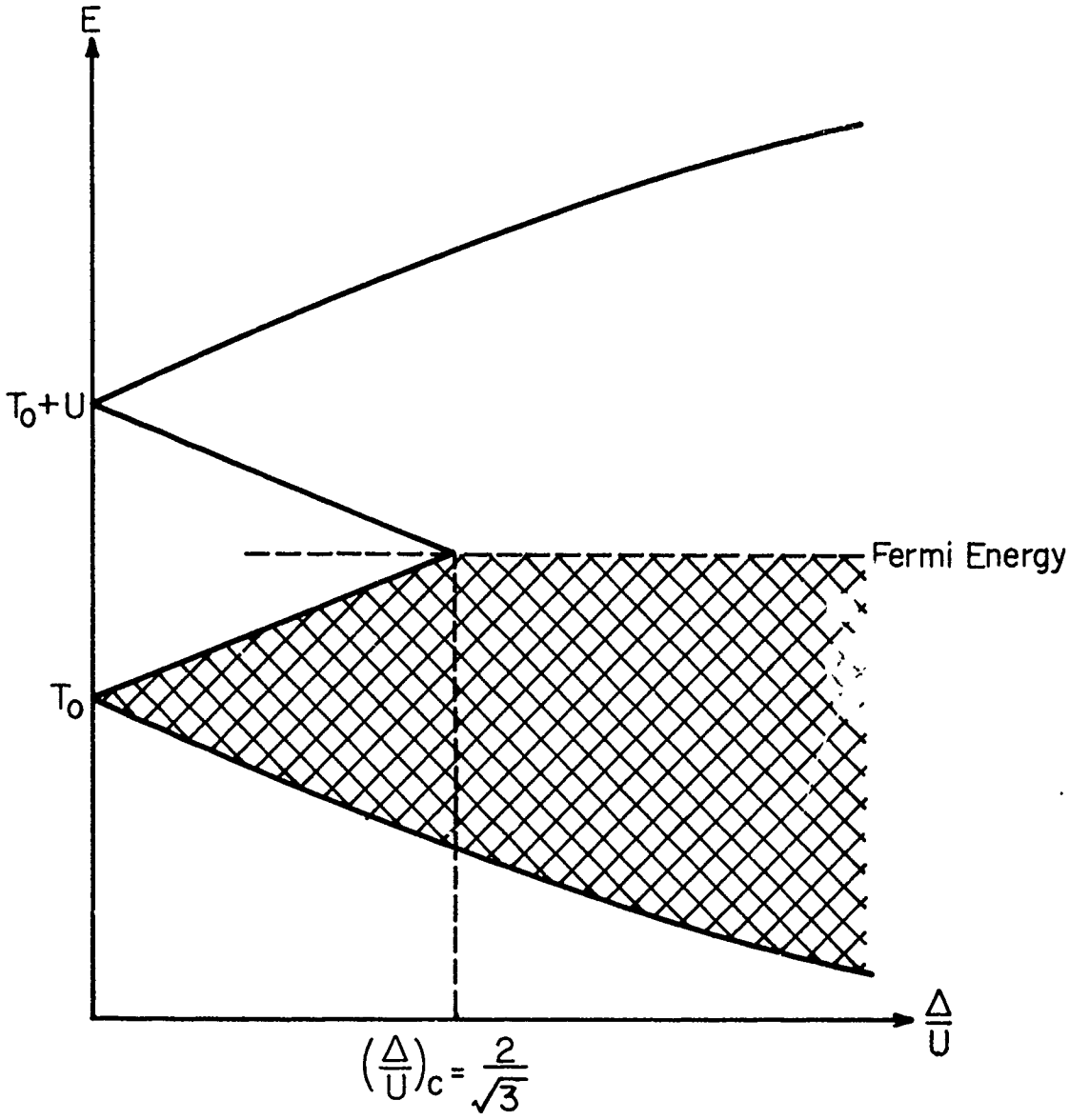

FIGURE I-1 Pseudoparticle band structure as a function of the ratio of bandwidth to intra-atomic Coulomb energy U for the case of a single s band. T_0 is the binding energy of the atomic level from which the s band arises (48).

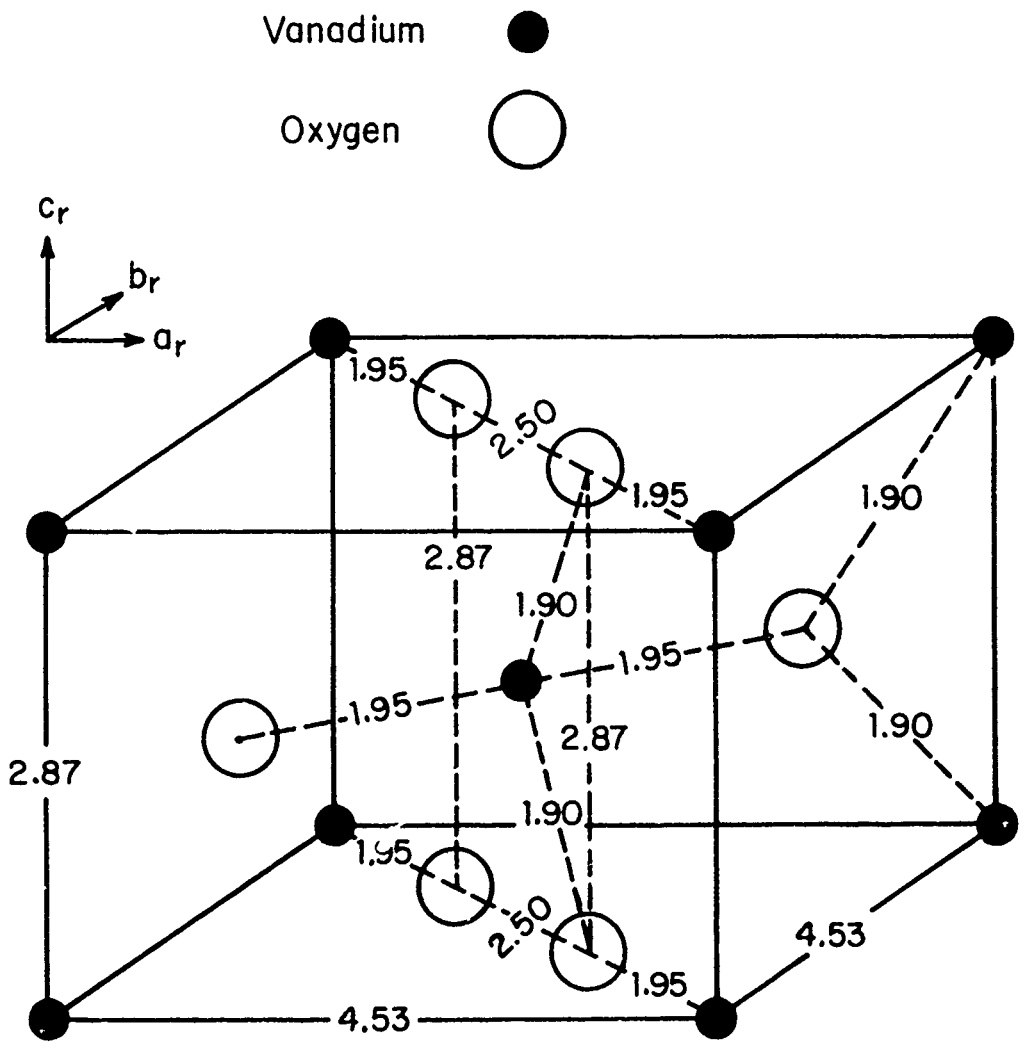

FIGURE I-2 The crystal structure of VO_2 in the high-temperature rutile phase; space group $P4_2/mnm$. Distances are in angstroms (41, 52)

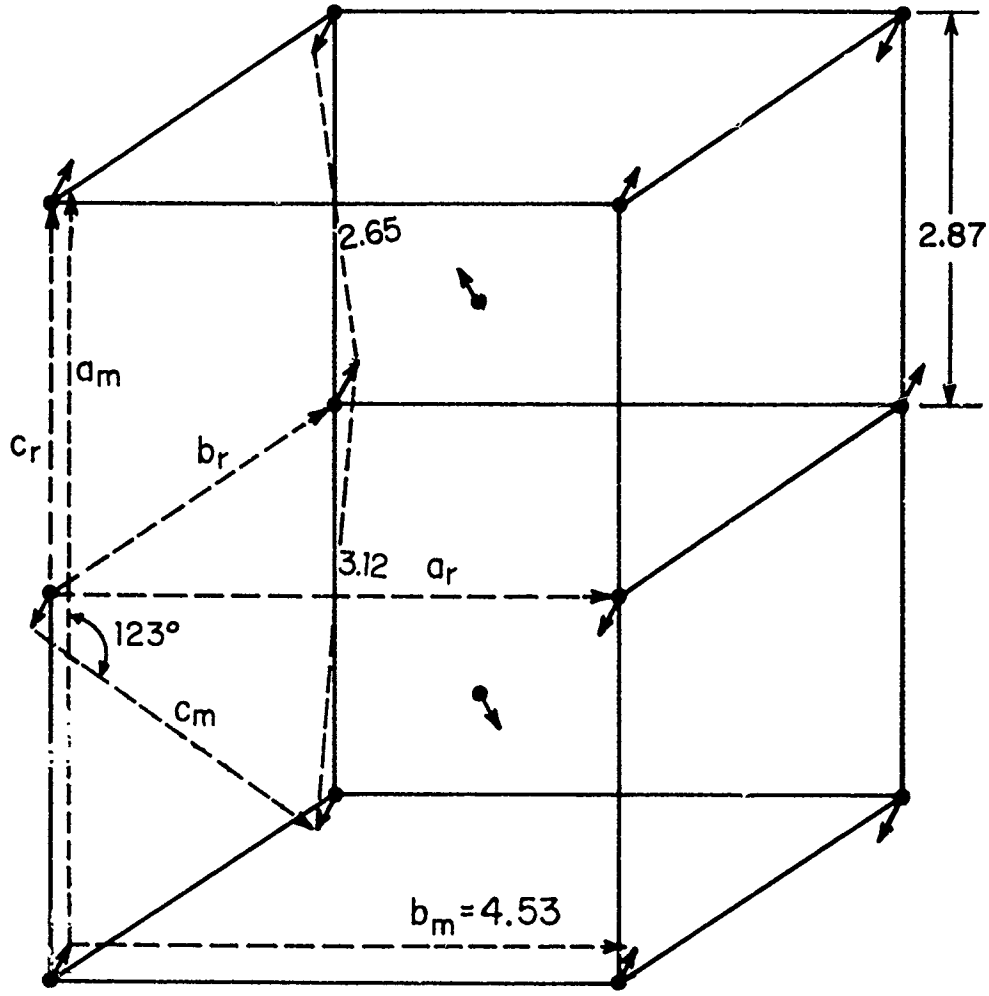

FIGURE I-3 Monoclinic $P2_1/c$ structure of the low-temperature VO_2 phase and its relationship to the rutile phase. Only the vanadium ions are shown. The displacement of the vanadium ions at the transition is demonstrated. Distances are in angstroms (41,84)

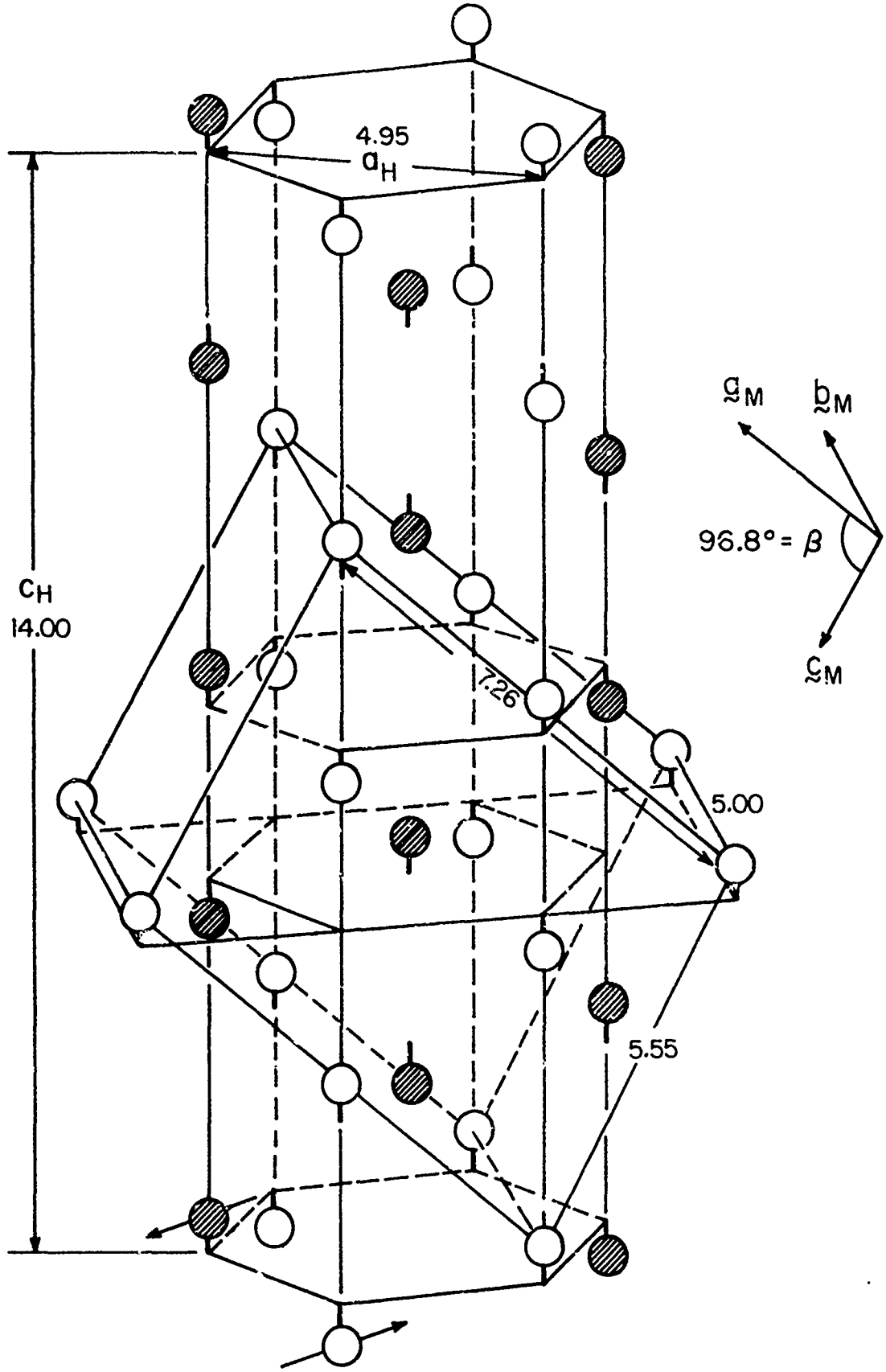

FIGURE I-4 The crystal structure of V_2O_3 showing both low-temperature monoclinic primitive cell (space group I2/a) and the high-temperature hexagonal cell (space group R$\bar{3}$c). Open and hatched circles refer to cations of different spin orientation in the low-temperature antiferromagnetic phase. Distances are in angstroms (28, 34)

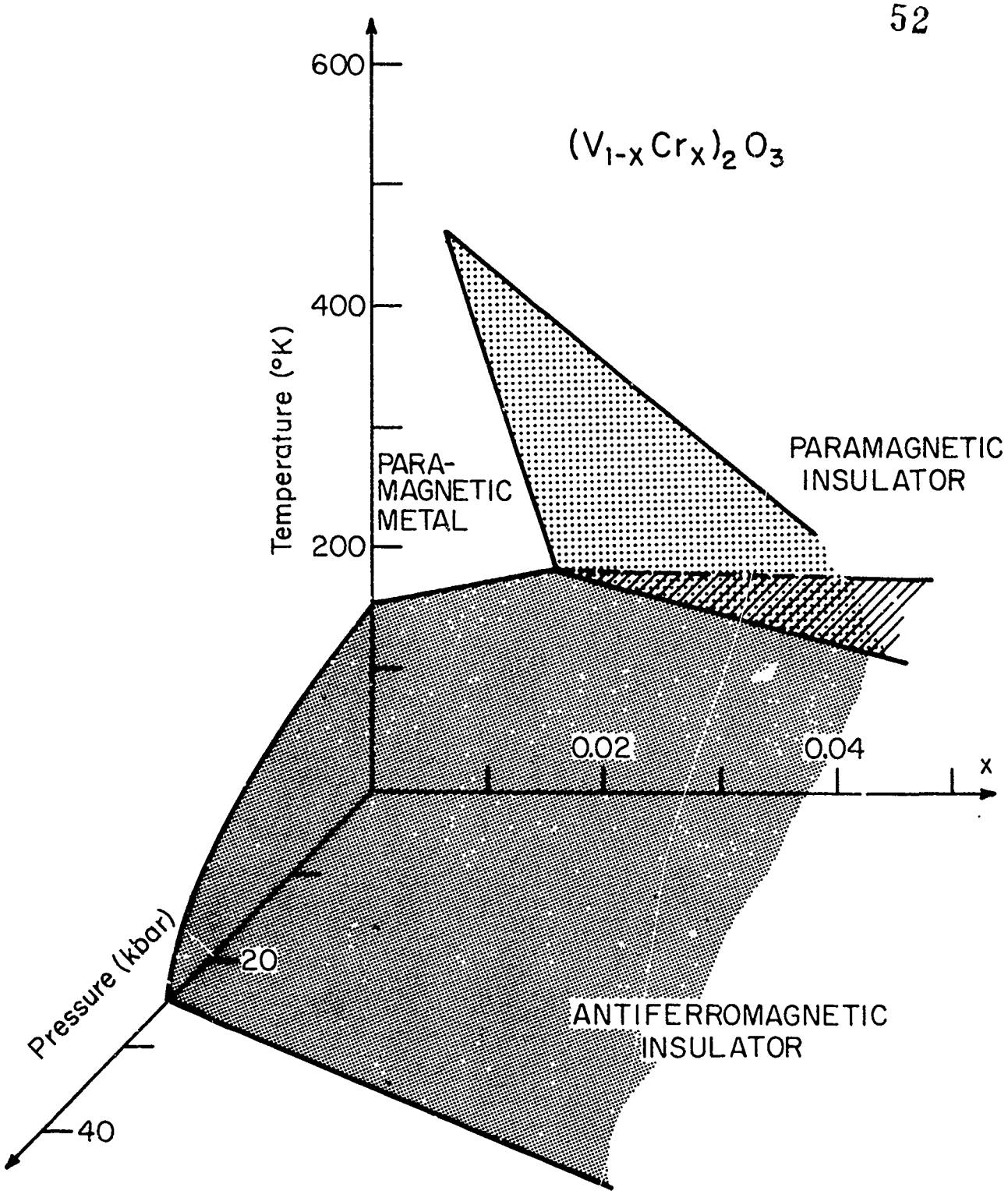

FIGURE I-5 Temperature-pressure-composition phase diagram of $(V_{1-x}Cr_x)_2O_3$ system (34).

CHAPTER II

PREPARATION OF FILMS AND CRYSTALS

In Chapter I we discussed the fact that one of the major experimental problems in studying the transition metal oxides is the preparation of high quality single crystals and films. In this chapter we will discuss some of the methods of growing films and crystals of V_2O_3 and VO_2.

Since the vanadium-oxygen system is very complex (see Fig. II-1), the growth of V_2O_3 and VO_2 crystals and films is complicated. We will begin by briefly discussing methods used by other investigators to grow single crystals and films of vanadium oxides. (Methods of obtaining sintered samples of these oxides will not be mentioned since sintered samples are usually poor substitutes for single crystals for physical measurements.) Then, we will describe the methods we used in the preparation of crystals and films of some of these oxides. We should point out that our purpose is not to investigate in detail the different growth processes in films and crystals of these vanadium oxides. Rather, we want to obtain some experience in growing good quality single crystals and films that will show a first order phase transition with a large resistivity change at the transition. There has been no exhaustive attempt, in our investigation, to explore the various conditions of growth nor to obtain the optimal growth parameters.

A. Earlier Methods of Preparation

1. VO_2 Crystals

VO_2 single crystals were first grown by Guggenheim (1) by the hydrothermal growth technique (2) and measured by Morin (1). These crystals showed a first order phase transition with a resistivity change of only a factor of $\sim 10^2$ at $\sim 350^\circ$K.

Single crystals of VO_2 have also been grown by flowing oxygen-free nitrogen gas past a platinum crucible containing both VO_2 and V_2O_5 powder heated to 1000°C. The partial oxygen pressure was low enough so that V_2O_5 was reduced to VO_2. This method was first used by Sasaki and Watanabe (3), who obtained crystals with resistivity changes up to a factor of 10^4. MacChesney et al. (4) and Everhart et al. (5) used the same method as Sasaki and Watanabe, but with different growth parameters, and were able to grow crystals as large as 1 cm in width. Their crystals had a resistance change at the transition of a factor of as large as 10^5 and a hysteresis on temperature cycling of 1°C.

Various vapor transport techniques of growing VO_2 single crystals were used by Kitahiro, Watanabe and Sasaki (6). They managed to grow crystals of VO_2 by reacting V_2O_5 with titanium in a heated sealed quartz tube. The crystals were small ($\sim$0.1mm x 0.2mm x 8mm) and showed a resistivity change of a factor of 3×10^4 within 1°C at 65.5°C.

Takei and Koide (7, 8) presented a new technique which was based on the chemical decomposition of $VOCl_3$ vapor with moisture in an inert or reducing atmosphere. They managed to obtain single crystals of

V_2O_5, VO_2, V_3O_5, and V_2O_3. The largest VO_2 crystals grown by this method were ~ 0.8 mm x 0.8 mm x 15 mm. There was a resistivity change of a factor of $\sim 10^4$ at $\sim 65^\circ$C. Using this same technique, epitaxial films of VO and VO_2 on appropriate substrates were also obtained. Growth of epitaxial films of V_2O_3 was not successful. This technique will be discussed in more detail later as we have adopted it in our preparation of these vanadium oxides.

In 1969, Bando, Nagasawa, Kato and Takada (9) adopted a technique used by Niemyski and Piekarczyk (14) for TiO_2 to produce single crystals of the vanadium oxides. This method proved to be very successful as they have managed to grow single crystals of V_2O_4 (9), V_3O_5 (10), V_6O_{11} (10), V_4O_7 (11), V_7O_{13} (11), V_5O_9 (12), and V_8O_{15} (13). This vapor transport method involved the use of tellurium tetracholoride ($TeCl_4$) as a transport agent. In all cases, the powders of each vanadium oxide of which single crystals were to be prepared was sealed in a heated and evacuated quartz tube with an appropriate amount of $TeCl_4$. The resultant single crystals in every case possessed the same chemical composition. This technique proved to be a very flexible method to obtain single crystals of many vanadium oxides, especially in the Magnéli phase system (V_nO_{2n-1} for $n=4,\ldots n$) where the chemical composition is very difficult to control. The quality and size of these crystals are reasonable. For instance, in VO_2, there was a resistivity change of a factor of $\sim 10^5$ within 1°C at 67°C. The crystal size was ~ 2-3 mm in width and ~ 1.6 cm in length (9). The only drawback in the method is

the toxic nature of $TeCl_4$; however, this is but a minor problem requiring only careful handling. Growth of epitaxial films of these oxides by this method has not yet been reported, but there is no apparant reason that it cannot be done.

The technique of growing crystals by slow cooling of VO_2 in a V_2O_5 flux, first used by Sobon and Greene (17), was adopted by Ladd and Paul (15, 16) to obtain high quality crystals of VO_2. An appropriate mixture of powders of VO_2 and V_2O_5 was sealed in an evacuated quartz tube, and heated to about 1100°C. Though the melting point of VO_2 is ~ 2000°C, it will dissolve readily in an appropriate amount of V_2O_5 when the temperature is ~ 800 C (see Fig. II-1). The temperature of the flux was then slowly reduced to room temperature (about 3°C/hour). Single crystals of VO_2 were subsequently obtained in a solidified V_2O_5 flux, which was dissolved. The crystals in each run ranged from large ones of ~ 1 mm x 1 mm x 10 mm to smaller but mechanically stronger ones. Resistivity measurements as a function of temperature were done on a few of these crystals (15, 16), and the insulator-metal transition was found to occur often within one degree of 65°C with a hysteresis on temperature cycling of ~ 1°C. The resistivity change was typically by a factor of 10^5.

2. V_2O_3 Crystals

Single crystals of V_2O_3 have usually been prepared by the flame fusion technique, one of many variations of the Verneuil method (18). In the flame fusion technique, material in the form of a fine powder, in

this case V_2O_3 powder, is continuously added to the molten top of a seed crystal with heat usually being provided by an oxy-hydrogen flame. The chief advantage of this method is that no crucible is required to hold the melt. It thus permits the growth of crystals from materials having very high melting points, and for which no non-reactive crucible materials can be found. The disadvantages are that the high thermal gradients present usually give rise to thermal strains in the crystals and that with the use of an oxy-hydrogen flame it is not always possible to adjust the ratio of oxygen to hydrogen freely to provide the correct oxygen partial pressure for the growth of stoichiometric oxides. In fact, this latter point most likely explains why VO_2 cannot be grown by the flame fusion technique (17).

Feinleib and Paul (19, 20) did their measurements on single crystals grown by Linde Co. (21) by the flame fusion technique. They found that the crystals exhibited a resistivity change of a factor of $\sim 10^7$ at $\sim 140^\circ K$ on cooling and $\sim 150^\circ K$ on heating. Goodman (22) also measured V_2O_3 crystals provided by Linde Co. and obtained a resistivity change of a factor of 10^8 at $\sim 160^\circ K$ on cooling. Austin and Turner's (23) Hall effect measurements on V_2O_3 crystals from Linde Co. were discussed earlier in Chapter I. The flame fusion technique was also used by Sobon and Greene (17) to grow V_2O_3 single crystals; no electrical data were reported by them as these crystals all cracked at $\sim 170^\circ K$ on cooling.

Single crystals of V_2O_3 were also produced by the flame fusion method at the Institute of Crystallography of the Academy of Sciences of the USSR (24). These crystals showed an electrical discontinuity of a factor of 10^6 at a transition temperature of $\sim 145^\circ K$ on cooling. On heating, the transition temperature was at $\sim 165^\circ K$.

Single crystals of V_2O_3 were prepared at Bell Telephone Laboratories by a flux method (25) similar to the method we used in growing VO_2 crystals, except that in preparing the V_2O_3 crystals, the choice of a suitable solvent for V_2O_3 was difficult. Potassium fluoride (KF) was finally chosen and gave satisfactory results. In brief, the growth procedure involves mixing VN with V_2O_5 in a platinum crucible and heating the mixture to 950°C. The mixture reacted to form V_2O_3 and was then transported through the molten KF to grow as single crystals in the cooler part of the crucible, which was placed in an argon controlled furnace. The resultant V_2O_3 crystals were quite soluble in boiling water, were ~ 5 mm across and ~ 1 mm thick in size, and were found to contain some VN (chemical analysis showed 1% nitrogen in the crystals). An electrical measurement of one of these crystals as a function of temperature has been reported (25) which showed a conductivity discontinuity of a factor of $\sim 10^6$ at ~150°K on cooling. There was a hysteresis in temperature cycling of ~10°C.

Single crystals of V_2O_3 were also grown by the vanadium oxychloride decomposition method discussed above. The crystals were thin platelets of about 1 mm wide. The resistivity discontinuity at 153°K on cooling of one of the crystals was about a factor of 10^4.

In reviewing various methods that many investigators have used to obtain single crystals of VO_2 and V_2O_3, we note that they all obtained single crystals with large conductivity changes at the phase transition. There were, however, variations in the magnitude of the discontinuity and the transition temperature, even in crystals prepared by similar

methods. These discrepancies can be explained by the sensitivity of the electrical characteristics of these oxides to the chemical composition and the impurity content. Since there are variations in the properties of single crystals of V_2O_3 and VO_2, we can expect that films of these oxides will fare much worse. In Sections 3 and 4, we will discuss some methods of preparation and some of the properties of the films of VO_2 and V_2O_3 that have been reported in the literature.

3. VO_2 Films

In 1967. Steensel, Burg and Kooy (26) reported that they had been able to grow VO_2 films by evaporating vanadium on glass substrates in an oxygen atmosphere of 5×10^{-5} torr and then heat-treating the films in oxygen after the deposition. The resultant films varied in thickness from 0.1μ - 1μ. The electrical characteristics usually varied from film to film. The resistivity discontinuity was not sharp, varying from a very small anomaly at the transition temperature to a maximum change of a factor of $\sim 10^3$ over a temperature interval of 10°C. The hysteresis on temperature cycling also varied from 5°C to 15°C. Nor was the transition temperature on heating constant, varying from 65°C to 70°C. Structural analyses were not reported on these films.

Koide and Takei (27) used the oxychloride decomposition technique described earlier, and obtained epitaxial films of VO_2 on single crystal TiO_2 and GeO_2 substrates. A typical film was 3μ - 20μ thick, although the growth conditions could be varied to give films as thick as 200μ. Resistivity measurements as a factor of temperature showed wide variations between samples. The best sample they reported showed a resistivity discontinuity of a factor of $\sim 10^3$ at $\sim$ 65°C.

MacChesney et al. (28) managed to grow VO_2 films by a technique involving the vapor deposition of V_2O_5 films on single crystal sapphire substrates by the reaction of $VOCl_3$ with CO_2. The V_2O_5 films were then reduced to VO_2 films by a mixture of CO and CO_2 gases. The resulting films (0.1 - 10μ) showed a sharp drop in resistance (10^3 ohms) at ~ 67°C. The hysteresis on temperature cycling was about 10°C.

Rozgonyi and Polito (29) first prepared V_2O_5 films of ~ 0.2μ thickness on single crystal sapphire substrates by oxidizing vanadium films deposited by DC sputtering of vanadium targets. The V_2O_5 films were then reduced to VO_2 films. The resistivity change of one of the films was a factor of $\sim 10^3$ at ~ 68°C. The films prepared by the above two methods were all polycrystalline.

The best VO_2 films reported were grown by reactive sputtering of vanadium targets (30, 31, 32). The VO_2 films were deposited on various kinds of substrates, for example single crystal sapphire, single crystal TiO_2 (rutile), amorphous glass and glassy ceramic. On single crystal rutile and sapphire substrates, epitaxial films of VO_2 were obtained with resistivity discontinuities as large as a factor of $\sim 4 \times 10^3$ at the transition temperature. Epitaxial films on sapphire substrates showed a transition temperature ~ 68°C, while those on rutile substrates had a transition temperature at ~ 58°C. In both cases, the hysteresis was less than 10°C. The films grown on glass and ceramic substrates were polycrystalline with a resistivity change of a factor of only 10^2 at about 68°C.

Since then, VO_2 films have been prepared by other authors using the same or similar techniques (33, 34, 35) leading to similar results.

A significant experiment on amorphous VO_2 films was done by Kennedy and Mackenzie in 1969 (36). The amorphous films were grown by radio-frequency sputtering of VO_2 powder target on cold substrates of single crystals of MgO, Al_2O_3, and SiO_2, and on glass. Kennedy and Mackenzie, using x-rays, found the films to be amorphous. The interesting feature of their experiment is the absence of the insulator-metal transition in these amorphous films. When annealed in argon for 24 hours at 600°C, the films became crystalline and a resistivity change of a factor of $\sim 10^2$ at $\sim 68^\circ$C appeared.

Mackenzie (37) later reported that amorphous VO_2 films grown at "apparent" substrate temperatures above 65°C had relatively high conductivity ($\rho \sim 5 \times 10^{-3}\ \Omega$cm), while those grown at "apparent" substrate temperatures below 66°C had low conductivity ($\rho \sim 10^2 - 10^3\ \Omega$-cm). He, however, did not clarify what he meant by "apparent" substrate temperature. From the experiments on the amorphous films, Mackenzie suggested that the electrical conductivities of these films were governed primarily by the short-range structure of the films, but that the insulator-metal transition in VO_2 depended on their long-range order.

4. V_2O_3 Films

There have been few reported attempts to grow V_2O_3 films. In one of these, Rozgonyi and Polito (29) managed to grow thin polycrystalline films of V_2O_3 using the same technique discussed on p. II-8. The

electrical characteristics of their films were poor when compared with those of the bulk crystals. The electrical conductivity as a function of temperature showed a change of a factor of $\sim 10^6$ at $\sim 125^\circ$K on cooling over a temperature interval of 25°C. There was also a hysteresis of about 30°C.

Hensler, Ross and Fuls (32) tried to grow V_2O_3 films by reactive sputtering of a vanadium target, but managed to obtain only a mixture of $VO_{1.2}$ and V_2O_3. Takei (8) also tried to grow V_2O_3 films on single crystal sapphire substrates by the vapor transport method discussed on p. II-2, with no success. Kennedy and Mackenzie (36, 37) reported that they had grown amorphous films on V_2O_3 by radio frequency sputtering of powdered V_2O_3 targets. As in the case of amorphous VO_2 film, these amorphous V_2O_3 films failed to show any insulator-metal transition. After annealing, the films became crystalline, and a large resistivity change of a factor of 10^8 occurred between room temperature and 77°K. However, since they provide no plot of resistivity as a function of temperature, the existence of a sharp insulator-metal transition in the crystallized film can only be inferred.

5. $(V_{1-x}Cr_x)_2O_3$ Crystals

We have discussed in Chapter I that, in addition to the low temperature phase transition at 150°K, there is a second first order phase transition in V_2O_3 crystals doped with an appropriate chromium concentration and grown by the flux method described on p. II-6. By adding Cr_2O_3 to the mixture of VN, KF, and V_2O_5, Remeika obtained

crystals of V_2O_3 with different chromium concentrations. Pure V_2O_3 crystals grown by this method were ~ 5 mm across and 1 mm thick. The size of the crystal in the mixed oxides decreased rapidly with increasing chromium content, and at $x \tilde{=} 0.12$, the crystals were less than 0.1 mm wide. The doped crystals, like the V_2O_3, had a considerable amount of nitrogen (probably ~1%) in them, and were quite soluble in boiling water.

B. Preparation of Films and Crystals of VO_2 and V_2O_3, and Crystals of $(V_{1-x}Cr_x)_2O_3$

Films and crystals of vanadium oxides are difficult to grow, not only because of the complex vanadium-oxygen system, but also because of the high melting points of most of these materials. Table II-1 lists the melting points of vanadium metal and some of the oxides in which we are interested.

Material	Melting Points (°C)
Vanadium V	1890 ± 10
Vanadium Dioxide (VO_2)	1967
Vanadium Sesquioxide (V_2O_3)	1970
Vanadium Pentoxide (V_2O_5)	690

Table II-1: Melting Points of Vanadium and Some Oxides (38).

Since VO_2 and V_2O_3 both have melting points of $\sim 2000^{\circ}C$, the preparation of films of these oxides by the evaporation of these oxides from tungsten and tantalum boats is not recommended. In addition, the oxygen partial pressure from the oxides tends to oxidize the boats at these high temperatures and the oxides of tungsten and tantalun are volatile. Nor is evaporation of vanadium metal from these boats successful, as the vanadium alloys with the tungsten and tantalum. In addition to the above difficulties, at high temperatures, VO_2 decomposes to lower oxides of vanadium and oxygen (26). Therefore, in the preparation of films and single crystals of VO_2 and V_2O_3, special care must be given to the selection of the appropriate growth techniques.

1. Radio Frequency Sputtering

Sputtering occurs when a target is bombarded by energetic ions causing some surface atoms to be ejected from the target. The surface atoms then collect on any surfaces which may be close to the target. (A detailed exposition of theories of sputtering may be found in the following references: 40, 41, 42, 43, 44, 45, 46.)

In our sputtering apparatus (see Fig. II-2), the energetic ions are provided in the manner described below. Electrons produced by thermionic emission from a tungsten filament are attracted towards an anode and during the process acquire energy from the electric field provided by the anode. When sufficient energy is attained, these emitted electrons will ionize the sputtering gas atoms. The ionization of these atoms will in turn provide secondary electrons, which can then participate

in further ionization of the gas atoms. Under proper operating conditions the resultant plasma of energetic ions and electrons can be sustained. Then, when a negative dc potential is applied to the target, the positive ions in the plasma will be attracted to the target and DC sputtering begins.

In our experiments, radio frequency sputtering (RF sputtering) was used to sputter pressed targets of V_2O_3 and VO_2. The difference between RF sputtering and DC sputtering is that in the former, a radio frequency alternating potential is applied to the target instead of the negative DC potential used in the DC sputtering. DC sputtering is adequate for sputtering metallic targets. On the other hand, if an insulating target is used in DC sputtering, the positive charges from the bombarding energetic ions will build up on the surface of the target and repel all further ions from bombarding the target. If an alternating potential is applied to this insulating target, the surface of the target will be periodically neutralized by the electrons in the plasma attracted to the target by the positive potential in every half cycle of the alternating potential. Therefore, the RF sputtering technique can be used for both metallic and insulating targets.

At room temperature, V_2O_3 is quite a poor metal ($\rho \sim 10^{-3}$ Ω-cm) while VO_2 is insulating ($\rho \sim 100$ Ω-cm). When powders of V_2O_3 and VO_2 are pressed into targets, their resistivity is usually higher (e.g., the resistivity of a pressed V_2O_3 target was found to be $\rho \sim 0.2$ Ω-cm at room temperature). Although it might be possible to sputter V_2O_3 (but not VO_2) targets by the DC technique, we decided to use RF sputtering to sputter both V_2O_3 and VO_2 targets.

Our sputtering apparatus is based on a RD Mathis model SP210A triode sputtering unit for both the RF and DC sputtering. A turbomolecular pump (Welch model 310A, made by the Welch Company, Illinois) enables us to reach a vacuum of 3×10^{-6} torr. A turbomolecular pump was chosen over a diffusion pump because of its high pumping speed, and its minimal oil contamination. Furthermore, the turbomolecular pump can be used to pump all non-corrosive gases and will not be damaged by an accidental exposure to atmospheric pressure.

This sputtering apparatus was originally assembled by Rossi (39) to grow NiO films by DC reactive sputtering. During our research work, further improven ents have been made. Figure II-2 is a schematic diagram of our sputtering system, and Fig. II-3 and Fig. II-4 show some of the equipment that has been used during our film preparation. We will identify each individual part later in the text.

The targets were made by pressing V_2O_3* or VO_2* powders in a $1\frac{1}{2}$" diamcter die. Figure II-3a shows the die that we used. It was made of Lehigh H stainless steel (47) which can withstand abrasions from the powders when under a uniaxial stress of about 5×10^4 psi. Generally, an eight gram load of V_2O_3 or VO_2 powder would give us a disc of $\sim 1\frac{1}{2}$" diameter and $\frac{1}{8}$" thick. The target to be sputtered was then mounted on an oxygen-free copper block with a diameter slightly smaller than that of the target by a solder of high thermal and electrical conductivity (Eccobond Solder 56c (48)). Figure II-3b shows the copper block with

---

*V_2O_3 powder obtained commercially from United Mineral and Chemical Corp., New York.
VO_2 powder obtained commercially from Alfa Inorganics, Beverly, Mass.

a pressed target of V_2O_3 mounted on it. Finally, the copper block with the target was mounted on the water-cooled electrode shown in Fig. II-2.

The substrates used were polished single crystals of sapphire of <0001>orientation obtained commercially from the Adolf Miller Co., Rhode Island. We further polished the sapphire substrates using first 1μ diamond paste and then 0.03μ syton to reduce the surface damage. The cleaning procedure for the substrates involved a five-minute scrub with Alconox and a rinse in hot water, followed by a rinse in distilled water. After they were boiled in H_2O_2 solution for ten minutes, they were rinsed in doubly distilled water and dried by blowing dry nitrogen gas over them. During the whole process (right after they were scrubbed in Alconox), they were placed in a specially built teflon basket (see Fig. II-3c) and never allowed to be dried in air. This elaborate cleaning process was used by Hensler et al. in cleaning their sapphire substrates before the deposition of VO_2 films (49).

The construction of the substrate heater is illustrated in Fig. II-4a, which also shows the substrate holder (the slot in the holder is designed to receive a standard size sapphire substrate, i.e., 0.310" square x 0.010" thick). A platinum-platinum 10% rhodium thermocouple was mounted next to the substrate.

During the presputtering process, a mechanical shutter (see Fig. II-4b) was usually placed just above the substrate and between the target and the substrate. Hence any film deposition would be on the shutter

and not on the substrate. When the operating sputtering conditions were stabilized, the shutter was removed and the actual film deposition began.

Argon gas was chosen as the sputtering gas, partly because of its inertness and partly because of its relatively large molecular weight when compared with other inert gases such as nitrogen; it thus provided a large sputtering rate. The argon gas, obtained commercially from the Igos Co., Massachusetts, with a stated purity of 99.995% was further purified by passing it through calcium turnings heated to 400°C.

V_2O_3 Films. The above sputtering system was used to grow V_2O_3 films by radio frequency sputtering of pressed V_2O_3 targets. Four polycrystalline films grown on sapphire substrates under very similar conditions. Typical operating conditions were: argon pressure at $\sim 1.6\mu$, radio frequency at 0.1 Mz, target voltage of ~ 1700 V, target current at ~ 110 ma, and substrate temperature at ~ 400°C. The sputtering lasted about five hours with a deposition rate of 1100°A/hour, as measured by an interferometer (Hilger and Watts Model 130). Three of the films grown had no post-deposition annealing, and one film, VS2, was annealed after deposition in the sputtering system (vacuum $\sim 7 \times 10^{-5}$ torr) at 300°C for two hours.

Reflection electron diffraction measurements on the films verified that these films possessed most of the rings expected for V_2O_3. Figure II-5 shows the reflection electron diffraction pattern of VS3. By assuming that the first ring corresponded to 3.65 Å of V_2O_3 from ASTM index, then the other rings corresponded to 2.70 Å, 2.46 Å, 2.32 Å, 2.17 Å, 1.83 Å, 1.68 Å, 1.46 Å, 1.42 Å, and 1.32 Å, with an

d (measured) (Å)	ASTM INDEX V_2O_3	
	d (Å)	I/I_o
3.65	3.65	60
2.70	2.70	80
2.46	2.47	60
2.32	2.32	2
2.17	2.18	20
	2.03	2
1.83	1.83	25
1.68	1.69	100
	1.61	2
	1.57	3
1.46	1.47	25
1.42	1.43	30
1.32	1.33	10

TABLE II-2. Comparison of lattice spacings of a V_2O_3 sputtered film obtained from reflection electron microscopy with the spacings listed in ASTM Index.

experimental uncertainty of about $\pm$ 1% on each peak. When compared with the ASTM Index of V_2O_3 (see Table II-2), we noticed that only three rings were missing: at 2.03 Å, 1.61 Å and 1.57 Å. Since these lines are the weakest in the series, their absence is not very surprising. The reflection electron diffraction patterns on other films were very similar and in all cases missing lines in the patterns corresponded to the weak lines in the ASTM series. Therefore, reflection electron microscopy measurements showed these films to be polycrystalline V_2O_3 films.

These films, however, did not show a distinct metal-insulator transition on cooling; their electrical resistivity at room temperature varied from $\sim 5 \times 10^{-4}$ to $10^{-3}\Omega$-cm, and typically showed a slight decrease from 2 to 8 times when the temperature was reduced from room temperature to that of liquid nitrogen.

These four films were then annealed at 600°C for 24 hours in a sealed quartz tube which had been flushed repeatedly with argon and evacuated to 10^{-5} torr. After the annealing, they all showed a large resistance increase (all had more than a factor of 10^3) when cooled from room temperature to that of liquid nitrogen. The electrical resistivity as a function of temperature of two of the films is shown in Fig. II-6. Despite the difference in the room temperature resistivity and the breadth of the structure, the resistivity change is about a factor of 10^2 at $\sim$150°K, which is close to the transition temperature of the bulk V_2O_3 crystal. The electrical measurements were done by the four probe method. Silver contacts were evaporated on a film which had been placed in a brass block and covered by a brass mask (see Fig. II-4c). Electrical leads were then attached to the silver contacts by silver epoxy. For VS2, the electrical measurement was made in a Janis Super Vari-Temp. Control Dewar Model 10-DT described in detail by Callendar (50) in his thesis. The electrical measurement on VS4 was done in a dewar designed by Ladd (16). Figure II-7 shows the copper block on which the film was mounted and the associated electrical and heater arrangements. The block was then placed in a stainless dewar and evacuated to 10^{-5} torr.

A cooling rate of 5°C/min could be obtained by immersing the dewar in liquid nitrogen and adjusting the heater current. Our temperature reading was accurate to within 1° K. Such low accuracy was quite sufficient to establish the alteration of the resistivity versus temperature relation caused by annealing.

Although the electrical characteristics of these films were different before and after annealing, the reflection electron diffraction measurements showed that the films remained polycrystalline V_2O_3 films after the annealing.

The effect of the annealing is not certain. One possibility is that the size of the crystallites increased. If this is the case, it may imply a minimum crystallite size or a minimum degree of order for a phase transition to propagate. As discussed earlier, Kennedy and Mackenzie (36) had already noted that amorphous films of V_2O_3 grown at temperature $\sim 130^{\circ}C$ were metallic both above and below the transition temperature. When annealed, a large change of resistance occurred between room temperature and 77°K. In VO_2, in addition to the absence of the phase transition, Mackenzie (37) also reported that the amorphous films deposited below the transition temperature were semiconducting while similar films deposited above the transition temperature remained metallic. If this is the case, one can deduce that the substrate temperature determines the local order, which, in turn, determines the transport mechanism, and that the insulator-metal transition is inhibited because the lattice cannot transform. The present measurements may suggest

the amorphicity is not necessary for the inhibition of the phase transition, only the greater disorder of a polycrystalline film.

Another plausible possibility is that annealing, even in a sealed quartz ampoule, changes the V-O balance, which might be important in view of the complex V-O system. Reflection electron microscopy identified the films to be of V_2O_3 structure, but it could not inform us of their exact chemical composition.

VO_2 Films. As an extension of our efforts in growing V_2O_3 films by the RF sputtering of V_2O_3 targets, a pressed target of VO_2 powder was prepared and sputtered under similar conditions as in V_2O_3. Two polycrystalline films were grown on single crystal sapphire substrates <0001> orientation, but reflection electron microscopy showed that the films were not VO_2. In fact, if we assume that the first ring corresponded to the first x-ray powder diffraction peak of $VO_{1.0}$ (51), then the rest of the rings matched with the diffraction peak of $VO_{1.0}$ to within 1%. The reason why VO_2 decomposed to VO is not known for sure. It might be due to the fact that the VO_2 target decomposed at the surface where the surface temperature could have been very high, or that if VO_2 film had indeed been grown, it might have been decomposed by the substrate temperature of 600°C. We may still be able to grow VO_2 films by this method, however, if a mixture of argon and oxygen gases, rather than argon gas alone, is used as the sputtering gas. The mixture might maintain an appropriate oxygen partial pressure in the system to allow growth of stoichiometric VO_2 films. A possible drawback to this

technique is that the reactive sputtering is not very suitable for our existing apparatus; the reasons for this are explained in the next section. In any event, our success in growing VO_2 films by the vapor transport technique to be discussed later led us to drop experimentation on the sputtering of this material.

2. Film Preparation in a Reactive Atmosphere

In our attempts to prepare VO_2 films in a reactive atmosphere, we used both electron beam gun evaporation and DC sputtering. In the former, vanadium metal in a water-cooled graphite crucible was evaporated in an oxygen atmosphere using a Veeco electron beam gun (Model VeB-6C). By adjusting the power of the gun — and thus the rate of evaporation — and the oxygen partial pressure, we should have been able to vary the vanadium-oxygen ratio in the films. Nevertheless, of the 20 or so films we grew, on BaF_2 and sapphire substrates, none showed a sharp resistance change near 67°C. Most of the films were grown with fixed oxygen partial pressure ($\sim 10^{-4}$ torr) and with varying electron gun power. There were marked differences in the electrical resistance in films grown under apparently similar conditions. The difficulties could be attributed to the many valence states of vanadium which permit it to combine with oxygen in various proportions. Therefore, the ratio of vanadium and oxygen present in the vacuum system has to be exactly right and very well controlled in order to grow good reproducible films. Since our electron beam system is a model without a fine regulation of the beam power, which was found to vary as much as 20% during runs that

typically lasted about 20 minutes, it is not surprising that the preparation of VO_2 film by this method in our system was unsatisfactory. A very well controlled electron beam system and a good regulator for the oxygen partial pressure in the vacuum system might very well allow growth of VO_2.

The same difficulties in using electron beam gun evaporation were encountered in the DC reactive sputtering of a vanadium target. The sputtering system we used was the same as the one described above, operated in the DC mode with the argon sputtering gas replaced by different mixtures of oxygen and argon gases as the sputtering gas. The gas mixtures we used were Ar 80%, O_2 20%; Ar 90%, O_2 10%; Ar 95%, O_2 5%; Ar 99%, O_2 1% and Ar 99.5%, O_2 0.5%. There were many variables in the sputtering process, among them, gas mixtures, sputtering pressure, substrate material, substrate temperature, and target current. Most films were grown on glass, Al_2O_3 and TiO_2 substrates with two gas mixtures (Ar 90%, O_2 10%; and Ar 99%, O_2 1%) by varying the sputtering pressure and/or the target voltage. None of the films that were grown — about 40 of them — showed any sharp resistivity change near 67°C. Again, we think that VO_2 films could have been grown if very well controlled operating conditions were possible.

No detailed reflection electron microscopy studies have been done on films grown either by electron beam gun evaporation or by DC reactive sputtering. Reflection electron diffraction measurements showed, in many cases, very faint rings and, in other cases, no clearly visible

structures at all. Hence, though the films are probably polycrystalline, the identification of these phases by reflection electron microscopy has been difficult.

3. Vapor Transport Technique

The vapor transport method used by Takei and Koide (7, 8) is considered to be a very flexible method of preparing high melting point materials. We therefore attempted to investigate the preparation of crystals and films by using their technique.

Figure II-8 shows a schematic of the apparatus and the reaction crucibles for both crystal and film growth. The quartz reaction chamber was heated by a resistance furnace controlled by a Barber-Colman electronic controller which regulated the temperature in the reaction crucible to about $\pm$ 5°C, as indicated by a Platinum-Platinum 13% Rhodium thermocouple placed next to the reaction chamber. Chemical vapors were passed into the reaction chamber through temperature baths controlled to within $\pm$ 5°C, and the flow rates of these vapors were regulated by flowmeters to better than $\pm$ 10% of their values. The chemical equations used in this method* are:

$$2VOCl_3 + 3H_2O \rightarrow V_2O_5 + 6HCl$$

$$VOCl_3 + H_2O + \frac{1}{2} H_2 \rightarrow VO_2 + 3HCl$$

$$2VOCl_3 + H_2O + 2H_2 \rightarrow V_2O_3 + 6HCl$$

*$VOCl_3$ solution was obtained commercially from Howe & French Company, Boston, Mass.

V_2O_3 Crystals. A few runs were made to produce crystals of V_2O_3. The best run yielded a reasonable number — about 50 — of V_2O_3 crystals roughly 2 mm in diameter by 0.5 mm long. The actual operating conditions can be explained by reference to Fig. II-8, with the parameters taking the following values: $T_1 = 800^{\circ}C$; $T_2 = 60^{\circ}C$; $T_3 = 30^{\circ}C$; $V_1 = 3.8$ cc/min; $V_2 = 0.36\ \ell$/min; $V_3 = 0.3\ \ell$/min; and reaction time = 160 hours. The parameters used here, as well as those used in the growth of V_2O_3 and VO_2 films by this method were chosen with reference to those used by Takei (8). Some adjustments of his parameters were necessary for our system, and our parameters were arrived at empirically after several trial runs. X-ray Debye Scherrer analysis showed the crystals were V_2O_3, and x-ray Laue back reflection using tungsten radiation showed them to be single crystals with the c-axis of V_2O_3 perpendicular to the plane of the platelet. Chemical analysis (52) showed them to be $68.0 \pm 0.5\%$ by weight of vanadium, while stoichiometric V_2O_3 should be 67.98% by weight of vanadium. Spectrographic analysis (52) established that the impurities which are observable by this analysis, were about 1 part per million.* Optical and optical microscopy examination showed one natural surface of each crystal to be usually very flat and shiny with no visible structure, making the crystals suitable for optical reflectivity measurement.

Figure II-9 shows the resistivity versus the temperature of one of the crystals, together with a comparison with previous investigations.

*Elements such as nitrogen, carbon, oxygen, and hydrogen, however, are not detectable by this method.

The data were obtained by a four point probe measurement done in the same apparatus as discussed earlier in this chapter. The actual resistivity value was estimated to within a factor of about 2 or 3 because of the irregular shape of the crystal.

Two additional crystal runs were made to try to reproduce the most successful run discussed above. In both of these runs, we obtained crystals about half the size of those grown in the best run. They were also identified to be V_2O_3 by the x-ray Debye Scherrer measurements. However, these crystals did not have the natural shiny optical surfaces that those grown in the best run possessed, and, therefore, were not used for optical measurements.

V_2O_3 Films. Because of our success in obtaining V_2O_3 crystals, we tried to grow epitaxial films of V_2O_3 on single crystal sapphire substrates with <0001> orientation. Several films were grown that showed large resistance changes (a factor of larger than 10^2) as the temperature was decreased from room temperature to 77°K. One of the films grown was scraped off the substrate and was checked by x-ray Debye-Scherrer measurements. The measurements showed faint rings whose positions corresponded to V_2O_3 x-ray lines from the ASTM index. But since the amount of scraped powder was very minute, there is a possibility of other phases existing in the film in smaller proportions. Reflection electron microscopy determined that these films were essentially epitaxial though it is possible that there were some small angle boundaries between the crystallites. By optical microscope examination, th[illegible]

surfaces were rough compared with those of the crystals, with needle-like protuberances on occasion. The thickness of these films were usually uneven, often thinner on the edge than in the middle. Measurement of their thickness was, therefore, difficult. We used a Pratt and Whitney electrolimit gauge (accurate to $\sim \frac{1}{4}$ micron) to estimate the thickness of the films.

Figure II-10a shows the reflection electron diffraction pattern of one of the films which was grown on a sapphire substrate cut with the c-axis perpendicular to the plane of the substrate. The film has a reasonably smooth surface, as can be seen in Fig. II-10b. Though we did not try to determine the orientation of the film on the substrate, some of the crystallites on the surface had a hexagonal shape, indicating that the film might have grown with the c-axis perpendicular to the plane of the substrate. The electrical resistivity measurements on the film as a function of temperature were done in the dewar discussed earlier in the chapter. Only a two probe measurement was done on this film because of its small physical size (see Fig. II-7). The resistivity value reported in the above figure is an approximate one, partly because of the uneven-ness of the film thickness, and partly because of the inaccuracy of a two probe measurement on an irregular-shaped film. Nevertheless, the film showed a resistance change of $\sim 10^2$ in the same region where the phase transition occurs in crystals of V_2O_3 (see Fig. II-9). This film was grown under the following conditions: $T_1 = 800^{\circ}C$; $T_2 = 60^{\circ}C$; $T_3 = 30^{\circ}C$; $V_1 = 3.8 cc/min$; $V_2 = 0.36 \ell/min$; $V_3 = 0.15 \ell/min$; reaction time $\tilde{=}$ 42 hours; with film thickness $\tilde{=} 2\mu$.

Reproducibility of the vapor transport film was not good. Under similar conditions, we tried twice to reproduce the above film; once we did get a film that showed a large resistance increase of a factor of $\sim 10^3$ from room temperature to the temperature of liquid nitrogen, but another time a thin discontinuous grey film was obtained.

VO_2 Films. Attempts were made to grow VO_2 films on single crystal sapphire substrates with <0001> orientation. Several films grown indicated resistance changes of more than a factor of 10^2 for the temperature interval from room temperature to $\sim 80^\circ C$. Figure II-11 shows the reflection electron diffraction pattern (indicated the film to be epitaxial) and the optical microscope picture of one of the films grown, under the following conditions; $T_1 = 800^\circ C$; $T_2 = 60^\circ C$; $T_3 = 30^\circ C$; $V_1 = 5.7$ cc/min; $V_2 = 0.36\ \ell$/min; $V_3 = 0.32\ \ell$/min; reaction time = 42 hours; with film thickness $\tilde{=} 1.5\mu$.

Figure II-12 shows the resistivity versus temperature plot of the film. The measurement was done in the dewar discussed earlier in this chapter. The resistivity value of the film as reported in the above figure, is only an approximate one, again because of the irregular shape of the film and the inaccuracy of the two probe measurement. A sharp resistance change of a factor of $\sim 10^2$ was indeed observed around $67^\circ C$, which is close to that of bulk crystals as demonstrated in Fig. II-12.

VO_2 Crystals. Several attempts were made to grow VO_2 crystals with no apparent success. Most of the runs produced crystals that had mixtures of different vanadium oxides, including VO_2. Since

high quality VO_2 crystals had already been successfully grown by Ladd and Paul (15), and since considerable time would have to be spent to obtain the proper growth conditions, we decided to proceed no further.

4. Tri-Arc Czochralski Crystal Growth Technique

$(V_{1-x}Cr_x)_2O_3$ Crystals. Single crystals of V_2O_3 and V_2O_3 doped with chromium were grown in a tri-arc furnace in Lincoln Laboratory.* Three electric arcs were used to heat a melt in a graphite crucible surrounded by a water-cooled copper block. The crystal was pulled from the center of the melt with a water-cooled seed rod. Use of this experimental setup eliminated the difficulty of finding crucible materials suitable for high temperature growth, since the melt was contained by a solid shell of the same substance in contact with the cooled crucible. Figure II-13 shows a cross-section drawing of the tri-arc Czochralski crystal growing furnace. (A detailed discussion of this technique of crystal growth can be found by referring to Reed and Pollard's paper (55)).

V_2O_3 and $(V_{1-x}Cr_x)_2O_3$ can be grown easily by this method because of their partial oxygen vapor pressure. Figure II-14 shows a plot of oxygen partial pressure versus oxygen-metal ratio for different elements (56). This was obtained from theoretical calculation of the free energy of formation of these materials at 1000°K. It is noted from the chart that the oxygen partial pressures of V_2O_3 and Cr_2O_3 are both very low and have approximately the same value. Therefore, if V_2O_3 crystals can be grown in the apparatus, growth of Cr_2O_3 crystals, and the alloys of Cr_2O_3 - V_2O_3 should not be difficult. In addition, because

* In collaboration with Dr. T.B. Reed.

of the very low oxygen partial pressure of both Cr_2O_3 and V_2O_3, negligible amounts of oxygen should be lost in the growth process, and the resulting crystals should be stoichiometric.

To grow crystals of V_2O_3, the graphite crucible was first charged with 10-30 grams of V_2O_3 powder. The furnace chamber was then flushed by argon for several minutes and then maintained just above atmospheric pressure by a steady flow of argon gas (~ 1000cc/min). The first arc was started by touching its tungsten cathode to the side of the graphite crucible. The cathode was then moved in to strike the charge. The other two arcs were started the same way, or by touching their cathodes to the first arc. The heat was then increased until a melt was formed. The seed, a molybdenum stud in our particular case, was then dipped into the melt and raised rapidly to form a small neck in the growing crystal in order to eliminate polycrystallinity. The crystal was then raised typically at 4 in/hr, and its diameter was increased either by decreasing the arc current or by moving the cathodes out toward the edge of the melt. During the pulling process, the melt and pull rod were both rotating at a speed of 50-100 cycles/min for better mixing and distribution of heat. When the crystal reached a reasonable size, the pulling rod was raised much faster so that the crystal would break away from the melt. The melt was then cooled slowly. Single crystals of V_2O_3 of reasonable sizes were usually also found in the cooled melt. Figure II-15 shows the crystals grown by this technique. The largest one obtained by pulling from the melt, and the others were grown in the melt.

Run	Chromium Concentration (average over a number of crystals)	Mass Spectroscopic Analysis Δ	Optical Measurements *	X-Ray Diffraction Measurements **
1	0		X	
2	0	X		X
3	0.0022		X	
4	0.0020	X		X
5	0.0045		X	X
6	0.0083			
7	0.010		X	X
8	0.014		X	X
9	0.018	X	X	X

Δ Results of mass spectroscopic analysis are listed on pp. II-33, 34.

* Results of optical measurements will be presented in Chapter IV.

** Results of x-ray diffraction measurements are shown in Fig. II-16.

TABLE II-3. List of Crystal Runs and Measurements on the Crystals

To grow single crystals of $(V_{1-x}Cr_x)_2O_3$, an appropriate mixture of V_2O_3 and Cr_2O_3 powders was used. Though similar operating procedures were followed, we found that it was much harder to pull a large crystal from the melt since the crystal would tend to crack easily.

Therefore, our doped crystals were usually grown by melting the mixed powders with the arcs, then cooling the melt to room temperature. They were usually ~ 2-3 mm across and 3-4 mm long. Table II-3 lists our crystal runs and some of the measurements that have been made on the crystals.

Chemical spectrophotometric analysis on one of the V_2O_3 crystals (Run #2) showed that it contained $68.0 \pm 0.1\%$ by weight of vanadium, while the stoichimetric V_2O_3 would contain 67.98% by weight of vanadium.

The experimental uncertainty in the chemical spectrophotometric analysis for the chromium concentration in the crystals obviously depends on the amount of chromium present in the test, and in our cases, it was within $\pm$ 4% for $x = 0.002$, and decreased to within $\pm$ 1% for $x = 0.02$. The chemical analysis of the doped crystals showed that the average doping concentrations (averaged over a number of crystals) in each run was ususally within 10% of the initial doping concentration in the powders. This was partially due to the fact that when the powders were heated up by the arcs, the trapped air in the powders often scattered the powders around, some of it often getting away from the crucible. Furthermore, some segregation (i.e., the ratio of two components in the solid phase usually is different from that in the liquid phase, and usually this ratio itself varies along the length of solid) inevitably must have occurred. When a two-component liquid solidifies, segregation often occurs (57).

To check the effects of segregation in our system, the chemical analysis was done on a number of crystals and on the grains from the melt obtained on the same crystal run (Run #6). It was found that the average chromium doping level of the crystals was x = 0.0083 and was only ~ 6% lower than that of the grains. Therefore, the segregation in $(V_{1-x}Cr_x)_2O_3$ was small when compared with the segregation of many two-component systems, such as indium or antimony in germanium (58). These small segregation effects were further demonstrated by a series of analyses on four doped single crystals (each about 3 mm across and 2 mm long). They were broken into two parts and chemical analyses were performed on the separate parts. The analyses showed that the chromium doping level, x, in one of the crystals grown in Run #5 was 0.0047 and that there was no variation in the doping level between the two parts of the crystal. A crystal obtained from each of Runs #8 and #9 evidenced only ~ 6% difference in the doping level between the two parts of the same crystal; the average chromium doping level, x, was found to be respectively 0.014 and 0.019. The analysis was also done on a second crystal from Run #9, and a difference of 10% in the doping level between the two parts of the same crystal was observed; the average doping level in this crystal was found to be 0.018.

Thus, the variation of chromium concentration within the crystals, as indicated by the chemical analyses, was small when the uncertainty of the chemical analyses themselves is taken into consideration. The slight variation in chromium concentration within these crystals was

probably due to the fact that the crystals were grown by a relatively rapid solidification from the melt. A detailed explanation of the effect of the rate of solidification on the segregation of a two-component system can be found in reference 57. It is sufficient to point out that in solidification, the two homogeneously-mixed components in the liquid phase are essentially quenched into the solid phase, resulting in very little segregation.

In the above-mentioned analyses of the four crystals, it can be seen that the segregation effects also cause slight variations of doping levels in different crystals from the same growth run. Therefore, chemical analyses, whenever possible, were done individually on crystals whose physical properties were measured, and particularly those whose optical properties were measured. The doping level reported for such a crystal was the average chromium concentration in the crystal. For a crystal which was not individually analyzed, its doping level was approximated by taking the doping level as determined from analyses of a number of crystals grown at the same time, subjected to an uncertainty level of $\pm$ 5% of its value.

Mass spectrographic analysis on a single crystal of V_2O_3 from Run #2 showed that the impurity contents were 130 p.p.m. of carbon; 300 p.p.m. of aluminum, 70 p.p.m. of iron; and less than 50 p.p.m. of nitrogen, titanium, molybdenum, potassium, and sodium each. In $(V_{1-x}Cr_x)_2O_3$ crystals, mass spectrographic analysis on a crystal from Run #4 showed impurity contents to be 360 p.p.m. of carbon,

100 p.p.m. of sodium; and less than 50 p.p.m. of nitrogen, silicon, potassium, and titanium each. On a crystal from Run #9, we found impurity contents to be 80 p.p.m. of carbon and less than 50 p.p.m. of sodium, nitrogen, aluminum, silicon, potassium and molybdenum each.

X-ray Laue back reflection measurements on V_2O_3 and doped V_2O_3 crystals all showed sharp diffraction spots indicating that they were single crystals. From x-ray diffraction measurements, we obtained lattice constants, a_H and c_H (as defined in a hexagonal lattice) of V_2O_3 and $(V_{1-x}Cr_x)_2O_3$ crystals as a function of doping concentrations (see Fig. II-16). We also noted that when x was between ~ 0.010 and ~ 0.015, there were two phases coexisting at room temperature. This co-existence of two phases was also observed by McWhan and Remeika (25).

V_2O_3 crystals and $(V_{1-x}Cr_x)_2O_3$ crystals grown by the flux method have been reported to be quite soluble in boiling water (25), though the exact solubility is not known. The solubility of a V_2O_3 crystal from Run #2, however, was examined by boiling it in water for twelve hours. Its weight was found to decrease only by $\sim 0.6\%$. Even this small weight decrease could have been caused by having some chips broken away from the crystal during boiling. A doped crystal from Run #9 which was boiled in water for five days, showed a weight decrease of only 0.2%. Therefore, in contrast to what has been reported, these crystals have very low, if any, solubility in water.

probably due to the fact that the crystals were grown by a relatively rapid solidification from the melt. A detailed explanation of the effect of rate of solidification on the segregation of a two-component system can be found in reference 57. It is sufficient to point out that in solidification, the two homogeneously-mixed components in the liquid phase are essentially quenched into the solid phase, resulting in very little segregation.

In the above-mentioned analyses of the four crystals, it can be seen that the segregation effects also cause slight variations of doping levels in different crystals from the same growth run. Therefore, chemical analyses, whenever possible, were done individually on crystals whose physical properties were measured, and particularly those whose optical properties were measured. The doping level reported for such a crystal was the average chromium concentration in the crystal. For a crystal which was not individually analyzed, its doping level was approximated by taking the doping level as determined from analyses of a number of crystals grown at the same time, subjected to an uncertainty level of $\pm$ 5% of its value.

Mass spectrographic analysis on a single crystal of V_2O_3 from Run #2 showed that the impurity contents were 130 p.p.m. of carbon; 300 p.p.m. of aluminum, 70 p.p.m. of iron; and less than 50 p.p.m. of nitrogen, titanium, molybdenum, potassium, and sodium each. In $(V_{1-x}Cr_x)_2O_3$ crystals, mass spectrographic analysis on a crystal from Run #4 showed impurity contents to be 360 p.p.m. of carbon,

100 p.p.m. of sodium; and less than 50 p.p.m. of nitrogen, silicon, potassium, and titanium each. On a crystal from Run #9, we found impurity contents to be 80 p.p.m. of carbon and less than 50 p.p.m. of sodium, nitrogen, aluminum, silicon, potassium and molybdenum each.

X-ray Laue back reflection measurements on V_2O_3 and doped V_2O_3 crystals all showed sharp diffraction spots indicating that they were single crystals. From x-ray diffraction measurements, we obtained lattice constants, a_H and c_H (as defined in a hexagonal lattice) of V_2O_3 and $(V_{1-x}Cr_x)_2O_3$ crystals as a function of doping concentrations (see Fig. II-16). We also noted that when x was between ~ 0.010 and ~ 0.015, there were two phases coexisting at room temperature. This co-existence of two phases was also observed by McWhan and Remeika (25).

V_2O_3 crystals and $(V_{1-x}Cr_x)_2O_3$ crystals grown by the flux method have been reported to be quite soluble in boiling water (25), though the exact solubility is not known. The solubility of a V_2O_3 crystal from Run #2, however, was examined by boiling it in water for twelve hours. Its weight was found to decrease only by $\sim 0.6\%$. Even this small weight decrease could have been caused by having some chips broken away from the crystal during boiling. A doped crystal from Run #9 which was boiled in water for five days, showed a weight decrease of only 0.2%. Therefore, in contrast to what has been reported, these crystals have very low, if any, solubility in water.

Electrical conductivity as a function of temperature was measured by Honig (59) on one of the V_2O_3 crystals grown by the tri-arc technique, and he observed a resistivity change of a factor of $\sim 10^7$ at 157°K on cooling and 168°K on heating (59). No electrical data have been collected on our doped crystals.

In this chapter, we have investigated various techniques of preparing films and crystals of VO_2 and V_2O_3, and the tri-arc technique of growing single crystals of $(V_{1-x}Cr_x)_2O_3$. We have also reported on some of their structural and electrical properties. We now turn to an examination of their optical properties.

C. Summary

Single crystals of V_2O_3, and crystalline films of V_2O_3 and VO_2, have been successfully grown by the vapor transport technique. RF sputtering of V_2O_3 targets was found to be suitable for the growth of crystalline films of V_2O_3. The tri-arc furnace was successfully used to produce single crystals of V_2O_3 and of $(V_{1-x}Cr_x)_2O_3$ alloys. On the other hand, for diverse reasons elaborated in the main text, single crystal VO_2 was not produced by us by vapor transport, films of VO rather than VO_2 were grown by sputtering of VO_2 targets, and films grown in a reactive atmosphere, whether using electron beam evaporation or DC sputtering did not appear to be VO_2 or V_2O_3.

The single crystals grown by these methods appear to be at least comparable in quality with those grown by the other techniques discussed in Section A. Indeed, the vapor-grown V_2O_3 may be freer of defects, and the tri-arc material more easily and more controllably reproduced.

Duplication of the success of Takei and Koide and of Bando et al. in growing VO_2 single crystals by vapor transport would appear to be a matter of adjustment of growth parameters only.

While the vapor transport method served us best for the production of crystalline films of VO_2 and V_2O_3, our success in sputtering crystalline V_2O_3 films, and earlier successes of other workers in growing crystalline VO_2 films in a reactive atmosphere, suggest that all of the methods cited will serve, provided care and patience are exercised in varying,controlling and regulating the deposition parameters. (Note here the experience of Sosnick (54) and Fuls et al. (30) in sputtering VO_2 films reproducibly.) Thus, for deposition in a reactive atmosphere, the partial pressure of oxygen must be well-regulated, and the vanadium deposition rate must be finely adjustable and controllable. For RF sputtering of targets of the desired material, the target and substrate temperatures and the sputtering rates must be optimized. Our success with the vapor transport technique probably stems from the fact that we spent considerable effort in varying and controlling the parameters there, and we had the advantage of knowledge of a combination of parameters found to be successful by the Japanese group. In spite of the difficulties of reproducibility, our films of VO_2 and V_2O_3 did clearly exhibit sharp transitions in resistivity (see Fig. II-12 for VO_2 and Fig. II-6 for V_2O_3). These films therefore appear to be suitable to obtain optical data in order to complement those of thin bulk single crystals, which was our primary purpose in growing them in the first place.

REFERENCES

1. F.J. Morin, Phys. Rev. Letters 3, 34 (1959).
2. "The Art and Science of Growing Crystals," J.J. Gilman, ed., p. 231, Wiley, 1963.
3. H. Sasaki and A. Watanabe, J. Phys. Soc. Japan 19, 1748 (1964).
4. J.B. MacChesney and H.J. Guggenheim, J. Phys. Chem. Solids 30, 225 (1969).
5. C.R. Everhart and J.B. MacChesney, J. Appl. Phys. 39, 2872 (1968).
6. I. Kitahiro, A. Watanabe and H. Sasaki, J. Phys. Soc. Japan 21, 196 (1966).
7. H. Takei and S. Koide, J. Phys. Soc. Japan 21, 1010 (1966).
8. H. Takei, Japan J. Appl. Phys. 7, 827 (1968).
9. Y. Bando, K. Nagasawa, Y. Kato and T. Takada, Japan J. Appl. Phys. 8, 633 (1969).
10. K. Nagasawa, Y. Bando and T. Takada, Japan J. Appl. Phys. 8, 1267 (1969).
11. K. Nagasawa, Y. Bando and T. Takada, Japan J. Appl. Phys. 8, 1262 (1969).
12. K. Nagasawa, Y. Bando and T. Takada, Japan J. Appl. Phys. 9, 407 (1970).
13. K. Nagasawa, Y. Bando and T. Takada, Japan J. Appl. Phys. 9, 841 (1970).
14. T. Niemyski and W. Piekarczyk, J. Crystal Growth, 1, 177 (1967).
15. L. Ladd and W. Paul, Solid State Comm. 7, 425 (1969).
16. L. Ladd, Tech. Rept. No. HP-26, Gordon McKay Laboratory, Harvard University, 1971 (unpublished).
17. L.E. Sobon and P.E. Greene, J. Am. Ceram. Soc. 49, 106 (1966) and private communication.

18. "The Art and Science of Growing Crystals," J.J. Gilman, ed., p. 398, Wiley, 1963.

19. J. Feinleib and W. Paul, Phys. Rev. 155, 841 (1967).

20. J. Feinleib, Tech. Rept. No. HP-11, Gordon McKay Laboratory, Harvard University, 1963 (unpublished).

21. Linde Company, Speedway Laboratory, Speedway, Indiana.

22. G. Goodman, Phys. Rev. Lett. 9, 305 (1962).

23. I.G. Austin and C.E. Turner, Phil. Mag. 19, 939 (1969).

24. V.P. Zhuze, A.A. Andreev and A.I. Shelykh, Sov. Phys. – Solid State 10, 2914 (1969).

25. D.B. McWhan and J.P. Remeika, Phys. Rev. B2, 3734 (1970).

26. K. van Steensel, F. Van de Burg and C. Kooy, Phillips Res. Rept. 22, 170 (1967).

27. S. Koide and H. Takei, J. Phys. Soc. Japan 22, 946 (1967).

28. J.B. MacChesney, J.F. Potter and J.J. Guggenheim, J. Electrochem. Soc. 115, 52 (1968).

29. G.A. Rozgonyi and W.J. Polito, J. Electrochem. Soc. 115, 56 (1968).

30. E.N. Fuls, D.H. Hensler and A.R. Ross, Appl. Phys. Lett. 10, 199 (1967).

31. G.A. Rozgonyi and D.H. Hensler, J. Vacuum Sci. and Tech. 5, 194 (1968).

32. D.H. Hensler, A.R. Ross and E.N. Fuls, J. Electrochem. Soc. 116, 887 (1969).

33. C.N. Berglund, IEEE Trans. Electron Devices ED-16, 432 (1969).

34. C.N. Berglund and R.H. Walden, IEEE Trans. Electron Devices ED-17, 137 (1970).

35. R.G. Cope and A.W. Penn, Brit. J. Appl. Phys. (J. Phys. D.) SER 2, 161 (1968).

36. T. N. Kennedy and J. D. Mackenzie, J. Non-Crystalline Solids 1, 326 (1969).

37. J. D. Mackenzie, "Congres. International Sur les Couches Minces," Cannes, France, p. 275, 1970.

38. "Handbook of Chemistry and Physics," R. C. Weast, ed., 52nd Edition, Chemical Rubber Co., p. B-152, 1971.

39. C. E. Rossi, Tech. Rept. No. HP-18, Gordon McKay Laboratory, Harvard University, 1968 (unpublished).

40. W. Crookes, Proc. Roy. Soc. London 50, 88 (1891).

41. F. Stark, Z. Electrochem. 15, 509 (1909).

42. G. K. Wehner, Phys. Rev. 108, 35 (1957).

43. G. K Wehner, J. Appl. Phys. 34, 3492 (1963).

44. F. Keywell, Phys. Rev. 97, 1611 (1955).

45. D. E. Harrison, Jr., J. Chem. Phys. 32, 1336 (1960).

46. R. S. Pease, Nuovo Cimento, Suppl. 13 (1960).

47. Austin-Hastings Co., Inc., Woburn, Mass.

48. Emerson & Cummings, Inc., Canton, Mass.

49. D. H. Hensler, Bell Telephone Lab., private communication.

50. R. H. Callender, Ph. D. Thesis, Gordon McKay Laboratory, Harvard University, p. 3-6, 1969 (unpublished).

51. Klemm von Wilholm and Ludwig Grimm, Zeit. alleg. Chem. 250, 42 (1942).

52. MIT Central Analytical Lab., M. I. T., Cambridge, Mass.

53. P. F. Bongers, Solid State Comm. 3, 275 (1965).

54. J. Sosnick, Bell Telephone Laboratories, private communication.

55. T. B. Reed and E. R. Pollard, J. Crystal Growth 2, 243 (1968).

56. T. B. Reed, "Free Energy of Binary Crystals," M.I.T. University Press, Cambridge, 1971.

57. "The Art and Science of Growing Crystals," J.J. Gilman, ed., pp. 278-279, Wiley, 1963.

58. "Semiconductors," N.B. Hannay, ed., p. 156, Reinhold Publ. Corp., New York, 1959.

59. J.M. Honig, Purdue University, Indiana, private communication.

60. K. Kosuge, J. Phys. Chem. Solids 28, 1613 (1967).

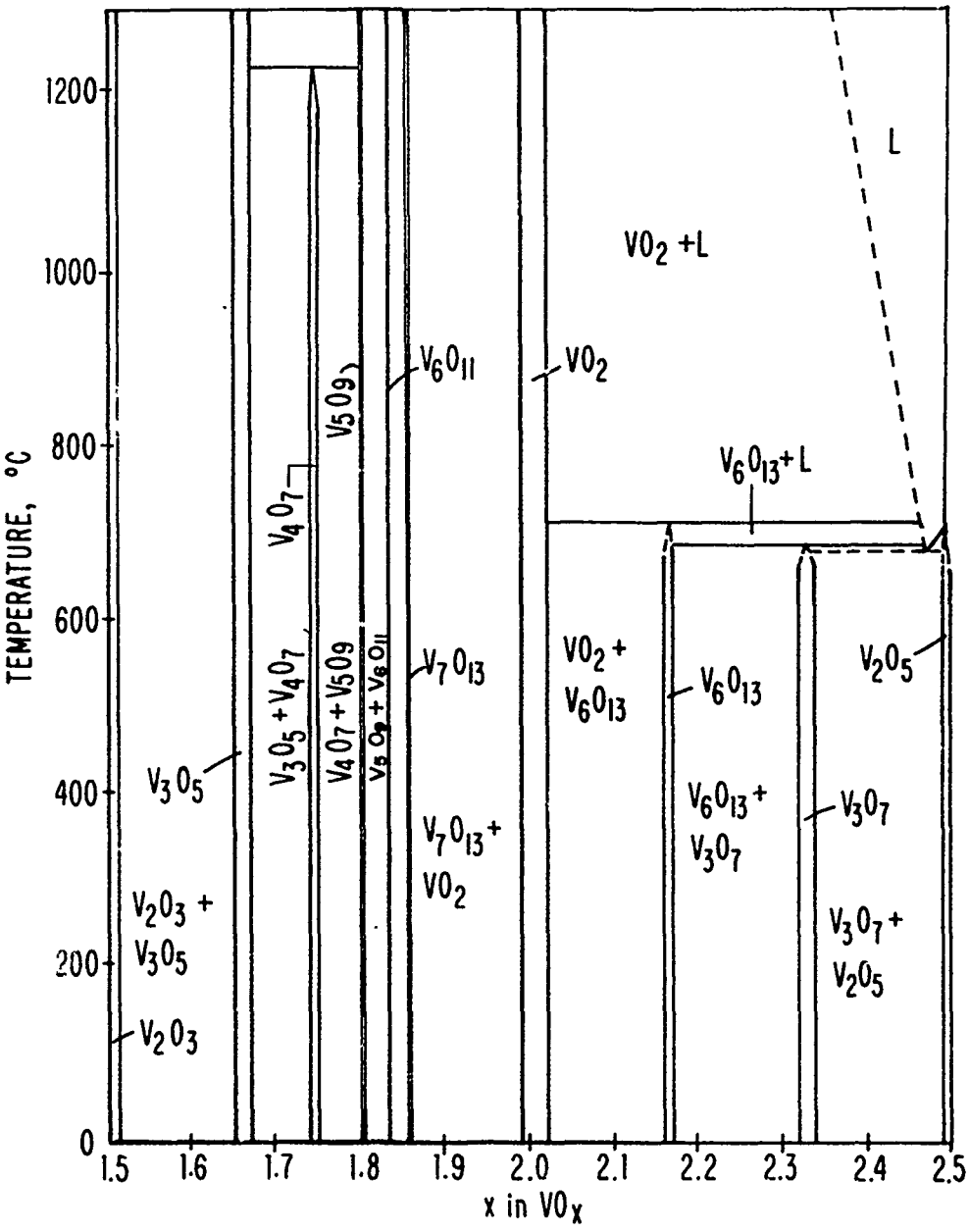

FIGURE II-1 Phase diagram of VO_x for x = 1.5 to 2.5 (60).

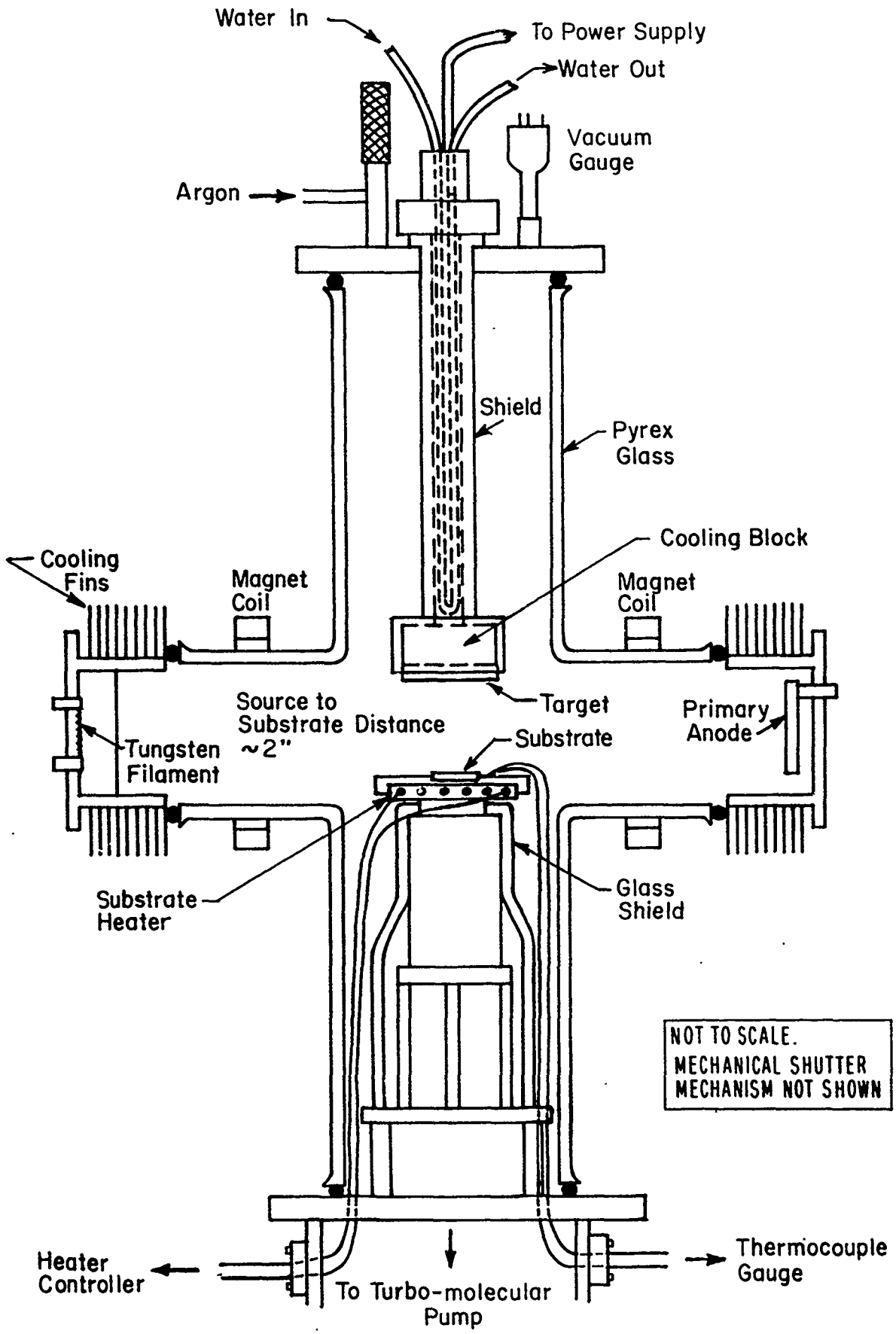

FIGURE II-2 Schematic diagram of our sputtering system.

Die

(a)

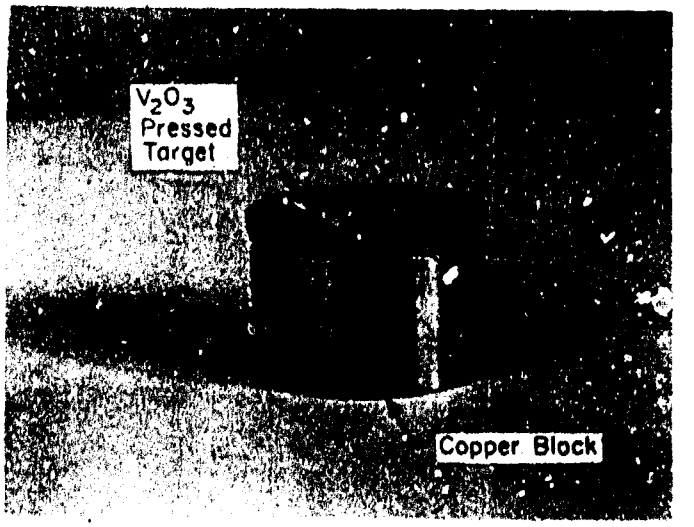

(b)

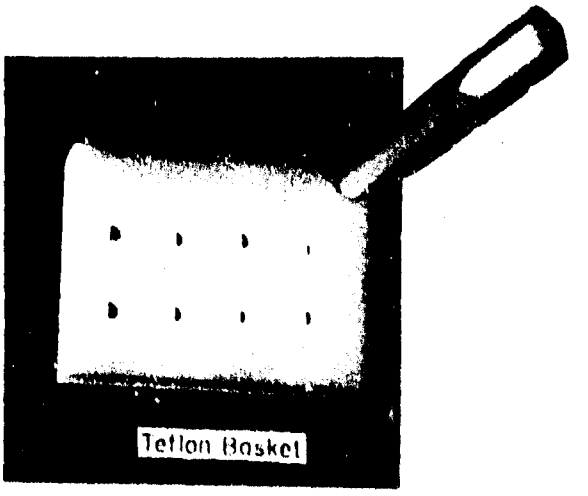

(c)

FIGURE II-3 Various parts used in sputtering.

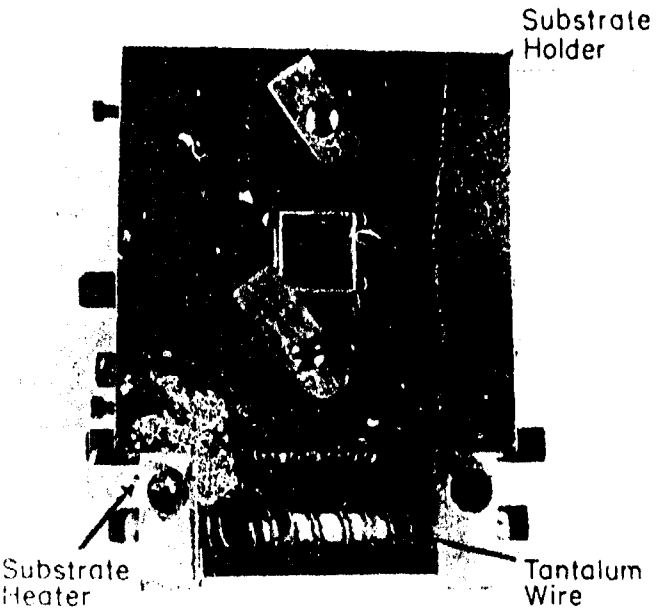

(a)

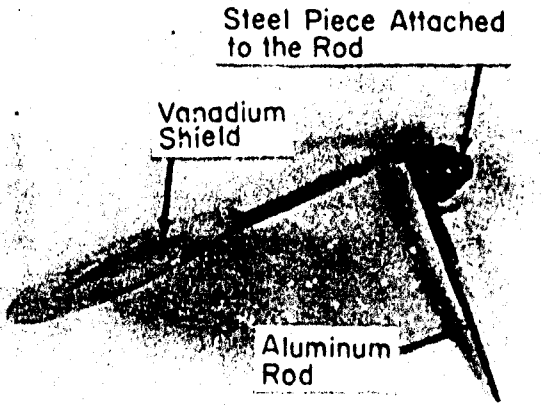

(b)

Shutter assembly is swung out of the path of deposition by a magnet (located outside of the bell jar of the sputtering system) which acts on the steel piece

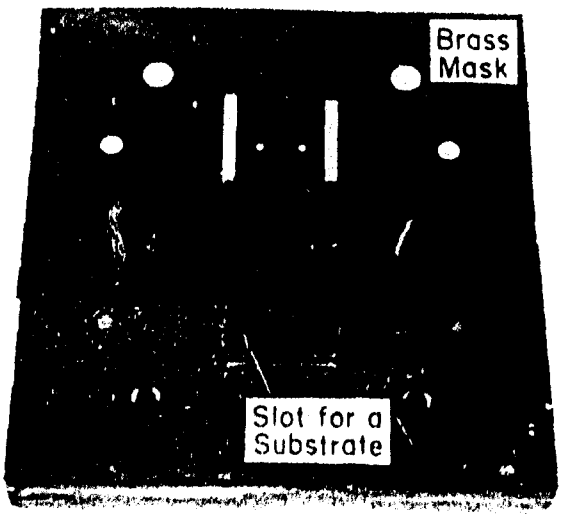

(c)

FIGURE II-4 Various parts used in sputtering.

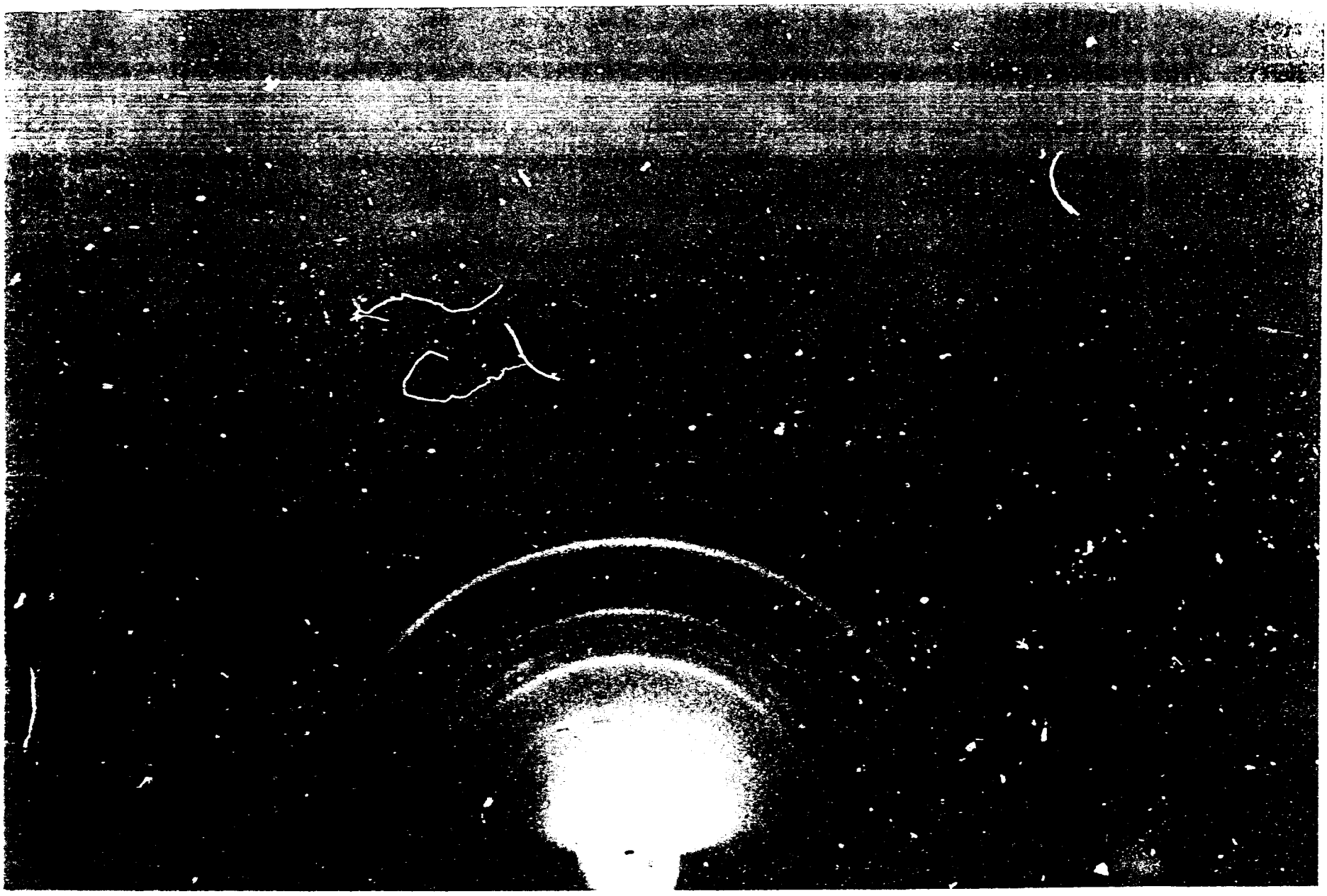

FIGURE II-5 Reflection electron diffraction pattern of a V_2O_3 sputtered film (Hitachi Electron Microscope Model HU-11).

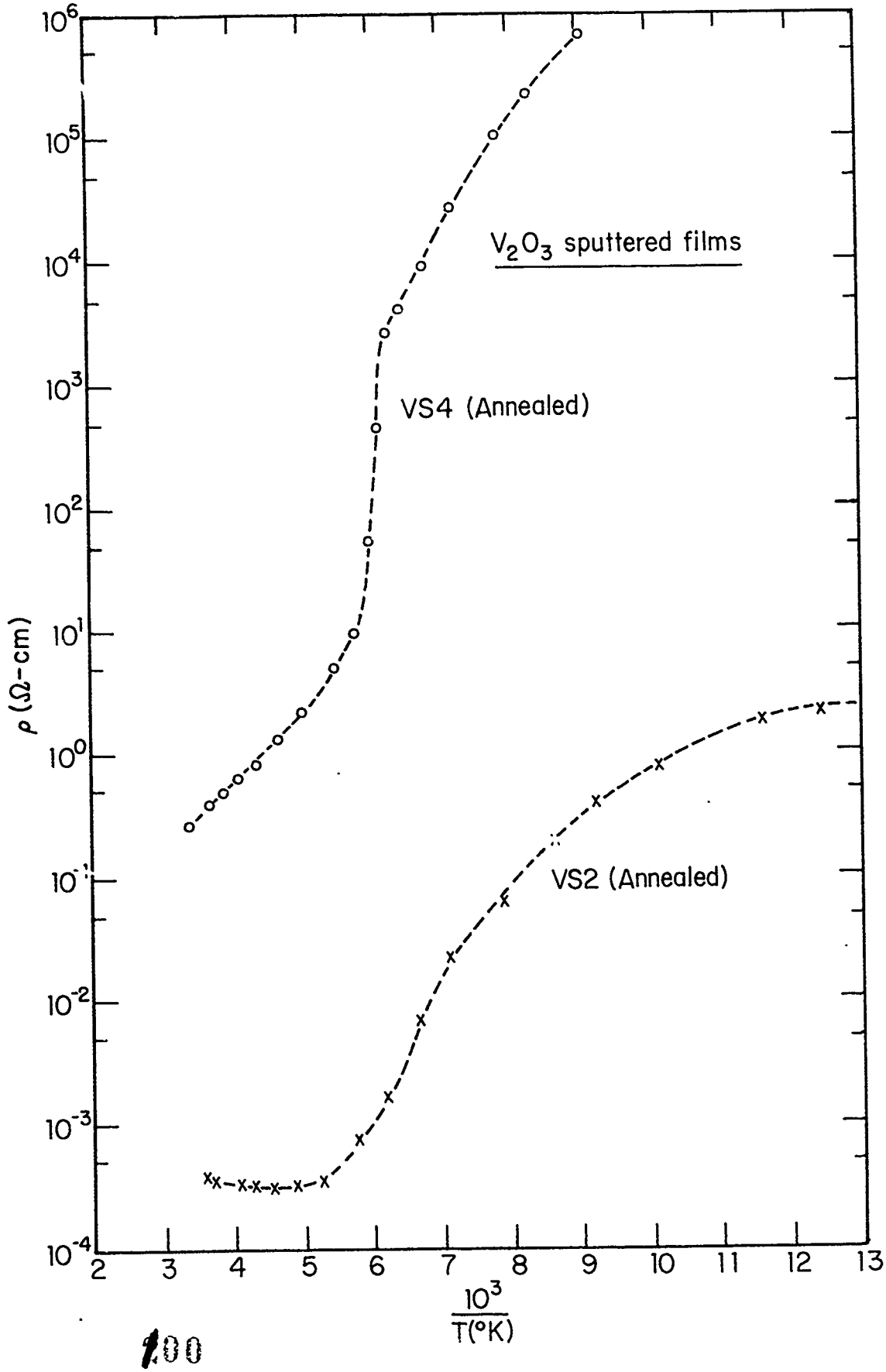

100

FIGURE II-6 Resistivity versus temperature of two annealed sputtered films of V_2O_3.

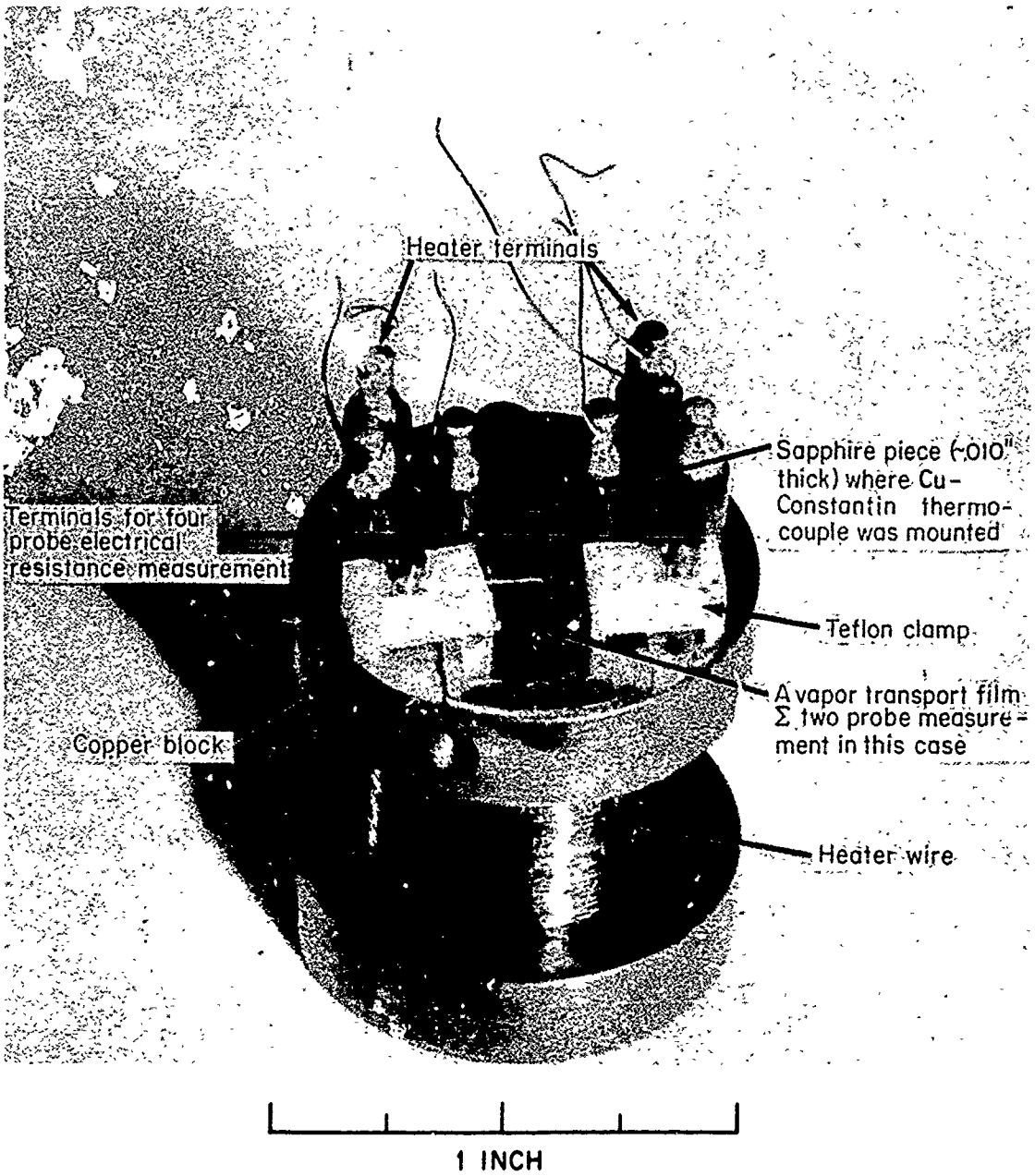

FIGURE II-7 Sample holder for resistance versus temperature measurements.

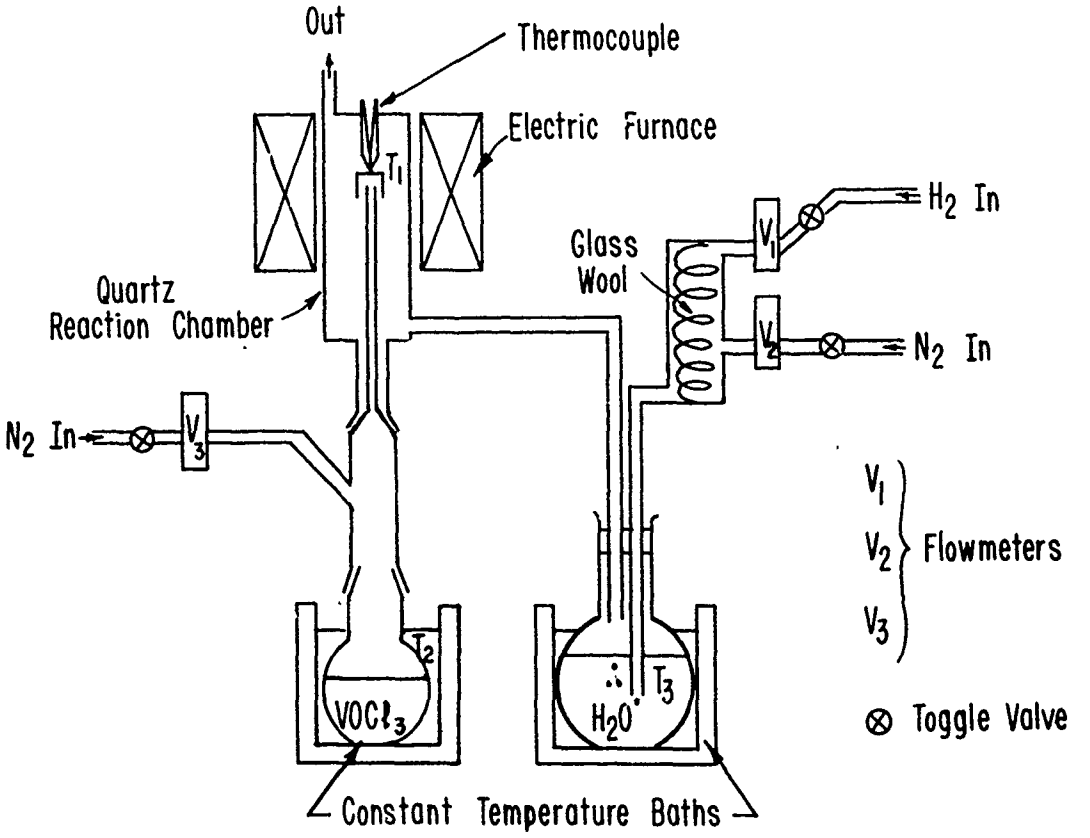

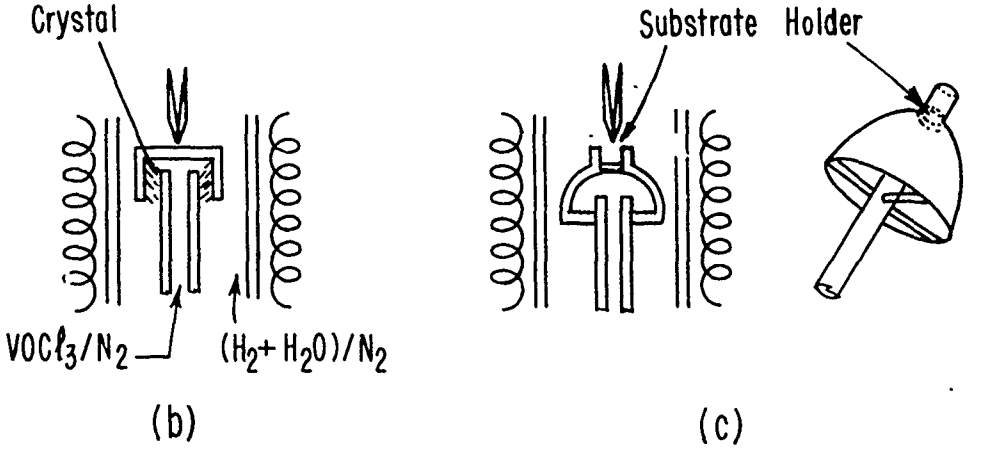

FIGURE II-8 (a) Schematic diagram of vapor transport apparatus.
(b) Detail of the crystal reaction crucible in the quartz reaction chamber.
(c) Detail of the film crucible in the chamber.

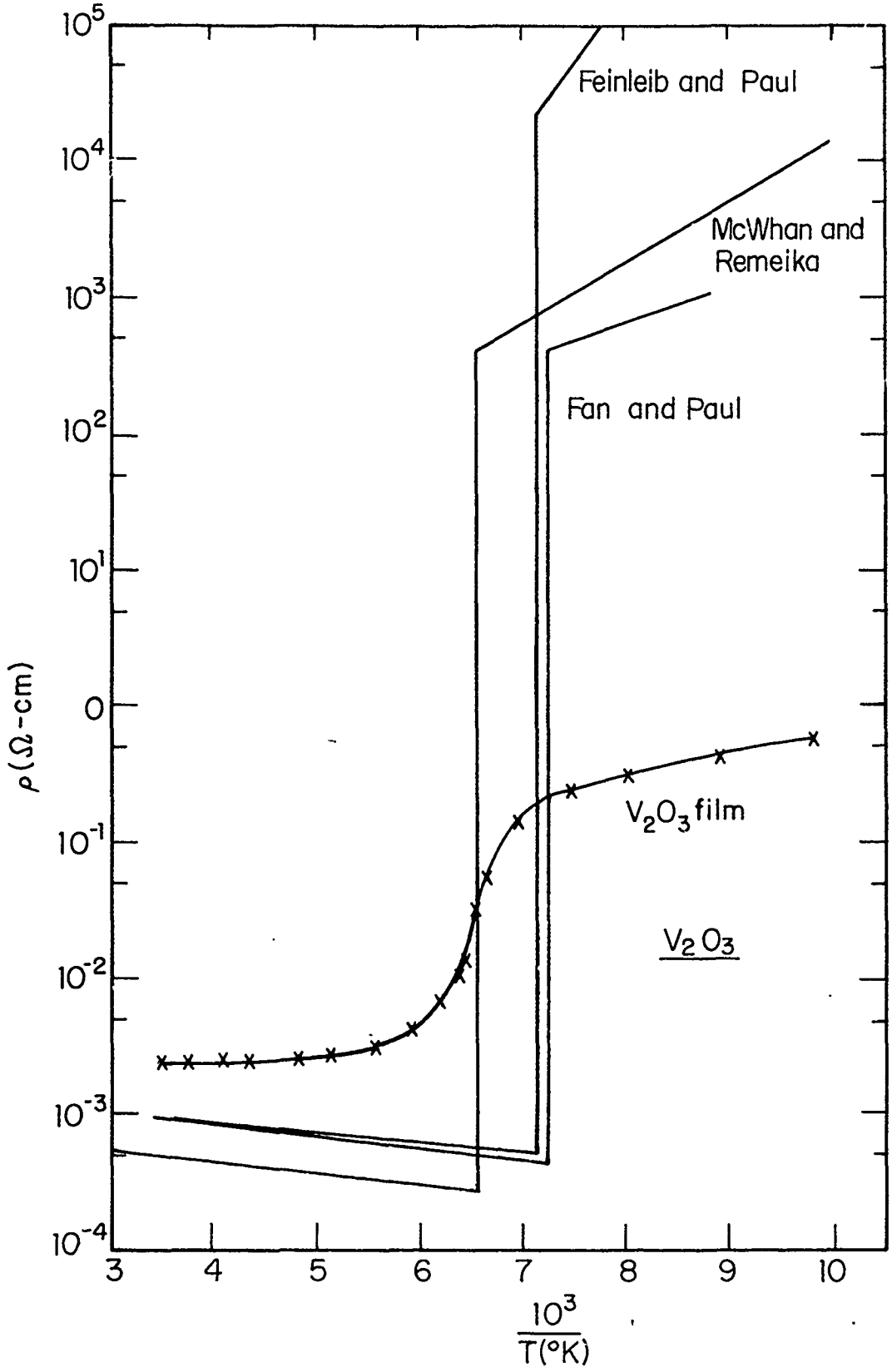

FIGURE II-9 Resistivity versus temperature of V_2O_3 crystals measured by several investigators (3, 19, 25) and of a V_2O_3 crystal and a V_2O_3 film grown by the vapor transport technique.

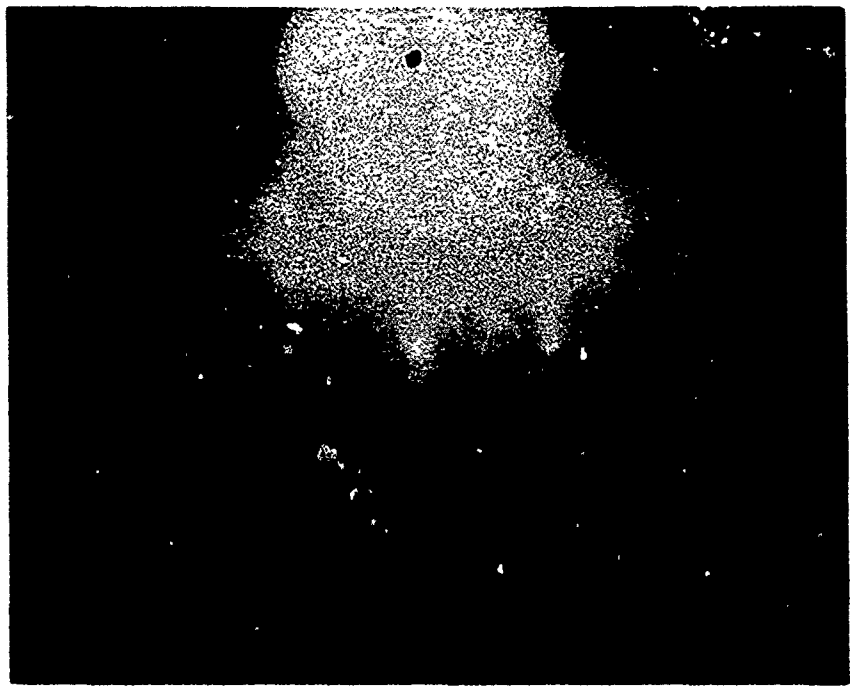

a

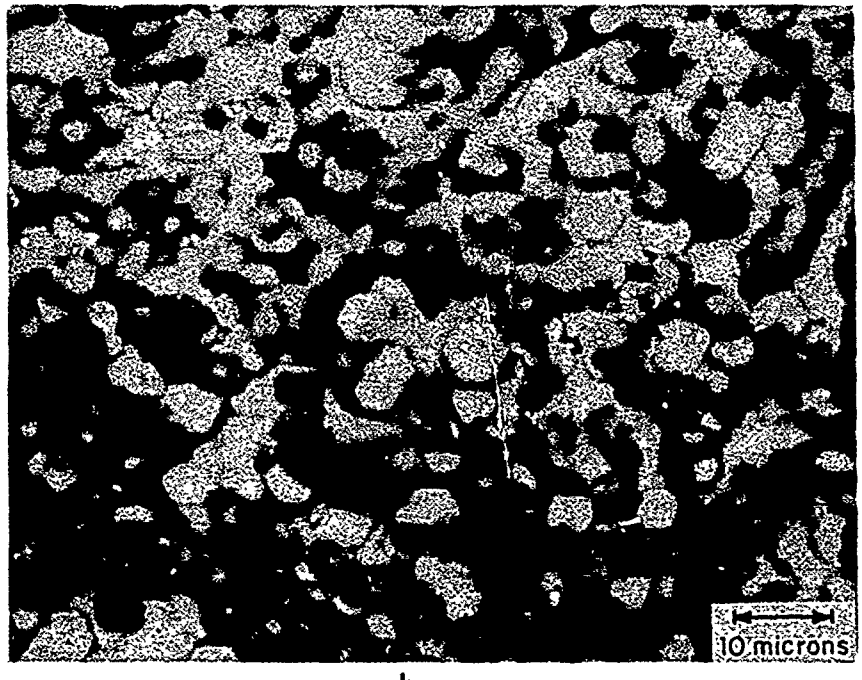

b

FIGURE II-10 (a) Reflection electron diffraction pattern. (b) Optical microscopic picture of a vapor transport V_2O_3 film (magnified 1500 times by a Universal Rikert Camera Microscope "MeF").

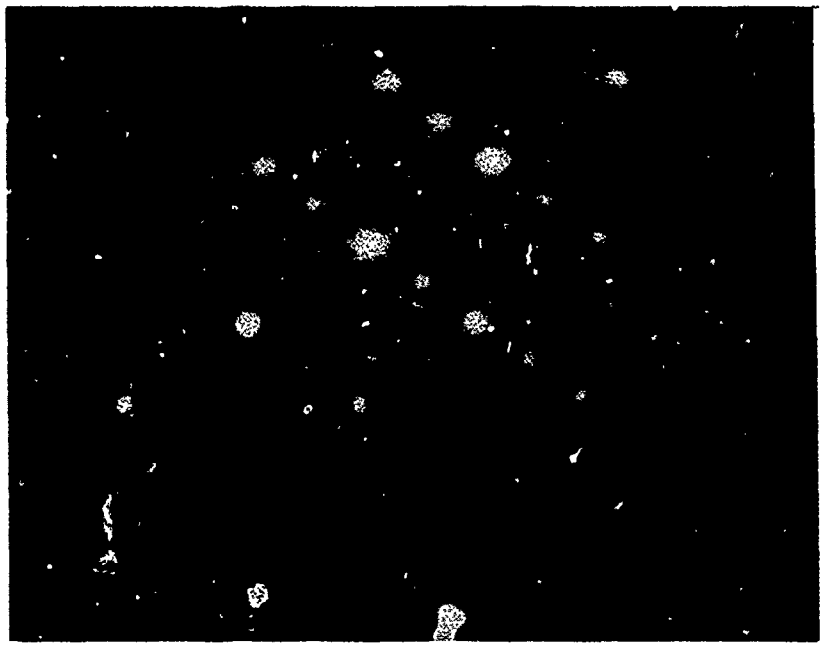

a

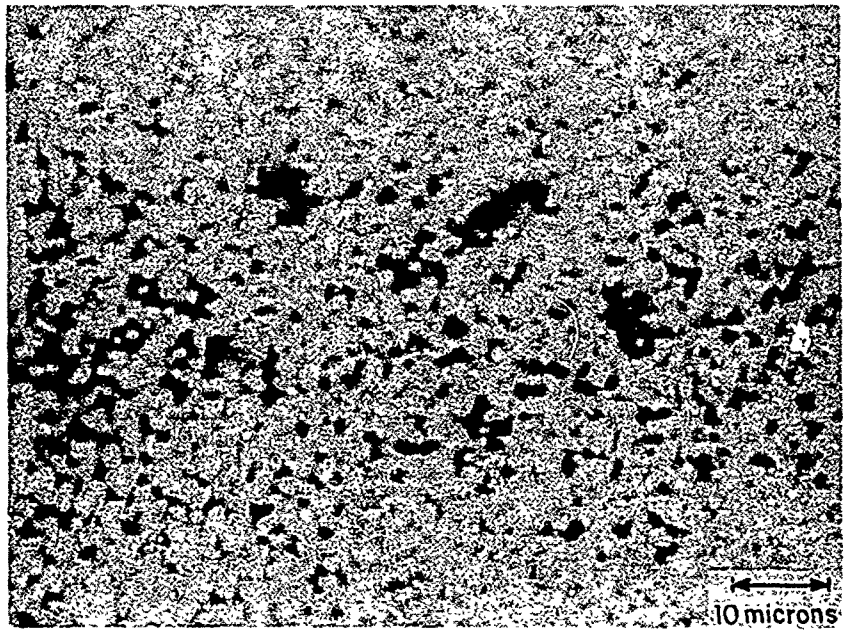

b

FIGURE II-11 (a) Reflection electron diffraction pattern. (b) Optical microscopic picture of a vapor transport VO_2 film.

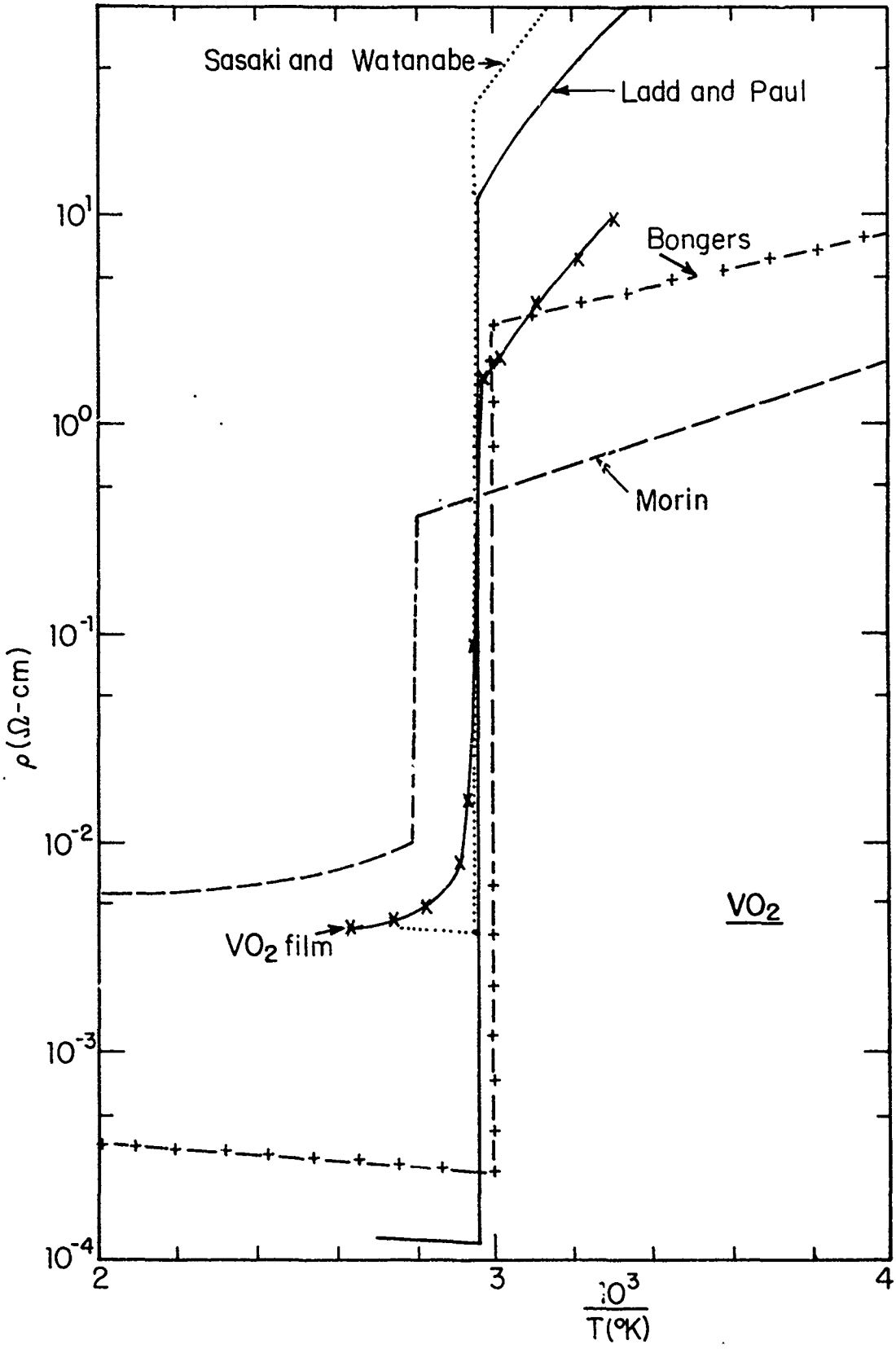

FIGURE II-12 Resistivity versus temperature of VO_2 crystals measured by several investigators (1, 3, 15, 53) and of a vapor transport VO_2 film.

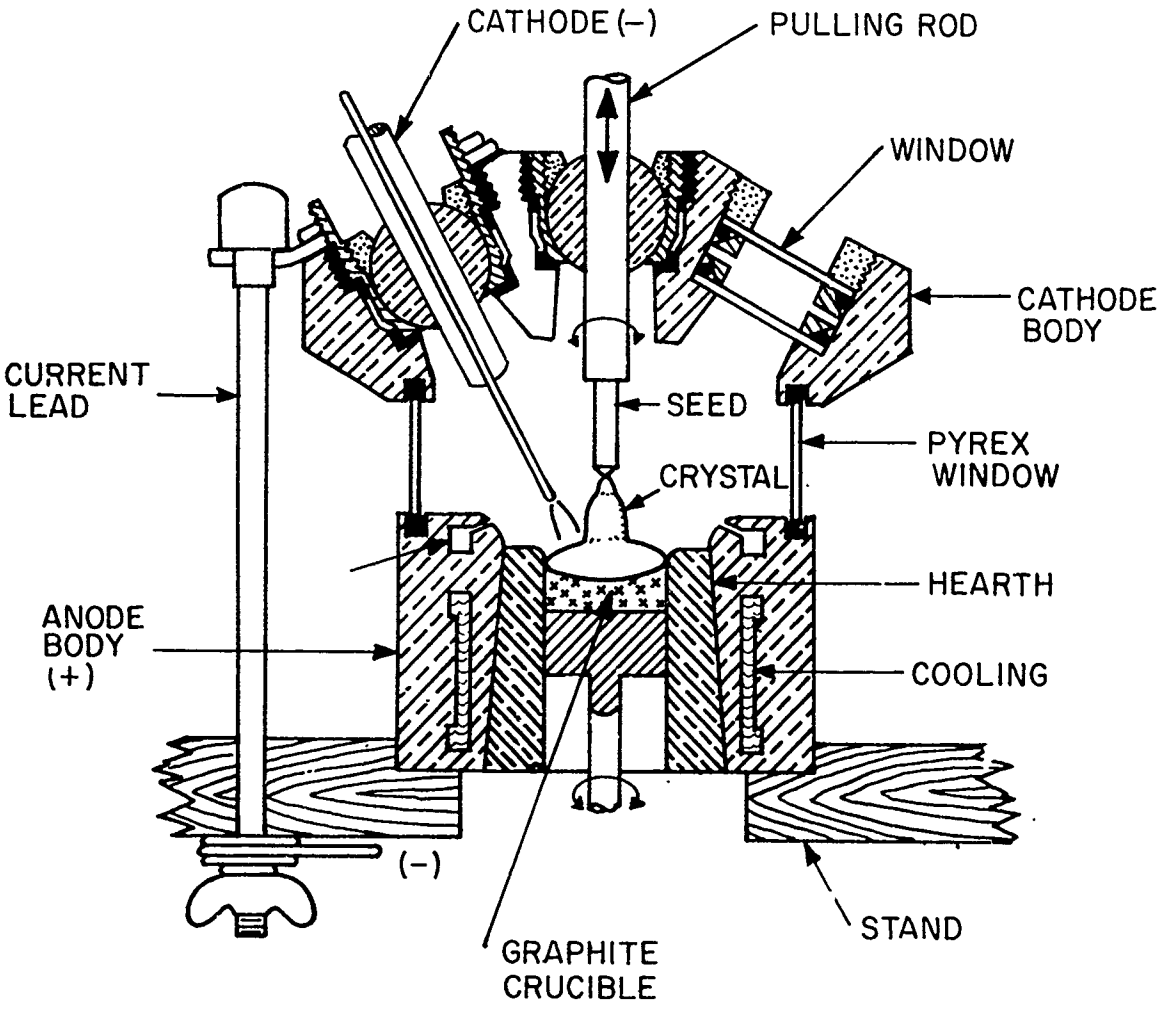

FIGURE II-13 Cross-section diagram of the tri-arc Czochralski crystal growing furnace.

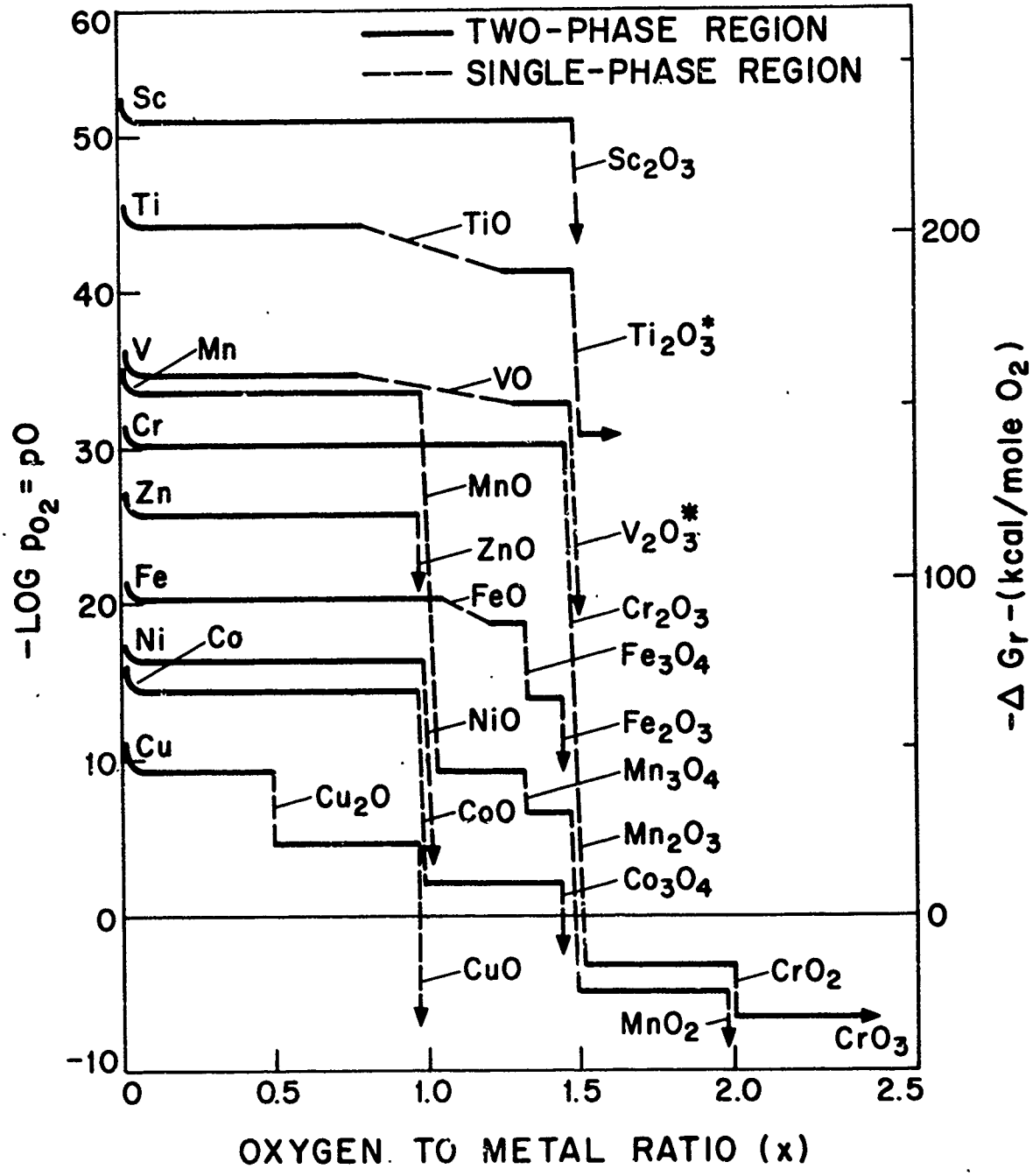

FIGURE II-14 Oxygen partial pressure versus oxygen-metal ratio for different elements. (56).

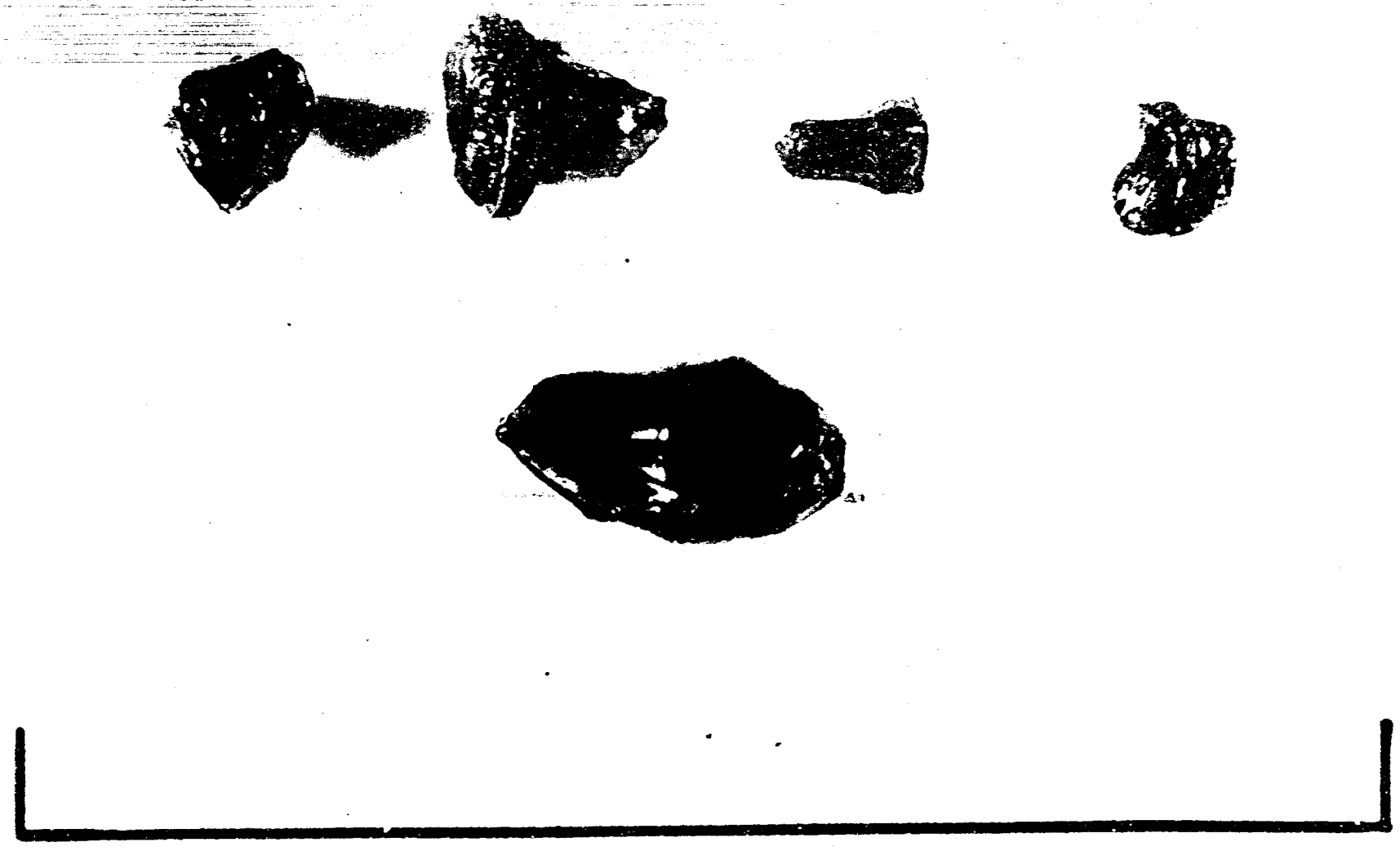

FIGURE II-15 Picture of V_2O_3 crystals from a crystal run in a tri-arc furnace.

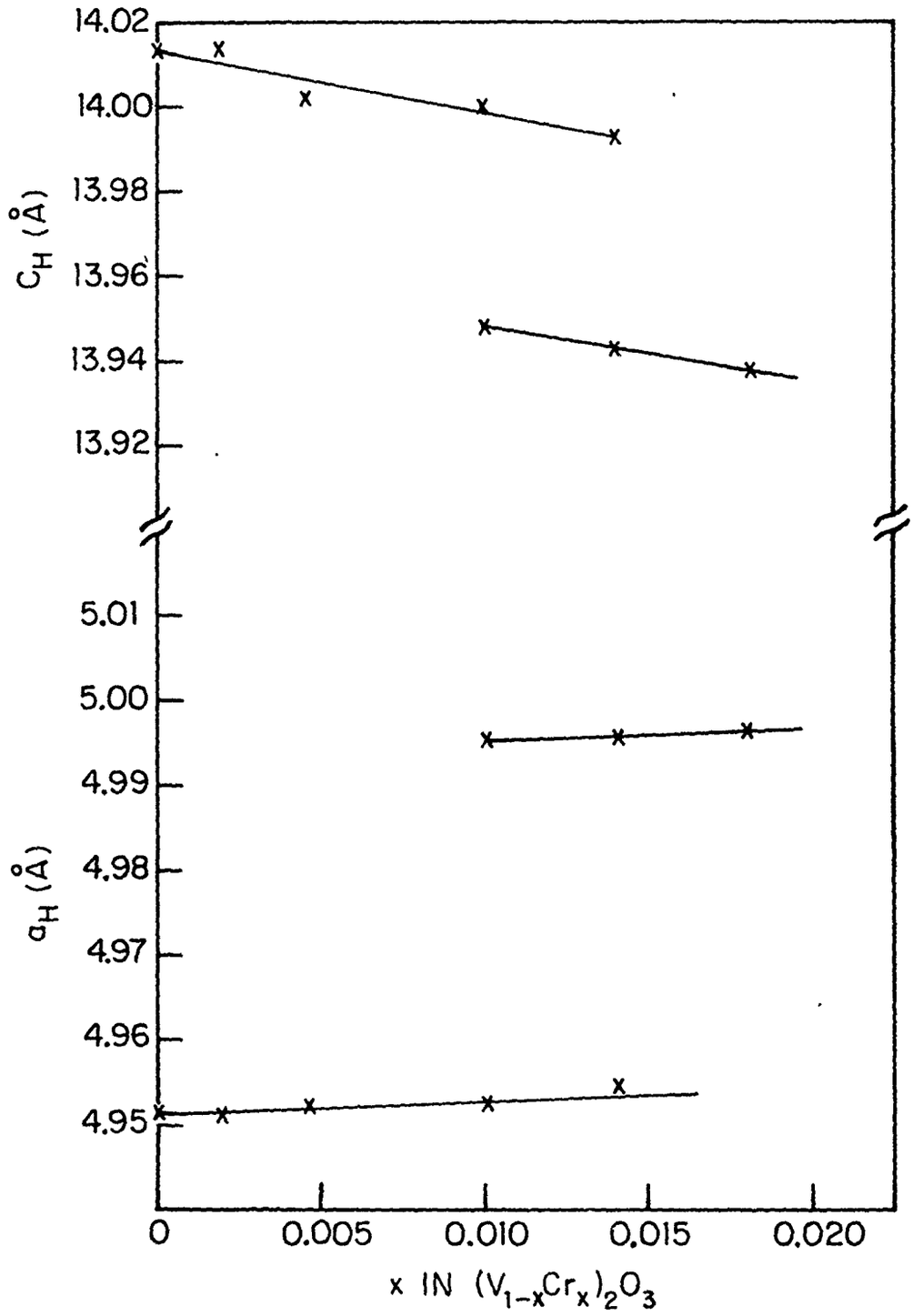

a_H obtained from the (300) peak
C_H obtained from the (226) peak
x is accurate to ± 5 % of its value

FIGURE II-16 Lattice constants of V_2O_3 and $(V_{1-x}\ Cr_x)_2O_3$ crystals as a function of chromium concentration.

CHAPTER III

DESIGN OF OPTICAL APPARATUS AND METHODS OF DETERMINING OPTICAL CONSTANTS

The electrical properties of materials which show the insulator-metal phase transition have been the object of considerable attention for quite some time, so that by comparison the work on optical properties has been much less extensive and detailed. In many of these materials the nature of the absorption and reflectivity spectra changes noticeably at the phase transition.

An examination of the optical properties and their changes at the transition may therefore increase our understanding of the properties of the insulating and metallic phases on both sides of the phase transition. In this chapter and in Chapter IV we will concentrate on the optical properties of the crystals and films of vanadium oxides and $(V_{1-x}Cr_x)_2O_3$ whose preparation was described in Chapter II.

A. Theories and Methods of Determining the Optical Constants of Solids

The theory of the optical properties of single crystals and films of ordinary metals and semiconductors is well known and has been extensively reviewed (1, 2, 3, 4, 5). Hence, rather than discuss the derivation of the theory in detail, we will instead simply define theoretical constants, their inter-relationship, and how they appear in expressions for experimentally measurable quantities such as transmission and reflectivity.

1. Optical Constants

The response of a solid with isotropic or cubic symmetry to incident electromagnetic radiation can be generally described in terms of three optical constants. Since one of the constants, namely the permeability of the material (μ), is generally very close to unity for non-magnetic materials, one has to deal only with the other two optical constants, which are related to each other through dispersion relations.

These two optical constants can consist of either 1) the refractive index n and the extinction coefficient k, or 2) ϵ_1 and ϵ_2 which are respectively the real and imaginary part of the complex dielectric constant ϵ. These two pairs of constants are related as follows:

$$\epsilon(\omega) = \epsilon_1(\omega) + i\,\epsilon_2(\omega) = [n(\omega) + ik(\omega)]^2 \qquad (3\text{-}1)$$

Let R_∞ be the reflectivity at normal incidence of a solid of sufficient thickness so that there is negligible reflection from the rear surface of the solid and T_∞ be the transmission at normal incidence, then R_∞ can be expressed in terms of n and k as follows:*

$$R_\infty = \frac{(n-n_s)^2 + k^2}{(n+n_s)^2 + k^2} \qquad (3\text{-}2a)$$

Generally, the solid is either in air or in a vacuum, where $n_s \tilde{=} 1$. Therefore, Eq. (3-2a) becomes

$$R_\infty = \frac{(n-1)^2 + k^2}{(n+1)^2 + k^2} \qquad (3\text{-}2b)$$

*The following equations can just as well be written in terms of ϵ_1 and ϵ_2.

Similarly, T_∞ can be expressed as

$$T_\infty = \{(1-R_\infty)^2 + 4R_\infty \sin^2\psi\}\, e^{-\alpha t} \qquad (3\text{-}2c)$$

where

α = absorption coefficient = $\frac{4\pi k}{\lambda}$

λ = wavelength of incident radiation

t = thickness of the sample

$\psi = \tan^{-1} \frac{2k}{n^2+k^2-1}$

If $n >> k$, Eq. (3-2c) becomes

$$T_\infty \cong (1-R_\infty)^2\, e^{-\alpha t} \qquad (3\text{-}2d)$$

As we mentioned earlier, the above equations, Eqs. (3-2a, b, c, d) are valid only if the reflection from the rear surface of the solid is negligible, that is when $e^{\alpha t} >> 4$.* For thin samples, where the reflection from the rear surface can no longer be neglected, then Eqs. (3-2a, b, c, d) have to be modified:

$$R = \frac{R_\infty ([1-e^{-\alpha t}]^2 + 4e^{-\alpha t} \sin^2\gamma)}{(1-R_\infty e^{-\alpha t})^2 + 4R_\infty e^{-\alpha t} \sin^2(\psi+\gamma)} \qquad (3\text{-}3a)$$

---

* This criterion can be easily verified from Eqs. (3-3a, b) to be described later).

and

$$T = \frac{e^{-\alpha t}([1-R_\infty]^2 + 4R_\infty \sin^2\psi)}{(1-R_\infty e^{-\alpha t})^2 + 4R_\infty e^{-\alpha t}\sin^2(\psi+\gamma)} \qquad (3\text{-}3b)$$

where

$\gamma = \frac{2\pi nt}{\lambda}$ (n is any integer)

t = thickness of a thin sample

R = reflected intensity of the thin sample at normal incidence

T = transmitted intensity of the thin sample at normal incidence.

The second term in the denominator in both Eq. (3-3a) and (3-3b) is an interference term. If no interference fringes are observed, say, because of thickness variation, we then average over γ and obtain:

$$R = \frac{R_\infty(1 - e^{-2\alpha t})}{1-R_\infty^2 e^{-2\alpha t}} \qquad (3\text{-}4a)$$

$$T = \frac{([1-R_\infty]^2 + 4R_\infty \sin^2\psi)\, e^{-\alpha t}}{1-R_\infty^2 e^{-2\alpha t}} \qquad (3\text{-}4b)$$

For thin films deposited on different substrate materials, the effects of substrates on R and T must be considered, and the formulae for R and T become much more complicated (4, 42). It will not be necessary for us to summarize them here, since we do not analyse our reflectivity and transmission measurements on thin films in order to obtain the optical constants.

When the angle of incidence of the incident radiation is not normal to the surface of a solid, where $e^{\alpha t} >> 4$, then Eqs. (3-2a, b, c, d) again have to be modified. We will consider only the reflected intensity at oblique incidence (6):

$$R_n = \frac{(a - \cos\phi)^2 + b^2}{(a + \cos\phi)^2 + b^2} \tag{3-5a}$$

$$R_p = R_n \frac{(a - \sin\phi \tan\phi)^2 + b^2}{(a + \sin\phi \tan\phi)^2 + b^2} \tag{3-5b}$$

where

R_n = the reflected intensity of the solid when the polarization of the incident radiation is perpendicular to the plane of incidence;

R_p = the reflected intensity of the solid when the polarization of the incident radiation is in the plane of incidence;

ϕ = the angle between the incident radiation and the normal to the surface of the solid;

$$a^2 = \frac{1}{2}\{[(n^2 - k^2 - \sin^2\phi)^2 + 4n^2k^2]^{1/2} + (n^2 - k^2 - \sin^2\phi)\}$$

$$b^2 = \frac{1}{2}\{[(n^2 - k^2 - \sin^2\phi)^2 + 4n^2k^2]^{1/2} - (n^2 - k^2 - \sin^2\phi)\}$$

In all the above equations, n and k are used to relate to experimentally measurable optical quantities, but it is actually the imaginary part of the dielectric constant, $\epsilon_2(\omega)$, that comes out most directly from the derivation of the optical properties of the solid from its band structure (2, 7). $\epsilon_1(\omega)$ can then be obtained from $\epsilon_2(\omega)$ by the dispersion relations.

2. Dispersion Relations

Under certain general assumptions, for example, that there is causality requirement and that the incident electric field is a square-integrable function with time, the dispersion relations can be derived using complex contour integration (8):

$$\epsilon_1(\omega) = 1 + \frac{2}{\pi} P \int_0^\infty \frac{\omega' \epsilon_2(\omega')}{\omega'^2 - \omega^2} d\omega' \qquad (3\text{-}6a)$$

$$\epsilon_2(\omega) = -\frac{2\omega}{\pi} P \int_0^\infty \frac{\epsilon_1(\omega')}{\omega'^2 - \omega^2} d\omega' + \frac{\sigma_o}{\omega} \qquad (3\text{-}6b)$$

where P means the Cauchy principal value of the integral;

σ_o = conductivity as $\omega \rightarrow 0$.

For non-metals, the second term in the right hand side of Eq. (3-6b) will be zero because σ_o becomes zero. The dispersion relations can also be expressed in terms of R and θ , as defined below:

$$r = \text{complex reflection coefficient} = |r| e^{i\theta} = Re^{i\theta} \qquad (3\text{-}7)$$

where θ is the phase angle and

$$\theta(\omega) = \frac{\omega}{\pi} P \int_0^\infty \frac{[\ln R(\omega') - \ln R(\omega)]}{\omega^2 - \omega'^2} d\omega' \qquad (3\text{-}8a)$$

or

$$\theta(E) = \frac{E}{\pi} P \int_0^\infty \frac{[\ln R(E') - \ln R(E)]}{E^2 - E'^2} dE' \qquad (3\text{-}8b)$$

where

$E = \hbar\omega$

$2\pi\hbar$ = Planck's constant.

Constants n and k can be obtained from R and θ by the following relations:

$$n = \frac{1-R}{1+R-2\sqrt{R}\cos\theta} \tag{3-9a}$$

$$k = \frac{2\sqrt{R}\sin\theta}{1+R-2\sqrt{R}\cos\theta} \tag{3-9b}$$

If the function R(E) is known over the entire spectral region, then from Eq. (3-8b) $\theta(E)$ can be calculated for all energies. With R and θ, Eqs. (3-9a) and (3-9b) will give us n and k, and ultimately ϵ_1 and ϵ_2. The above method of obtaining the optical constants is frequently referred to as the Kramers-Kronig analysis.

We should point out that Eqs. (3-9a) and (3-9b) are derived for solids of sufficient thickness such that reflection from the rear surface is negligible (i.e., for $e^{\alpha t} >> 4$).* For a sample where the above condition is not valid, the expressions for R and T in terms of the optical constants n and k become too complicated to be inverted in closed forms (refer to Eqs. (3-3a) and (3-3b)). It will, then, no longer be feasible to obtain the optical constants of the sample by Kramers-Kronig analysis. In the next section, we will present a detailed discussion of this analysis.

---

*Thus R(E) should actually be labelled as $R_\infty(E)$; however, it is clear from the context.

3. Kramers-Kronig Analysis

Equation (3-8a) can be rewritten as (3):

$$\theta(\omega) = -\frac{1}{2\pi}\int_0^\infty \ell n\, R(\omega')\,\frac{d}{d\omega'}\,\ell n\left|\frac{\omega'-\omega}{\omega'+\omega}\right|\,d\omega' \qquad (3\text{-}10a)$$

If we integrate Eq. (3-10a) by parts we obtain (3, 9)

$$\theta(\omega) = -\frac{1}{2\pi}\left[\ell n R\,(\omega')\,\ell n\left|\frac{\omega'-\omega}{\omega'+\omega}\right|\right]_0^\infty$$

$$+\frac{1}{2\pi}\int_0^\infty \frac{d}{d\omega'}[\ell n\, R(\omega')]\;\ell n\left|\frac{\omega'-\omega}{\omega'+\omega}\right|\,d\omega' \qquad (3\text{-}10b)$$

The first term in this equation is zero at $\omega' = 0$ and ∞. The phase angle θ is then given by the integral over $\frac{d\,\ell n\, R(\omega')}{d\omega'}$ which is multiplied by a weighing function that peaks sharply at $\omega' = \omega$ and approaches zero at frequencies far from ω. Therefore, the derivative of ℓnR near ω influences the value $\theta(\omega)$ much more than that of ℓnR at remote points on the frequency scale. In practice, since R is measured only in a limited range of frequencies, errors are introduced in the calculation of θ and hence in n and k; these errors arise from the extrapolation of $R(\omega')$ beyond the range of measurements. From Eq. (3-10b), it can be seen that these errors are tolerably small if ω' is well removed from the end points of the measured range. In the case $\frac{1}{R}\,\frac{dR}{d\omega'} \simeq 0$ outside the measured region, then the extrapolation errors in the Kramers-Kronig analysis become very small over the entire

measured region. In most optical spectra, however, the reflectivity is generally still varying at the highest frequencies used in the measurement. We, therefore, have to extrapolate the measured reflectivity in a sensible way which will minimize errors.

In extrapolation, the chief difficulty is extrapolation on the high energy end of the reflectivity spectrum. This is due to the fact that, in metals, the reflectivity at low energies can be assumed to go to 1.0 as $\omega \to 0$. Similarly in the case of a semiconductor, the reflectivity at $\omega \to 0$ can generally be calculated using the static dielectric constant of the material.

There are a few extrapolation procedures that are commonly used. One approach is to extrapolate $R(\omega)$ to higher frequencies using the formula (10)

$$R(\omega) = R_1 \left(\frac{\omega_1}{\omega}\right)^p \qquad (3-11)$$

where

ω_1 = upper frequency limit of measurement, and

R_1 = reflectivity at $\omega = \omega_1$.

The parameter p is varied in order to obtain values of n and k that agree best with the experimental n and k at low energies in the range of measurement. Another method of extrapolating $R(\omega)$ to higher energies is to assume:

$$R(\omega) = R_1 e^{\beta(\omega_1 - \omega)} \qquad (3-12)$$

where β is taken to fit the measured derivative of $R(\omega)$ at $\omega = \omega_1$ (11). Here, the integration range must be cut off at a certain frequency, ω_2, in order to avoid divergence of the integral in Eq. (3-8a). ω_2 is again chosen so that Kramers-Kronig analysis gives the constants n and k which will fit some experimental n and k at low energies. There are other methods, such as the one that uses damped harmonic oscillators, to extrapolate the reflectivity spectrum in the high energy region. The parameters of these oscillators are adjusted to give values of n and k which are comparable to experimental n and k at certain energies.

In addition to the errors introduced by the extrapolation, we can have large errors in the optical constants from the inaccuracies of experimental measurements. From Eq. (3-8a), the value of $\theta(\omega)$ depends on the natural logarithm of $R(\omega)$. The natural logarithm of a function whose values are equal to or smaller than one is a rapidly varying function. The logarithm of $R(\omega)$ is such a function. In fact, the smaller the value of $R(\omega)$ gets, the more sensitive $\theta(\omega)$ becomes to the experimental errors in $R(\omega)$.

Furthermore, judging from Eq. (3-2a), when k is small, and especially when $k << n$, then R is nearly independent of k. Therefore, in such a region, reflectivity data cannot yield accurate values of k, and the values of k depend on the reflectivity spectrum outside the region where k is small. The extrapolation of the reflectivity spectrum then becomes critical.

4. Oscillator Fit Method

To comprehend the oscillator fit method, we need first to understand why it is reasonable to express the dielectric constant of a solid in terms of oscillators. In general, the complex dielectric constant of a solid can be divided into four terms, three of which are expressed as sums of damped harmonic oscillator terms and the fourth is a Drude term. At this point, we are interested only in the first three terms. Two of the three terms represent contributions from the excitations of transverse optical phonons, and from the electronic transitions from bands below the valence band to the conduction bands. These contributions to the dielectric constant have been shown to be adequately represented by sums of oscillators (12, 13). The third term represents the contribution from electronic transitions from the valence band to the conduction bands. The contribution from these transitions to the dielectric constant is often expressed as follows (13):

$$\epsilon(\omega) \simeq 1 + \frac{4\pi e^2}{m} \int \frac{f(\omega')\, N_\alpha(\omega')\, d\omega'}{(\omega'^2 - \omega^2) - \frac{i\omega}{\tau(\omega')}} \qquad (3\text{-}13)$$

where

$N(\omega')$ = the density of valence band states separated by an energy $h\omega$ from conduction band states.

$f(\omega')$ = oscillator strength, and

$\tau(\omega')$ = relaxation time.

But if the transitions are between narrow bands, or in the limit between atomic levels, than $N_\alpha(\omega')$ can be approximated by a sum of delta functions, and Eq. (3-13) is reduced to a sum of oscillators, with

each transition from the valence band to a conduction band approximated by a damped harmonic oscillator.

When the bands involved in the transitions are no longer narrow, then the contribution to the complex dielectric constant from each transition from the valence band to a conduction band usually cannot be expressed in terms of a single damped oscillator; but a sum of oscillators has to be used. The reason for using a sum of oscillators can be explained by referring to Eq. (3-13). The integrand in the second term of that equation is in the form of a damped harmonic oscillator term. From calculus, this integral can be approximated by a sum of oscillators at discrete frequencies.

It must be remembered, however, that when the bands are narrow, the oscillator used has a one to one correspondence with the transition between the bands, but when the bands are not narrow, it is no longer correct to identify one oscillator with a particular transition; in fact, several oscillators may together represent a single transition.

Since different sets of oscillators can be chosen to give rise to the same contribution to the complex dielectric constant, the loss of physical significance of the parameters of these oscillators is obvious. In an oscillator fit method, the complex dielectric constant of a solid where the free electron contribution is negligible can be adequately represented as follows:

$$\epsilon(\omega) = \epsilon_1(\omega) + i\,\epsilon_2(\omega) = 1 + \sum_i \frac{S_i}{1 - \frac{\omega^2}{\omega_i^2} - i\,\Gamma_i\left(\frac{\omega}{\omega_i}\right)} \qquad (3\text{-}14a)$$

where

S_i = parameter associated with the oscillator strength of the i^{th} oscillator

Γ_i = linewidth of the i^{th} oscillator

ω_i = resonance frequency of the i^{th} oscillator.

If we are interested in an optical spectrum within a limited spectral range, as is usually the case, the contribution of the oscillators whose resonance frequencies are far from the range of frequency under examination is then reduced to a sum of their respective oscillator strengths — this is evident by inspecting the form of Eq. (3-14a). Equation (3-14a) can then be reduced to

$$\epsilon(\omega) = \epsilon_\infty + \sum_{i=1}^{N} \frac{S_i}{1 - \left(\frac{\omega}{\omega_i}\right)^2 - i\,\Gamma_i\left(\frac{\omega}{\omega_i}\right)} \qquad (3\text{-}14b)$$

where

ϵ_∞ = 1 + contributions to $\epsilon(\omega)$ from oscillators far from the spectral range of interest in the frequency scale, and

N = the number of oscillators required to given an adequate representation of the dielectric constant in the spectral range of interest.

The reflectivity of the solid can then be derived from the dielectric constant. For a solid of sufficient thickness such that $e^{\alpha t} >> 4$, Eq. (3-2b) can be rewritten as follows:

$$R_\infty(\omega) = \left| \frac{\sqrt{\epsilon(\omega)} - 1}{\sqrt{\epsilon(\omega)} + 1} \right|^2 \qquad (3\text{-}15)$$

Though we have shown that, in theory, we can always express the complex dielectric constant of a solid in terms of a sum of oscillators, in practice, we find that we cannot use an unlimited number of oscillators in our oscillator fit method because of computational limitations. The computational time required to get a good fit to a reflectivity spectrum using a large number of oscillators (say, 10) is very long (after more than 30 minutes); this proves to be a drawback of the method. Further discussion of this point will be presented in Chapter IV when we discuss the optical results.

We will, now, consider a special case where the reflectivity spectrum of a solid is in the spectral range where the optical phonon excitations are important. As we have discussed earlier, the representation of the complex dielectric constant of such a solid can be adequately expressed as a sum of damped harmonic oscillators. The parameters of the fitted oscillators usually provide us with some idea of the strength, frequency and relaxation time of each transverse optical phonon mode which is excited by the incident radiation. This technique has been used successfully by several authors to obtain the parameters of optical phonon modes in various solids (14).

Verleur (15), using Eq. (3-14b), fitted a reflectivity spectrum of silicon from 0.5 to 10 eV with six oscillators. He, then, used the derived parameters of the oscillators that gave a good fit to the measured spectrum to calculate optical constants n and k and found them in good agreement with those values obtained by Phillipp and Taft who used a Kramers-Kronig analysis (16).

Where a crystal becomes transparent, that is when $e^{\alpha t} < 4$, or when thin transparent films are involved, Eqs. (3-9a) and (3-9b) are no longer valid, and the expressions for R and T in terms of n and k become too complicated to be inverted in closed forms. Kramers-Kronig analysis is no longer feasible. To obtain the optical constants in these cases, two quantities, such as the transmission of two films (TT) of different thickness or the reflectivity and transmission of the same film (RT), are measured at each frequency. In all cases, the thickness is determined by other means. The RT method has its disadvantages; Grant and Paul (17) have shown that small experimental errors in some wavelength regions, especially where $n^2 - k^2 \simeq 1$ can lead to large inaccuracies in the calculated optical constants.

Grant (42) and Nillson (18) found that the TT method would not run into the same trouble as the RT method when $n^2 - k^2 \simeq 1$. However, they found that considerable errors in the values of the optical constants could result from the TT method, unless the thicknesses of the two films were carefully chosen. For example, Grant (42) showed that for germanium films in the spectral range between 0.2μ and 0.6μ reasonably accurate values of the optical constants could be obtained if the thicknesses of the two films were 100 Å and 300/400 Å. For some other combinations, say, 50 Å and 100 Å, large errors in the optical constants would result.

Verleur (15) adopted the oscillator fit method to obtain optical constants from the transmission and reflectivity spectra of thin films. Equation (3-15) is, of course, not applicable for thin films. Verleur then used the appropriate formulae for R and T (15) which contain the

known optical constants of the substrate in addition to the unknown ϵ_1 and ϵ_2 of the film. Thus R and T can still be fitted using Eq. (3-14b). To compare his method with the RT method, he fitted the transmission spectrum of a germanium film reported by Grant and Paul (17), and obtained optical constants which were closer to those of bulk crystals than those obtained by Grant and Paul using the RT method. Figure III-1 shows that the optical constants n, and k obtained by Verleur using the oscillator fit method and the constants obtained by Grant and Paul using the RT method. In the region where $n^2 - k^2 \tilde{=} 1$, the RT method (as indicated by Grant and Paul), cannot give accurate values of n and k while the oscillator fit method is not subjected to this limitation.

Verleur, Barker and Berglund (19) extend this technique to obtain the optical constants of thin films and crystals of VO_2. For the insulating state of VO_2, they used Eq. (3-14b); for the metallic state of VO_2, they added a free electron Drude term to Eq. (3-14b), resulting in the following:

$$\epsilon(\omega) = \epsilon_\infty - \frac{\omega_n^2}{\omega^2 + i\omega_c\omega} + \sum_{i=1}^{N} \frac{S_i}{1 - \left(\frac{\omega}{\omega_i}\right)^2 - i\Gamma_i \frac{\omega}{\omega_i}} \qquad (3\text{-}16)$$

where

$$\omega_n = \left(\frac{4\pi n_c e^2}{m^*}\right)^{1/2}$$

$$\omega_c = \frac{e}{\mu_{opt.}\, m^*}$$

n_c = concentration of conduction carriers of optical mobility $\mu_{opt.}$ and optical effective mass m^*.

The method has since been used by others to obtain the optical constants of bulk crystals and thin films of various kind of material in the spectral region where interband electronic transitions are important (20, 21, 22, 23).

In summary, let us list, and amplify on where necessary, the advantages and disadvantages of the oscillator fit method as compared to the Kramers-Kronig analsis.

Advantages. 1) In Kramers-Kronig analysis, extrapolation is often needed and different methods of extrapolation have been used in earlier studies (10, 11). The values of the optical constants in the spectral range of interest usually depend on the parameters used in the extrapolation procedures. In practice, the extrapolation parameters have to be adjusted so that the calculated optical constants, at some frequencies inside the spectral region, will fit some known optical constants obtained by other means. In the oscillator fit method, however, extrapolation (strictly speaking, it is not extrapolation in the sense used in Kramers-Kronig analysis) is usually not required unless it is necessary to give a reasonable fit to an optical spectrum in the spectral range of interest. Extrapolation, if needed, is achieved by assigning oscillators outside the spectral range of interest, and the parameters of the assigned oscillators are automatically adjusted in the oscillator fit method so that an adequate fit is obtained in the range of interest. Thus, in the oscillator fit method, no prior knowledge of the values of optical constants in the spectral range of interest is needed. The resultant

optical constants are, however, still subject to some uncertainties. We will discuss them on p. III-19, and again in Chapter IV.

2) As mentioned earlier, the oscillator fit method enables us to obtain the optical constants of the transparent crystals and films; this is not feasible using the Kramers-Kronig analysis. And the RT and TT techniques, which are frequently used in evaluating the optical constants of thin films, may, in some instances, fail to give accurate values of optical constants. The oscillator fit method, in these instances, may well be superior to the RT and TT method.

3) In regions where Reststrahlen effects are dominant, or where electronic excitations are between narrow bands or atomic levels, this method will give us directly their frequency, oscillator strength and relaxation time.

4) Referring to Eq. (3-16), the oscillator fit method will provide us with the parameters of the free electron absorption. From these parameters, the optical effective mass and optical mobility of the conduction electrons can be obtained, provided that the concentration of the conduction electrons is known. In Kramers-Kronig analysis, this is, not directly possible.

Disadvantages. 1) The oscillator fit method usually requires more computational time than does the Kramers-Kronig analysis. Numerical analysis and programming procedures are much more complicated.

2)When an absorption spectrum of a solid is very assymetrical, as in the case of an absorption edge, or is due to electronic transitions

between broad bands, it may require a substantial number of oscillators to adequately fit the absorption spectrum, and the length of computational time required becomes a serious factor.

3) In the oscillator fit method, the curve fitting procedure is usually provided by a nonlinear minimization technique, which has one problem, viz., convergence often occurs at a point other than the absolute minimum. Though this problem is not serious since we are interested only in the resultant dielectric constant and not in the parameters of the oscillators, sometimes a convergence may occur that leads to a poor fit and, in some cases, small structures in the optical reflectivity or transmission spectrum may not be fitted well during the fitting procedure. As long as an adequate fit is obtained, however, reasonable optical constants can be obtained.

5. Angular Dependence and Other Techniques of Determining Optical Constants

There are other techniques for obtaining optical constants of opaque solids where $e^{\alpha t} >> 4$. In this section, we are interested only in crystals that satisfy this condition. When a light beam, whose electric field is polarized either perpendicular or parallel to the plane of incidence, is incident on a solid at different angles of incidence, the reflected intensity of the beam is described by either Eq. (3-5a) or (3-5b). Since we have two unknowns, n and k, we need only two independent measurements to determine them; and judging from Eqs. (3-5a) and (3-5b), several choices of these measurements are possible. One way — sometimes called the angular dependence technique — is to measure the

reflected intensity, R_n or R_p, of the solid at two different angles of incidence (6, 24). Another way is to measure both R_n and R_p at one angle of incidence (25). Yet a third way is to determine the ratio of R_n/R_p for two angles of incidence (26). In still another technique, ellipsometry, the optical constants of a solid can be obtained by measuring changes in the state of polarization of light upon reflection from the surface of the solid (27).

The above methods show that it is possible to obtain values of n and k of an opaque solid directly without resorting to the indirect techniques of Kramers-Kronig analysis and oscillator fit. Although it is not always feasible to use these direct techniques to obtain the optical constants in a wide spectral range because of the lack of appropriate instruments, it is quite feasible to use them to find values of n and k at some particular frequencies in the spectral range of interest. By requiring the measured values of n and k at these particular frequencies to fit the calculated values of n and k obtained by the Kramers-Kronig analysis or the oscillator fit technique, extrapolation uncertainties in both techniques can be greatly reduced.

We determined the n and k values of some of our crystals by measuring the angular dependence of the reflected intensity of these crystals as a function of the incidence angle ϕ at different frequencies, which were provided by a helium-neon laser and an argon-ion laser. Light polarized in the plane of incidence was used because the reflected intensity of a solid for light polarized perpendicular to the plane of incidence usually did not vary with ϕ as much as for light polarized in the plane of incidence (6).

Since there were two unknowns, n and k, only two measurements of R_p at two different angles of incidence were actually required to determine them (see Eq. (3-5b)). However, in order to minimize the experimental errors in R_p which could lead to substantial errors in n and k (6), we usually measured the R_p of each crystal at more than ten different angles of incidence ϕ and used an automatic curve fitting procedure to obtain values of n and k that would give a calculated R_p versus ϕ curve that would fit well with the experimental curve.

6. Discussion

The theories and methods of determining the optical constants of a solid are based on several assumptions; aside from those generally valid for dispersion relations, they include the following: 1) that the solid is optically isotropic (a solid which is isotropic or cubic in crystal symmetry), 2) that the solid is non-optically active (a solid which does not rotate the polarization of an incident light on passing through it), 3) that the solid possesses no net charges, and 4) that the local field effects in the solid are negligible. The formulation of the optical properties of solids for which the latter three assumptions are not applicable is very complicated and, in general, not necessary for common solids, and therefore will not be discussed here.

We will, however, briefly describe the optical constants of an optically non-isotropic solid since the crystals we have investigated are all non-cubic. The optical constants of such solids are usually not scalars, and the real and imaginary parts of the complex dielectric

constants become second-rank tensor quantities. It is known that a second-rank tensor can always be diagonalized by judiciously choosing three mutually orthogonal principal axes. In a crystal which belongs to one of the following crystal symmetry classes: tetragonal, hexagonal, trigonal and orthorhombic — the principal axes are along the crystallographic axes of the crystal for all wavelengths and the real and imaginary parts of its complex dielectric constant share the same set of principal axes. Therefore, if optical reflectivity R or transmission T measurements are made with the incident electric field polarized along any one of the principal axes, the values of n and k or ϵ_1 and ϵ_2, obtained from the R or T spectrum using the Kramers-Kronig analysis or the oscillator fit method, will give us the optical constants along this particular axis. If these measurements are made along each of the three principal axes in the solid, we will then obtain the components of the dielectric constant tensor along those axes, and hence, the complex dielectric constant tensor for the solid can be determined. If, however, for some reason, the electric field of the incident radiation is either unpolarized or not along any of the principal axes, then the optical constants obtained will be a superposition of those components of the dielectric tensor along those principal axes on which the incident radiation have effects.

When the materials being investigated are either crystals which belong to the monoclinic or triclinic crystal symmetry classes, or thin films which are non-cubic in nature and are not epitaxial, amorphous, or perfectly polycrystalline, the choice of the principal axes for the

real and imaginary parts of the dielectric constants becomes very difficult, if not impossible. In monoclinic and triclinic crystals, even if the principal axes can be found, they will usually vary with the wavelengths of the incident radiation and the set of principal axes for the real part usually will not coincide with that for the imaginary part of the dielectric constant (3). Therefore, in general practice, when optical reflectivity and transmission measurements are done on one of these materials, either with the electric field along one of the crystallographic axes or with unpolarized light, the optical constants derived from the Kramers-Kronig analsis or the oscillator fit method should be interpreted as constants that will give us the measured values of reflectivity or transmission when used in the appropriate equations, and thus this fact must be given careful consideration, if these derived constants are used to compare with those calculated from band structures or any such methods.

In our optical investigations of VO_2 and V_2O_3, the crystals transformed, respectively, from monoclinic to tetragonal structure at $\sim 340^{\circ}K$, and from monoclinic to corundum structure (almost hexagonal) at $\sim 150^{\circ}K$, with increasing temperature. If the electric field polarization of the incident radiation is aligned along one of the principal axes of these crystals in its high temperature state (either along c- or a-axis in crystals with the tetragonal or hexagonal symmetry), then the electric field will usually not be polarized along any of the principal axes in the low temperature monoclinic state, thus making polarization studies on

this class of materials difficult and hardly fruitful. Because of this and the limited availability of crystals with large physical dimensions, we have not concentrated on studies of polarization effects on the optical properties of solids. Also, it has turned out that at room temperature, in V_2O_3 crystals and V_2O_3 crystals doped with chromium, no significant optical anisotropy was observed in the spectral range of our interest, and hence, the polarization effects on their optical properties are not important.

B. Numerical Analysis and Programming Techniques

In this section, we will describe some of the characteristics of our computer programs for Kramers-Kronig, oscillator fit, and angular dependence analyses.

1. Kramers-Kronig Analysis

For the Kramers-Kronig Analysis, Eqs. (3-8b), (3-9a) and (3-9b) were used. The computer program, similar to the one used by Rossi (28), computed the integrand in Eq. (3-8b) at each discrete photon energy for which the measured reflectivity value was available. The integral was then approximated by multiplying the average value of the integrand between each adjacent pair of energies by the difference ΔE between the energies, and then summing the results (trapezoidal rule). The integral between the two energies adjacent to the energy where $E = E'$ was taken as the average of the integrand at the two adjacent energies times the energy difference.

Above the energy E_{max} where the reflectivity data were not available, the reflectivity spectrum was approximated by $R_{max}(\frac{E_{max}}{E})^p$ (see Eq. (3-11)) where R_{max} was the value of reflectivity at E_{max} and p was an adjustable parameter. The integration of the phase integral from E_{max} to ∞ was:

$$\frac{1}{2\pi} \ell n \frac{R(E)}{R(E_{max})} \ell n \left| \frac{E_{max}+E}{E_{max}-E} \right| + \frac{\rho}{\pi} \sum_n (2n+1)^{-2} (\frac{E}{E_{max}})^{2n+1}$$

This sum was computed to 50 terms in the program.

The values of p were varied from 0.0 to 5.0 by increments of 0.1, and the usual procedure, where applicable, was to print out and plot the optical constants n, k, ϵ_1, ϵ_2, and α only when a certain p gave values of n and k at some energies which were within $\pm$ 5% of those values obtained by the angular dependence measurements (to be discussed later).

A complete Fortran listing of the program is given on p. A-1 to A-5.

2. scillator Fit Method

The oscillator expressions we used in our analysis were Eq. (3-14b) for semiconductors and Eq. (3-16) for metals. They were rewritten in te. .is of the photon energies and expressed as follows:

(for semiconductors)

$$\epsilon(E) = \epsilon_\infty + \sum_{i=1}^{N} \frac{S_i}{1 - (\frac{E}{E_i})^2 - i\Gamma_i (\frac{E}{E_i})} \qquad (3\text{-}17a)$$

(for metals)

$$\epsilon(E) = \epsilon_{\infty} - \frac{E_n^2}{E^2 + iE_c E} + \sum_{i=1}^{N} \frac{S_i}{1 - (\frac{E}{E_i})^2 - i\Gamma_i(\frac{E}{E_i})} \qquad (3\text{-}17b)$$

where $E = \hbar\omega$ and $2\pi\hbar$ = Planck's Constant.

The actual procedure of fitting a measured optical spectrum, in our case, the reflectivity spectrum of a bulk crystal, consisted of a guess at the number of oscillators needed, the parameters of these osciilators, the parameters for the Drude's term, and ϵ_{∞}. The reflectivity of the crystal was then calculated by Eqs. (3-15) which was rewritten as follows:

$$R_{cal}(E) = \left| \frac{[\epsilon(E)]^{1/2} - 1}{[\epsilon(E)]^{1/2} + 1} \right|^2 \qquad (3\text{-}18)$$

The parameters were adjusted until an adequate fit of the calculated reflectivity $R_{cal}(E)$ to $R_{exp}(E)$ was obtained over the spectral range of interest. Unless an automatic fitting procedure is adopted, obtaining the optical constants by this method is a formidible task.

Minimization of a nonlinear function of many independent variables is a problem of great difficulty. There are a few methods that have been used, such as nonlinear least-square fit and the steepest descent method, which were used by Rivery (22). However, it is frequently very laborious, if not practically impossible, to calculate the gradients of the function to be minimized, which is necessary for the above two methods. In addition, programming techniques become difficult.

Therefore, there are considerable advantages in using minimization procedures that do not require the derivatives of the function to be minimized. A few procedures are indeed available and they include the simplex pattern search method (29, 30), the method proposed by Powell (31), and the method proposed by Peckham (32). We will not discuss the advantages and disadvantages of each of these methods. It is sufficient to point out that Eq. (3-17a, b) are very complex, and that the derivatives of these equations are even more so. We chose to use the simplex method for our fitting procedure since the simplex method is computationally very compact, and a great majority of its instructions are additions and subtractions or logical orders. There are a few multiplications, but no divisions at all except on entering and leaving the computational routine. The method may take a little longer computational time than other methods such as the steepest descent method, but the easy definition of the problem and the programming convenience more than compensate for this possible disadvantage. We should point out that Scouler and Raccah independently developed their oscillator fit procedure also using the simplex method (23).

The general concept of the simplex method to minimize a function of n variables (henceforth referred to as objective function) is to set up a simplex of (n+1) vertices, that is, to select (n+1) points in the space of n variables and to calculate the values of the function at selected points. Then, by comparing the calculated values of the objective function at those points, the vertex with the highest value (the

worst point in minimization) is replaced by another point with a lower value of the objective function, which in turn is determined according to certain systematic operations (to be described later). This method forces the objective function to approach the minimum by, at each step of the operation, discarding the worst point of a simplex and adopting a better point for a new simplex. This procedure is repeated until the minimum is achieved.

Figure III-2 shows a flowchart of the simplex method we used (30). A brief description of the procedure follows: we consider initially, the minimization of a function of n variables $(x_1, \ldots\ldots\ldots x_n)$ without any constraints. $P_0, P_1, \ldots . P_n$ are the (n+1) points in the n-dimensional space that define the current simplex. Let y_i be the functional value at P_i, and h and ℓ be the suffices such that

$$y_h = \max_i (y_i) \qquad (h = \text{high})$$

$$y_\ell = \min_i (y_i) \qquad (\ell = \text{low})$$

We then define $\overline{P}$ as the centroid of the points with $i \neq h$, and $(P_i P_j)$ for the distance from P_i to P_j. At each stage in the minimization process, P_h is replaced by a new point; three operations are used — reflection, contraction and expansion. These operations are defined as follows: the reflection of P_h is denoted by P^*, and its coordinate are defined by the relations:

$$P^* = (1 + \alpha)\overline{P} - \alpha P_h \qquad (3\text{-}19a)$$

where α, the reflection coefficient, is a positive constant.

Thus, P^* is on the line joining P_h and $\overline{P}$, on the far side of $\overline{P}$ from $\overline{P}_h$ with $(P^*\overline{P}) = \alpha (P_h\overline{P})$. If y^* lies between y_h and y_ℓ, then P_h is replaced by P^* and we start again with the new simplex.

If $y^* < y_i$, that is, if the reflection has produced a minimum, then we expand P^* to P^{**} by

$$P^{**} = \gamma P^* + (1 - \gamma)\overline{P} \tag{3-19b}$$

where γ, the expansion coefficient, is the ratio of the distance $(P^{**}\overline{P})$ to $(P^*\overline{P})$ and is usually greater than unity. If $y^* < y_\ell$, we replace P_h by P^{**} and restart the process. However, if $y^{**} > y_\ell$, then we have a "failed" expansion, and we replace P_h by P^* before restarting.

If on reflecting P to P^* we find that $y^* > y_i$ for all $i \neq h$, that is replacing P by P^* leaves y^* the maximum, then we define a new P_h to be either the old P_h or P^*, whichever has the lower y value and form

$$P^{**} = \beta P_h + (1 - \beta)\overline{P} \tag{3-19c}$$

where β, the contraction coefficient, is the ratio of the distance $(P^{**}\overline{P})$ to $(P\overline{P})$ and lies between 0 to 1. We then accept P^{**} for P_h and restart the process, unless $y^{**} > \min (y_h, y^*)$, that is, the contracted point is worse than the better of P_h and P^*. For such a "failed" contraction, we replace all the P_i's by $(P_i + P_\ell)/2$ and restart the process.

In Eqs. (3-17a and b), none of the parameters, from physical arguments, should be zero or negative. This constraint is incorporated into our minimization procedure by the following method. At any stage

during the operation, when one or more of the parameters becomes zero or negative, the functional value of the objective function is replaced by a large positive value. If we investigate the flowchart carefully, the designated large positive value effectively forms a barrier such that any trespassing by the simplex will be followed automatically by contraction moves which will eventually keep the simplex inside the confine.

A final point about the general concept of the simplex method concerns the criterion used for halting the procedure. The criterion chosen is to compare the "standard error" of the y's in the form

$$\sqrt{\frac{\sum_i (y_i - \bar{y})^2}{n}} < c_1 \qquad (3\text{-}20)$$

where

c_1 is a preassigned constant,

$\bar{y}$ is the average of all y_i's, and

n is the number of variables.

When the standard error falls below c_1, the fitting procedure stops. The reasoning behind this criterion is that in the curve fitting problem, we are not so interested in finding the exact values of x_i's, but in obtaining the minimum that gives us a good fit between the calculated and experimental curves.

We will now concentrate on the specific characteristics of our curve fitting procedure. The objective function to be minimized is

$$y = \sum_{j=1}^{K} \left[1 - \frac{R_{exp}(E_j)}{R_{cal}(E_j)} \right]^2 \qquad (3\text{-}21a)$$

where $j = 1, \ldots . K$ (the number of input data points),

$R_{exp}(E_j)$ = the experimental value of reflectivity at E_j,

$R_{cal}(E_j)$ = the calculated value of reflectivity from Eq. (3-18) and either Eq. (3-17a or 3-17b).

The (n+1) points in the simplex are selected by the following procedure. Judging from a given reflectivity spectrum to be fitted, we estimated, initially, the number of oscillators required and the values of the parameters needed (the number of variables total to n, say). This gives us one point in the n-dimensional space. The other n points are set up in the space by systematically adding to the value of each parameter 0.1 one at a time, for n times. This gives the (n+1) points in the space clustering around the initial point, and the pattern search begins with the initial simplex.

The values of the coefficients α, β and γ in Eqs. (3-19a, b, and c) were chosen as suggested by Nelder and Mead (30) to be

$\alpha = 1.0$

$\beta = 0.5$

$\gamma = 2.0$

The large positive constant used as a constraining barrier was set to be 10^{49}. The constant c_1 in Eq. (3-20) was chosen to be 10^{-6},

which would give us a reasonable fit. For cases where we have obtained optical constants n and k by the angular dependence method, the objective function y in Eq. (3-21a) is modified to

$$y = \sum_{j=1}^{K} \left\{ \left(1 - \frac{R_{exp}(E_j)}{R_{cal}(E_j)}\right)^2 * c_2 + \sum_{m_{i=1,\ldots \ell}} \left[\left(1 - \frac{k_{exp}(E'_{m_i})}{k_{cal}(E'_{m_i})}\right)^2 + \left(1 - \frac{n_{exp}(E'_{m_i})}{n_{cal}(E'_{m_i})}\right)^2 \right] \right\} \qquad (3\text{-}21b)$$

where

E'_{m_i} = photon energy at which n and k values are known

m_ℓ = number of known k or n values; in our program, $m_\ell = 2$.

c_2 = weighing constraint; in our program, we set it at 4.0,

suffice cal = calculated value from Eq. (3-18) and either Eq. (3-17a) or (3-17b),

suffix exp = experimental value.

Typically from a given reflectivity spectrum, we guessed the number of oscillators required, and the values of the parameters. The initial guess can be quite poor. If the initial guess is very poor, Eq. (3-20) usually will not be satisfactory after ~ 25 minutes on the SDS Sigma 7 computer. An adjustment of the parameters will generally provide us with a reasonable fit that will satisfy Eq. (3-20) within 25 minutes, unless the number of oscillators chosen was too few. If the number of oscillators chosen are too few, then even if Eq. (3-20) is satisfield within 25 minutes, we will obtain a theoretical reflectivity curve that does not have all the fine structures of the experimental curve.

However, when too many oscillators are assigned, one of the oscillators will have its parameters approaching zero, and we will then discard the oscillator. In general, the final values of these adjustable oscillators parameters are dependent on their initial values. The final optical constants are, however, quite independent of the initial set, and this is not too surprising in view of the discussions we presented earlier. Some initial sets give better fits than others, and we usually selected a set that gave the best fit — that is, the set of parameters that gave us the smallest value of the objective function y — to the experimental values from a number of runs using different initial values. We, however, noticed that the parameters of the Drude's term was not very sensitive to their initial guesses and that the resultant ... are usually within 20% of each other from runs that give good f... perimental curve.

Finally, as in most curve fitting problems, the selection of the points of a spectrum are quite important. Data points should be selected with proper care to reflect the important features of the reflectivity spectra.

In conclusion, the oscillator fit method by the simplex pattern search method is quite straightforward, and after a few trial runs, a reasonable fit is often obtained.

A complete Fortran listing is given on p. B-6 to B-16, for fitting a reflectivity curve of V_2O_3 at 300°K (the optical constants are reported in Chapter IV).

3. Angular Dependence Method

The automatic curve fitting computer program was written by Raccah and Landon (34) at MIT Lincoln Laboratory. The same simplex pattern search method as the one we used in the oscillator fit method was used in the minimization of the objective function.

$$y = \sum_{j=1}^{K} \left(1 - \frac{R_{P_{exp}}[\phi_j]}{R_{P_{cal}}[\phi_j]}\right)^2 \qquad (3\text{-}22)$$

where $j = 1, \ldots . K$ (the number of input data points)

$R_{P_{exp}}(\phi_j)$ = the experimental value of the reflected intensity at ϕ_j

$R_{P_{cal}}(\phi_j)$ = the value of the reflected intensity at ϕ_j calculated from Eq. (3-5b).

The parameters used in the simplex pattern m[illegible]re slightly different from those we used in the oscillator fit method, but the basic operation remains the same.

The coefficients in Eqs. (3-19a, b, c) were:

$\alpha = 1.1$

$\beta = 0.51$

$\gamma = 3.0$

The criterion used in halting the fitting procedure was in the form

$$\left|\frac{y_h - y_\ell}{y_h}\right| < 10^{-4} \qquad (3\text{-}23)$$

where

$y_h = \max_i (y_i)$

$y_\ell = \min_i (y_i)$

which, though slightly different from Eq. (3-20), is basically very similar. Since there were only two parameters n and k to be adjusted, in contrast to the many parameters used in the oscillator fit method, Eq. (3-23) was usually satisfied in less than half a minute on an IBM Model 67 computer. The results of the angular dependence measurements are presented in Chapter IV.

C. Experimental Optical Apparatus Design and Operation

In order to make reflection and transmission measurements on our crystals and films of V_2O_3 and VO_2, two spectrometers were used. We will describe them briefly in this section. In addition, we will present the optical setup for our angular dependence measurements.

1. Single Beam Spectrometer for both Reflection and Transmission Measurements

The single beam spectrometer and associated optics has been described in detail in Ladd's technical report (35).

The light is chopped at 600 Hz by a Princeton Applied Research (abbreviated (PAR)) Model BZ-1 chopper. The sample optics for both reflectivity and transmission measurements, and the detector optics are shown in Fig. III-3. Since this is a single beam design, two measurements have to be made with each sample — an I_o measurement with the sample out of the optical path, and an I measurement with the sample in the optical path. The reflection or transmission is then found by taking the ratio I/I_o. The drifting of light sources plus focussing errors are the main sources of uncertainty in transmission and reflectivity measurements, with an accuracy no better than $\pm$ 5%.

Measurements at temperatures below room temperature were done in an optical dewar specially designed for our spectrometer (see Fig. III-4). Because of the leaks through the thermocouple wires and heater leads, the lowest temperature we were able to achieve was about 100°K when liquid nitrogen was used.

Our detection electronics and the various detectors we used have also been discussed in detail (35). Here, we will show only a diagram summary of the detectors and their associated electronics (Fig. III-5).

Generally, a CaF_2 prism has been used since it has a very good operating spectral region from 250 mm to 8μm. The CaF_2 prism has been carefully calibrated using the absorption lines of atmospheric water vapor, carbon dioxide and polystyrene, and emission lines from a Hg-Zn-Cd arc discharge lamp. There is an uncertainty in the wavelength calibration of less than 0.2% which is accurate enough for our measurements.

2. Ratio Reflectometer

Most of our optical measurements were made using the spectrometer described above. However, in a series of experiments where we investigated the changes in the optical reflectivity between the paramagnetic metallic state and the paramagnetic insulating state in V_2O_3 and chromium doped V_2O_3 crystals as a function of temperature, there was a need for a ratio reflectometer.

A ratio reflectometer has quite a few advantages over the single beam spectrometer, and a detailed discussion of the superiority of

such a setup has been presented by McElroy (36). In a single beam spectrometer, the spectral range of interest is swept twice; once with the sample in the light beam and once without the sample. The two resultant traces are divided to give the percent of light reflected.

There are a few major disadvantages to this method. Drift in the optical system, especially the light sources, occurs between the two sweeps, and limits the resolution of amplitude changes. This problem is more pronounced in our experiment because the reflected light at a particular wavelength has to be monitored for as long as several hours as a function of slowly varying temperature.

A second disadvantage is the delay in time that results from the laborious process of measuring the intensities of I_o and I, dividing them, and then plotting the results before the experiment can be evaluated. This objection is not just a matter of convenience. It is not unusual that one experiment suggests another, and if results are not known immediately, it may be difficult or impossible to return to the original conditions. Changes in experimental conditions, during the course of the experiment, may be difficult to detect. In our experiments, V_2O_3 samples oxidize when heated to temperatures over $\sim 400^{\circ}K$ unless they are adequately protected by a protective atmosphere. Any changes in our samples could be rapidly indicated by a ratio reflectometer.

In our single beam spectrometer, reflectivity is not measured at normal incidence, but at an angle within $\sim 10^{\circ}$ from the normal. Although this small deviation from normal incidence usually causes

negligible changes in the measurement, especially in the case of unpolarized incident radition (37, 38), it is possible that this might lead to errors, especially when measurements with polarized radiation are being used. A normal incidence reflectometer eliminates even this risk.

We, therefore, collaborated with Dr. Paul Raccah of Lincoln Laboratory in improving the design of a normal incidence ratio reflectometer suitable for our purposes. Figure III-6 shows a schematic of the optical apparatus. The quartz prism monochromator, obtained commercially from Oriel Optics (Model F-11-20), has an in-line configuration of the entrance and exit beams and installation into an optical path without disturbing its direction becomes possible. Its light weight and miniature size (~ 2 3/8" x 7" x 1 7/8") enables easy mounting of the unit in the system. With a slit width of 0.1 mm, the monochromater has a wavelength resolution better than 2% in the spectral range of our interest which is between 0.6 eV and 2.0 eV; this resolution is adequate for our measurement. The light from the monochromator is chopped by a PAR Model 125 light chopper at 83 Hz. Then the light beam is divided into two beams by a quartz beam splitter. One beam is focussed by a quartz lens on the sample to be measured (~ 1 mm x 1 mm spot); the other beam provides the reference channel. Two additional quartz lenses focus the divided beams onto the center of two matched lead sulphide (PbS) detectors. The two PbS detectors (obtained from Infrared Industries, Waltham, Mass.) were selected from ten detectors and the difference in the spectral response of the two matched ones was less

than 0.5% from 2.00 eV to 1.20 eV and less than 3% from 1.20 eV to 0.60 eV. Slight adjustments were made to the reflectivity spectra corresponding to the matching characteristics of the two detectors. Since the signal in a PbS detector depends on its biasing circuits and its physical characteristics, we calibrate the biasing circuits of the two detectors by adjusting the readout reflectivity of an aluminum mirror to its calibrated value at 1.96 eV.

The main sources of experimental uncertainty are from optical misalignment and electronic noises and drifts, especially in the PAR 230 Divider, where the accuracy of ratio of two signals decreases when one signal becomes much smaller than the other. For a ratio close to 1.0, the accuracy is found to be better than $\pm$ 0.5%. For a ratio close to 0.2, the accuracy is close to $\pm$ 1.0%.

Therefore, with proper care in optical alignment, the reflectivity readout should be better than $\pm$ 1% of the reflectivity for a sample whose reflectivity ratio is larger than 0.5. The uncertainty increases when the reflectivity gets smaller and is close to $\pm$ 2% when the reflectivity ratio is $\sim$ 0.2. Figure III-7 shows the reflectivity of a sample measured by this ratio reflectometer and the single beam spectrometer described earlier. The reflectivity curve, obtained by the single beam spectrometer, was normalized at 1.96 eV to 20.2%, which had been obtained earlier by a near normal incidence reflectivity measurement using a helium-neon laser. The reflectivity spectra obtained in the two

systems are similar in the spectral range (within the experimental uncertainty of the systems).

For some of our measurements, a high temperature optical sample holder was needed to provide a sample temperature as high as 600°K. Since V_2O_3 crystals oxidize at high temperature, they were protected by a steady flow of forming gas (argon 85% and hydrogen 15%). An adequate flow was found to be ~30 cu.ft./hour. If the flow was lower, the reflectivity of the sample changed after the heating cycle; in particular, the reflectivity at low photon energies (around 0.6 eV) decreased markedly after the heating cycle. The protection technique works chiefly because V_2O_3 cannot be reduced by hydrogen gas to lower oxides in our operating temperature region (39). Figure III-8 shows a detailed schematic of this high temperature sample heater. The heating was provided by a cartridge heater whose current was regulated by a Tempres temperature controller so that the sample temperature was regulated to $\pm$ 2°C.

In high temperature measurements, the problem was further complicated because the PbS detectors were ambient-temperature sensitive; then its signal level would change by ~1% for every °C change (40). Thus, in high temperature experiment, the PbS detectors were placed in heat-insulated chambers with quartz windows for light transmission and the detectors were in a steady stream of dry nitrogen gas. This system was calibrated by heating a polished aluminum metal piece to 600°K in the forming gas. The change of reflectivity ($\frac{\Delta R}{R}$) at 0.65 eV

(the photon energy at which the reflectivity was usually monitored in our experiments) was found to be less than 1%.

Therefore, if we assume that the reflectivity of aluminum mirror is insensitive to temperature changes — and this is not an unreasonable assumption — then our setup should be able to see reflectivity changes as low as 1% in this temperature interval.

For experiments at temperatures below room temperature, the optical dewar described in Fig. III-4 was used. Quartz windows were used in the dewar. To balance the effect of having one quartz window in the sample channel, we also put a quartz window (double in thickness of the one in the dewar; that is, light passes the window in the dewar twice) in the reference channel.

3. Optical Setup for Angular Dependence Measurements*

In order to minimize experimental uncertainties in our angular dependence measurements on small samples, we need a very narrow collimated light beam with sufficient intensity and with polarization in the plane of incidence. This can be easily obtained by the use of lasers. The helium-neon laser (Spectra Physics Company, Model 119) emits coherent radiation at 632.8nm (1.96 eV) with the polarization in the plane of incidence. An argon ion laser (Coherent Radiation Co., Model 54), however, gives off coherent radiation at five different wavelengths, with two principal lines, one at 514.5nm and one at 488.0nm. We selected the line at 488.0nm (2.54eV) since it is not so close to

*In collaboration with Dr. Paul Raccah , Lincoln Laboratory.

1.96 eV as the other principal line at 514.5nm (2.41 eV). In the case of the argon ion laser, the emitted polarization is perpendicular to the plane of incidence, and two polarizers are used to rotate the polarization into the plane of incidence. The unwanted polarization, that is, the amount of light still polarized perpendicular to the plane of incidence, is less than 0.15% in both the helium-neon laser and the argon ion laser.

Since our crystals are quite small (typically 2-3 mm across), we used a system of two quartz lenses to obtain a narrow collimated beam ($\sim$0.2 mm diameter and a divergence of $\sim 1/10^{o}$). A detailed schematic of the setup using the argon ion laser is shown in Fig. III-9. Two silicon photovoltaic detectors were used as detectors and the two detectors' signals were fed into two PAR Model 211 amplifiers, and followed by two PAR Model 220 lock-in amplifiers (the laser light was chopped at 800 Hz to eliminate stray light). The two dc signals from the lock-in amplifiers were divided by the PAR 230 Divider and fed into a teletype which was used as a digital voltmeter. Such a ratio system eliminates the errors from the drifts of laser power during the experiments.

Owing to the particular configuration of the experimental setup, the outputs of the PAR 230 Divider with the laser beam at different angles of incidence on the crystal being measured were normalized by the output of the PAR 230 Divider obtained by placing the silicon detector B between the crystal and the quartz lens of focal length 2.5cm (see Figure III-9).

Careful alignment was needed so that for $\phi = 0^{\circ}$, the light was reflected back along the incident light path. Also, since the detector B (see Fig. III-9) was not coupled to the rotation of the sample, by geometrical argument, the center of the rotation axis does not have to be on the main optical light path (PP' in Fig. III-9). This facilitates the optical alignment (41). To ensure that the beam will always be incident on the center of the sample for all angles of incidence, the rotating table was mounted on a moving platform for convenient optical alignment.

We estimated our uncertainty in ϕ to be about 1/5 degree and the reflectivity to have an uncertainty of $\sim 1\%$, mainly because of the slight nonuniformity of the signal response across the silicon detectors and the drift in electronics.

In Chapter IV, we will present the optical measurements obtained using the above experimental setups, and the optical constants derived from these measurements using the Kramers-Kronig analysis, the oscillator fit method, and the angular dependence method.

REFERENCES

1. F. Stern, Solid State Physics, Vol. 15, F. Seitz and D. Turnbull, ed., p. 299, 1963.

2. H. Ehrenreich, Proc. of Intl. School of Physics, "Enrico Fermi" Course XXXIV, Academic Press, J. Tauc ed., p. 106, 1966.

3. D. L. Greenaway and G. Harbeke, "Optical Properties and Band Structure of Semiconductors," Pergamon Press, 1968.

4. O. S. Heavens, "Optical Properties of Thin Solid Films," Dover Publication Co., 1965.

5. W. Paul, J. of Vac. Sci and Tech. 6, 483 (1969).

6. W. R. Hunter, J. Opt. Soc. Am. 55, 1197 (1965).

7. W. Heitler, "The Quantum Theory of Radiation," Oxford Univ. Press, London, 1954.

8. J. S. Toll, Phys. Rev. 104, 1760 (1956).

9. H. J. Bowlden and J. K. Wilmshurst, J. Opt. Soc. Am. 53, 1073 (1963).

10. H. R. Phillipp and E. A. Taft, Phys. Rev. 113, 1002 (1959).

11. M. R. Rimmer and D. A. Dexter, J. Appl. Phys. 31, 775 (1960).

12. T. S. Moss, "Optical Properties of Semiconductors," p. 15, Academic Press, 1959.

13. J. M. Ziman, "Principles of the Theory of Solids," p. 229, p. 233, Cambridge Univ. Press, 1965.

14. W. G. Spitzer and D. A. Kleinman, Phys. Rev. 121, 1324 (1961); A. S. Barker, Jr., Phys. Rev. 136, 1290 (1964).

15. H. W. Verleur, J. Opt. Soc. Am. 58, 1356 (1968).

16. H. R. Phillipp and E. A. Taft, Phys. Rev. 120, 37 (1960).

17. P. M. Grant and W. Paul, J. Appl. Phys. 37, 3110 (1966).

18. P. O. Nilsson, Appl. Opt. 1, 435 (1968).

19. H.W. Verleur, A.S. Barker and C.N. Berglund, Phys. Rev. 172, 172 (1968).

20. C.J. Powell, J. Opt. Soc. Am. 60, 78 (1970).

21. C.J. Powell, J. Opt. Soc. Am. 60, 214 (1970).

22. J. Rivory, Optics Comm. 1,334 (1970)

23. W.J. Scouler and P.M. Raccah, Bull. Am. Phys. Soc., Ser. 11, 15, 289 (1970).

24. R. Tousey, J. Opt. Soc. Am. 29, 235 (1939).

25. I. Simon, J. Opt. Soc. Am. 41, 336 (1951).

26. J.N. Hodgson, Proc. Phys. Soc. (London) B67, 269 (1954).

27. J.A. Faucher, G.M. McManus and H.J. Trurnit, J. Opt. Soc. Am. 48, 51 (1958).

28. C.E. Rossi, Tech. Rept. No. HP-18, Gordon McKay Laboratory, Harvard University, 1968 (unpublished).

29. W. Spendley, G.R. Hext and F.R. Himsworth, Telenometrics 4, 441 (1962).

30. J.A. Nelder and R. Mead, The Computer Journal 7, 308 (1964).

31. M.J.D. Powell, The Computer Journal 7, 155 (1964).

32. G. Peckham, The Computer Journal 13, 418 (1970).

33. J.F. Nye, "Physical Properties of Crystals," p. 23, Clarendon Press, 1957.

34. P. Raccah and S. Landon, MIT Lincoln Laboratory, private communication.

35. L. Ladd, Tech. Rept. No. HP-26, Gordon McKay Laboratory, Harvard University, 1971 (unpublished).

36. P.T. McElroy, Tech. Rept. No. HP-20, Gordon McKay Laboratory, Harvard University, 1968 (unpublished).

37. R.W. Ditchburn, "Light," Vol. 2, p. 554, Wiley, 1964.

38. D. W. Berreman, Appl. Opt. 6, 1519 (1967).

39. K. Kosuge, J. Phys. Chem. Solids 28, 1613 (1967).

40. Infrared Industries, Waltham, Mass., private communication.

41. W. R. Hunter, Appl. Optics 6, 2140 (1967).

42. P. M. Grant, Tech. Rept. HP-14, Gordon McKay Laboratory, Harvard University, 1965.

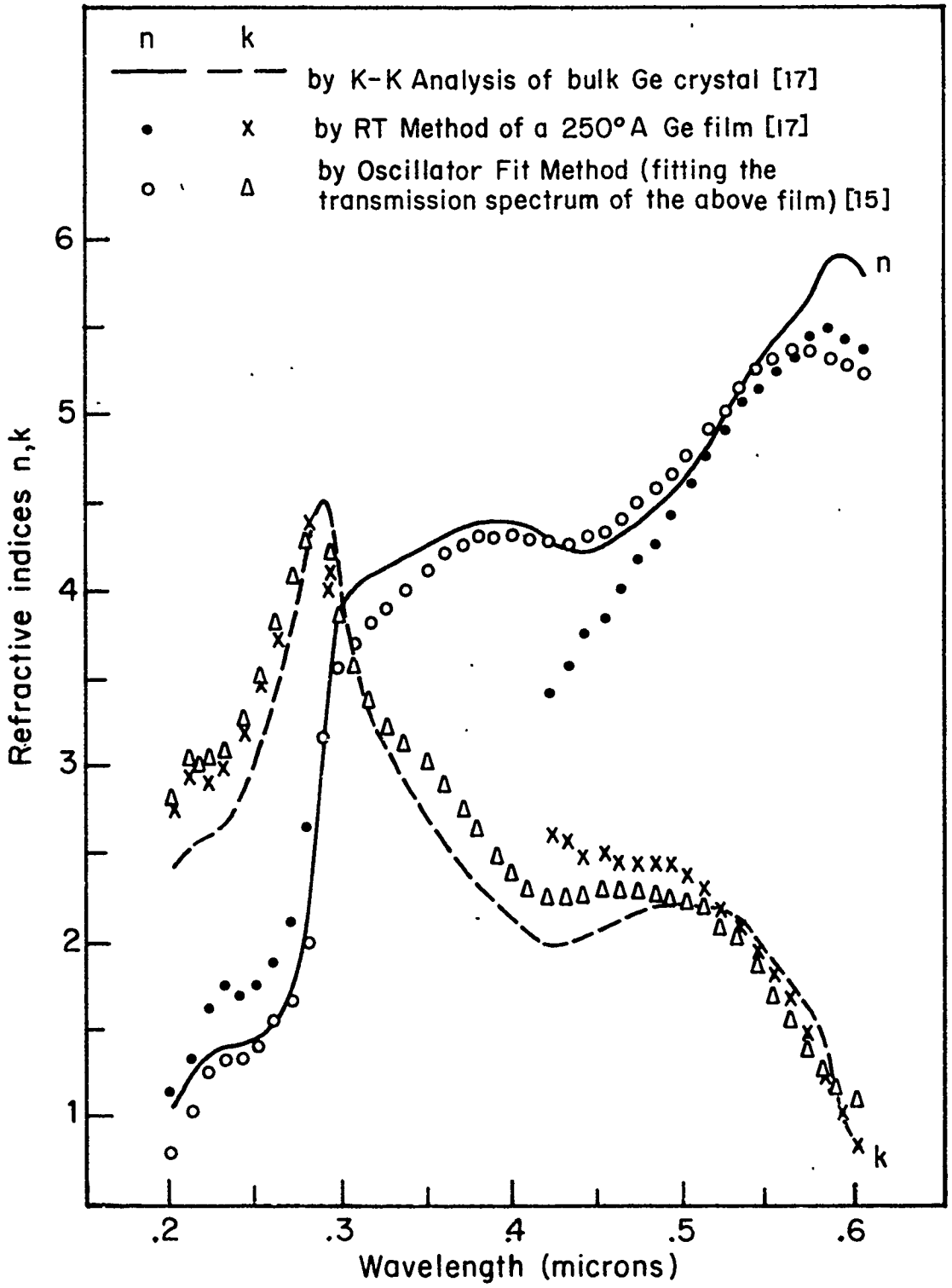

FIGURE III-1 A comparison of different methods of evaluating the optical constants n and k of germanium (15).

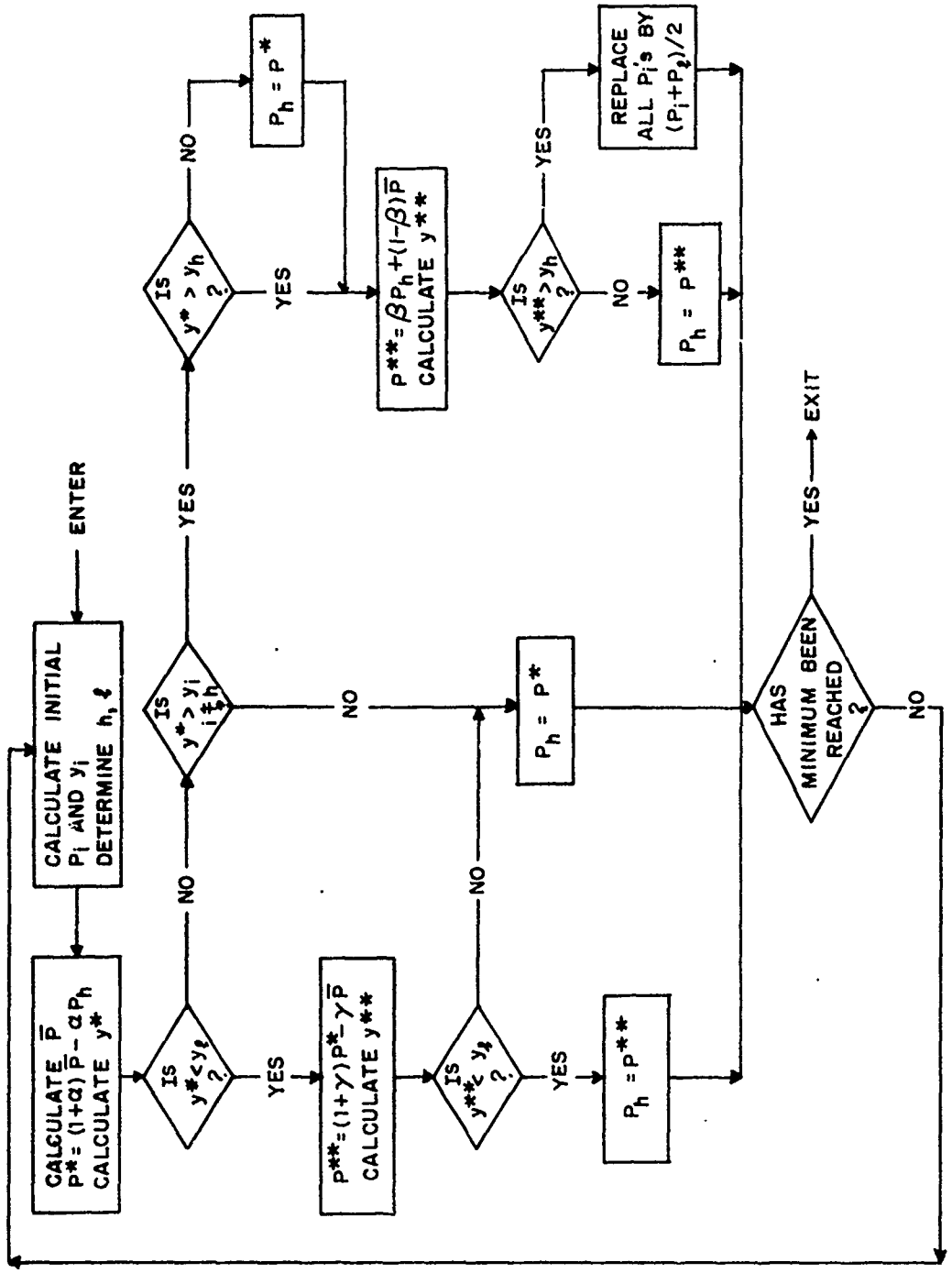

FIGURE III-2 Flowchart of the simplex method (30).

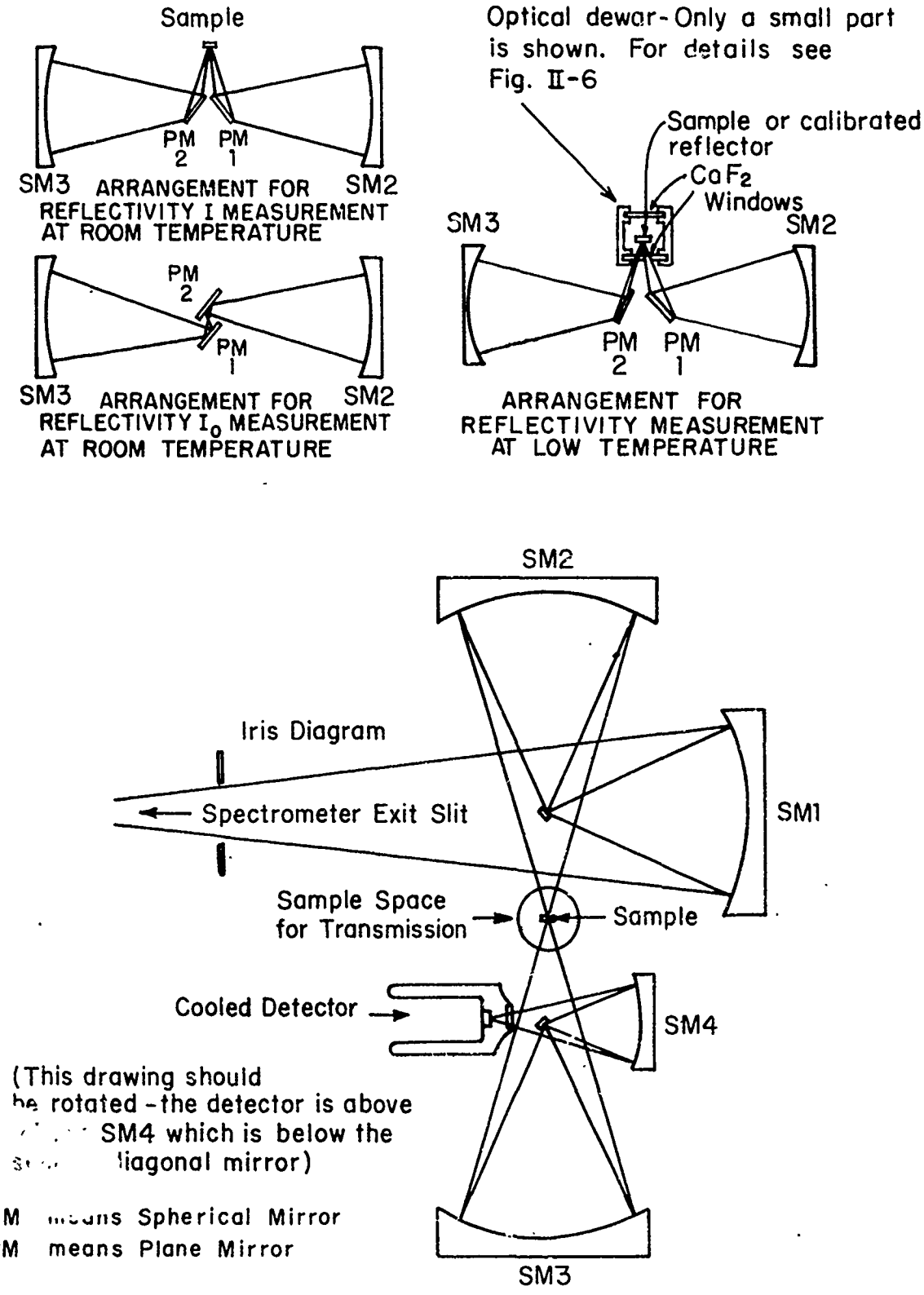

FIGURE III-3 The schematic diagram of the sample and detector optics of the single beam spectrometer (35).

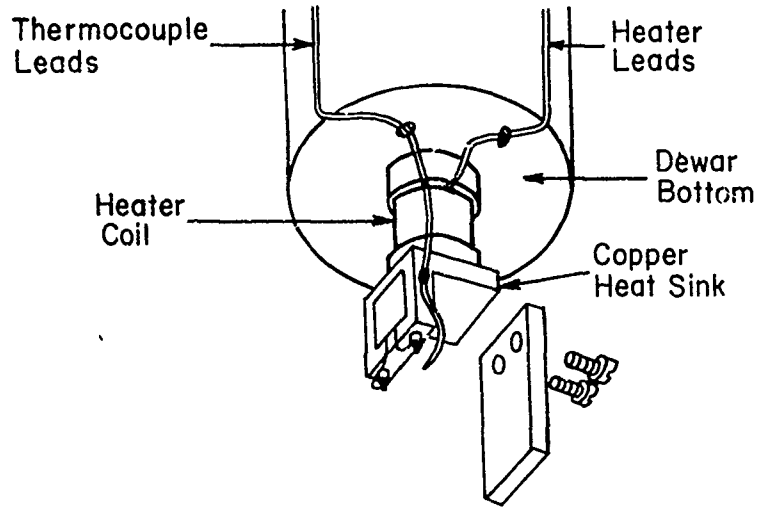

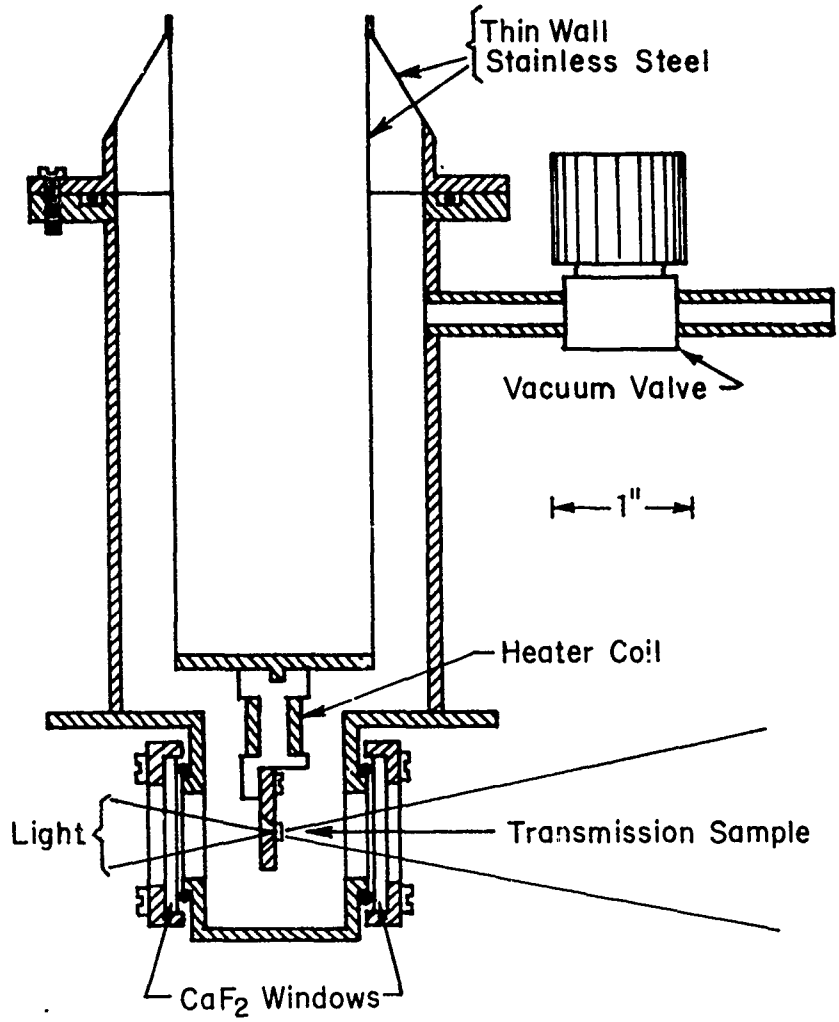

FIGURE II-4 An optical dewar designed for the single beam spectrometer (35).

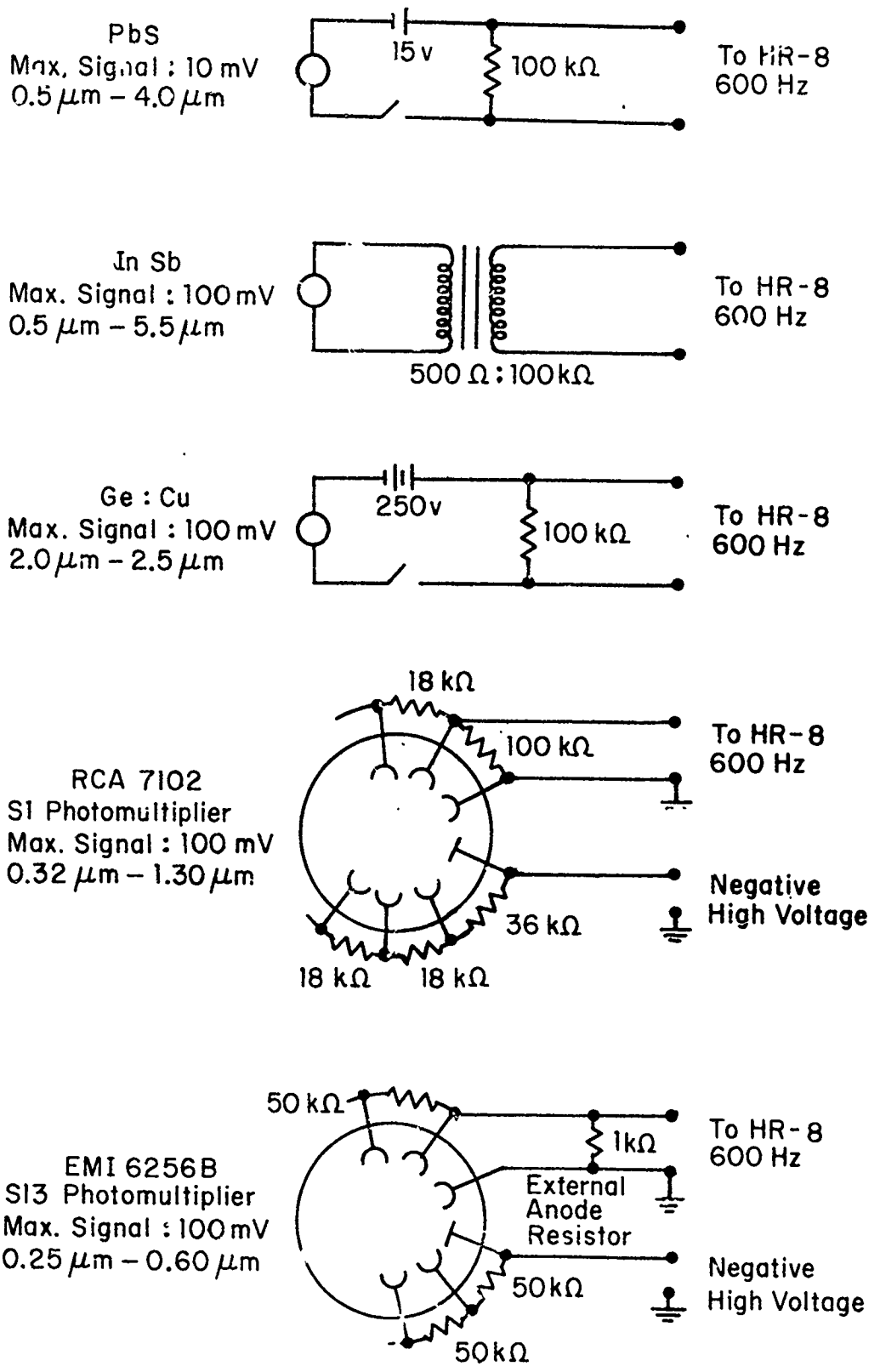

FIGURE III-5 The diagram summary of our detectors and their associated electronics (35).

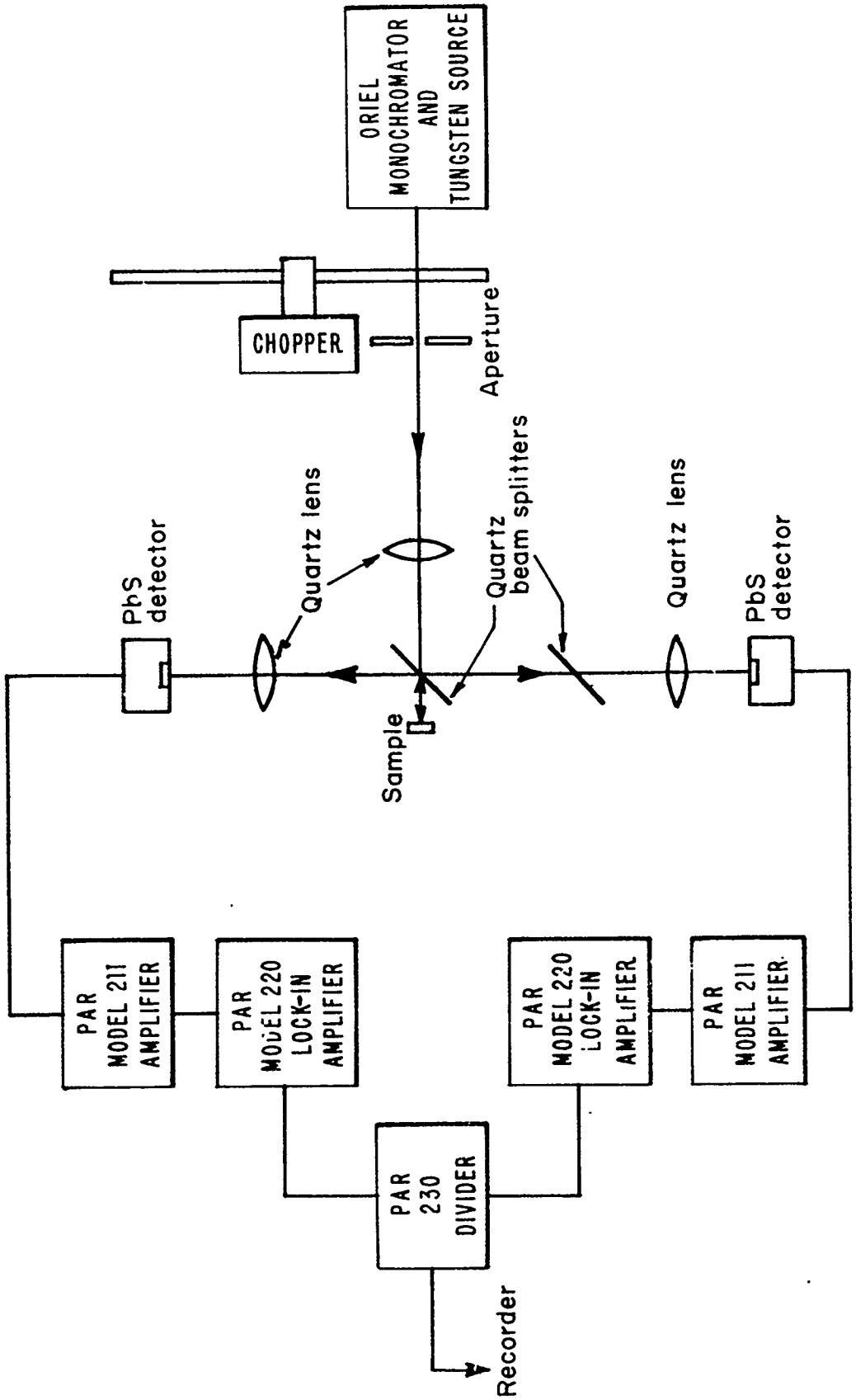

FIGURE III-6 The schematic diagram of the ratio reflectometer and its associated electronics.

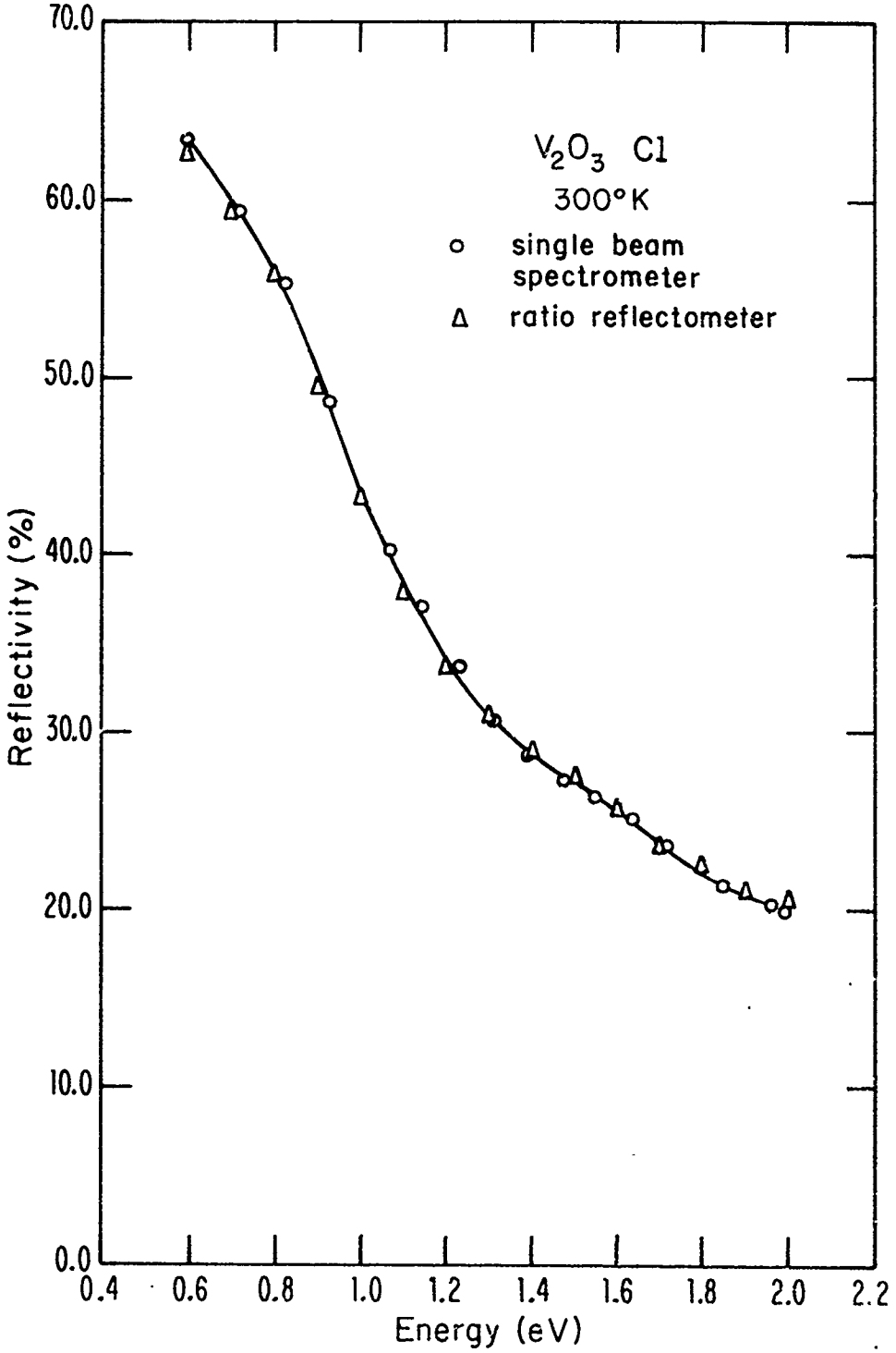

FIGURE III-7 The reflectivity of a V_2O_3 sample measured in both the single beam spectrometer and the ratio reflectometer.

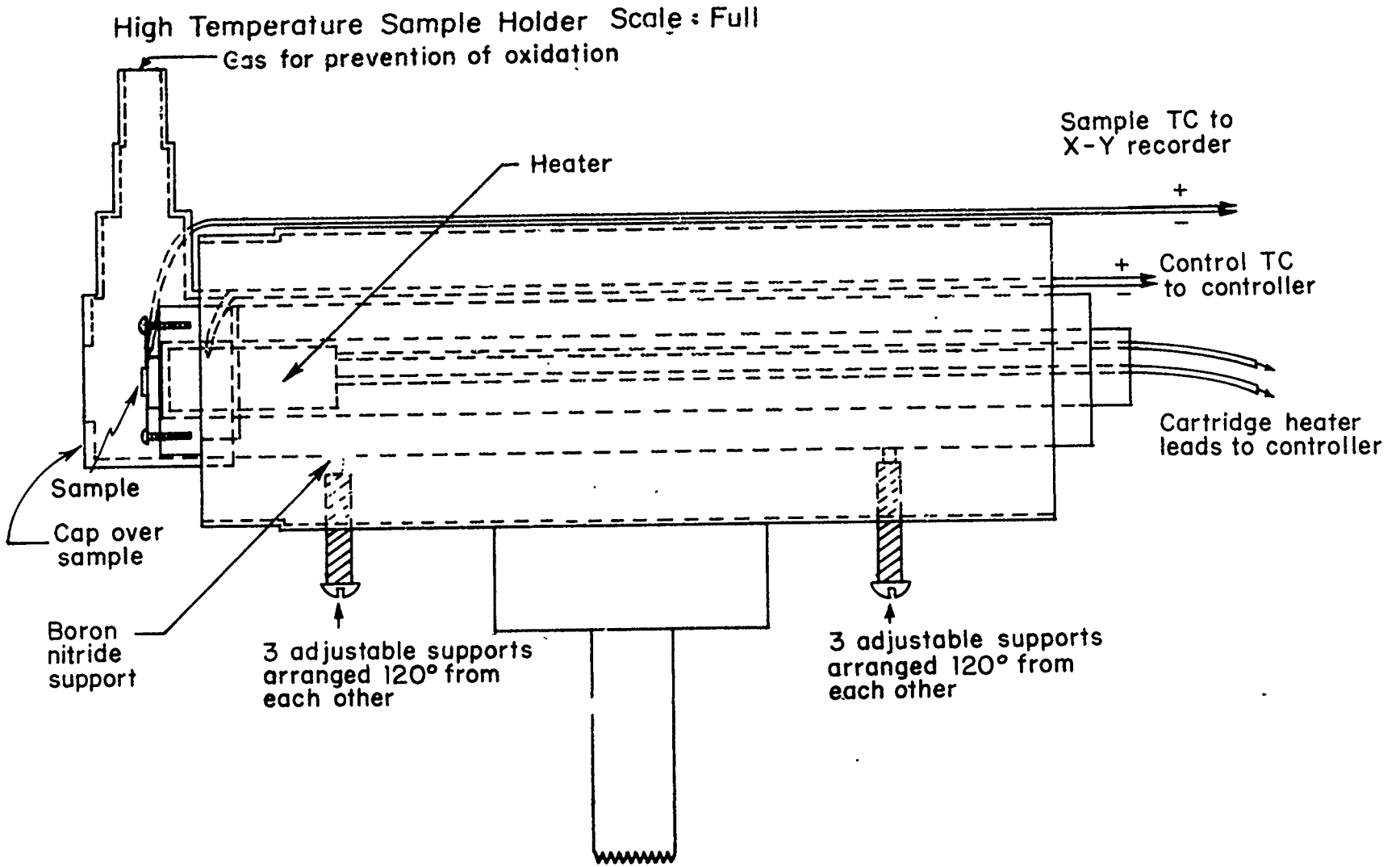

Note : Unless specified, the screws are made of stainless steel, and the rest of the setup of brass
The adjustable supports are used for optical alignment.
T C means Thermocouple (Chromel - Alumel)

FIGURE III-8 The schematic diagram of the high temperature optical sample holder.

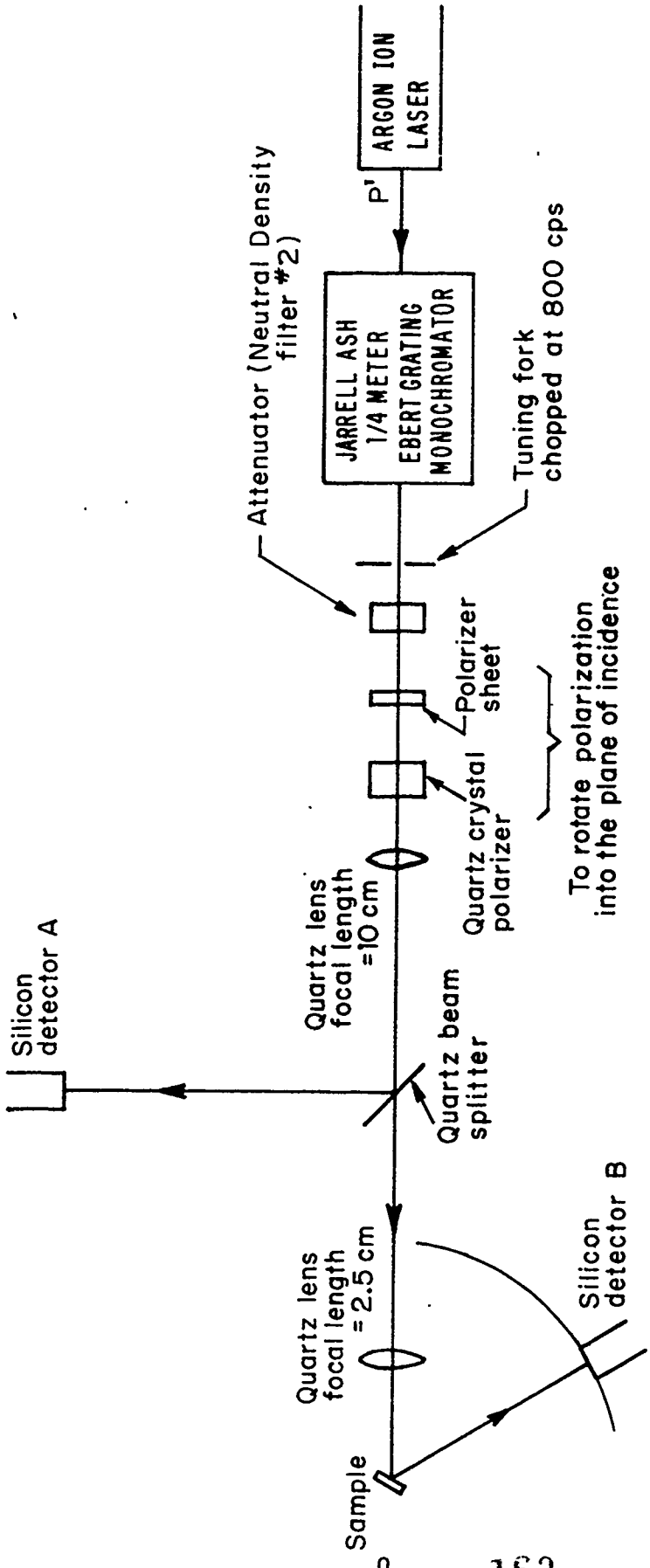

FIGURE III-9 The optical set-up for the angular dependence measurements.

CHAPTER IV

OPTICAL RESULTS AND DISCUSSION

In this chapter, we shall report the results of our optical measurements on VO_2, V_2O_3 and $(V_{1-x}Cr_x)_2O_3$. Most of our measurements were done on single crystals of V_2O_3 and $(V_{1-x}Cr_x)_2O_3$. The optical properties of VO_2 single crystals have already been reported by Ladd and Paul (1) and Ladd (2). We shall, however, present the optical constants we have derived from the reflectivity curves of VO_2 reported by Ladd (2). The optical properties of films will then be presented as a comparison to those of bulk crystals. Since the films have much smaller changes in resistivity at the phase transition than those of bulk crystals (see Chapter III) and since their thickness is usually uneven, and their surfaces rough, no optical constants were derived from measurements on the films.

A. Introduction

Most of our optical measurements were made on unoriented crystals, mainly because, in our experimental observation, we had found no significant optical anisotropy in such crystals at room temperature. Here, we will elaborate on this question.

In separate studies, it has been found that the dc electrical conductivity of V_2O_3 crystals in the metallic state exhibits no significant anisotropy (3, 4). Feinleib and Paul (3) reported that the anisotropy ratio of V_2O_3 crystals (the ratio of resistivity along the c-axis to resistivity along the a-axis of the crystal) varied from 0.9 at 275°K to

1.1 at 625°K. While a lack of anisotropy in the dc electrical conductivity of a crystal does not necessarily imply a lack of anisotropy in the frequency dependent optical constants, it is not uncommon to find no significant optical anisotropy in uniaxial crystals. For example, in quartz (SiO_2) which is hexagonal in structure, the refractive indices n_e, obtained with the electric field vector along the c-axis, and n_o, obtained with the electric field vector perpendicular to the a-axis, were reported in the wavelength interval from 0.19μ to 2.18μ and were found to be within 1% of each other over the entire wavelength region (5). In sapphire (Al_2O_3), which has the corundum structure, n_e and n_o were measured in the interval from 0.54μ to 0.67μ and they too were found within 1% of each other (5). And Chandrasekharan and Damany (6), who investigated the optical constants of Al_2O_3 in the vacuum ultraviolet region from 0.61μ to 0.32μ, reported that the refractive indices n_e and n_o were within 1.5% of each other over this wavelength region.

To confirm that there is no significant optical anisotropy in our crystals we performed an experiment* on a V_2O_3 crystal from Run #1 (x-ray Laue back reflection pattern showed the front surface $\sim[01\bar{1}2]$, which is $\sim 58^\circ$ from the c-axis), and on a $(V_{0.982}Cr_{0.018})_2O_3$ crystal from Run #9 (x-ray Laue back reflection pattern showed the front surface to be $\sim 20^\circ$ away from the c-axis) at room temperature. These crystals will henceforth be referred to as B1 and R1 respectively. The crystals were mounted on a rotating disk so that the axis of rotation was along the incident optical path of the ratio-reflectometer described in

*In collaboration with Dr. Paul Raccah, Lincoln Laboratory.

Chapter III. The incident light was polarized by a quartz crystal polarizer in such a way that the electric field was perpendicular to the plane of incidence. Since the c-axis was not perpendicular to the front surface of either of the crystals, the incident polarization should have different effects on the c-axis and a-axis when the crystals were rotated about the optical axis. We did the polarization studies at four photon energies: 2.0eV, 1.5 eV, 1.0 eV, and 0.65 eV. As we rotated the crystals, their reflectivity remained within $\pm$ 1% of their values, which is within the range of experimental uncertainty of the optical setup. Therefore, the experiment indicated that there was no significant anisotropy in the crystals between 0.6 eV and 2.0 eV; please note that a lack of optical anisotropy in a crystal between 0.6 eV and 2.0 eV does not necessarily imply that there is no anisotropy over the whole spectral region.

We then turned to other observations to demonstrate further the lack of optical anisotropy in these crystals. We found that the optical constants B1 and R1 obtained from the angular dependence measurements were very similar to those derived by the oscillator fit method from the near-normal incidence reflectivity measurements (at the same energies: 1.96 eV and 2.54 eV respectively). For reasons we will discuss later in this chapter, we concluded from the above observation that the optical anisotropy in these crystals is not significant.

Since we observed no significant optical anisotropy, our measurements could be done on unoriented, mechanically polished crystals —

this was fortunate since almost all our crystals were too small (approximately 2-3 mm across and 3 mm long) for crystal orientation anyway.

The crystals were first polished by 10μ Al_2O_3 paste, followed by 5μ and 2μ diamond pastes and finished with 1μ diamond paste. They were then rinsed in alcohol and in de-ionized water, and blown dry with dry nitrogen gas. The samples prepared this way have very similar optical surfaces, as demonstrated by the close resemblance of the reflectivity spectra of the two V_2O_3 crystals C1 and C2 (they were cut from a boule from Run #2 with c-axis perpendicular to the plane of the crystals, and the reflectivity spectra are shown in Fig. IV-1).

B. Angular Dependence Measurements*

We have discussed earlier in Chapter III that the values of optical constants evaluated from a reflectivity spectrum by either the oscillator fit method or the Kramers-Kronig analysis could be subject to errors. To minimize the possibility of errors, we obtained the values of n and k at two photon energies (1.96 eV and 2.54 eV) by the angular dependence measurements, and then required the calculated values of n and k obtained by the Kramers-Kronig analysis or the oscillator fit method to fit the measured values at the above mentioned photon energies (for detailed discussion see Chapter III). We will present the results of the angular dependence measurements in this section.

Angular dependence measurements were done on C1 and C2 crystals at room temperature. Figures IV-2 and IV-3 show the reflectivity R_p

*In collaboration with Dr. Paul Raccah, Lincoln Laboratory.

of C1 and C2 as a function of incidence angle ϕ at both 1.96 eV and 2.54 eV. Using the angular dependence curve fitting procedure described in Chapter III, we obtained reasonable fits between the theoretical and the experimental values of R_p as a function of ϕ. The values of n and k, which provide such fits, are listed as follows:

For C1:

At 1.96 eV, n = 1.77 and k = 1.10

At 2.54 eV, n = 1.82 and k = 0.90

For C2:

At 1.96 eV, n = 1.78 and k = 1.10;

At 2.54 eV, n = 1.81 and k = 0.90

Angular dependence measurements were also done on R1. The measured and fitted R_p versus ϕ values are shown in Fig. IV-4 and their optical constants are listed as follows:

At 1.96 eV, n = 2.02 and k = 1.14;

At 2.54 eV, n = 1.86 and k = 0.96.

Error Analysis. Since Eq. (3-5b), used in the angular dependence method, is very complex, error analyses by mathematical means would be difficult. Instead, we took a different approach. First, an angular dependence measurement was done on the V_2O_3 crystal B1 at 2.54 eV; the optical constants obtained were n = 1.79 and k = 0.89. Then to investigate the effect of the absolute values of R_p on the values of n and k, we multiplied all the R_p values of B1 by a factor of 1.05. After fitting the newly generated data using Eq. (3-5b), we obtained no change

in n and an increase of ~ 3% in k. Similarly, by multiplying the experimental R_p values of B1 by 0.95 and fitting the newly generated data, we again found no change in n, and a decrease of ~ 3% in k. By keeping R_p values the same as the experimental values but by increasing each corresponding value of ϕ by 5 degrees, we found an increase of ~8% in n and a slight decrease (~ 1%) in k. Obviously, the above analysis holds true only for this particular set of n and k. However, since the values of n and k obtained for all our crystals are in the vicinity of the above values (n = 1.79, k = 0.89), we should expect similar dependence of the n and k of C1, C2 and R1 on the experimental accuracy of R_p and ϕ. In our optical setup, the uncertainty in ϕ from the alignment errors, as stated in Chapter III, should not exceed 1/5 degree and the accuracy of R_p should be within $\pm$ 1%. Therefore, the actual experimental uncertainties in ϕ and R_p should cause very small errors in n and k.

There are, however, other sources of error, namely, surface scattering and polarization effects. In angular dependence measurement, surface scattering could become important when the surface of the material is rough. Strictly speaking, the effects of surface scattering on our measurements can be considered as two parts; the first part is independent of the incidence angle ϕ and will affect equally the absolute values of R_p at all ϕ's. Its effects have been shown to be small in our earlier investigation of effects on n and k by the uncertainties in the absolute values of R_p. The second part of the surface scattering effects

is dependent on ϕ and the effects usually become important for large angles of incidence. To demonstrate that this part is also unimportant to our measurements, we deleted the experimental value of R_p of C1 at $\phi = 70^\circ$ from the initial set of data points (at 2.54 eV), and proceeded to fit this new set of data points. If the surface scattering were important, we should expect an appreciable change in n and k; however, we obtained n = 1.81 and k = 0.90 which are very similar to those obtained from the initial set of data points (n = 1.82 and k = 0.90), thus indicating that the surface scattering effects are not important.

Our measurements were done with the electric field of the incident radiation polarized in the plane of incidence. If in the incident beam, the electric field were to contain a component which is polarized perpendicular to the plane of incidence, there is a possibility of error because the R_p* and R_n* as a function of ϕ are expressed by different equations (see Eqs. (3-5a and 5b)).

To incorporate this mixing effect into Eq. (3-5b), we modified it:

$$R = R_p + pRn \qquad (4\text{-}1)$$

where

$$p = \frac{\text{intensity of incident radiation with the electric field polarized perpendicular to the plane of incidence;}}{\text{intensity of incident radiation with the electric field polarized in the plane of incidence}}$$

p was measured and found to be less than 0.0015 in our system. We then fitted the experimental values of the reflectivity of C2 as a function

---

*$R_p(R_n)$, as defined in Chapter III, is the reflectivity of a crystal when the electric field of incident radiation is polarized in (perpendicular to) the plane of incidence.

of ϕ at 2.54 eV using Eq. (4-1) with p = 0.0015, and obtained n = 1.82 and k = 0.89, which again are very close to n = 1.81 and k = 0.90 obtained by fitting the experimental values using Eq. (3-5b).

There was also the indication that any effects of optical anisotropy on the optical constants at 1.96 eV and 2.54 eV were negligible. If there is any significant anisotropy, then a good fit of the theoretical curve to the experimental values of R_p versus ϕ for all ϕ will be difficult to obtain. This was not the case in our experiments. Furthermore, even if the crystals were anisotropic and good fits were obtained between the theoretical curves and the experimental curves, the optical constants n and k obtained should be different from those derived from near-normal incidence reflectivity spectra of those crystals using the oscillator fit method. We will see later that the constants obtained from both the angular dependence measurements and the oscillator fit method are very similar.

From the above discussions of all the possible sources of error, we feel that our accuracy in determining n and k should be better than $\pm$ 5% of their values, and we will proceed to use them in our later analyses.

C. Optical Results on V_2O_3 and $(V_{0.982}Cr_{0.018})_2O_3$ and VO_2 Using the Single Beam Spectrometer

1. V_2O_3

a. $T > T_t$

The optical reflectivity of the two V_2O_3 crystals C1 a[illegible] was measured in the single beam spectrometer described in Chapter III

and in Ladd's work (2). A great part of the uncertainty in the reflectivity measurements using the spectrometer is due to re-focussing errors. To eliminate this source of uncertainty in our experiment, we normalized the reflectivity values of C1 and C2 at 1.96 eV to 20.2% and 20.1% respectively; these values were obtained from near-normal incidence reflectivity measurements using a helium-neon laser. Figure IV-1 shows the resulting reflectivity curves of both C1 and C2 at room temperature.

Since the values of n and k at both 1.96 eV and 2.54 eV for C1 are close to those for C2, and since the reflectivity spectra of these two crystals are also similar, we have only to derive the optical constants for one of the curves, in our case, for the reflectivity spectrum of the C1 crystal; the other crystal, C2, should give similar results.

Figure IV-5 shows the theoretical reflectivity curve obtained from an oscillator fit to the experimental reflectivity data of C1. In this particular fit, we used Eq. (3-17b) to express the complex dielectric constant $\epsilon(\omega)$ and used Eq. (3-21b) as the objective function in the fitting procedure so that the values of n and k at 1.96 eV and 2.54 eV obtained from the oscillator fit were constrained to approach those values obtained from the angular dependence measurements. Table IV-1 shows the values of n and k obtained from this fit.

Figures IV-6, 7, and 8 show respectively ϵ_1 (the real part of the dielectric constant ϵ), ϵ_2 (the imaginary part of the dielectric constant ϵ)

Method	At 1.96 eV		At 2.54 eV	
	n	k	n	k
Angular Dependence	1.77	1.10	1.82	0.90
Oscillator Fit using Eq. (3-21b)	.79	1.10	1.79	0.89
Oscillator Fit using Eq. (3-21a)	1.81	1.10	1.81	0.86
Kramers-Kronig p = 1.0	1.83	1.08	1.81	0.86
Kramers-Kronig p = 1.1	1.81	1.09	1.79	0.87
Kramers-Kronig p = 1.2	1.78	1.09	1.76	0.88
Kramers-Kronig p = 1.3	1.76	1.10	1.73	0.89

TABLE IV-1. Optical constants n and k of a V_2O_3 crystal (C1) at room temperature, obtained by different methods.

and the absorption coefficient α as a function of photon energy. We then used the same initial values of the parameters in Eq.(3-17b), but changed the objective function from Eq. (3-21b) to Eq. (3-21a), so that the optical constants at 1.96 eV and 2.54 eV were allowed to take any values. Judging from the reasonable fit shown in Fig. IV-5, we would expect the values of n and k at 1.96 eV and 2.54 eV should not be very different from those obtained from the angular dependence method. If, then, the values of the optical constants at 1.96 eV and 2.54 eV obtained from a reasonable fit to the experimental data were very much

different from the values obtained from the angular dependence method, then it would suggest three possible situations: 1) the oscillator fit method by itself is not adequate to give accurate values of n and k at 1.96 eV and 2.54 eV; 2) the angular dependence method did not give us accurate results, probably because of an optical anisotropy; or 3) the reflectivity spectrum has appreciable errors.

Figure IV-9 shows the theoretical reflectivity curve obtained from the oscillator fit to the experimental data using Eq. (3-21a) and Figs. IV-10, 11, and 12 show ϵ_1, ϵ_2 and α, respectively, as a function of photon energy obtained from this fit. These curves are all similar to the respective curves in Figs. III-6, 7, and 8. The values of the optical constants at 1.96 eV and 2.54 eV are also listed in Table IV-1, and they, indeed, are close to those obtained from the angular dependence measurements, indicating that none of the above three possible situations actually pertains.

One could then ask whether it was actually necessary to obtain the optical constants at 1.96 eV and 2.54 eV using the angular dependence measurements, since the oscillator fit method using Eq. (3-21a) did give us quite accurate values of n and k at 1.96 eV and 2.54 eV (as demonstrated above); or, to put the question differently, will the oscillator fit always give us the correct values of the optical constants? To answer this question, one must re-examine the oscillator fit method carefully. In this method, the complex dielectric constant $\epsilon(\omega)$ is expressed in terms of a series of oscillator terms and, for metals, a

Drude term (see Eq. (3-17a) or Eq. (3-17b)), and the values of the reflectivity are calculated using Eq. (3-18). Then, the parameters of the oscillator terms and the Drude term are automatically adjusted until a good fit is obtained between the calculated and measured reflectivity values. If we have only one experimental data point to be fitted, then judging from Eq. (3-18). we can select an infinite number of combinations of ϵ_1 and ϵ_2 that will give a calculated reflectivity value close to the measured one. However, in practice, we always have data points in a wide spectral range, and hence correct selection of ϵ_1 and ϵ_2 is much easier since the values of ϵ_1 and ϵ_2 have to be related to each other through Eq. (3-17a) or Eq. (3-17b). There is still no absolute guarantee, however, that we will obtain the correct set of ϵ_1 and ϵ_2. A theoretical study of how this uncertainty can influence our results is very difficult and is dependent on each particular spectrum. To examine the effects of this uncertainty, or non-uniqueness, we obtained three different sets of parameters that gave good fits to the reflectivity spectrum of C1 (by using different sets of initial values of the parameters in Eq. (3-17b)). A comparison of the values of n and k obtained from these fits at 1.96 eV and 2.54 eV with those values obtained by the angular dependence measurements should give us some idea of the seriousness of the effects of this non-uniqueness. We found that in all these three fits, the values of n and k at 1.96 eV and 2.54 eV we. e still close to

the measured values. Here, we will report the results of the worst match.* Figure IV-13 shows the theoretical fit to the experimental data obtained from the oscillator fit method using Eq. (3-21a). The values of n and k at 1.96 eV and 2.54 eV are as follows:

at 1.96 eV, $n = 1.75$, $k = 1.11$

at 2.54 eV, $n = 1.72$, $k = 0.89$

The plots of ϵ_1, ϵ_2, and α versus photon energy resulting from this fit are shown in Figs. IV-14, 15, and 16. Though there are some differences in the values of these optical constants from those reported earlier, especially for E > 2.5 eV, the general features of these curves are still very similar to their corresponding curves reported above.

---

* The criterion for the best match is to choose the particular fit such that the value of the function f, defined below, is at a minimum:

$$f = \left(\frac{n_{cal} - n_{meas}}{n_{meas}}\right)_{1.96\,eV} + \left(\frac{n_{cal} - n_{meas}}{n_{meas}}\right)_{2.54\,eV}$$

$$+ \left(\frac{k_{cal} - k_{meas}}{k_{meas}}\right)_{1.96\,eV} + \left(\frac{k_{cal} - k_{meas}}{k_{meas}}\right)_{2.54\,eV}$$

where

subscript "meas" = measured value, and
subscript " cal" = calculated value.

Therefore, while our investigation is not very exhaustive, the oscillator fit method most probably can provide us reasonable values of optical constants. If we still need more accurate values of the constants, then we have to obtain the values of the optical constants at some photon energies in the spectral range of our interest, say n and k, by other methods such as the angular dependence method. The calculated values of n and k obtained from the oscillator fit method are then constrained to approach those obtained from the angular dependence method. By this approach, correct selection of values of ϵ_1 and ϵ_2 can be assured.

We then did a Kramers-Kronig analysis on the reflectivity curve of C1 (the data points of the reflectivity spectrum were spaced at photon energy intervals of 0.05 eV). Equation (3-11) was used in the extrapolation procedure (discussed in Chapter III); p was varied from 0.0 to 5.0 by increments of 0.1. Only four values of p, namely p = 0.0, p = 1.1, p = 1.2, and p = 1.3, gave values of n and k at 1.96 eV and 2.54 eV that were within $\pm$ 5% of the measured values (see Table IV-1). From the table it can be noted that the Kramers-Kronig analysis using p = 1.1 and p = 1.2 gave values of n and k which were very close to the measured values, though a slightly better match was obtained using p = 1.2 than was obtained using p = 1.1.* Figures IV-17, 18, and 19

*The criterion for the best match is to choose the particular p such that the value of the function f, defined below, is a minimum:

$$f = \left(\frac{n_{cal} - n_{meas}}{n_{meas}}\right)_{1.96\,eV} + \left(\frac{n_{cal} - n_{meas}}{n_{meas}}\right)_{2.54\,eV} + \left(\frac{k_{cal} - k_{meas}}{k_{meas}}\right)_{1.96\,eV} + \left(\frac{k_{cal} - k_{meas}}{k_{meas}}\right)_{2.54\,eV}$$

where
subscript "meas" = measured value, and
subscript "cal" = calculated value.

show respectively the plots of ϵ_1, ϵ_2 and α versus photon energy. In Fig. IV-17 and Fig. IV-18, the curves were obtained using p = 1.2. Figure IV-19 shows the plots of α versus photon energy for p = 1.1, p = 1.2 and p = 1.3; though the curves are quite similar, there are some differences among them for photon energies greater than 2.0 eV, Therefore, it appears that if we do not have any previous knowledge of n and k at 1.96 eV and 2.54 eV, the proper selection of p that will give us correct values of n and k will be difficult in the Kramers-Kronig analysis, while in the oscillator fit method, we have a much better chance to obtain reasonable values of n and k.

In summary, the plots of ϵ_1, ϵ_2 and α versus photon energy, obtained using the above three different approaches, are similar. except for some minor differences that arose from the curve fitting and from extrapolation uncertainties. Also, in all the ϵ_2 curves, we observe structures at about 0.6 eV, 1.5 eV and 4.3 eV. There is a weak, broad structure between 2.0 eV and 2.4 eV. Further discussion of these structures will be presented in Chapter V.

As mentioned in Chapter III, the oscillator fit method allows us to extract the free electron contribution directly from the reflectivity spectrum. The parameters of the free electron contribution can vary somewhat depending on the initial values of the parameters used (within 20%). Furthermore, in our oscillator fit method, our parameters are obtained with the assumption that we have a one-band model with all the conduction electrons having the same mobility and effective mass. This is, of course, a serious approximation, and the values of the

optical mobility and the values of the effective mass of the conduction electrons, obtained from the calculation shown below, are thus only an order of magnitude calculation, and should be interpreted as such.

From the oscillator fit method where the values of n and k at 1.96 eV and 2.54 eV were constrained to approach the values measured in the angular dependence measurements, we obtained:

$E_n = 3.54\,eV,$

$E_c = 0.678\,eV.$

Where E_n and E_c are defined as follows:

$$\omega_n = \frac{E_n}{\hbar} = \frac{4\pi n_c e^2}{m^*} \qquad (4\text{-}2)$$

$$\omega_c = \frac{E_c}{\hbar} = \frac{e}{\mu_{opt} m^*} = \frac{1}{\tau_c} \qquad (4\text{-}3)$$

where

n_c = concentration of conduction electrons/holes of optical mobility μ_{opt}, and optical effective mass m*.

τ_c = relaxation time of the conduction electrons/holes.

In V_2O_3, there are 3.92×10^{22} vanadium ions cm^{-3}. As mentioned in Chapter I, there are two outer d electrons per vanadium ion left after all the bonding requirements are fulfilled. If we assume a one-band model and that these outer electrons all become conduction electrons, then n_c is equal to 7.84×10^{22} cm^{-3}. Using $E_n = 3.54\,eV$ and $E_c = 0.678\,eV$, and the above value of n_c in Eq. (4-2) and Eq. (4-3), we obtain $m^* = 9.1\,m_e$ and $\mu_{opt} = 0.19\,cm^2/V\text{-sec}$, where m_e = free

electron mass. Furthermore from Eq. (4-3), we obtained τ_c = 9.8×10^{-16} sec.

Though it might be questionable for us to compare the value of the optical mobility with that of the Hall mobility,* it is nevertheless interesting to see whether they are within the same order of magnitude.

Hall effect measurements have been done on V_2O_3 by several people (7, 8, 9). The results obtained varied among the studies. Rosevear and Paul (7) measured a V_2O_3 crystal grown by us using the vapor transport technique and found $R_H\sigma = 0.95 \pm 0.2$ cm^{-3}/V sec, which would correspond, in a one-band model, to a carrier concentration of 1.6×10^{22} cm^{-3} and Hall mobility $\mu_H = 0.95 \pm 0.2$ cm^2/V-sec. Austin and Turner (8) found $R_H\sigma = 0.4$ cm^2/V-sec, which would correspond, in a one-band model, to a Hall carrier concentration of 2.7×10^{22} cm^{-3} and $\mu_H = 0.4$ cm^2/V-sec. Zhuze et al. (9) found $R_H\sigma = 0.4$ cm^2/V-sec, which could compare, in a one-band model, to a carrier concentration of 3.8×10^{22} cm^{-3} and $\mu_H = 0.4$ cm^2/V-sec. (The above-mentioned workers all found that the Hall carriers would correspond to holes in a one-band model.) Hence, in a one-band model, the values of Hall mobility measured are in the same order of magnitude as that of the optical mobility.

*This is especially true if the one-band model is not valid, and one has to consider overlapping bands. In the metallic state of V_2O_3, the metallic conductivity could very well be caused by mixed conduction. The Hall measurements, as well as our optical measurements, however, would not be able to give us the values of prevalent parameters in such cases. The one-band model, therefore, represents the simplest approximation.

Finally, a comparison can be made between the value of the optical mobility and Hall mobility with that of the mobility obtained using the following equation.

$$\sigma = ne\mu \qquad (4\text{-}4)$$

where

σ = conductivity,

μ = mobility, and

n = number of charge carriers.

If we assume a one-band model and assume $n = 7.84 \times 10^{22} cm^{-3}$ and $\sigma = 5 \times 10^{3} (\Omega\text{-}cm)^{-1}$ (the resistivity of a bulk V_2O_3 crystal as reported in Chapter II) then $\mu = 0.4 cm^2/V\text{-}sec$, which is of the same order of magnitude as the values of Hall mobility and optical mobility described above.

In the oscillator fit method where the values of n and k at 1.96 eV and 2.54 eV were not constrained to approach the measured values, we obtained $E_n = 3.50$ eV and $E_c = 0.656$ eV, similar to those values we used in the above calculation Therefore, similar results can be expected.

Finally, we should point out that the crystals C1 and C2 were cut from the same boule grown in the tri-arc furnace. V_2O_3 crystals grown by the vapor transport technique have also been measured optically. We found that the optical reflectivity spectrum at room temperature of the as-grown crystal resembled that of VO_2 (to be shown later). After

the crystal was lapped, the spectrum became that of V_2O_3 indicating that a small layer of VO_2 had very probably been removed. Since these crystals were very small and often cracked during lapping, they were not used further for definitive determination of the optical properties. Because x-ray, chemical analysis, electrical conductivity measurements and Hall effect measurements all showed that the crystals were V_2O_3, the VO_2 film must be very thin. The thin film was probably caused by the oxidation that occured during the shutdown of the vapor transport apparatus. At the end of each crystal run, the furnace and the gas flows were shutdown at the same time. Though the system was supposedly a closed system (see Chapter II), inevitably some air would leak in during the cooling of the furnace causing the surfaces of the crystals to oxidize.

b. $T < T_t$.

Figure IV-20 shows the experimental reflectivity data of a V_2O_3 crystal, C1, at 120°K together with the theoretical reflectivity curve obtained from the oscillator fit method. The reflectivity measurements were done in our single beam spectrometer using the optical dewar described in Chapter III. Above 1 eV, the low temperature reflectivity curve is similar to that at room temperature. Below 1 eV, a peak at about 0.8 eV and a shoulder around 0.4 eV appeared.

The optical constants ϵ_1, ϵ_2, and α obtained from the oscillator fit are shown in Figs. IV-21, 22, and 23 respectively. The absorption coefficient α was found to decrease steadily below 1 eV with a shoulder

around 0.4 eV. Using Eq. (3-4b) and the absorption coefficients, the transmission of a thin 0.5μ V_2O_3 crystal was calculated and plotted (see Fig. IV-24). Though the theoretical reflectivity curve does not match exactly with the experimental data (see Fig. IV-20), the structures in the predicted transmission spectrum are quite apparent. When this predicted spectrum is compared with the transmission spectra measured in the single beam spectrometer on thin films of V_2O_3,* grown by sputtering and vapor transport techniques, the similarity in shape between them is quite obvious (see Fig. IV-25).

From the transmission spectrum, as well as from the absorption coefficient α versus photon energy curve, we notice that there is no sharp absorption edge as in germanium and silicon. The absence of a sharp absorption edge was also noted by Feinleib and Paul (3), using a transmission measurement on a thin (~25μ thick) V_2O_3 crystal (see Fig. IV-25).

We should point out that the reflectivity spectrum has not been analyzed by the Kramers-Kronig analysis since we do not have the necessary prior knowledge of any of the optical constants in the spectral range of our interest to enable us to select the proper extrapolation parameters for the reflectivity spectrum at both the high and low photon energy regions.

---

*The structural and electrical properties of these films were presented in Chapter II.

In summary, at $T > T_t$, we have structures in the ϵ_2 curve (Fig. IV-7 or 15 or 18) at around 0.6 eV, 1.5 eV, 2.0-2.4 eV, and 4.3 eV. At $T < T_t$, structures are observed in the ϵ_2 curve (Fig. IV-22) at around 0.4 eV, 0.9 eV, 1.5 eV, 2.0-2.4 eV, and 4.3 eV. We will interpret these results in Chapter V.

2. $(V_{0.982}Cr_{0.018})_2O_3$

As discussed earlier in Chapters I and II $(V_{1-x}Cr_x)_2O_3$ crystals would undergo a phase transition from a metallic state into an insulating state at room temperature at a critical chromium concentration $x \tilde{=} 0.010$. However, x-ray diffraction studies in our doped crystals showed that for $x = 0.010$ and 0.014, both the metallic and insulating phases coexisted at room temperature. Therefore, to study the optical properties of the insulating state of a doped crystal at room temperature, we chose a $(V_{0.982}Cr_{0.018})_2O_3$ crystal, which has the largest chromium concentration among all our crystals runs, and which has been shown by x-ray diffraction studies to contain no metallic phase (see Chapter II).

The reflectivity of the $(V_{0.982}Cr_{0.018})_2O_3$ crystal (R1) at room temperature was measured in the single beam spectrometer. As in the case of V_2O_3, the reflectivity at 1.96 eV was normalized to 22.2%, the value measured in a near-normal incidence reflectivity measurement using a helium-neon laser.

Figure IV-26 shows the theoretical reflectivity curve obtained from the oscillator fit to the experimental reflectivity data. The fit was obtained using Eq. (3-17a) as the expression for the dielectric constant $\epsilon(\omega)$ and using Eq. (3-21b) as the objective function, that is, the values

of n and k at 1.96 eV and 2.54 eV obtained from the oscillator fit method were constrained to approach the measured values of n and k at 1.96 eV and 2.54 eV. Table IV-2 shows the list of n and k values

Method	At 1.96 eV		At 2.54 eV	
	n	k	n	k
Angular Dependence	2.02	1.14	1.86	0.96
Oscillator Fit using Eq. (3-21b)	2.02	1.14	1.85	0.95
Oscillator Fit using Eq. (3-21a)	2.01	1.13	1.86	0.93
Kramers-Kronig p = 1.2	2.05	1.11	1.86	0.92
Kramers-Kronig p = 1.3	2.02	1.12	1.83	0.94
Kramers-Kronig p = 1.4	1.99	1.14	1.80	0.95
Kramers-Kronig p = 1.5	1.95	1.15	1.77	0.96

TABLE IV-2. Optical constant n and k of a $(V_{0.982}Cr_{0.018})_2O_3$ crystal (R1) at room temperature, obtained by different methods.

obtained by the different methods we used, and, in particular, shows that by this method, we obtained n = 2.02 and k = 1.14 at 1.96 eV, and n = 1.85 and k = 0.96 at 2.54 eV. These values are very close to those obtained by the angular dependence method. Figures IV-27, 28, and 29 show respectively the plots of ϵ_1, ϵ_2, and α versus photon energy obtained from the above fit.

As in the case of the V_2O_3 crystals (C1), the reflectivity spectrum was then fitted using Eq. (3-21a) as the objective function.* In this case, the optical constants n and k at 1.96 eV and 2.54 eV were allowed to take any values. Figure IV-30 shows the theoretical reflectivity curve obtained. The plots of ϵ_1, ϵ_2, and α versus photon energy are shown in Figs. IV-31, 32, and 33 respectively.

The values of n and k at 1.96 eV and 2.54 eV obtained from this fit are also listed in Table IV-2. They are again similar to those obtained by the angular dependence method.

In the oscillator fit method, the values of the optical constants obtained are obviously dependent on how good a fit we can obtain between the experimental reflectivity data and the theoretical curve. When a poor fit occurs, some fine structures in the optical constants will be lost. This can be illustrated well in the following results. Figure IV-34 shows the theoretical reflectivity curve obtained from the oscillator fit to the experimental data of R1 (using Eq. (3-21a)). Figures IV-35, 36, and 37 show the ϵ_1, ϵ_2 and α curves as a function of photon energy. There were some differences between these curves and the corresponding curves shown in Figs. IV-31, 32, and 33, especially at photon energies between 2.0 eV and 2.5 eV where the fit was quite poor. The values of n and k obtained from the fit were as follows:

at 1.96 eV, n = 1.97, k = 1.15 at 2.54 eV, n = 1.83, k = 0.94

*The initial values of the parameters in the fitting program were kept the same as those used to obtain the fit shown in Fig. IV-26.

These values were not as close to those obtained from the angular dependence measurements as those values obtained from the fits reported earlier.

Despite some difference, however, when the plots of ϵ_1, ϵ_2, and α versus photon energy obtained from all the fits using either Eq. (3-21a) or Eq. (3-21b) were compared with one another, the resultant curves were similar.

Kramers-Kronig analysis of the reflectivity spectrum yielded results similar to those obtained from the oscillator fit method and they are shown in Figs. IV-38, 39, and 40. As in the case of V_2O_3, the values of p in Eq. (3-11) were varied from 0.0 to 5.0 by increments of 0.1. Four values of p, namely 1.2, 1.3, 1.4, and 1.5, were obtained which gave n and k values at 1.96 eV and 2.54 eV that were within $\pm$ 5% of the measured values. The values of n and k corresponding to each of the four values of p are listed in Table IV-2, judging from which, both p = 1.3 and p = 1.4 gave very good fits between the calculated and measured values of n and k. Since for p = 1.3, we got a slightly better match (the same criteria as used in V_2O_3), Figs. IV-38 and 39 were plotted with p = 1.3. In Fig. IV-40, α was plotted as a function of photon energy for both p = 1.3 and p = 1.4; a slight difference in the curves was observed, indicating uncertainty arising from extrapolation.

In summary, as in V_2O_3 the optical constants of R1 obtained from the above three different approaches gave essentially the same results.

The ϵ_2 versus photon energy curve, obtained by any of the three approaches, shows a strong peak at around 0.6 eV, and structures at around 1.5 eV, 2.0-2.4 eV and 4.3 eV. The positions of these structures are essentially in the same location as those in V_2O_3 at room temperature, with one marked difference: the absorption coefficient in $(V_{0.982}Cr_{0.018})_2O_3$ decreases more sharply after 1 eV than it does V_2O_3. In fact, α at 0.2 eV in the doped crystal is only $2 \times 10^4 cm^{-1}$ while in V_2O_3 at 0.2 eV, α is $1.5 \times 10^5 cm^{-1}$. Further discussion of these optical results will be presented in Chapter V.

3. $\underline{VO_2}$. Optical reflectivity and transmission results on VO_2 single crystals have been reported by Ladd and Paul (1) and by Ladd (2). The reflectivity spectra reported by Ladd (2) on one of the thin samples used for his transmission measurements were fitted by our oscillator fit method, and the resultant optical constants are discussed here.

a. $T > T_t$

Figure IV-41 shows the theoretical reflectivity curve obtained from an oscillator fit method to the experimental reflectivity data reported (2). The resultant plots of ϵ_1, ϵ_2, and α (obtained by using Eq. (3-21a)) as a function of photon energy are shown in Figs. IV-42, 43, and 44. Structures are observed at $\sim$ 0.7 eV, 2.9 eV and 3.5 eV in the ϵ_2 curve. We also obtained parameters of the free electron contribution using the oscillator fit method: E_n = 3.63 eV and E_c = 0.500 eV. In VO_2, there are

3.15×10^{22} vanadium ions cm^{-3}. As mentioned in Chapter I, there is only one outer d electron per vanadium ion left after all the bonding requirements are fulfilled. If we assume a one-band model* and these outer electrons all became conduction electrons, then n_c in Eq. (4-2) would become $3.15 \times 10^{22}\ cm^{-3}$. Using the above values of E_n, E_c and n_c in Eq. (4-2) and Eq. (4-3), we then obtain $m^* = 3.3 m_e$ and $\mu_{opt} = 0.7\ cm^2/V\text{-}cm$. From Eq. (4-3), we obtain $\tau_c = 1.4 \times 10^{-15}$ sec.

Hall effect measurements have been done in the metallic state of VO_2 by Barker et al. (10) and Rosevear and Paul (7). Barker et al. measured $R_H\sigma = 16\ cm^2/V\text{-}sec$, which would correspond, in a one-band model, to a Hall mobility of $16\ cm^2/V\text{-}sec$ and a Hall electron concentration of $3 \times 10^{21}\ cm^{-3}$. Rosevear and Paul, however, obtained $R_H\sigma = 0.35 \pm 0.05\ cm^2/V\text{-}sec$, which would correspond, in a one-band model, to a Hall mobility of $0.35 \pm 0.05\ cm^2/V\text{-}sec$ and a Hall electron concentration of $(1.2 \pm 0.2) \times 10^{23}\ cm^{-3}$. This electron concentration is approximately four times the maximum number of conduction electrons allowed, which suggests that the one-band model may not be correct and that there is two-band conduction in the metallic state.

Again, for the purpose of obtaining order of magnitude, we can use the one-band model to obtain the carrier mobility using Eq. (4-4). By assuming $n_c = 3.15 \times 10^{22}\ cm^{-3}$, $\sigma = 10^4\ (\Omega\text{-}cm)^{-1}$ (the resistivity of bulk VO_2 at its metallic state as measured by Ladd and Paul (1)),

---

*The reason that we consider only a one-band model is the same as for the case of V_2O_3, and will not be repeated here.

we obtained $\mu = 2\,cm^2/V\text{-sec}$ which is again of the same order of magnitude as the values of the Hall mobility and the optical mobility reported above.

b. $T < T_t$

Figure IV-45 shows the theoretical reflectivity curve obtained by fitting the experimental reflectivity data reported (2). Plots of ϵ_1 and ϵ_2 versus photon energy are shown in Figs. IV-46 and 47. In the ϵ_2 curve, we observe structures at $\sim 1.1\,eV$, $3.0\,eV$ and $3.6\,eV$.

Figure IV-48 shows a plot of an absorption coefficient α as a function of photon energy. The absorption coefficient shows an absorption edge at $E < \sim 1.1\,eV$, with $\alpha \tilde{=} 1.2 \times 10^4\,cm^{-1}$ at $0.6\,eV$. Ladd (2) reported that from his transmission measurement, α of this crystal should be about $5 \times 10^3\,cm^{-1}$. The discrepancy between the calculated and measured values could be due to several factors; 1) experimental errors in measuring the reflectivity and transmission curves, 2) the uncertainties in the oscillator fit method that arise in fitting an absorption edge (as discussed in Chapter III), and/or 3) the uncertainties, estimated by Ladd (2) to be about $\pm$ 10%, in the crystal thickness, but which, alone, would not explain all the discrepancy; one or both of the first two factors must also have played a part.

Despite the discrepancy in the measured and calculated values of α at $0.6\,eV$, it is still apparent that there is an absorption edge near $0.6\,eV$ though not as sharp as in germanium and silicon (see Fig. IV-49, where in addition to the values of α derived from Ladd's results, we

also included that α-vs-photon energy curves reported by Verleur et al. (12)) and this fact confirms the transmission measurement on single crystals of VO_2 by Ladd and Paul (1) and the transmission measurement of thin films of VO_2 by Verleur et al. (12). This absorption edge was further demonstrated by our transmission measurement of a VO_2 film grown by the vapor transport technique — the electrical and the structural properties of the film have been shown in Chapter II. Figure IV-50 shows the transmission and the apparent reflectivity of the film in both the metallic state and the insulating state. Though the absolute value in reflectivity is different from that of bulk crystals, because of the surface roughness of the film, the general shape of the spectra of the film and of the bulk crystals is very similar (see Figs. IV-41, 45).

D. Optical Reflectivity Studies of Metal-Insulator Transitions in $(V_{1-x}Cr_x)_2O_3$

As we have discussed in Chapter III, McWhan, Remeika et al. (13, 14, 15) observed a first order metal-to-insulator transition in $(V_{1-x}Cr_x)_2O_3$ with an increase in temperature in a narrow range of chromium compositions (x = a value between ~ 0.005 and ~0.016). In optical measurements on single crystals in this composition range, we have observed abrupt changes in optical reflectivity as a function of temperature which are presumably associated with the metal-insulator transition; such abrupt changes had not been observed in previous reflectivity measurements (16). The single crystals were unoriented,

we obtained $\mu = 2\,cm^2/V\text{-}sec$ which is again of the same order of magnitude as the values of the Hall mobility and the optical mobility reported above.

b. $T < T_t$

Figure IV-45 shows the theoretical reflectivity curve obtained by fitting the experimental reflectivity data reported (2). Plots of ϵ_1 and ϵ_2 versus photon energy are shown in Figs. IV-46 and 47. In the ϵ_2 curve, we observe structures at ~ 1.1 eV, 3.0 eV and 3.6 eV.

Figure IV-48 shows a plot of an absorption coefficient α as a function of photon energy. The absorption coefficient shows an absorption edge at $E < \sim 1.1$ eV, with $\alpha \tilde{=} 1.2 \times 10^4\,cm^{-1}$ at 0.6 eV. Ladd (2) reported that from his transmission measurement, α of this crystal should be about $5 \times 10^3\,cm^{-1}$. The discrepancy between the calculated and measured values could be due to several factors; 1) experimental errors in measuring the reflectivity and transmission curves, 2) the uncertainties in the oscillator fit method that arise in fitting an absorption edge (as discussed in Chapter III), and/or 3) the uncertainties, estimated by Ladd (2) to be about $\pm$ 10%, in the crystal thickness, but which, alone, would not explain all the discrepancy; one or both of the first two factors must also have played a part.

Despite the discrepancy in the measured and calculated values of α at 0.6 eV, it is still apparent that there is an absorption edge near 0.6 eV though not as sharp as in germanium and silicon (see Fig. IV-49, where in addition to the values of α derived from Ladd's results, we

also included that α-vs-photon energy curves reported by Verleur et al. (12)) and this fact confirms the transmission measurement on single crystals of VO_2 by Ladd and Paul (1) and the transmission measurement of thin films of VO_2 by Verleur et al. (12). This absorption edge was further demonstrated by our transmission measurement of a VO_2 film grown by the vapor transport technique — the electrical and the structural properties of the film have been shown in Chapter II. Figure IV-50 shows the transmission and the apparent reflectivity of the film in both the metallic state and the insulating state. Though the absolute value in reflectivity is different from that of bulk crystals, because of the surface roughness of the film, the general shape of the spectra of the film and of the bulk crystals is very similar (see Figs. IV-41, 45).

D. Optical Reflectivity Studies of Metal-Insulator Transitions in $(V_{1-x}Cr_x)_2O_3$

As we have discussed in Chapter III, McWhan, Remeika et al. (13, 14, 15) observed a first order metal-to-insulator transition in $(V_{1-x}Cr_x)_2O_3$ with an increase in temperature in a narrow range of chromium compositions (x = a value between ~ 0.005 and ~0.016). In optical measurements on single crystals in this composition range, we have observed abrupt changes in optical reflectivity as a function of temperature which are presumably associated with the metal-insulator transition; such abrupt changes had not been observed in previous reflectivity measurements (16). The single crystals were unoriented,

mechanically polished samples, and optical reflectivity measurements * were made in the ratio reflectometer described in Chapter III.

Five samples were measured, namely, x = 0 (B1 from Run #1, see Table II-3), x = 0.0022 (Run #3), x = 0.0047 (Run #5), x = 0 010 (Run #7), and x = 0.014 (Run #8). For x = 0, x = 0.0022 and x = 0.0047, a high temperature optical sample holder was used. For x = 0.010 and x = 0.014, an optical low temperature dewar was used. Both the high temperature sample holder and the dewar were described in Chapter III.

Two types of reflectivity-versus-temperature behavior were observed. For the V_2O_3 crystal and the $(V_{1-x}Cr_x)_2O_3$ crystal where x = 0.0022, the reflectivity at 0.65 eV decreased continuously with increasing temperature and did not exhibit any hysteresis. These curves are shown in Figs. IV-51 and IV-52; in both cases, we noticed that a somewhat anomalous variation occurred between 400°K and 500°K. This anomaly is presumably associated with the second order transition that takes place in this temperature interval, as evidenced by electrical measurements (3), and x-ray measurements (13). It is difficult to assign the transition temperatures T_t for these two samples. The transition temperature of each of the two samples was taken as the average of the temperatures where the reflectivity-versus-temperature curve begins to depart from the straight line extrapolation at both the high temperature and low temperature ends. For x = 0, we obtained $T_t \tilde{=} 465^{\circ}K$, and for x = 0.0022, $T_t \tilde{=} 435^{\circ}K$. These values of T_t are,

---

*In collaboration with Dr. Paul Raccah.

subject to some uncertainty. Figure IV-53* and Fig. IV-54 show the reflectivity-versus-photon energy curves of the two samples at different temperatures. There are a few interesting features in these curves: 1) the reflectivity-versus-photon energy curves at room temperature remained the same before and after the temperature cycle, indicating the surfaces of the crystals did not oxidize in the protective atmosphere of the forming gas; 2) the structure near 1.5 eV is visible at all temperatures, and 3) the reflectivity of the samples at photon energy above $\sim$ 1.8 eV remained the same at all temperatures (within the experimental uncertainty of the optical setup).

For samples with x = 0.0047, x = 0.010 and x = 0.014, abrupt changes in reflectivity were observed with large hysteresis on temperature cycling. Figures IV-55, 56, and 57 show the reflectivity at 0.65 eV as a function of temperature of these crystals. Abrupt reflectivity changes were observed in all these crystals. Such abrupt changes are presumably associated with the abrupt changes in the electrical measurements reported by McWhan and Remeika (13), who described this transition as a first order transition with some characteristics of a Mott

---

*The reflectivity-versus-photon energy curve of B1 did not match very well with that of C1 or C2. This is not so surprising since the crystals were grown in different crystal runs. A slight change in stoichiometry could cause a change in the number of charge carriers in the crystals (V_2O_3 crystals were found to have different resistivities at room temperature (3, 13)). This change in charge carrier density will affect the optical reflectivity spectrum, especially in the free electron absorption region.

transition. For those crystals that underwent the first order phase transition, there was evidence that the crystals cracked on going through the phase transition; the cracking was observed partly from the changes in reflectivity at room temperature before and after the temperature cycling, and partly from the cracks visible after the temperature cycline. In fact, the crystal at $x = 0.0047$, as grown, already had some fine cracks. This was due to the fact that the crystal on cooling down from the melting temperature during the growth process had already undergone a phase transition. Because of the problem of crystal cracking, slight optical adjustments were done to focus the incident light on the best spot of each crystal (that is, the reflectivity value is maximum at this spot). In some cases, no apparent improvement was observed, and in others, noticeable improvements were observed. Though part of the reflectivity changes observed was indeed due to crystal cracking (for example, the reflectivity of the doped crystal at room temperature, as shown in Fig. IV-55, was lower after the temperature cycling), it is apparent that most of the abrupt reflectivity changes at the phase transition must have been due to the transition itself. Crystal cracking could cause only decreases in reflectivity values, and could not explain the sudden increases observed in reflectivity values.

Figures IV-58, 59, and 60 show the reflectivity-versus-photon energy curves at different temperaturesfor samples with $x = 0.0047$, $x = 0.010$ and $x = 0.014$. An interesting point is that at low photon energy, the reflectivity of the metallic state of the doped crystals is not as high as that of undoped V_2O_3 crystals — this is especially

noticeable at photon energy near 0.6 eV. It indicates that the so-called metallic state of the doped crystals is different from that of the undoped crystal; this fact corresponds to the findings of McWhan et al. (13) who reported that the resistivity of the metallic state of the doped crystal $(V_{0.990}Cr_{0.010})_2O_3$ was about two orders of magnitude higher than that of the undoped crystals.

Other points of interest are: 1) the structure at ~ 1.5 eV is visible at all temperatures; and 2) the reflectivity of the metallic state of the doped crystals is lower than that of the insulating state for photon energy above 1.2 eV. Though it might not be very appropriate to compare the metallic state of V_2O_3 with that of a doped crystal, at room temperature, we found that at 1.96 eV the reflectivity of V_2O_3 crystals C1 and C2 (metallic state) is about 20%. This value is indeed lower than that of a crystal of $(V_{1-x}Cr_x)_2O_3$, R1, where $x = 0.018$; at room temperature the crystal is in its insulating state and its reflectivity at 1.96 eV is about 22%.

Table IV-3 lists the transition temperature T_t for the crystals we measured, and Fig. IV-61 is a plot of these temperatures as a function of chromium concentration, indicating clearly the two types of phase transition. A discussion of the mechanism or mechanisms of the transition will be presented in Chapter V.

In summary, in this chapter, we have presented optical measurements on V_2O_3 and $(V_{1-x}Cr_x)_2O_3$. Optical constants were obtained from angular dependence measurements, and from reflectivity spectra using the oscillator fit method and Kramers-Kronig analysis. In Chapter V, we will further interpret these optical results and their implications.

Composition x	Transition Temperature		Average Transition Temperature
	Metal to Insulator	Insulator to Metal	
0	~ 465°K		~ 465°K
0.0022	~ 435°K		~ 435°K
0.0047	436°K	377°K	406°K
0.010	352°K	286°K	319°K
0.014	303°K	232°K	268°K

TABLE IV-3. Transition temperatures obtained in reflectivity measurements on $(V_{1-x}Cr_x)_2O_3$

REFERENCES

1. L. Ladd and W. Paul, Solid State Comm. 7, 425 (1969).
2. L. Ladd, Tech. Rept. No. HP-26, Gordon McKay Laboratory, Harvard University, 1971 (unpublished).
3. J. Feinleib and W. Paul, Phys. Rev. 155, 841 (1967).
4. K. Kosuge, J. Phys. Soc. Japan 22, 55 (1967).
5. A. Smakula, "Phys. Properties of Optical Crystals," p. 99, U.S. Dept. of Commerce, 1952.
6. V. Chandrasekharan and H. Damany, Appl. Optics 7, 939 (1968).
7. W. Rosevear and W. Paul, to be published.
8. I.G. Austin and C.E. Turner, Phil. Mag. 19, 939 (1969).
9. V.P. Zhuze, A.A. Andreev and A.I. Shelykh, Sov. Phys. -- Solid State 10, 2914 (1969).
10. A.S. Barker, Jr., H.W. Verleur, and H.J. Guggenheim, Phys. Rev. Letters 17, 1286 (1966).
11. W. Rosevear, Tech. Rept., Gordon McKay Laboratory, Harvard University (to be published).
12. H.W. Verleur, A.S. Barker, Jr., and C.N. Berglund, Phys. Rev. 172, 172 (1968).
13. D.B. McWhan and J.P. Remeika, Phys. Rev. B2, 3734 (1970).
14. A. Jayaraman, D.B. McWhan, J.P. Remeika and P.D. Dernier, Phys. Rev. B2, 3751 (1970).
15. A. Menth and J.P. Remeika, Phys. Rev. B2, 3756 (1970).
16. A.S. Barker, Jr. and J.P. Remeika, Solid State Comm. 8, 1521 (1970).

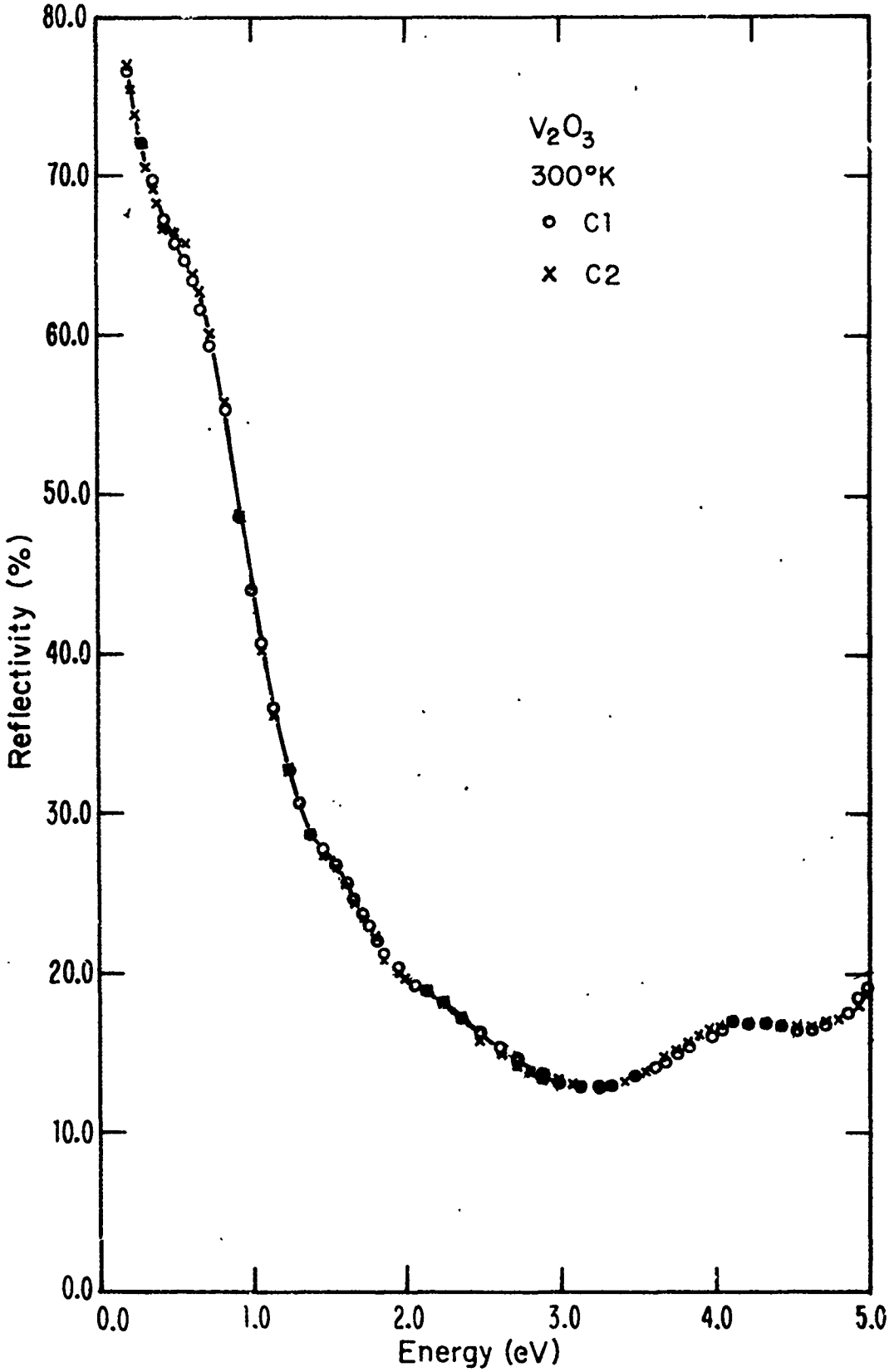

FIGURE IV-1 The reflectivity of two V_2O_3 crystals C1 and C2 at 300°K

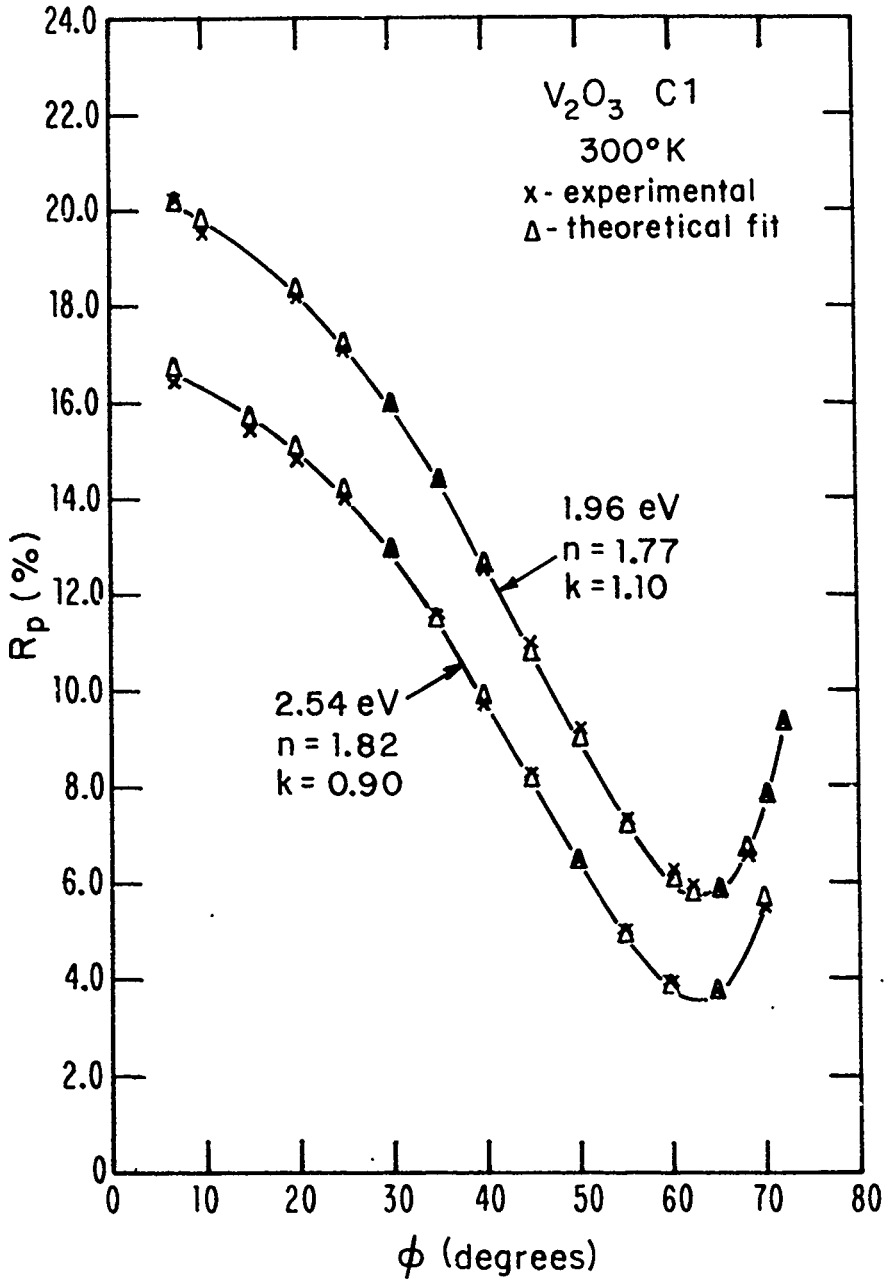

FIGURE IV-2 The reflectivity of a V_2O_3 crystal (C1) as a function of incidence angle ϕ.

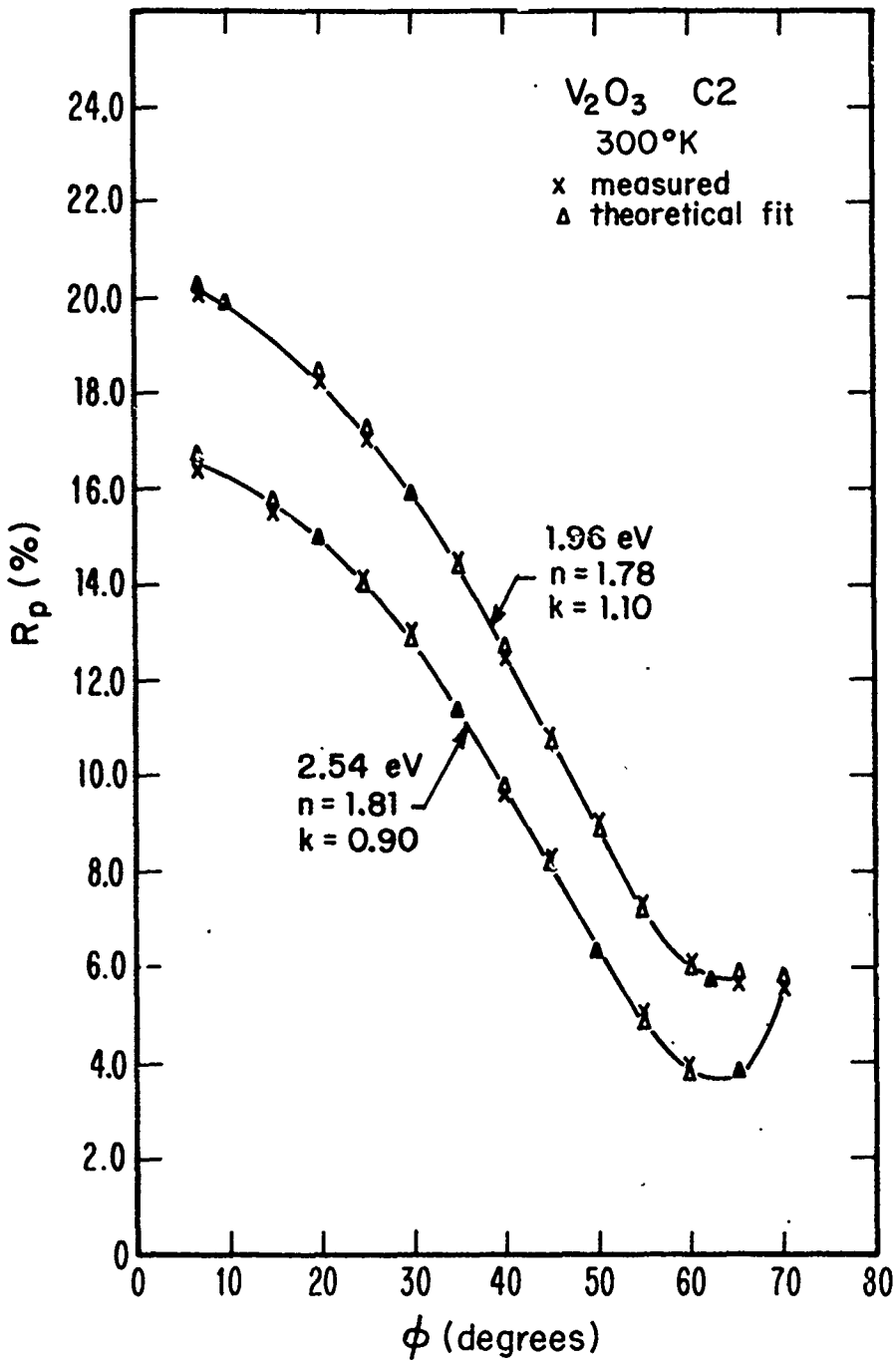

FIGURE IV-3 The reflectivity of a V_2O_3 crystal (C2) as a function of incidence angle ϕ.

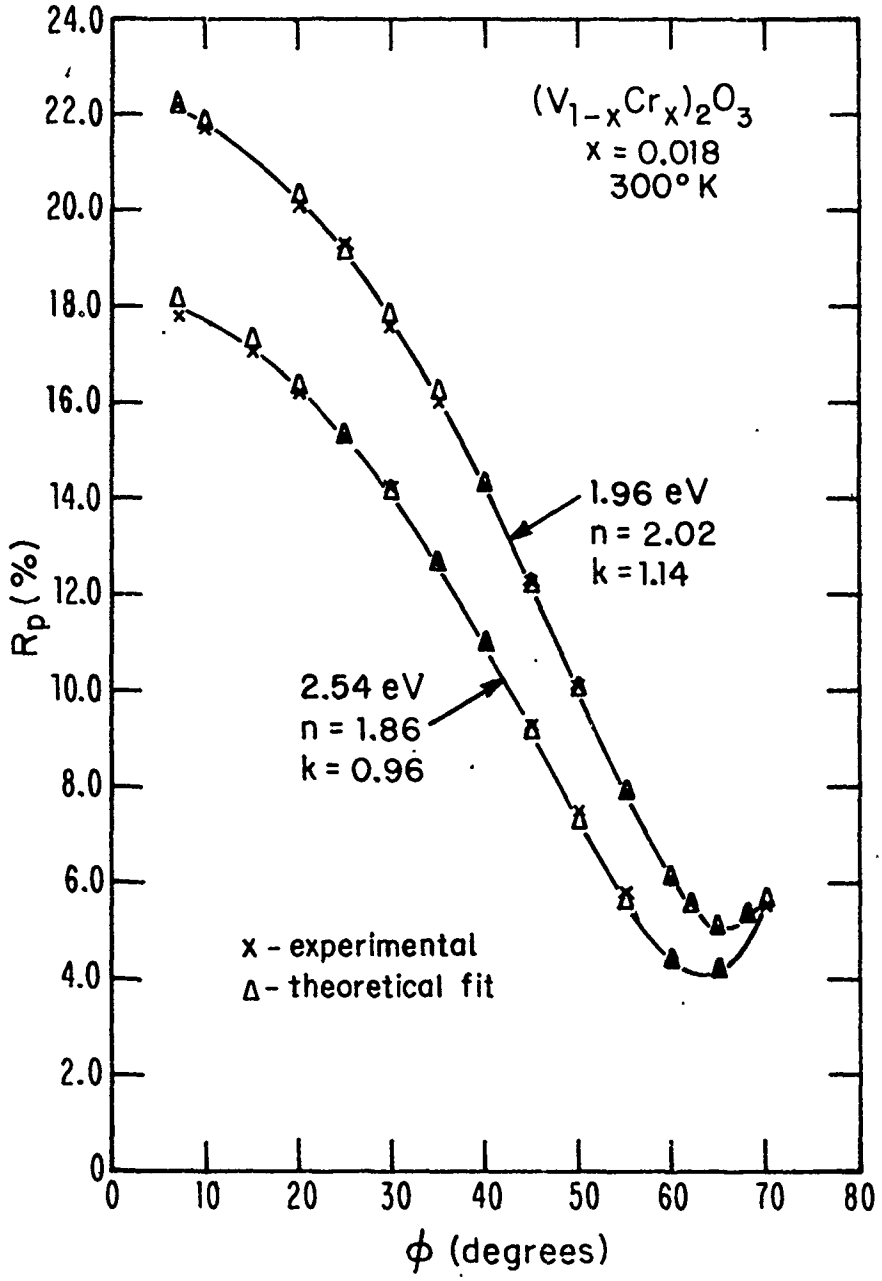

FIGURE IV-4 The reflectivity of a $(V_{1-x}Cr_x)_2O_3$ crystal where x=0.018 as a function of incidence angle ϕ.

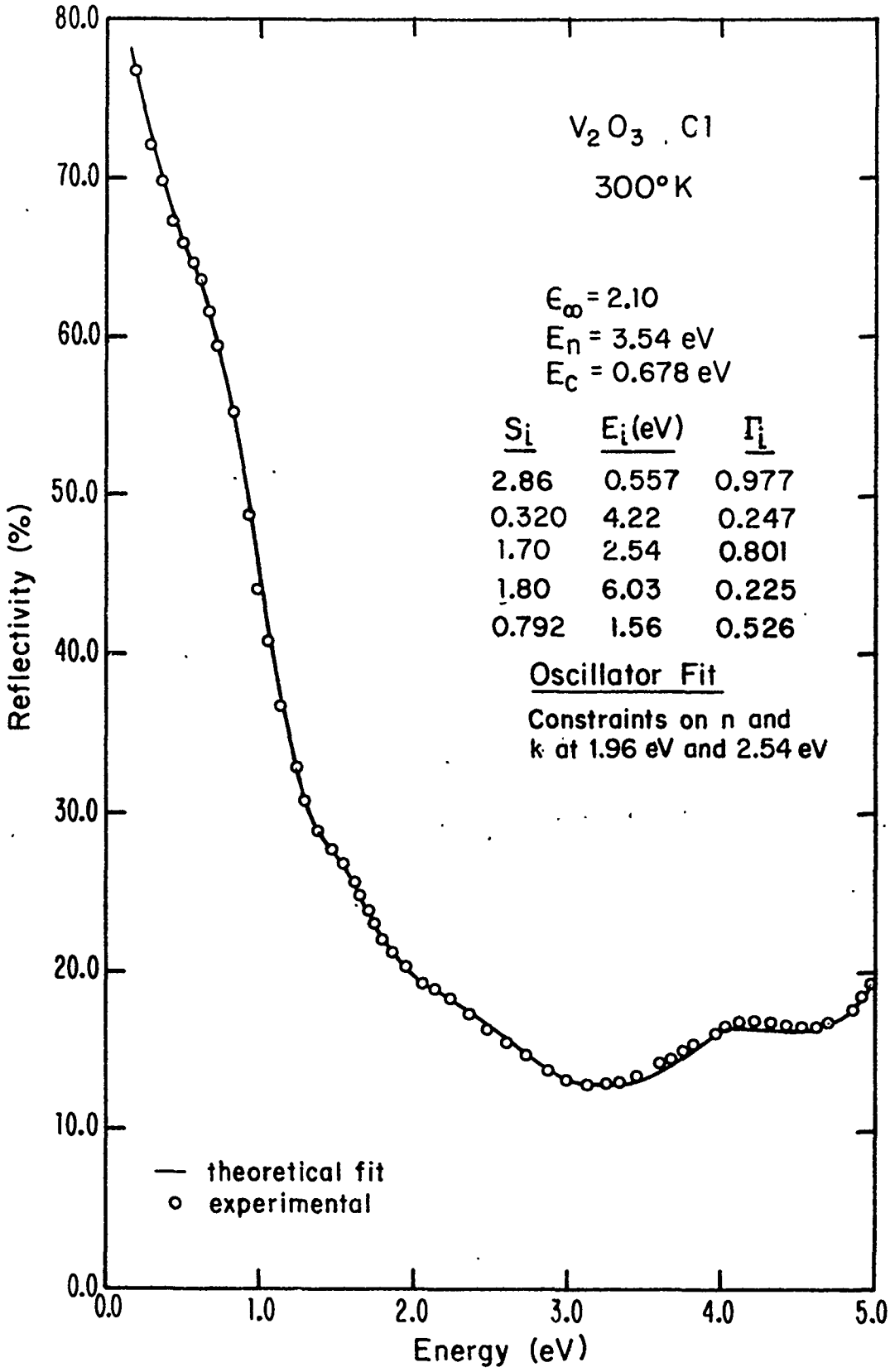

FIGURE IV-5 A theoretical fit to the experimental reflectivity data of Cl by the oscillator fit method where n and k at 1.96eV and 2.54eV are constrained to approach those obtained from the angular dependence measurements.

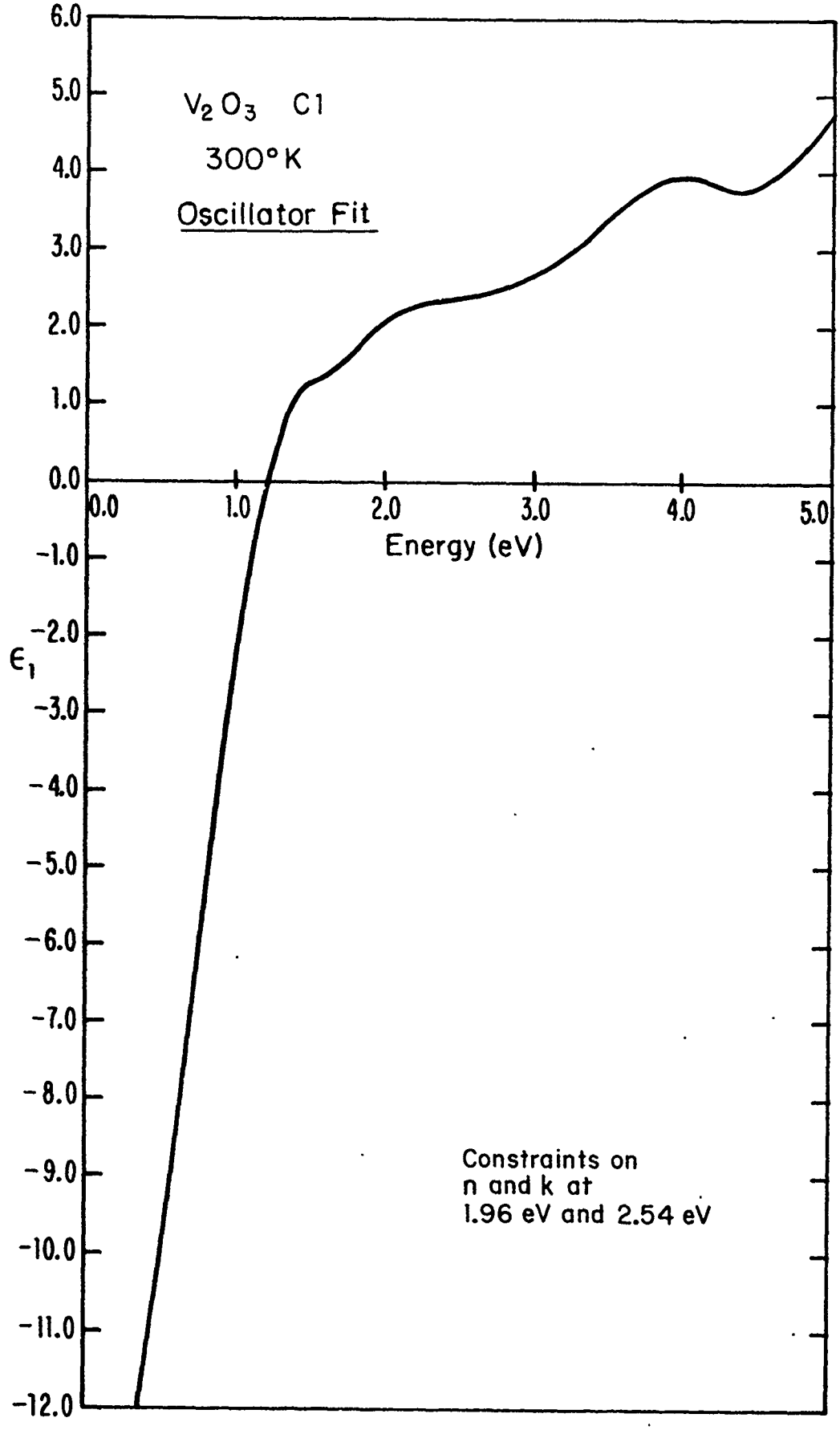

FIGURE IV-6 ϵ_1 curve of C1, obtained from the fit shown in Fig. IV-5.

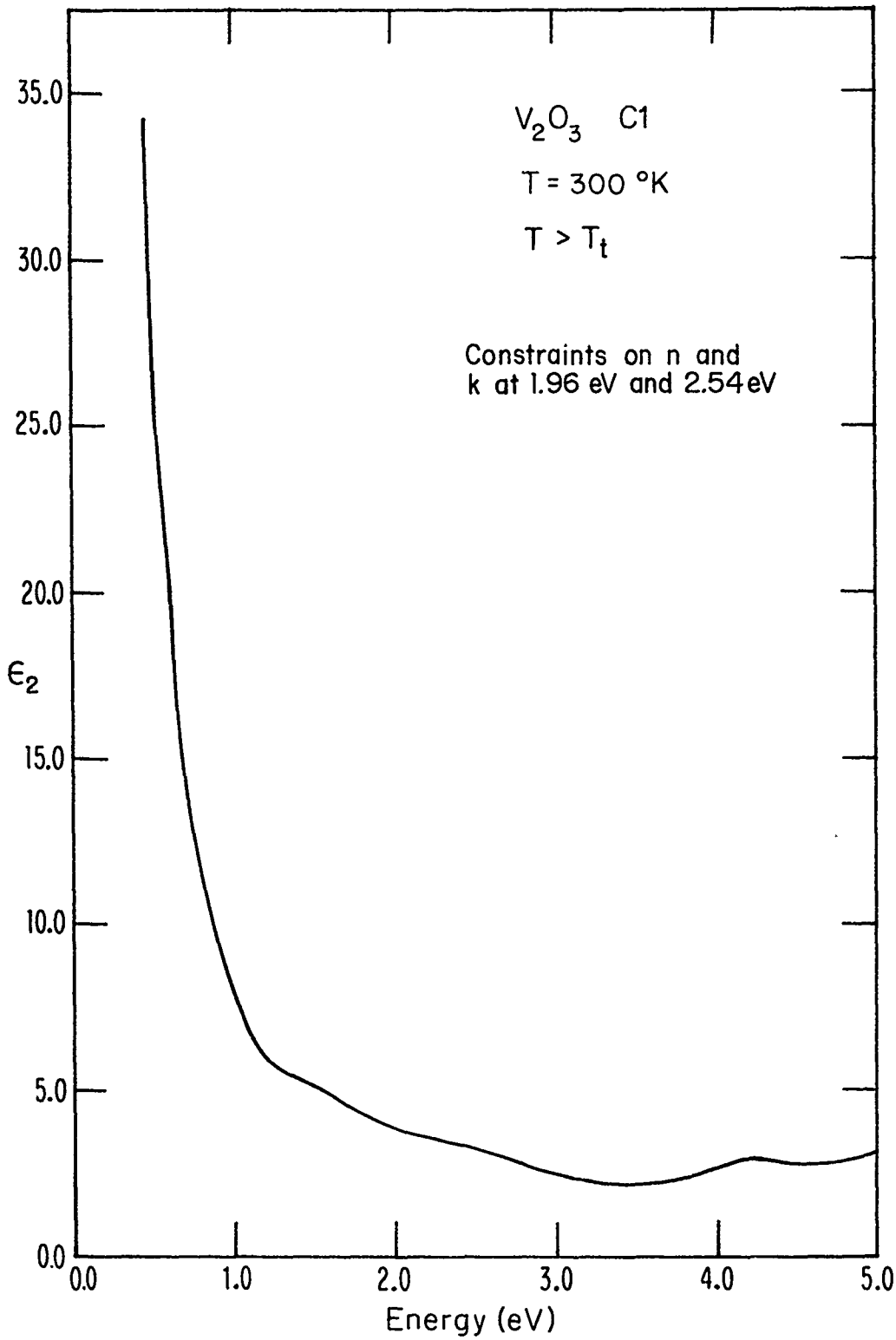

FIGURE IV-7 ϵ_2 curve of C1, obtained from the fit shown in Fig. IV-5

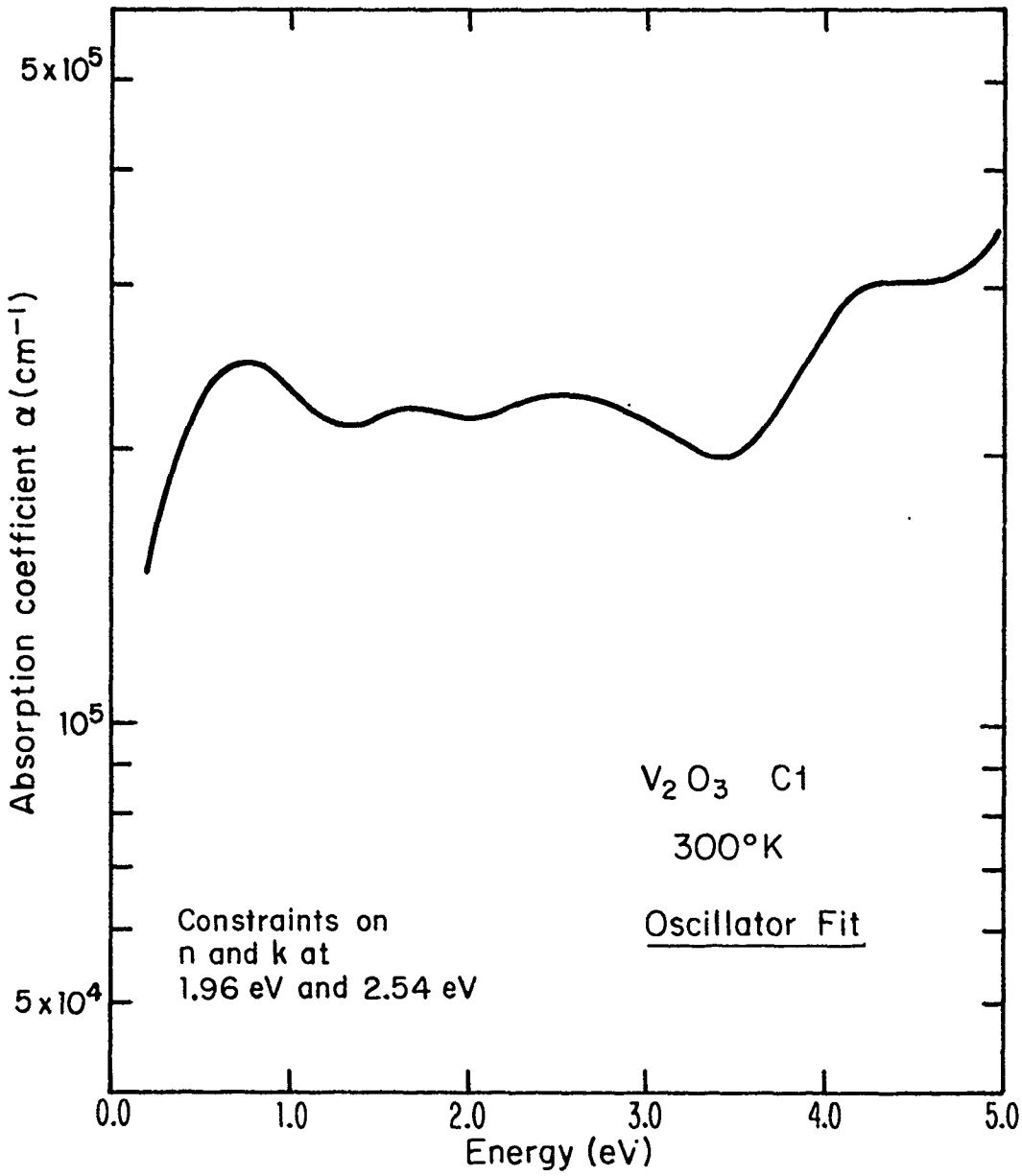

FIGURE IV-8 α curve of C1, obtained from the fit shown in Fig. IV-5.

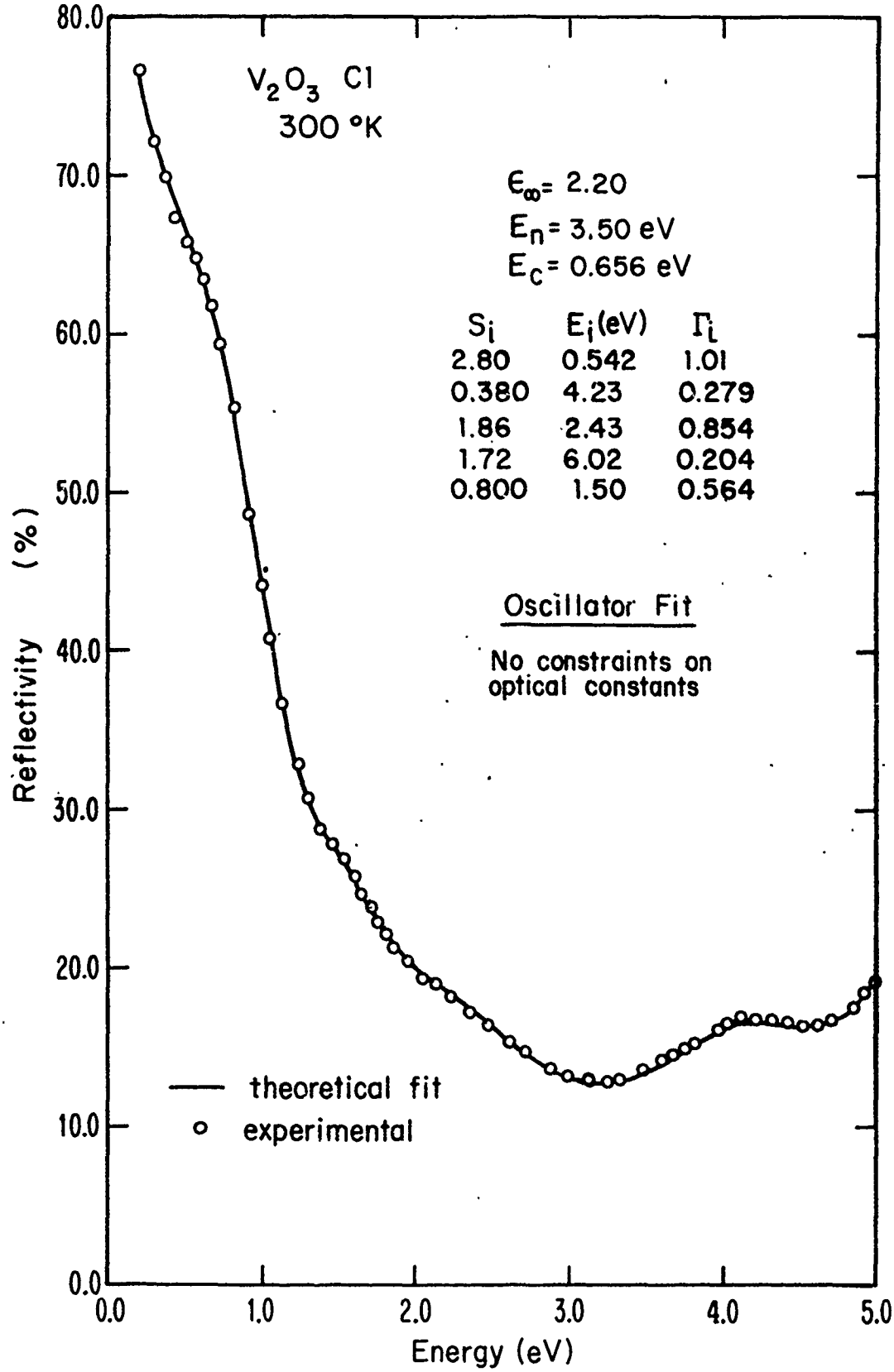

FIGURE IV-9 A theoretical fit to the experimental reflectivity data of C1 by the oscillator fit method where n and k at 1.96eV and 2.54eV are not constrained.

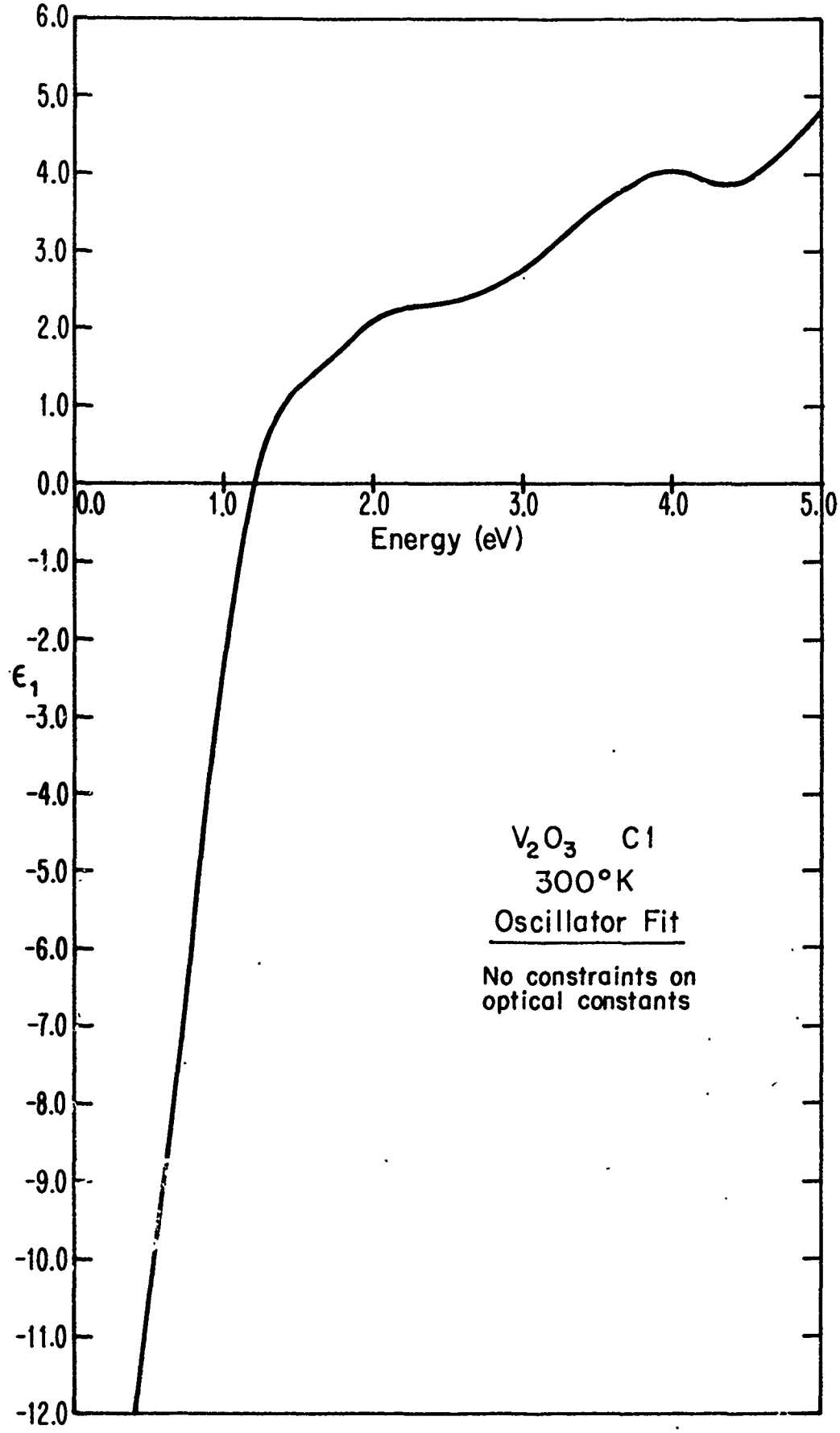

FIGURE IV-10 ϵ_1 curve of C1, obtained from the fit shown in Fig. IV-9

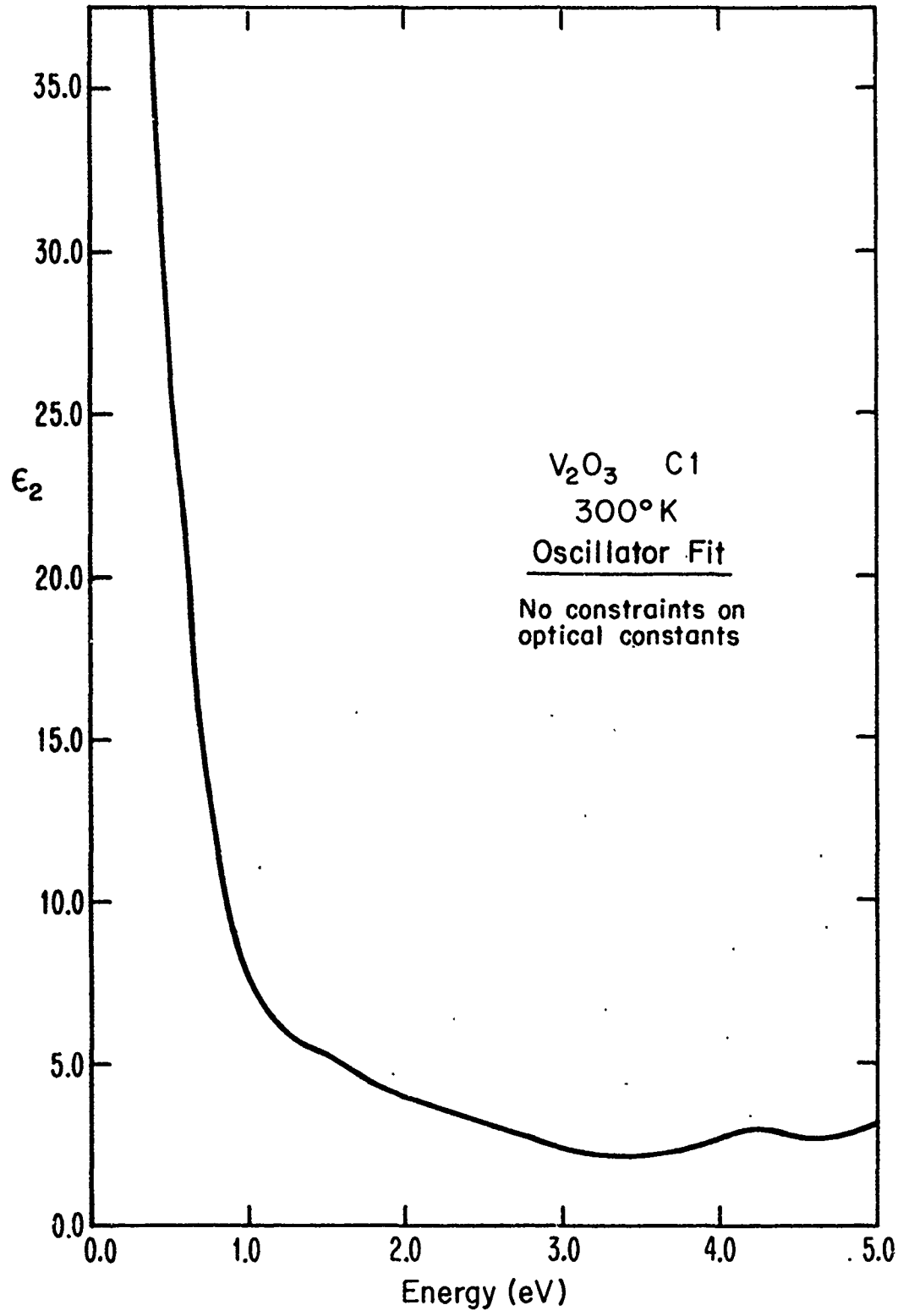

FIGURE IV-11 ϵ_2 curve of C1, obtained from the fit shown in Fig. IV-9.

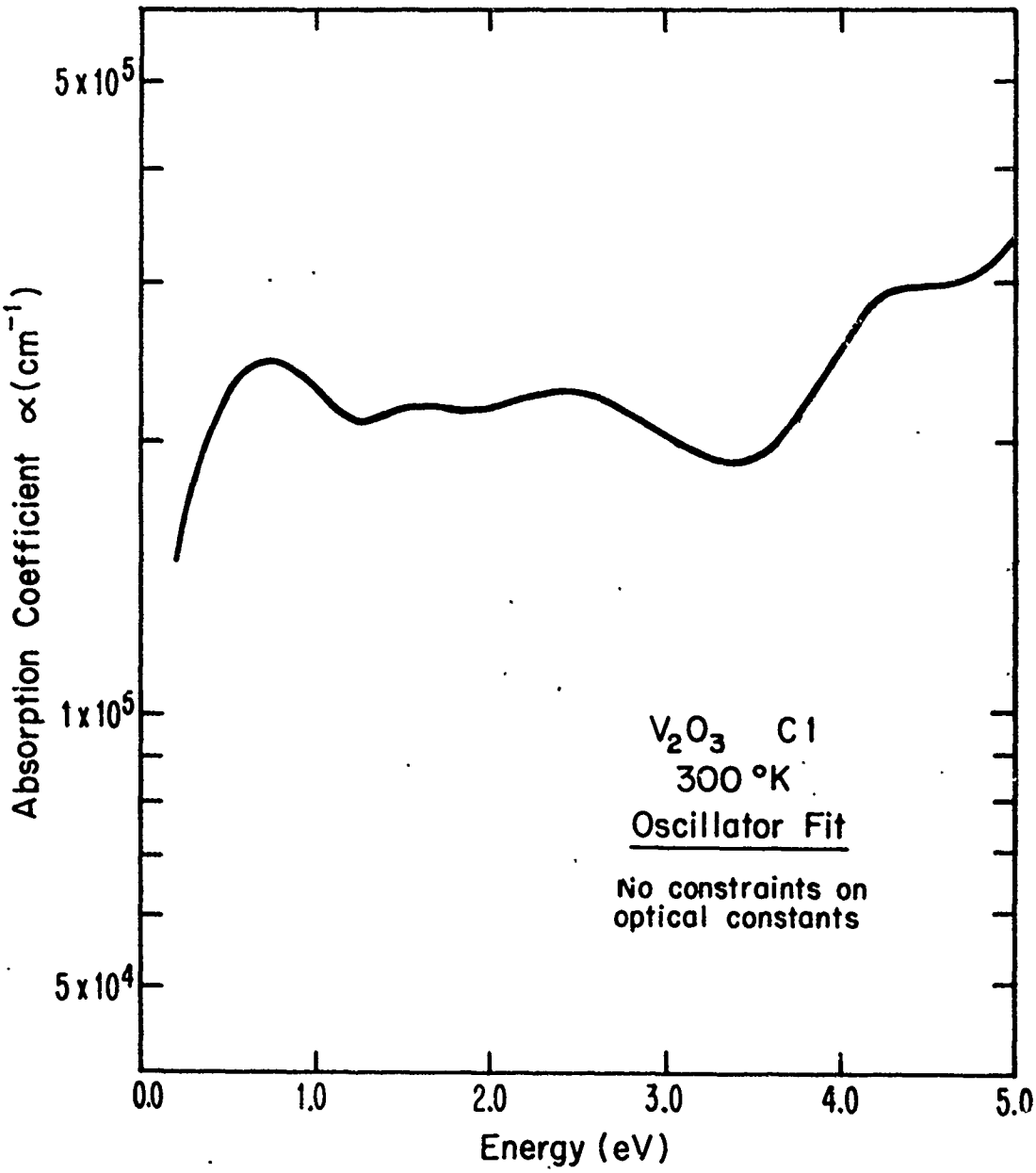

FIGURE IV-12 α curve of C1, obtained from the fit shown in Fig. IV-9.

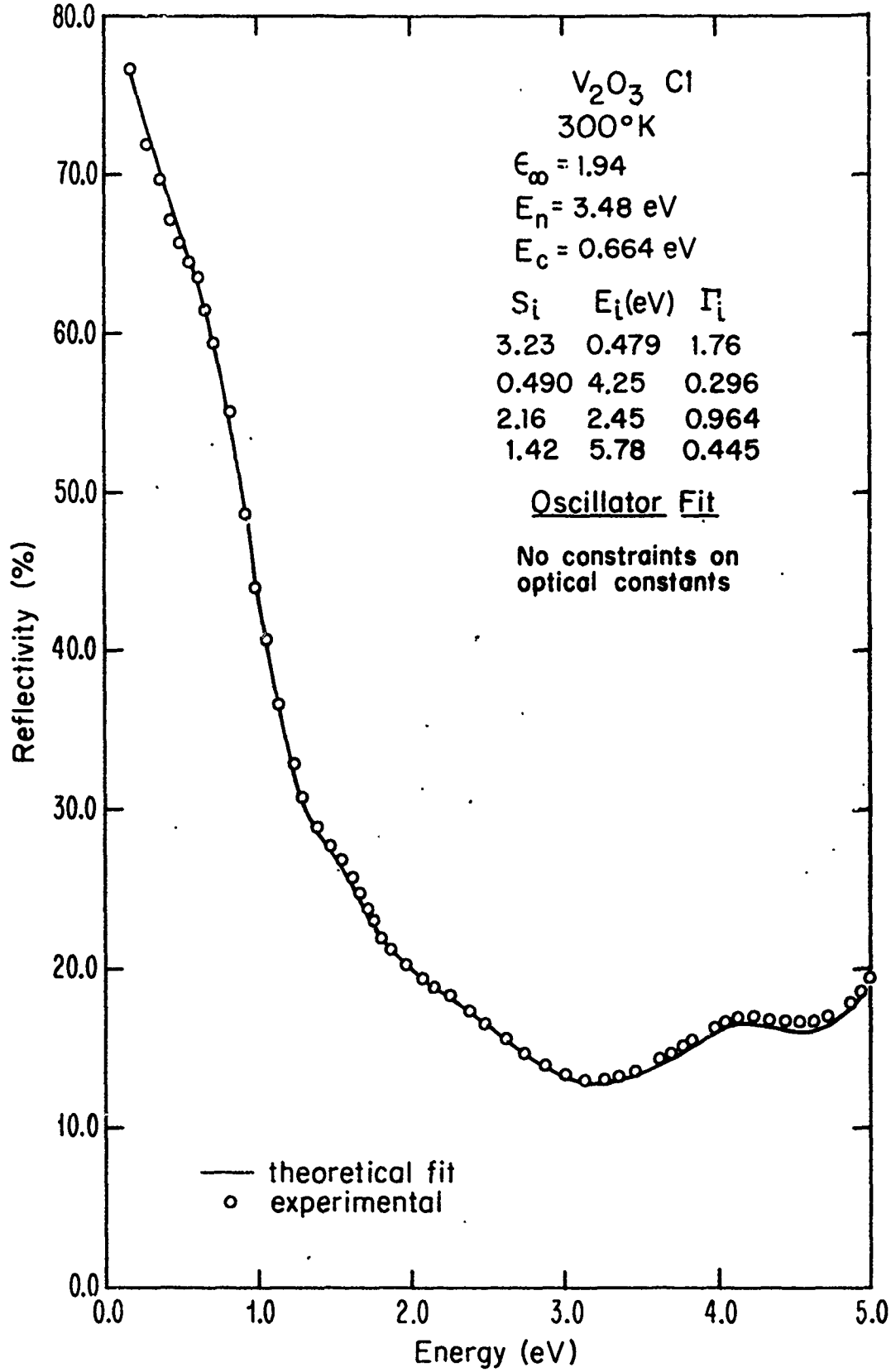

FIGURE IV-13 A theoretical fit to the experimental reflectivity data of C1 by the oscillator fit method where n and k at 1.96eV and 2.54 eV are not constrained.

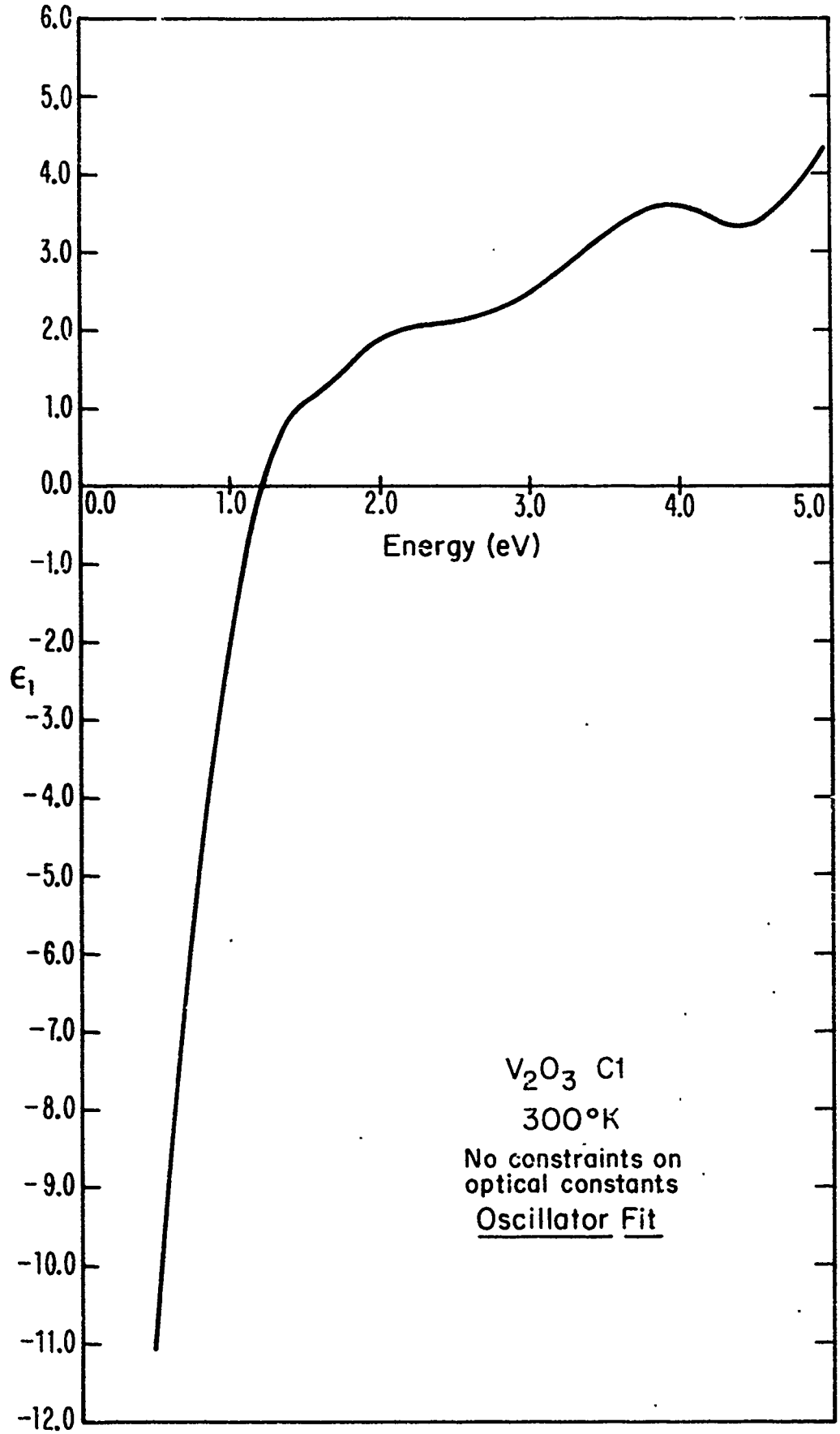

FIGURE IV-14 ϵ_1 curve of C1, obtained from the fit shown in FIG. IV-13.

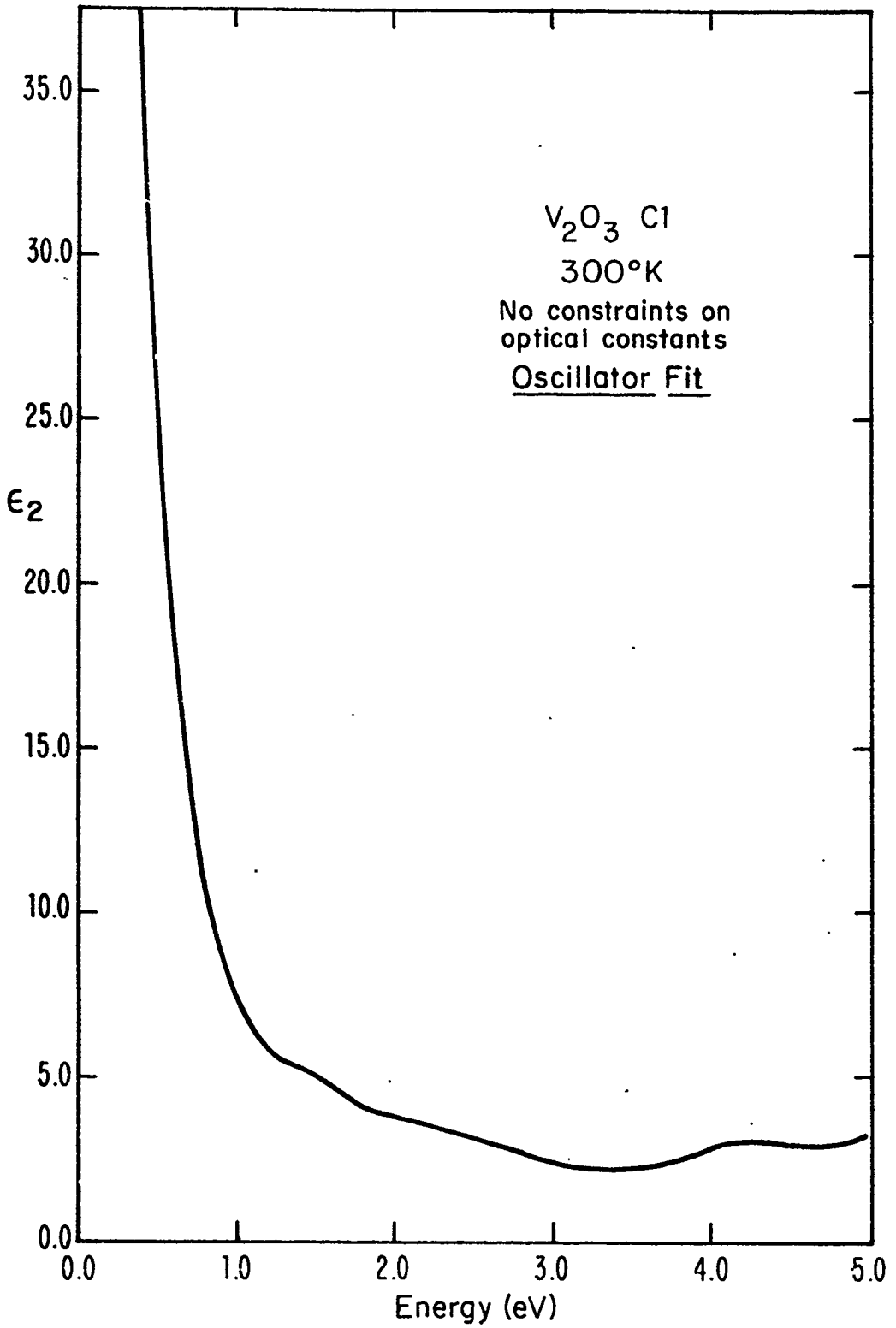

FIGURE IV-15 ϵ_2 curve of C1, obtained from the fit shown in Fig. IV-13.

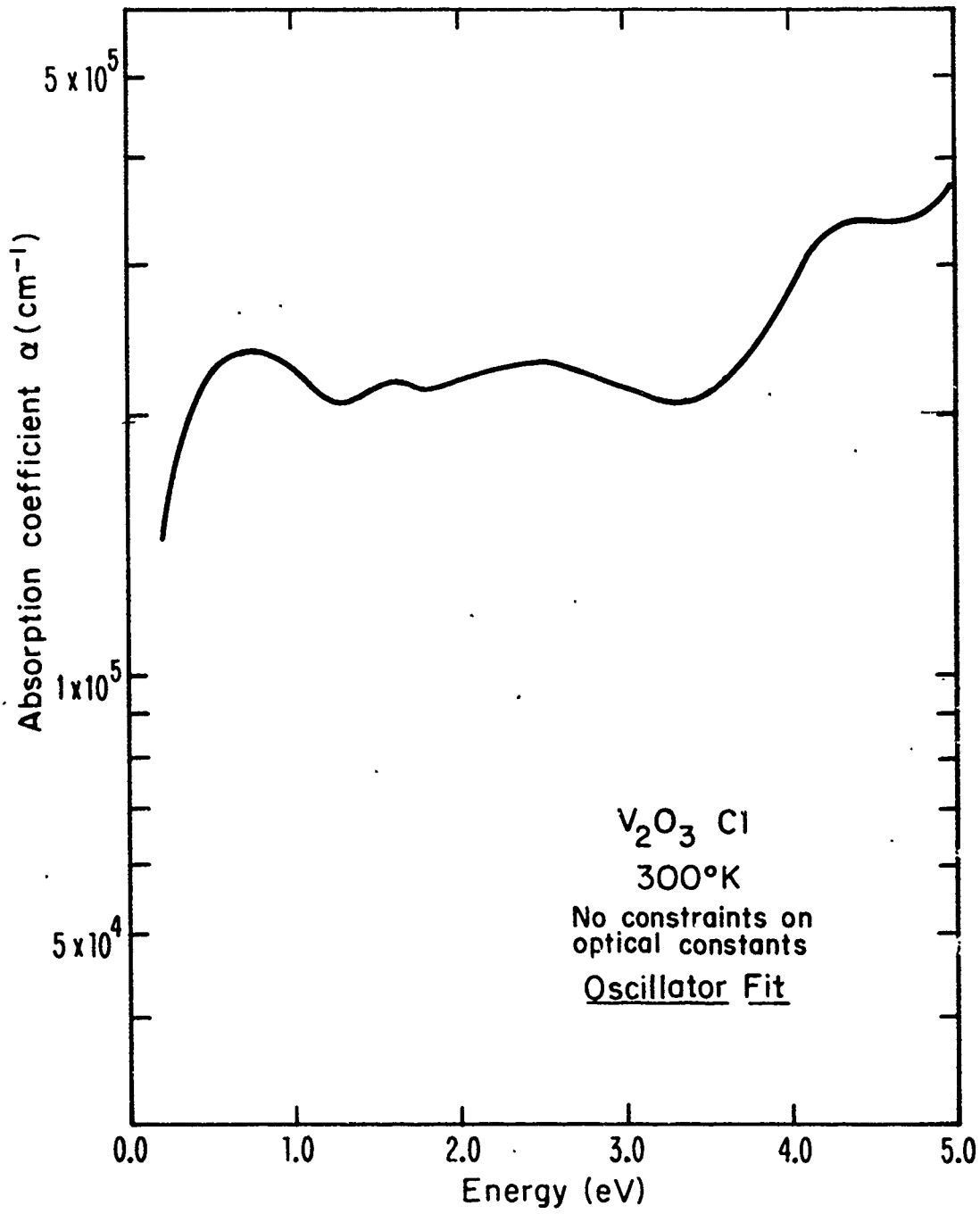

FIGURE IV-16 α curve of C1, obtained from the fit shown in Fig. IV-13.

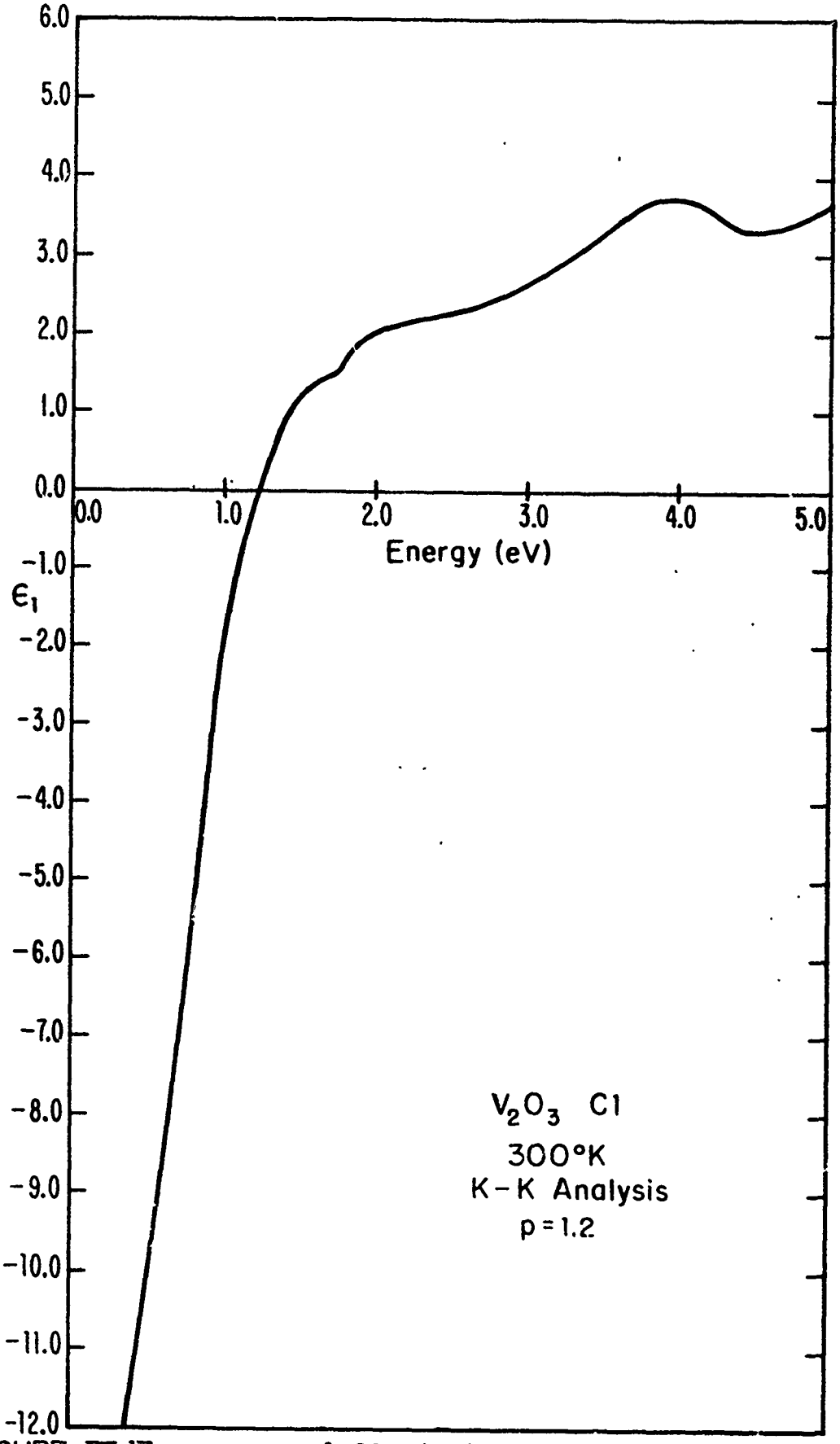

FIGURE IV-17 ϵ_1 curve of C1, obtained from the Kramers-Kronig analysis of the reflectivity spectrum of C1.

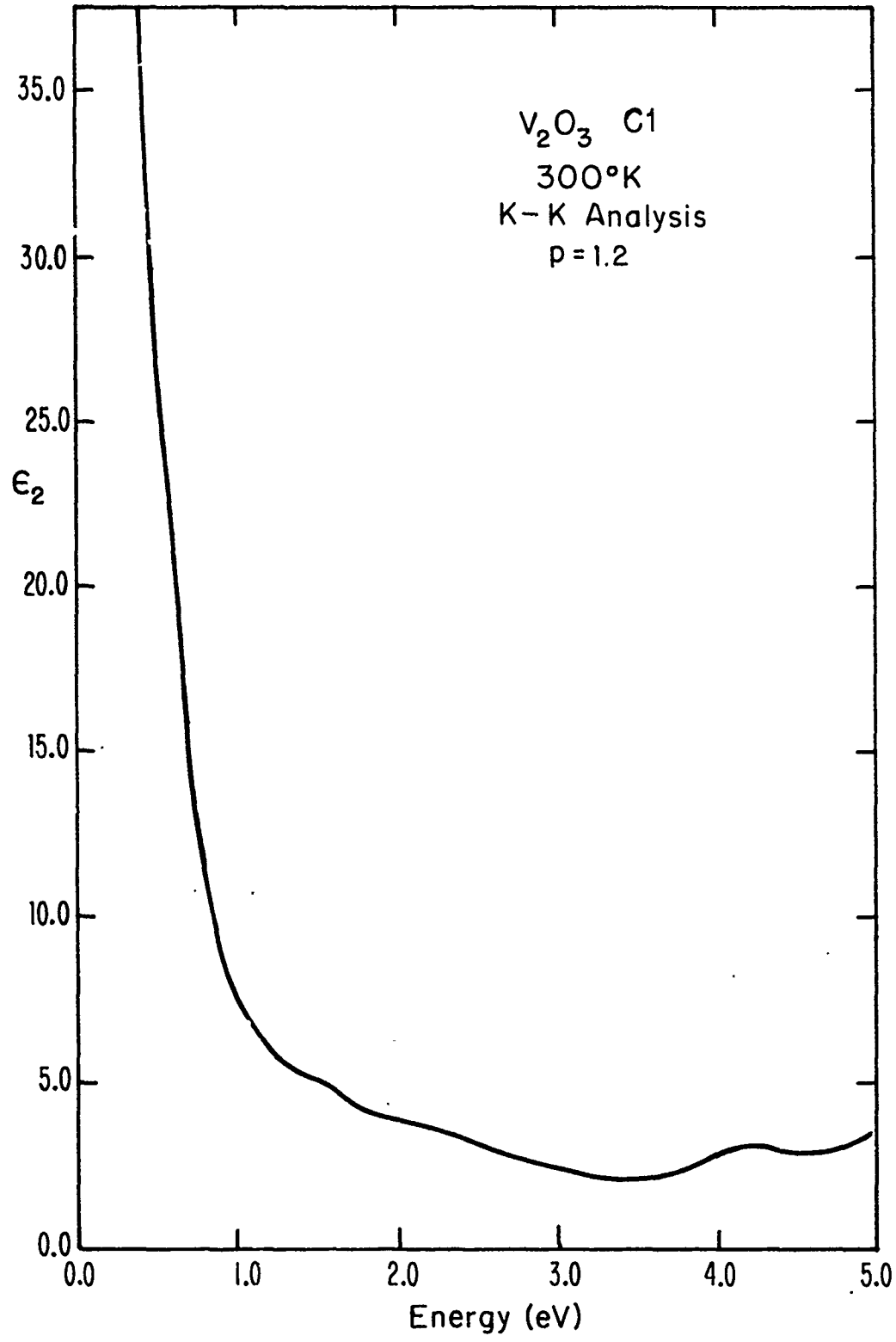

FIGURE IV-18 ϵ_2 curve of C1, obtained from the Kramers-Kronig analysis of the reflectivity spectrum of C1.

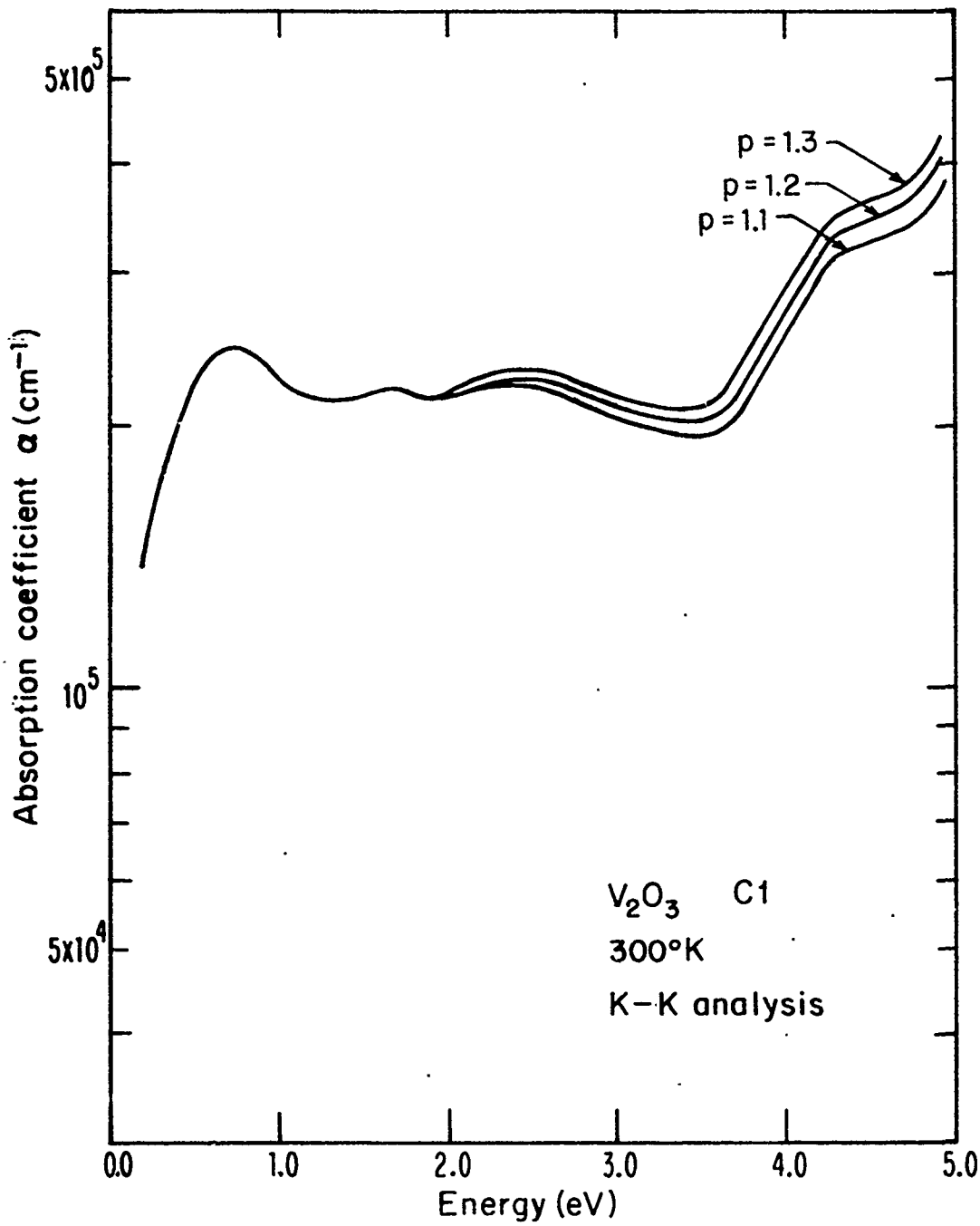

FIGURE IV-19 α curve of C1, obtained from the Kramers-Kronig analysis of the reflectivity spectrum of C1.

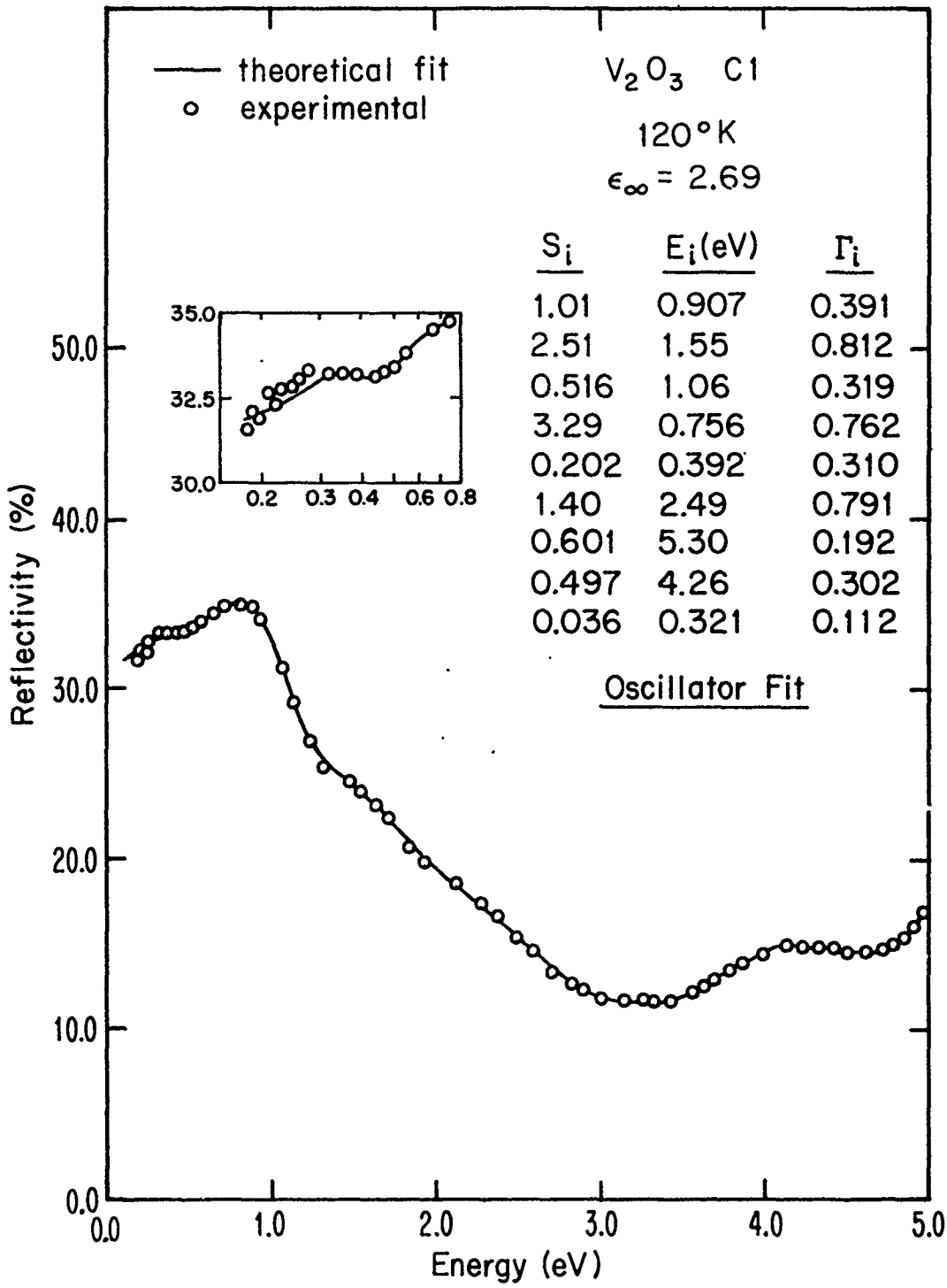

FIGURE IV-20 A theoretical fit to the experimental data of C1 by the oscillator fit method (at 120°K).

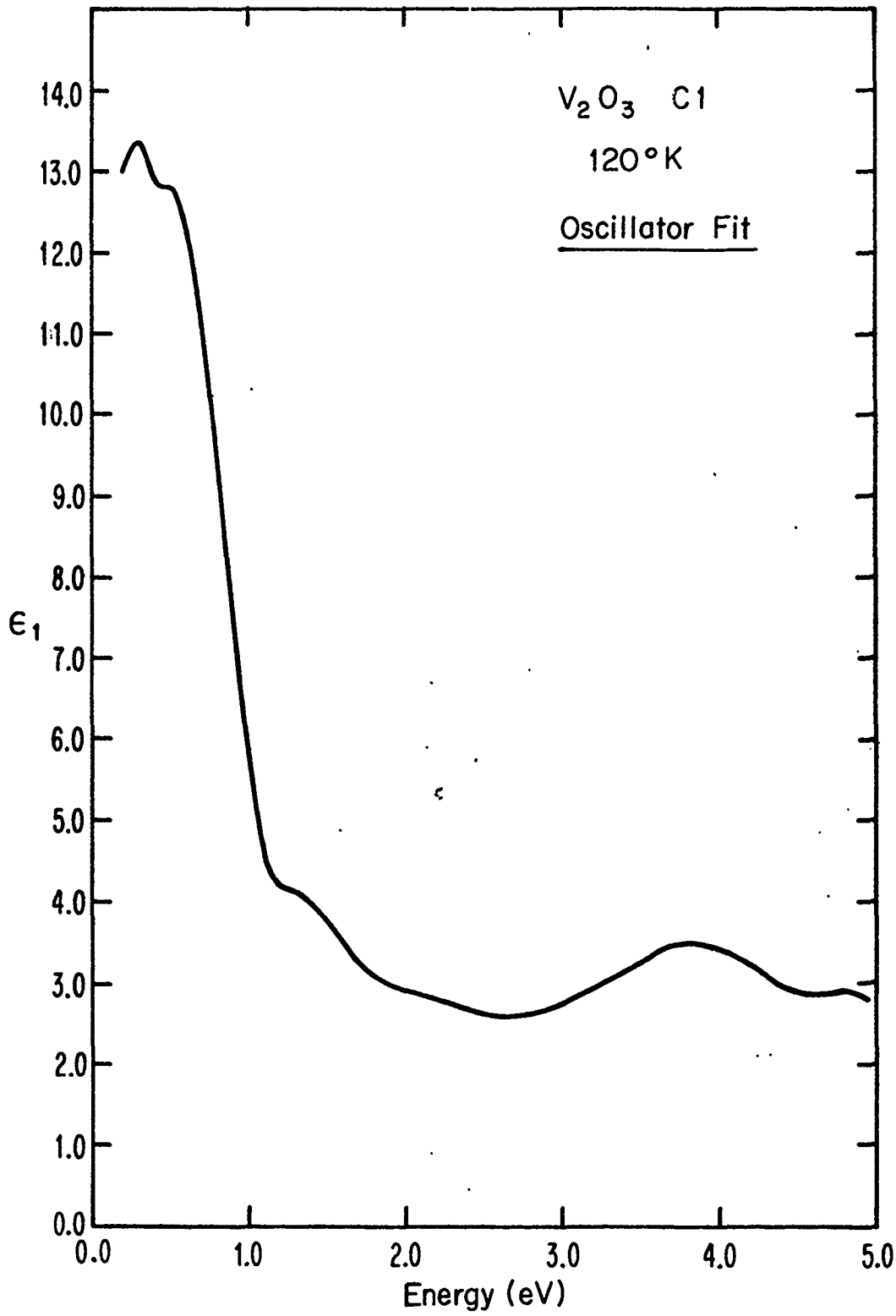

FIGURE IV-21 ϵ_1 curve of C1, obtained from the fit shown in Fig. IV-20.

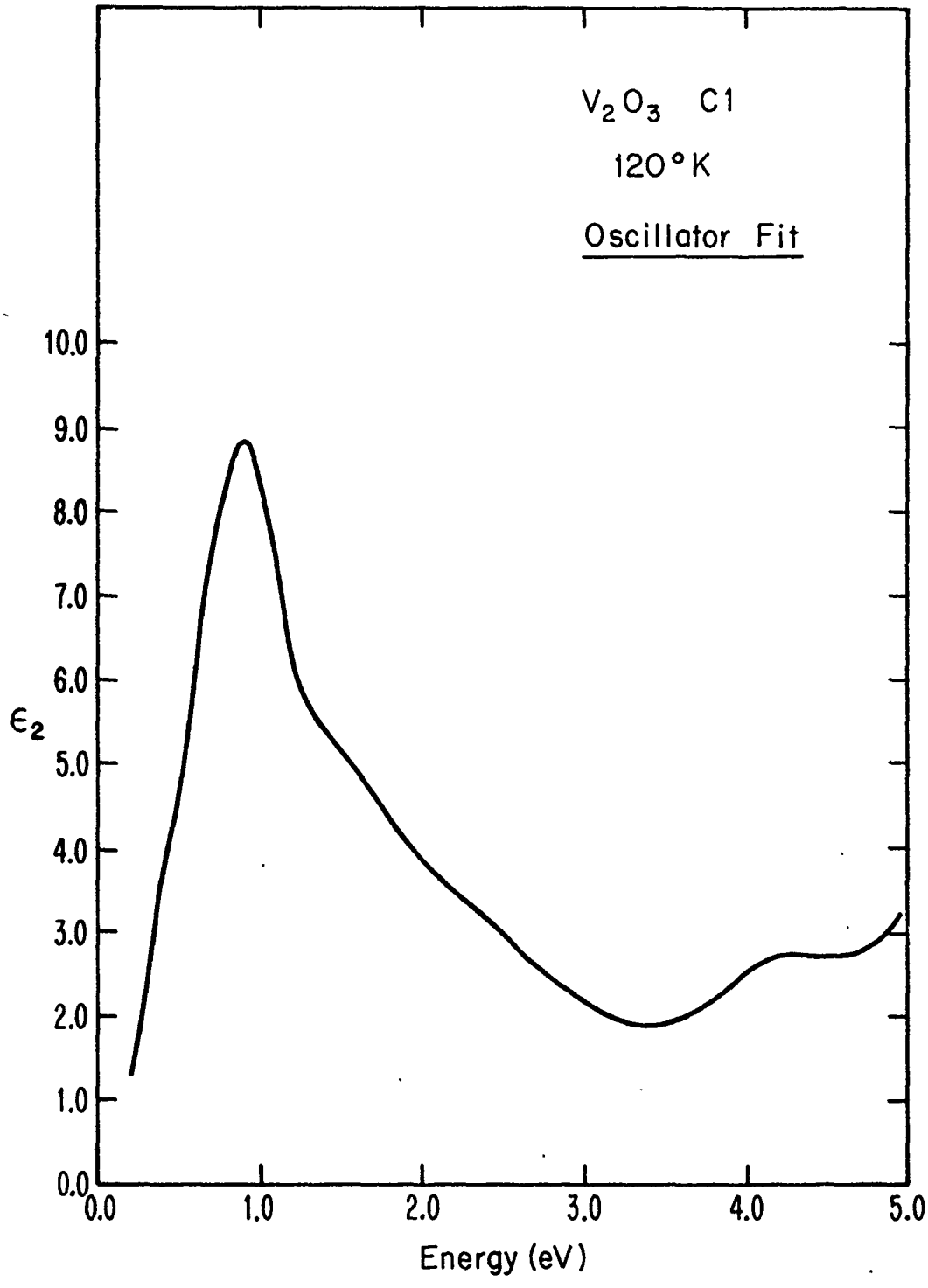

FIGURE IV-22 ϵ_2 curve of C1, obtained from the fit shown in Fig. IV-20.

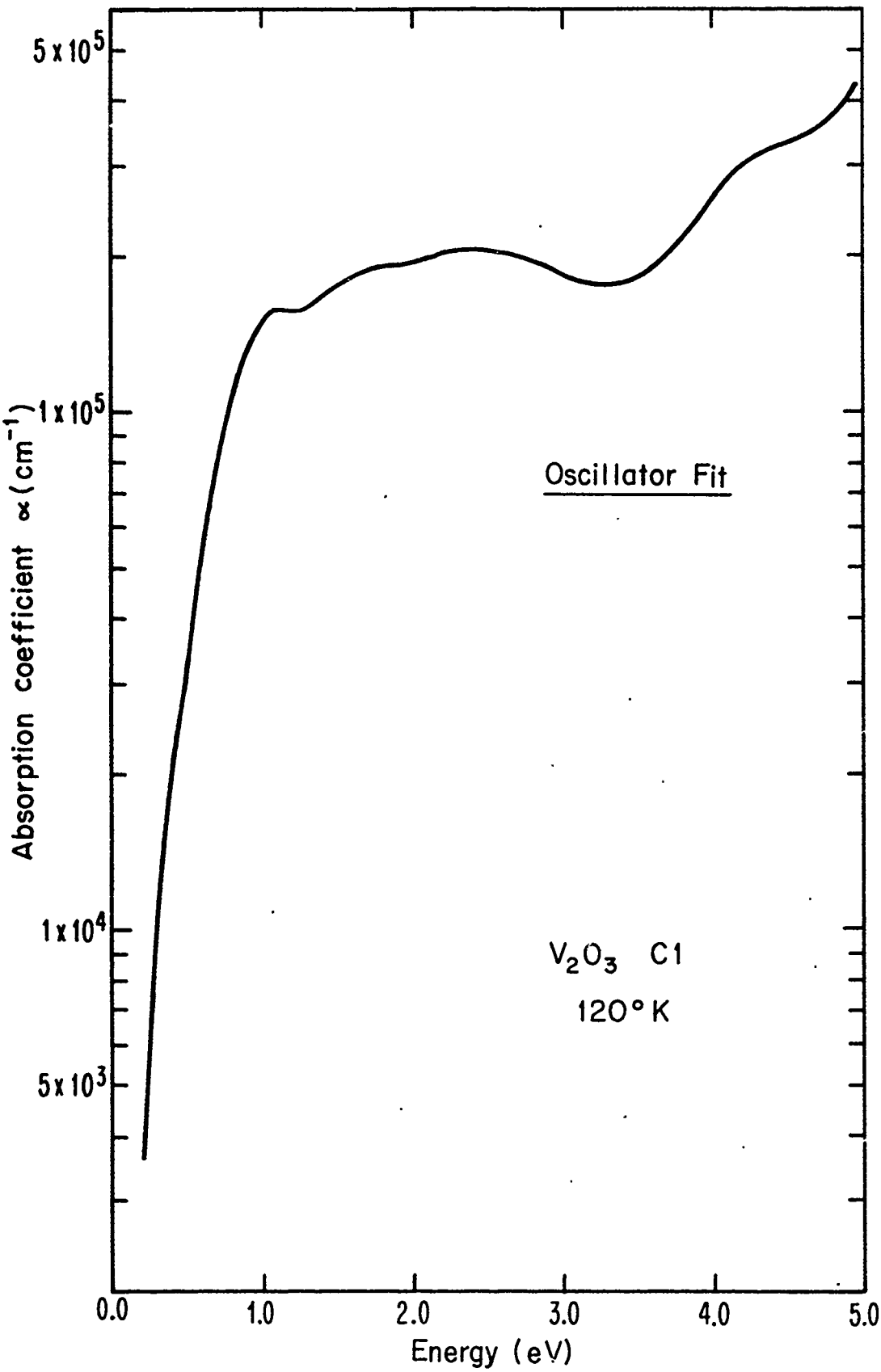

FIGURE IV-23 α curve of C1, obtained from the fit shown in Fig. IV-20.

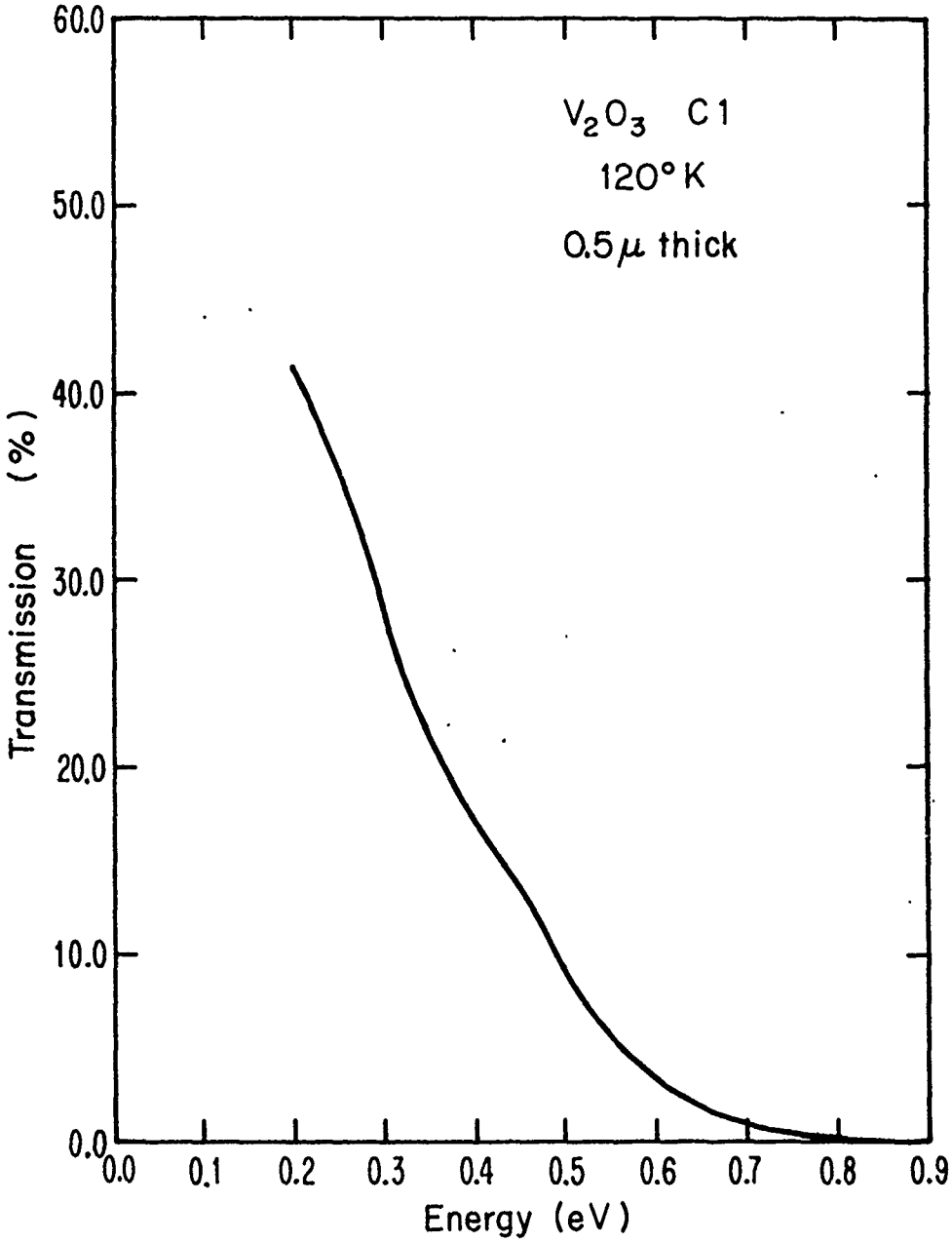

FIGURE IV-24 Predicted transmission of a single V_2O_3 crystal of 0.5μ thickness at 120°K.

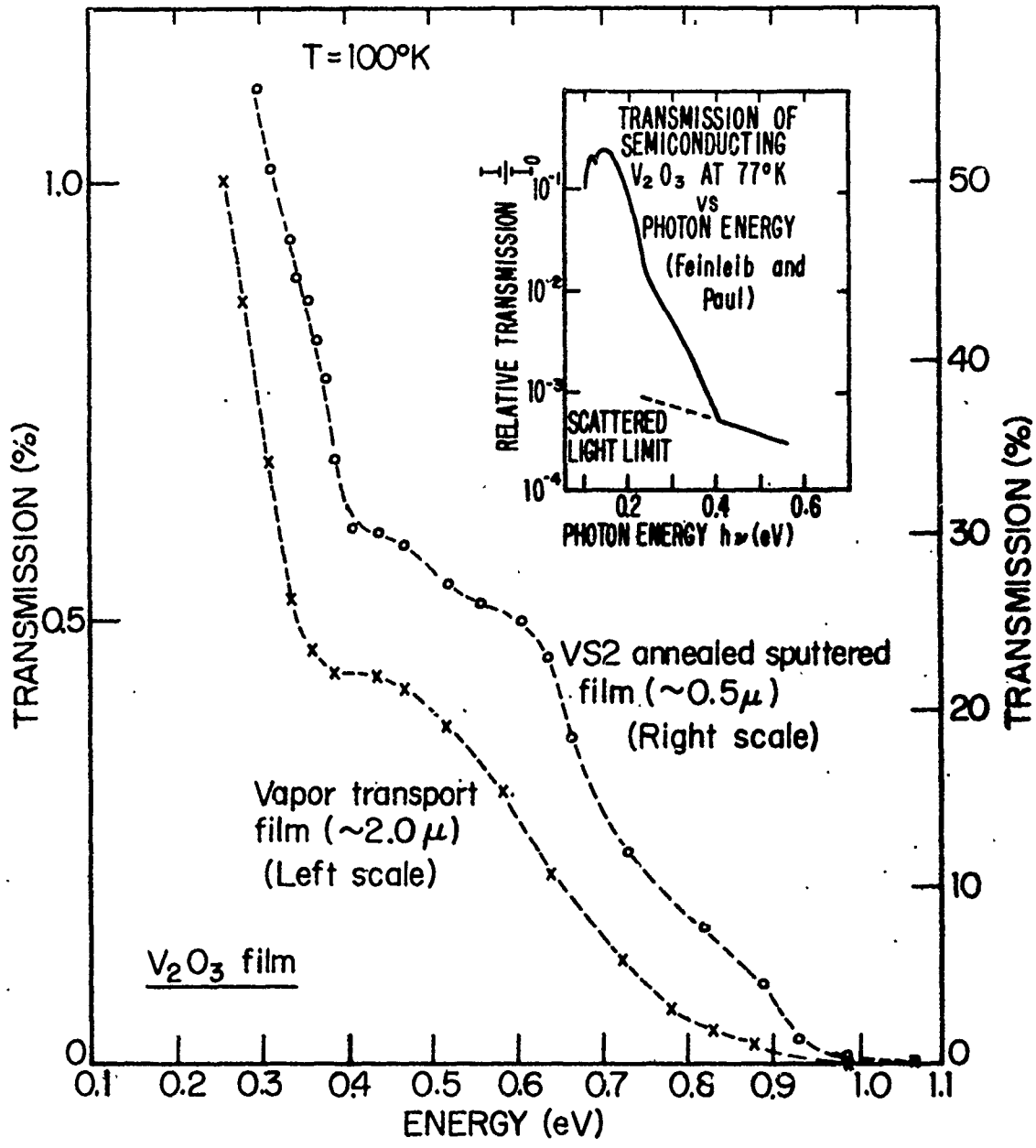

FIGURE IV-25 Low temperature transmission of a V_2O_3 film grown by vapor transport and of an annealed V_2O_3 sputtered film, compared with that of a single crystal measured by Feinleib and Paul (3).

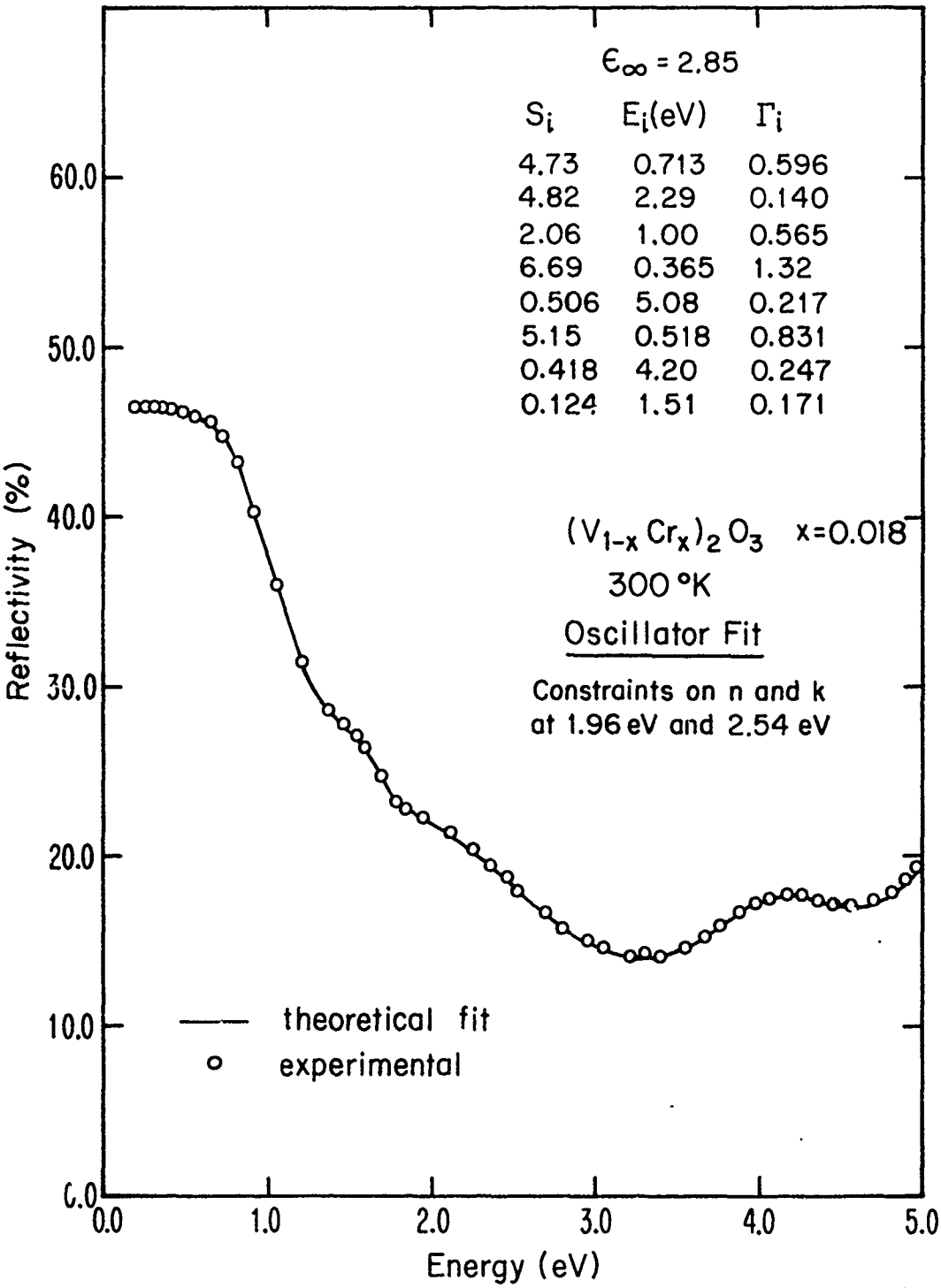

FIGURE IV-26 A theoretical fit to the experimental reflectivity data of a $(V_{0.982}Cr_{0.018})_2O_3$ crystal, where the values of n and k at 1.96eV and 2.54eV are constrained to approach those obtained from the angular dependence measurements.

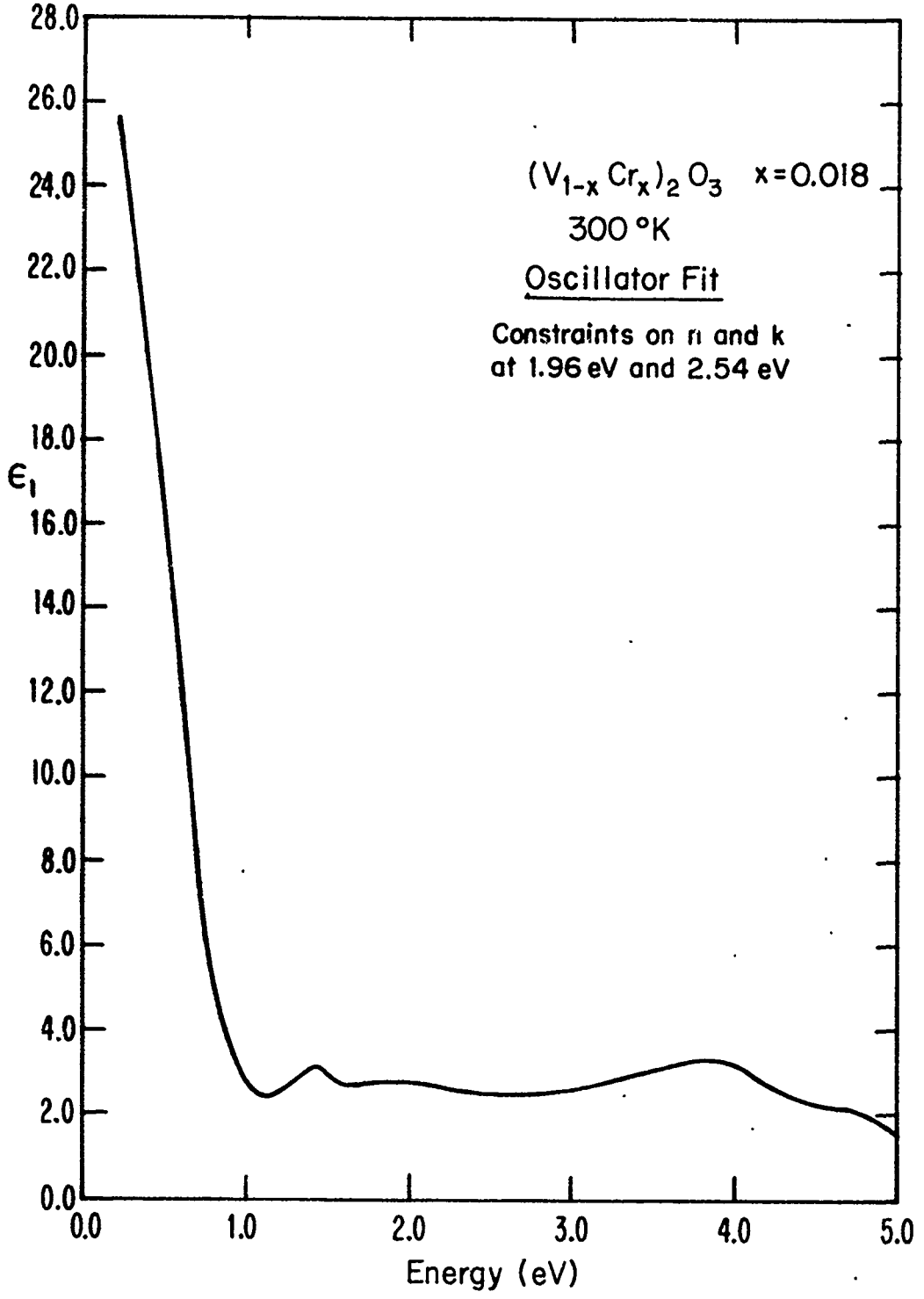

FIGURE IV-27 ϵ_1 curve of the $(V_{0.982}Cr_{0.018})_2O_3$ crystal, obtained from the fit shown in Fig. IV-26.

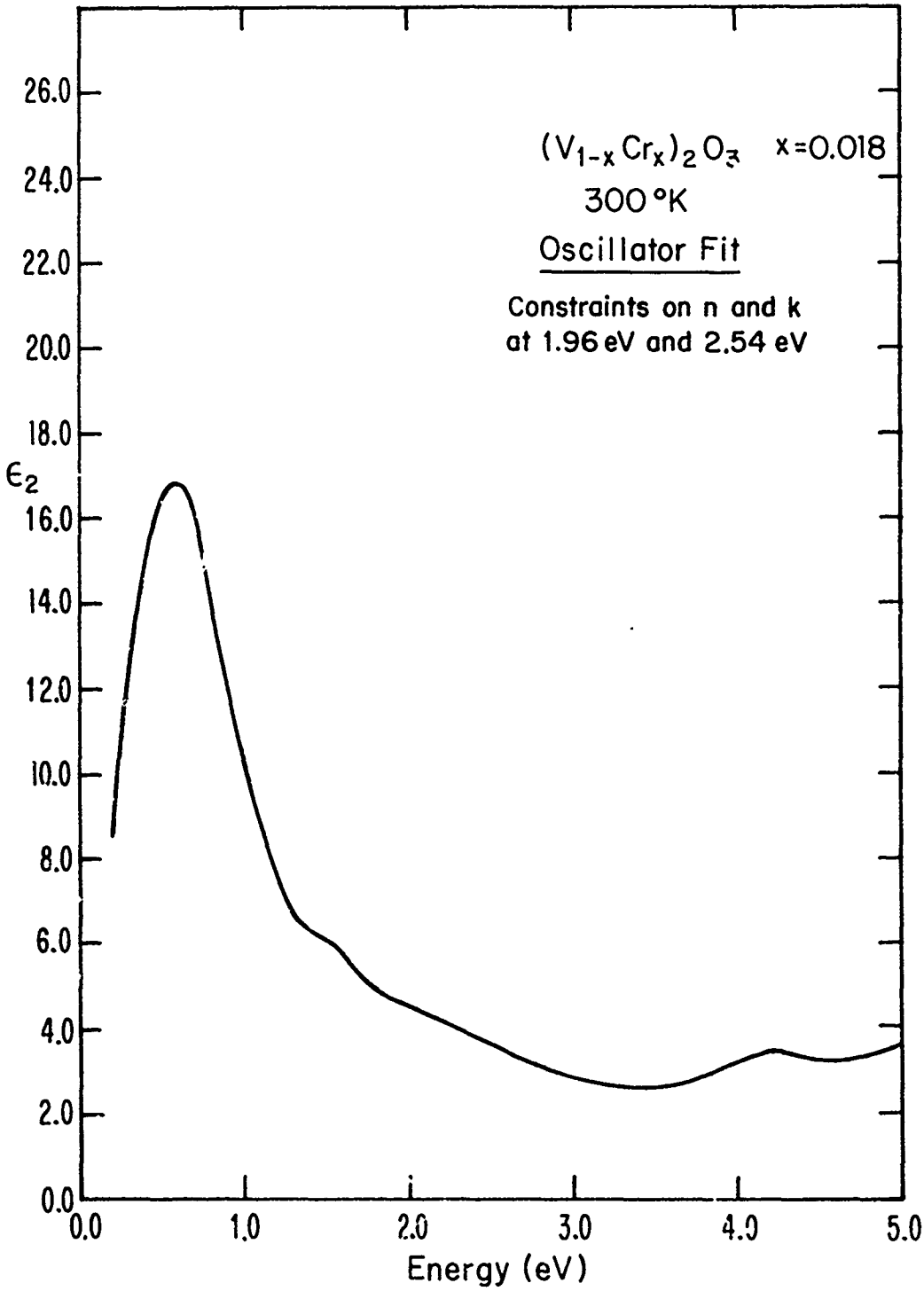

FIGURE IV-28 ϵ_2 curve of the $(V_{0.982}Cr_{0.018})_2O_3$ crystal, obtained from the fit shown in Fig. IV-26.

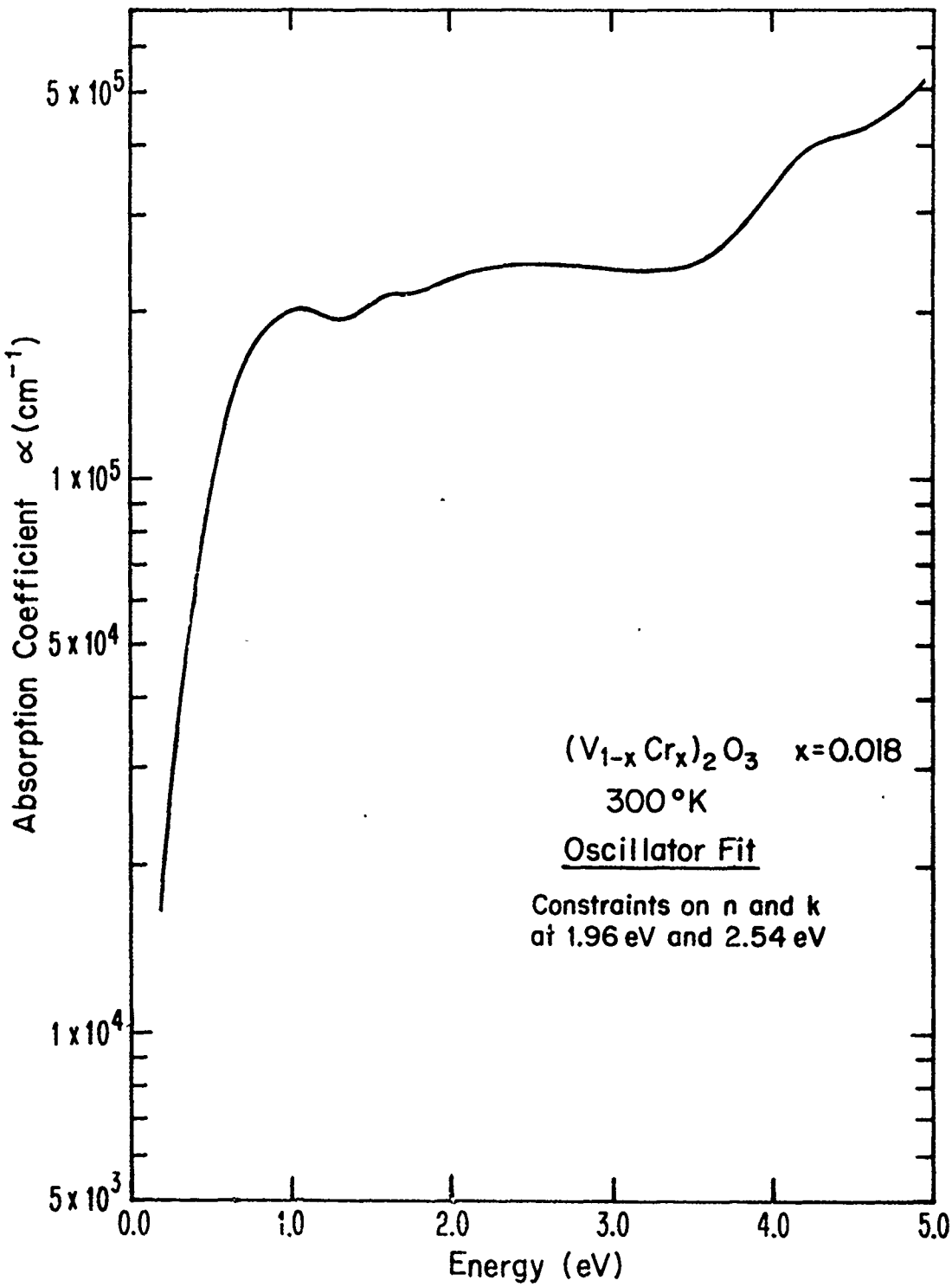

FIGURE IV-29 α curve of the $(V_{0.982}Cr_{0.018})_2O_3$ crystal, obtained from the fit shown in Fig. IV-26.

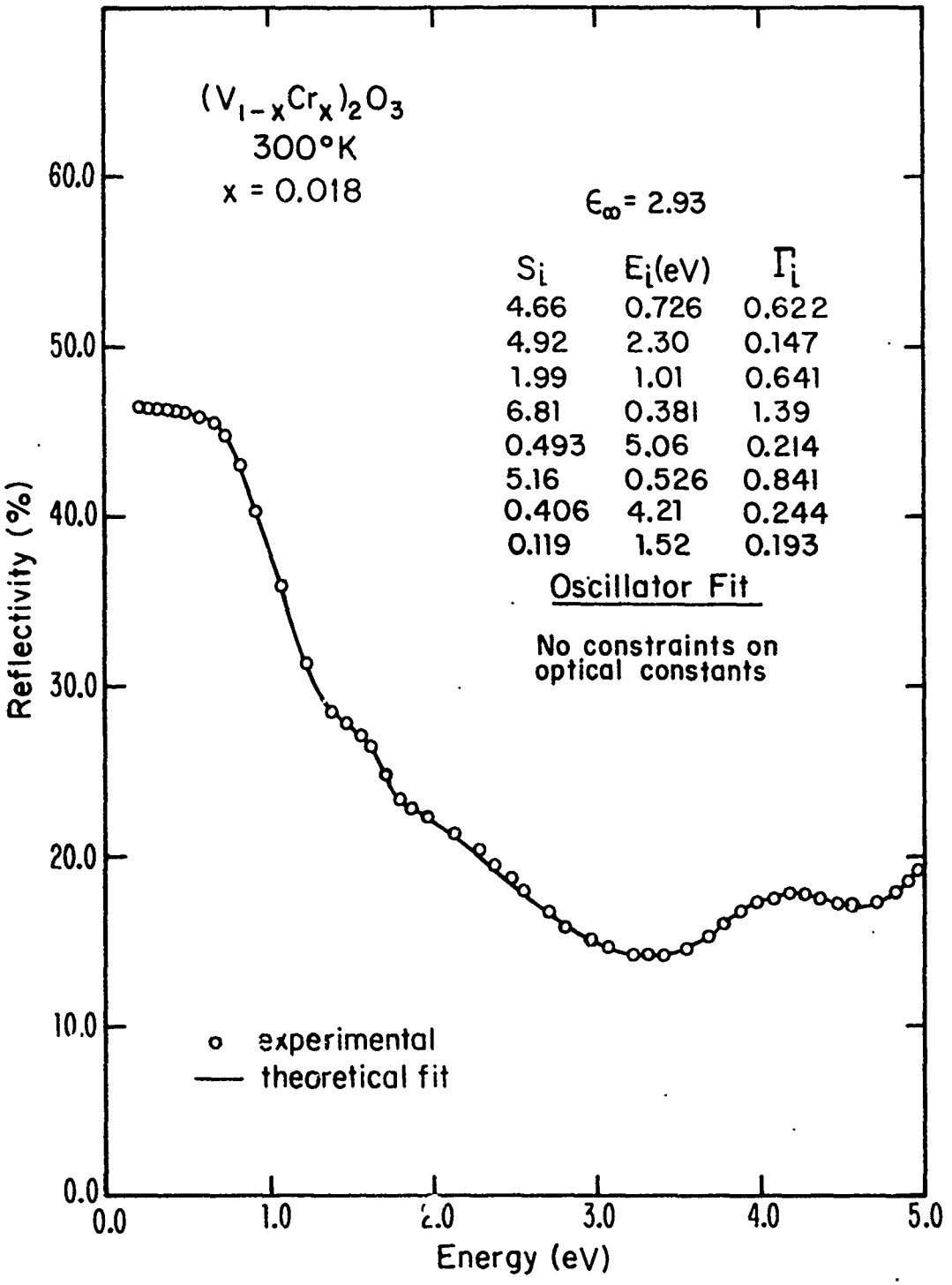

FIGURE IV-30 A theoretical fit to the experimental data of the $(V_{0.982}Cr_{0.018})_2O_3$ crystal, where the values of n and k at 1.96eV and 2.54eV are not constrained.

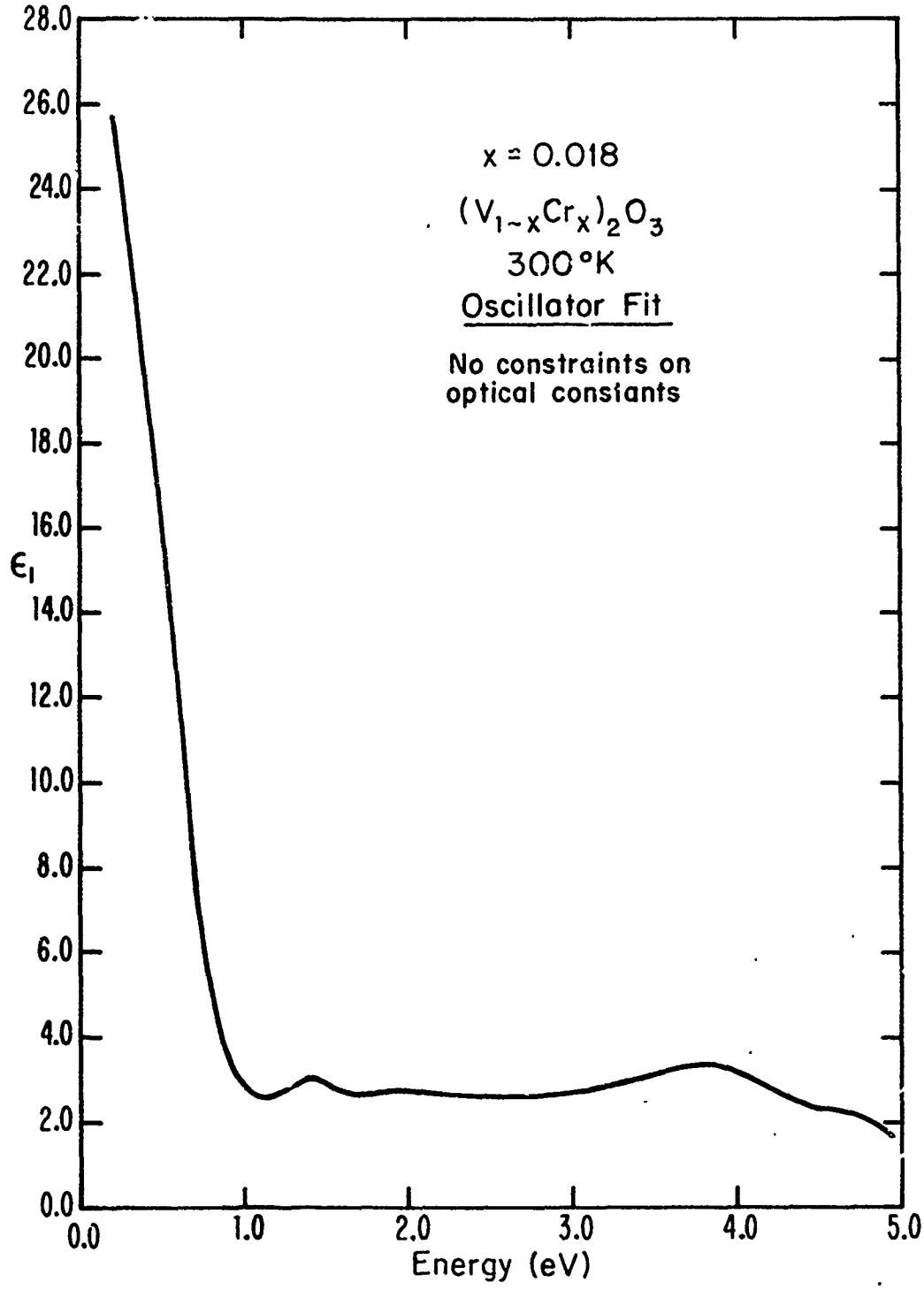

FIGURE IV-31 ϵ_1 curve of the $(V_{0.982}Cr_{0.018})_2O_3$ crystal, obtained from the fit shown in Fig. IV-30,

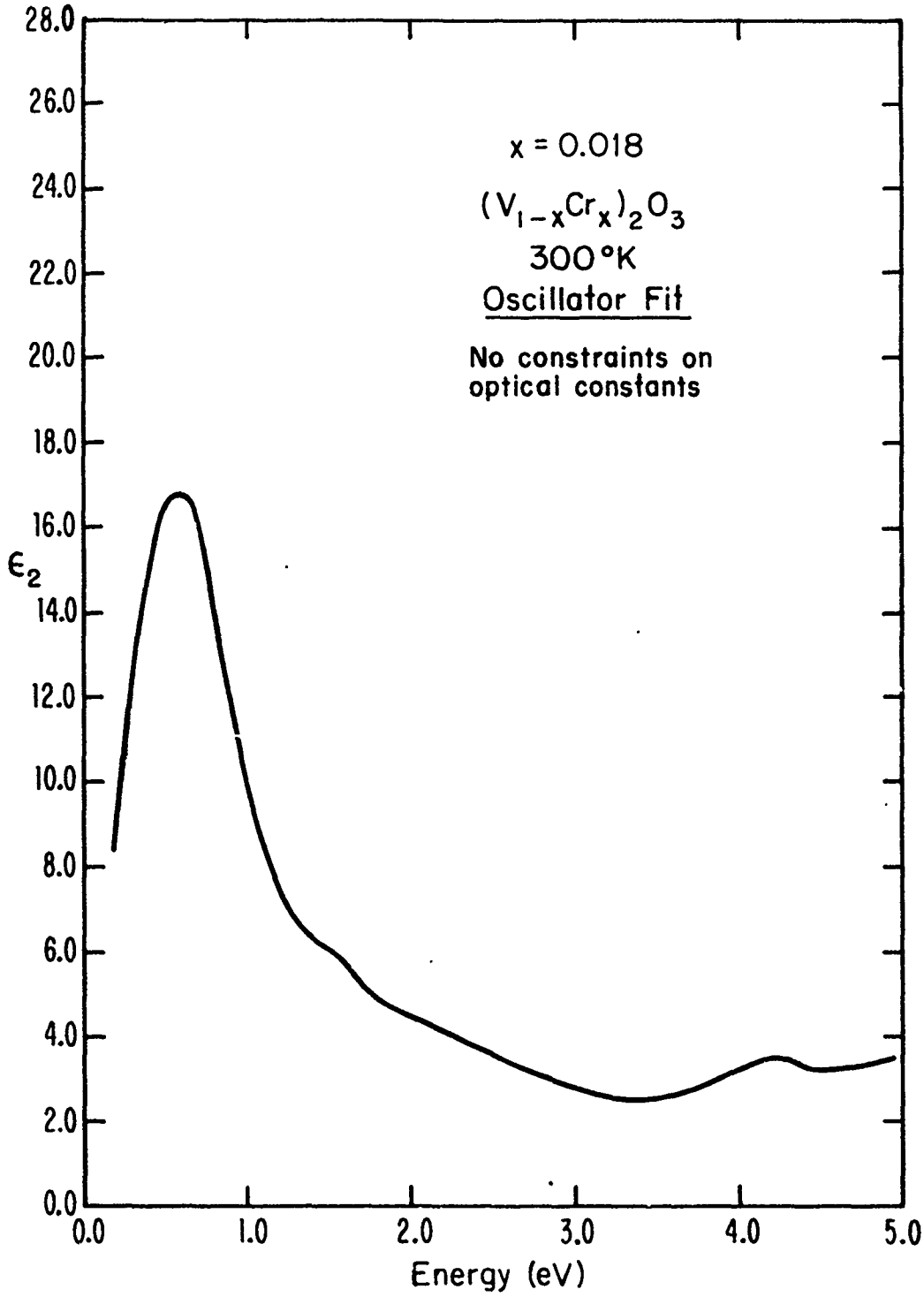

FIGURE IV-32 ϵ_2 curve of the $(V_{0.982}Cr_{0.018})_2O_3$ crystal, obtained from the fit shown in Fig. IV-30.

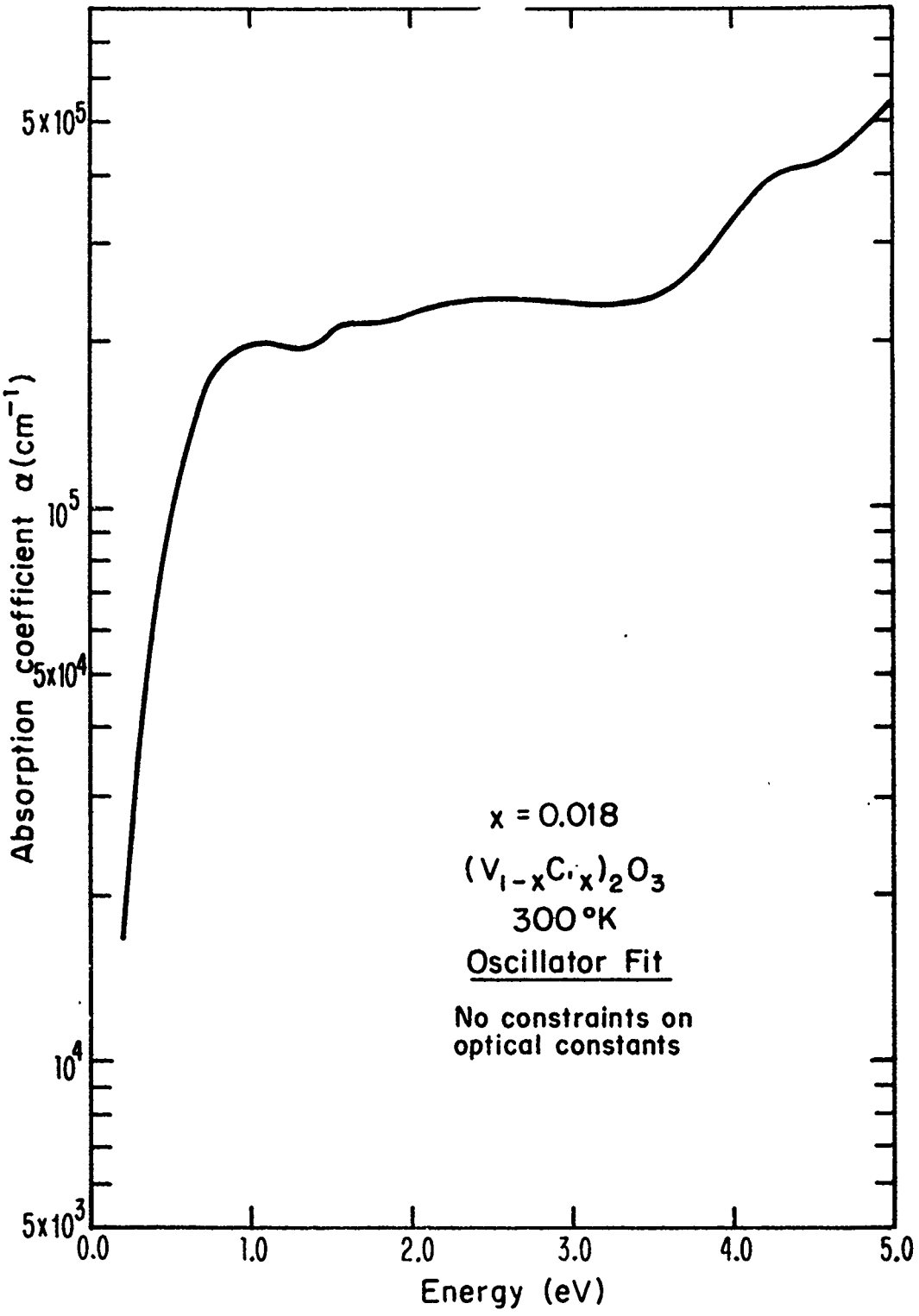

FIGURE IV-33 α curve of the $(V_{0.982}Cr_{0.018})_2O_3$ crystal, obtained from the fit shown in Fig. IV-30.

233

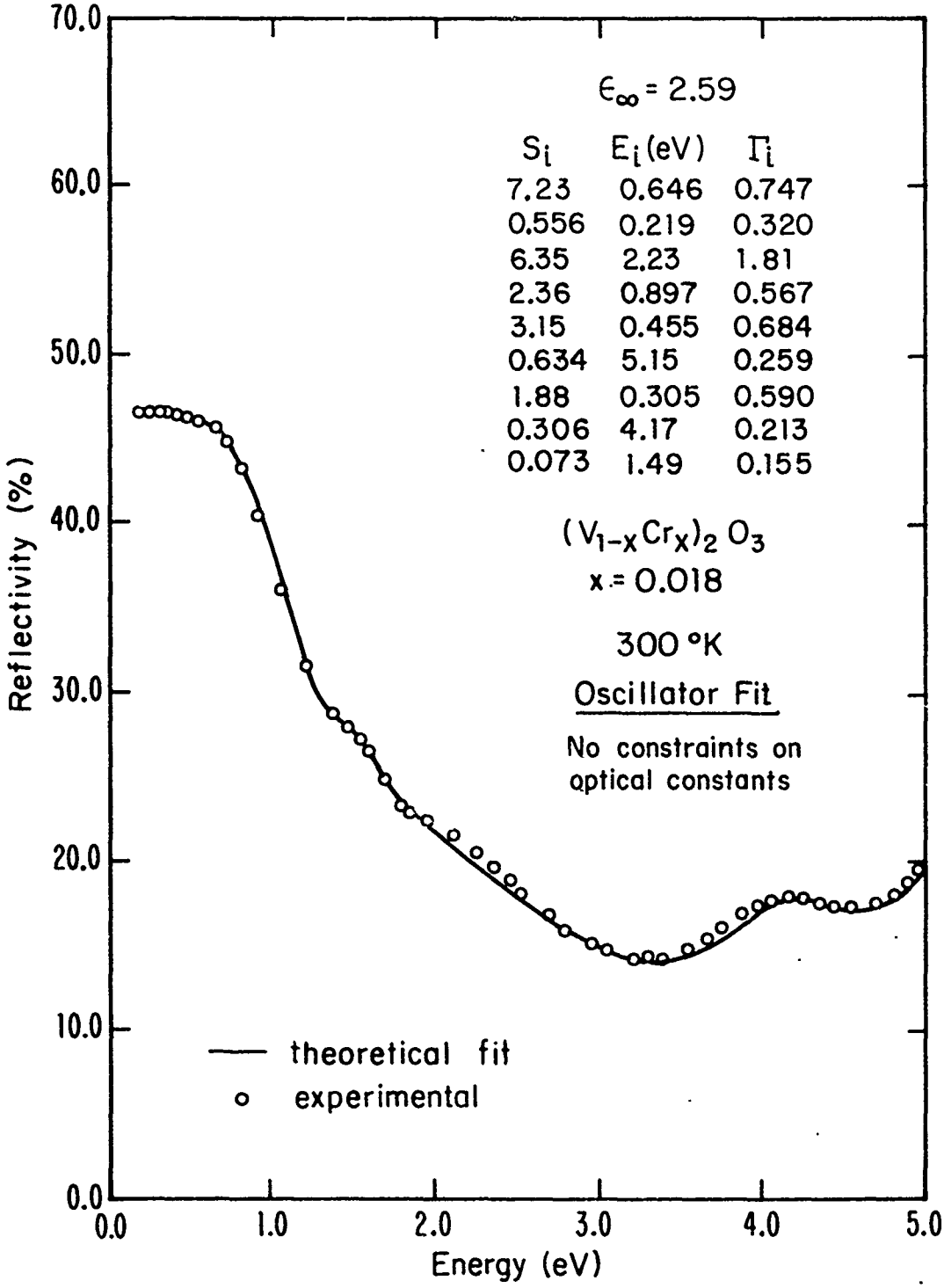

FIGURE IV-34 A theoretical fit to the experimental data of the $(V_{0.982}Cr_{0.018})_2O_3$ crystal by the oscillator fit method, where the values of n and k at 1.96 eV and 2.54 eV are not constrained. This is a poorer fit than the one shown in Fig. IV-30.

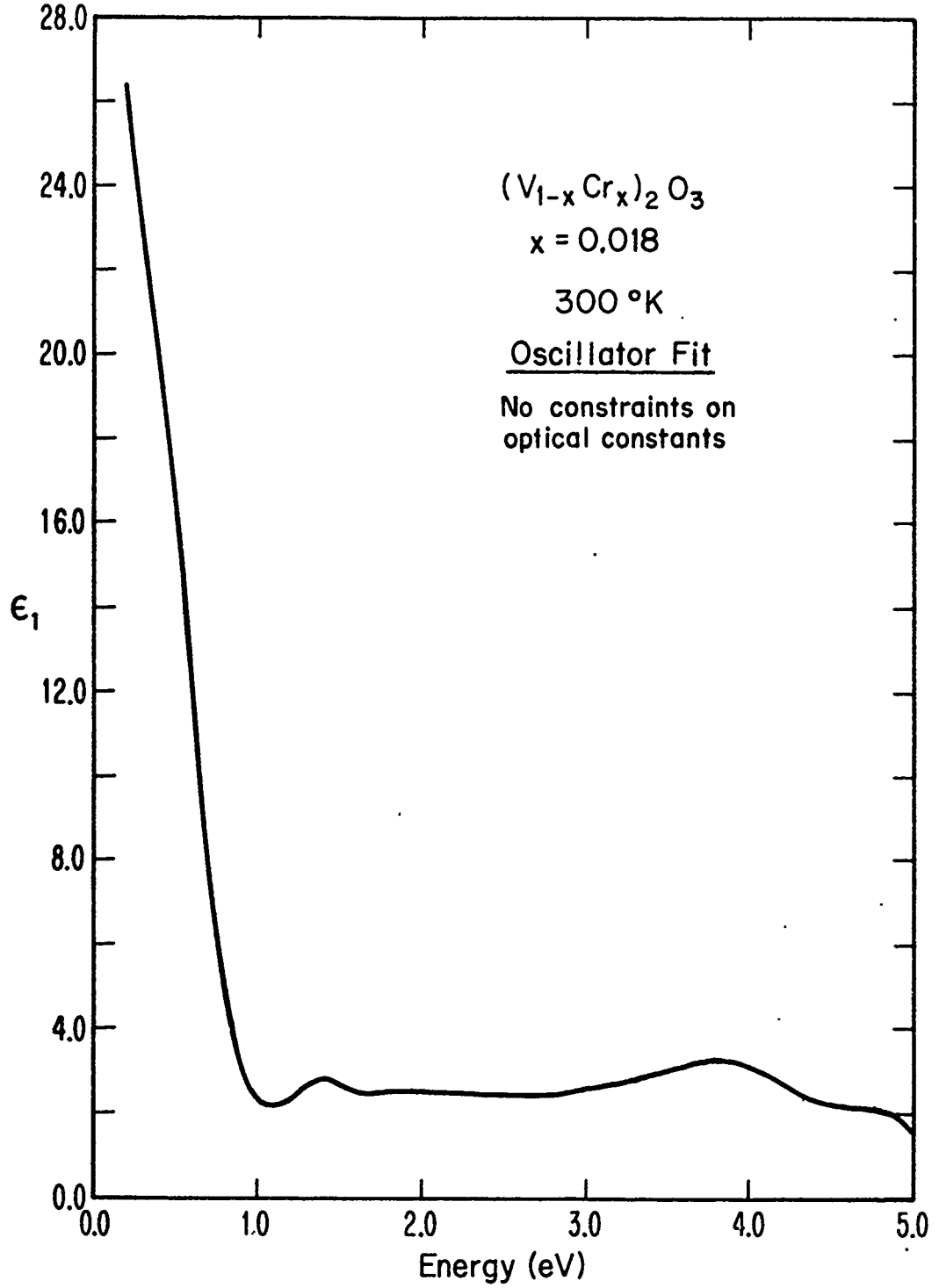

FIGURE IV-35 ϵ_1 curve of the $(V_{0.982}Cr_{0.018})_2O_3$ crystal, obtained from the fit shown in Fig. IV-34.

235

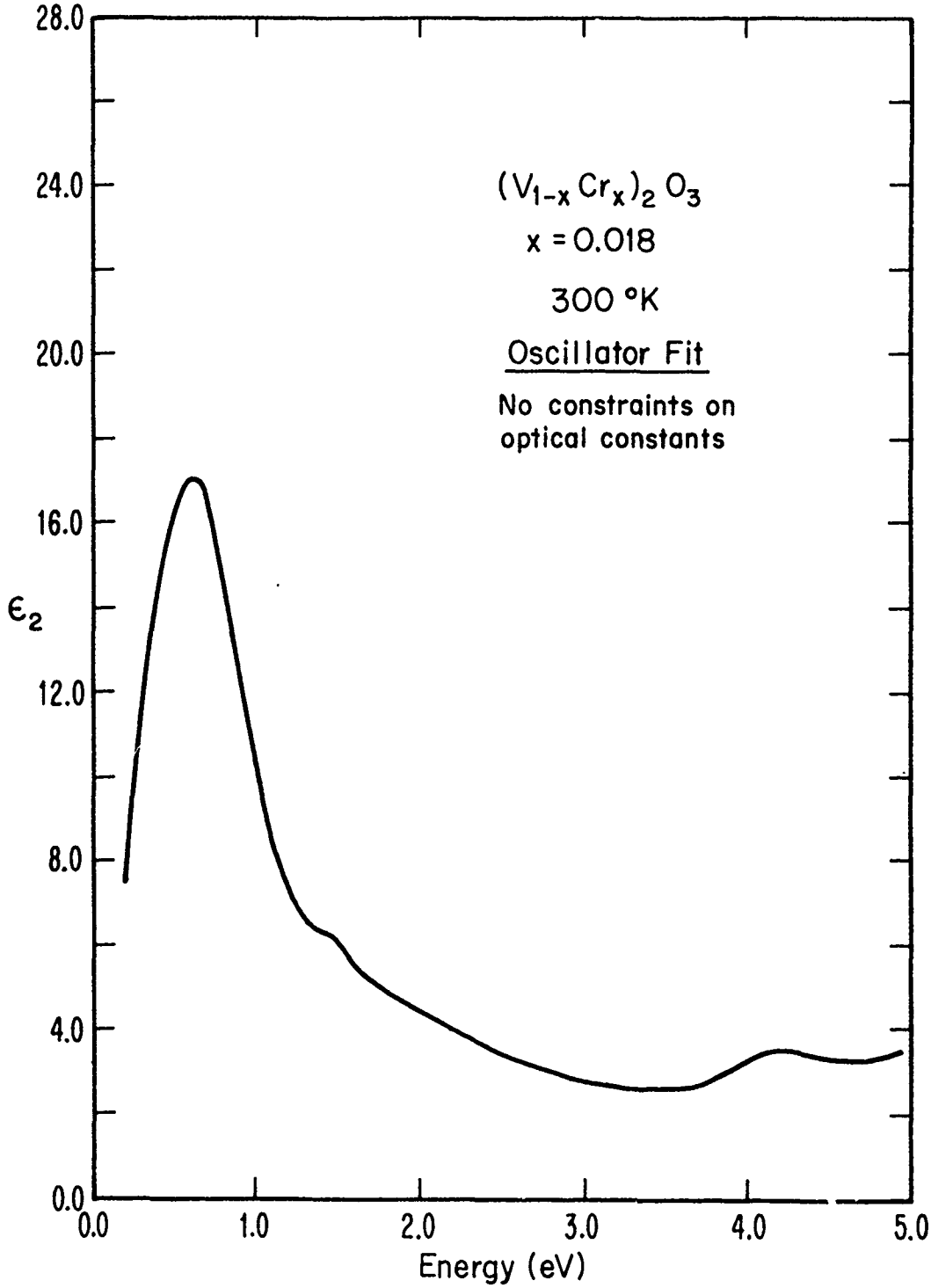

FIGURE IV-36 ϵ_2 curve of the $(V_{0.982}Cr_{0.018})_2O_3$ crystal, obtained from the fit shown in Fig. IV-34.

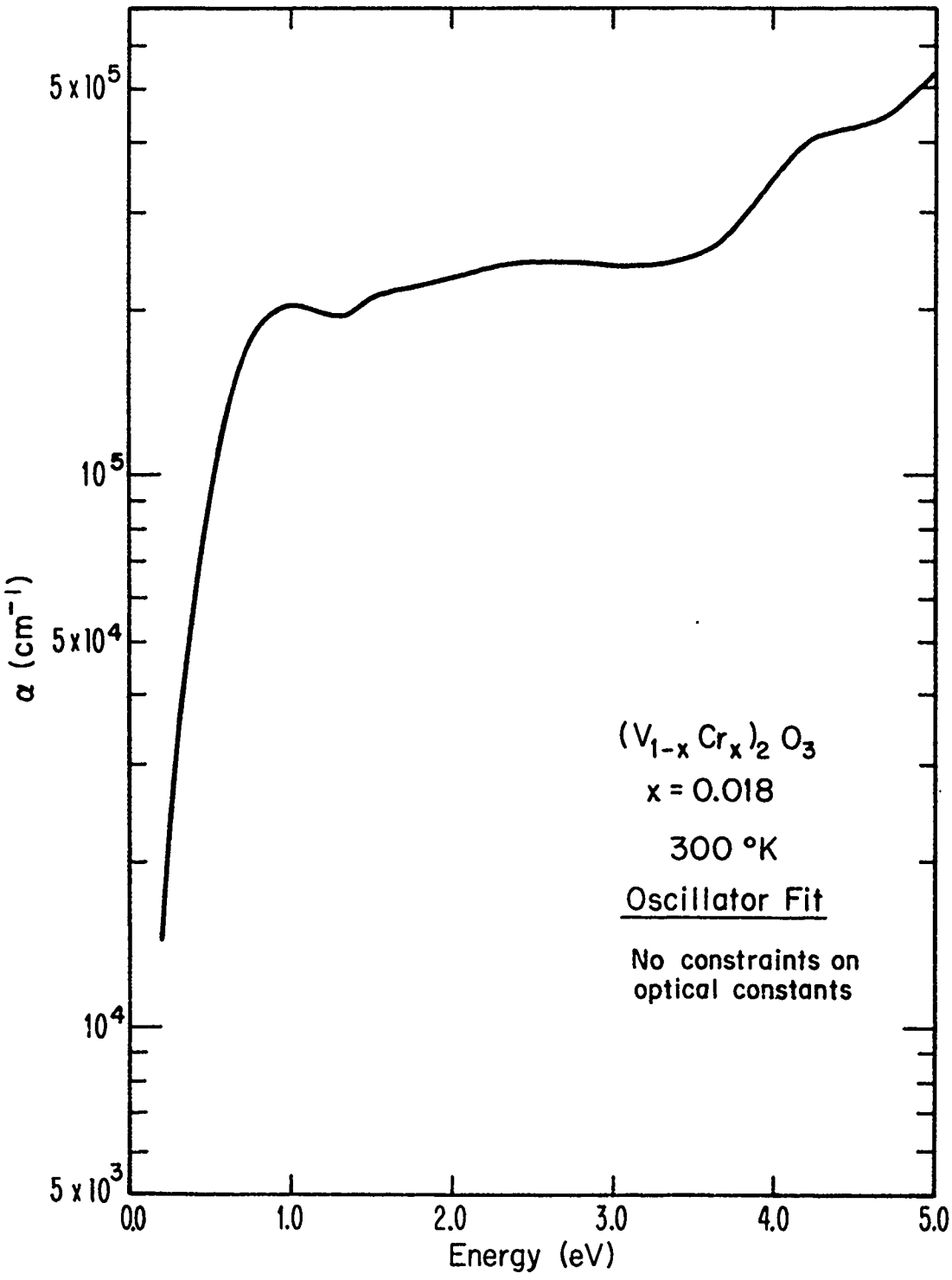

FIGURE IV-37 α curve of the $(V_{0.982}Cr_{0.018})_2O_3$ crystal, obtained from the fit shown in Fig. IV-34.

237

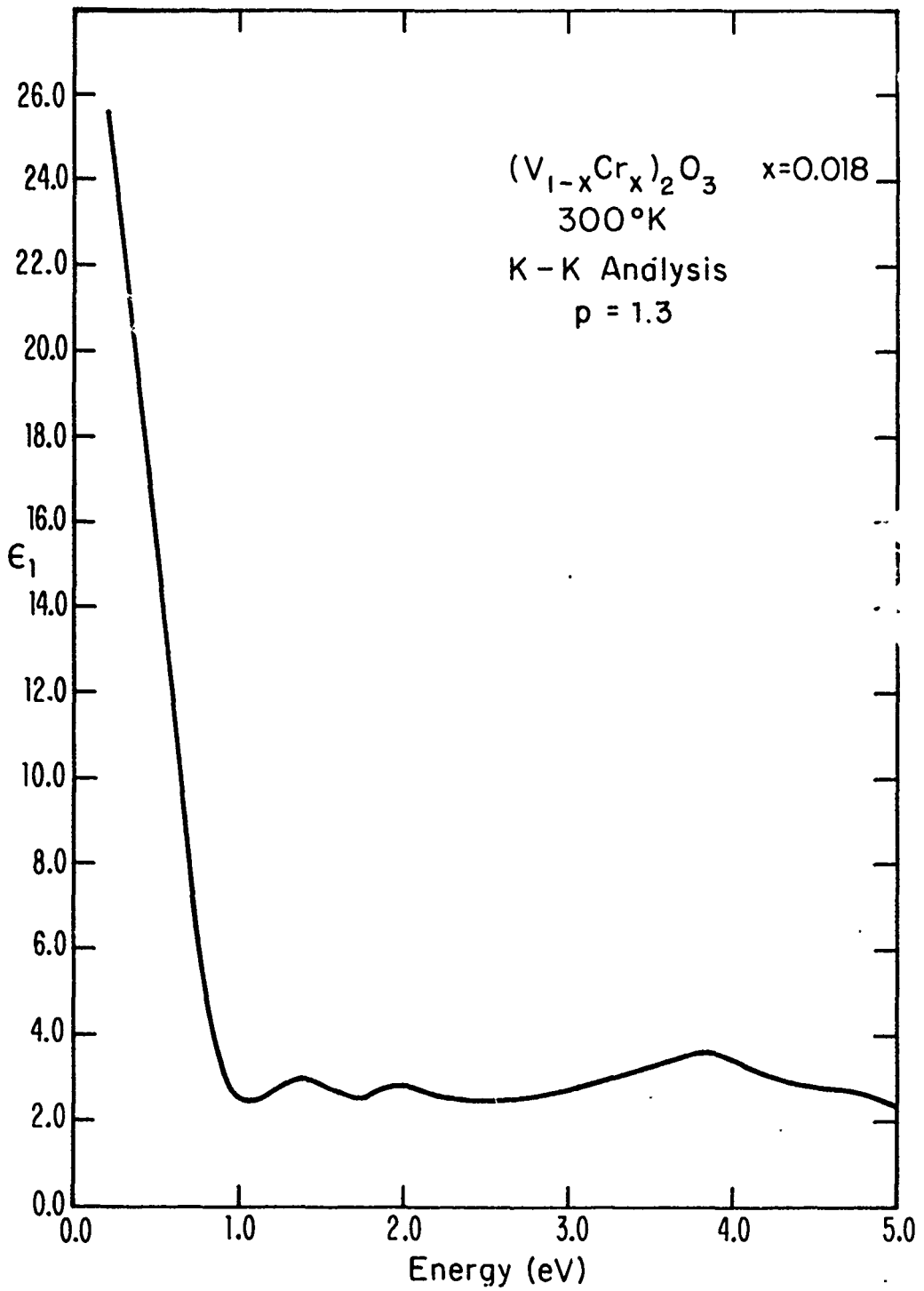

FIGURE IV-38 ϵ_1 curve, obtained from the Kramers-Kronig analysis of the reflectivity spectrum of $(V_{0.982}Cr_{0.018})_2O_3$.

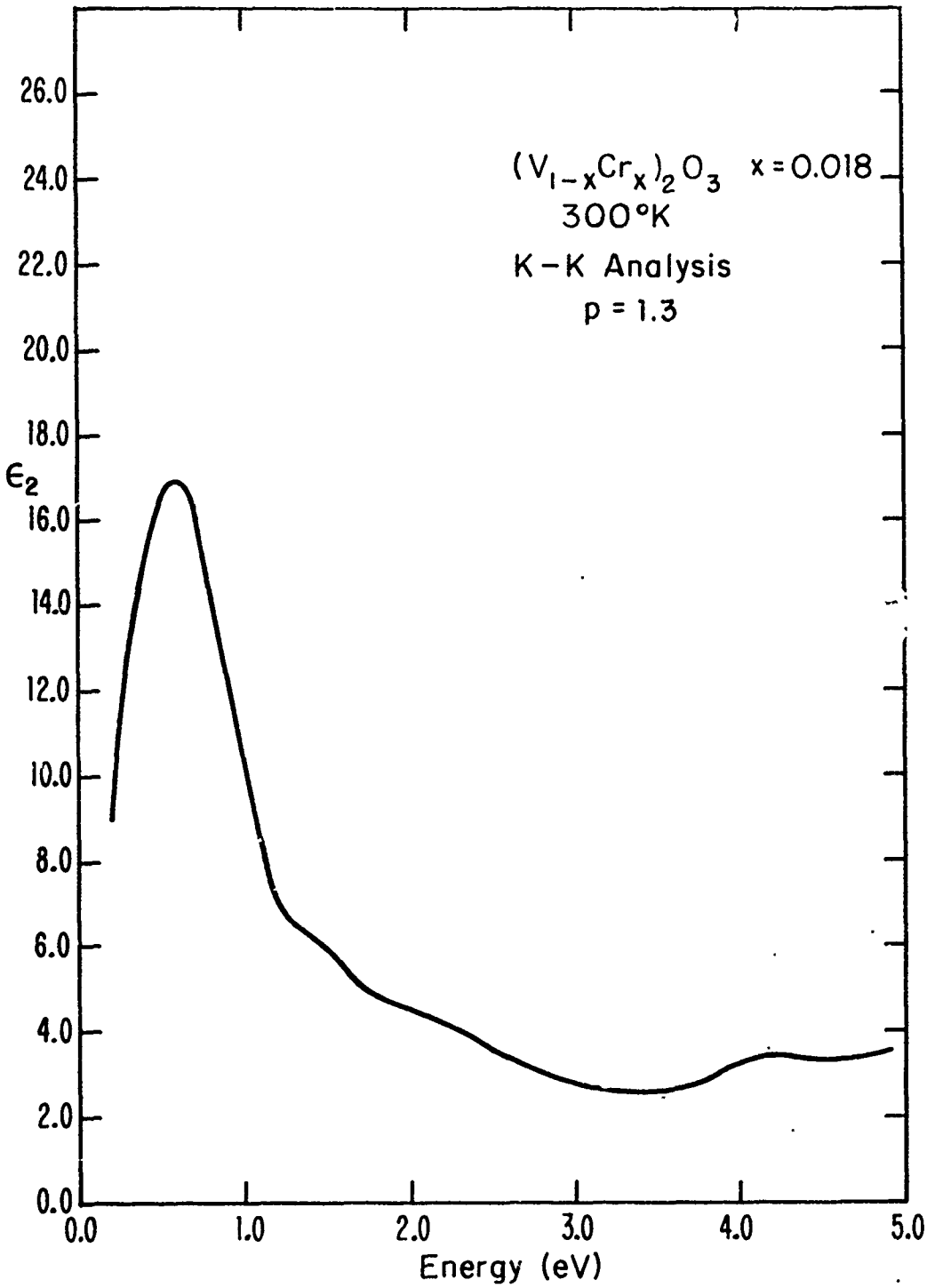

FIGURE IV-39 ϵ_2 curve, obtained from the Kramers-Kronig analysis of the reflectivity spectrum of $(V_{0.982}\ Cr_{0.018})_2O_3$.

239

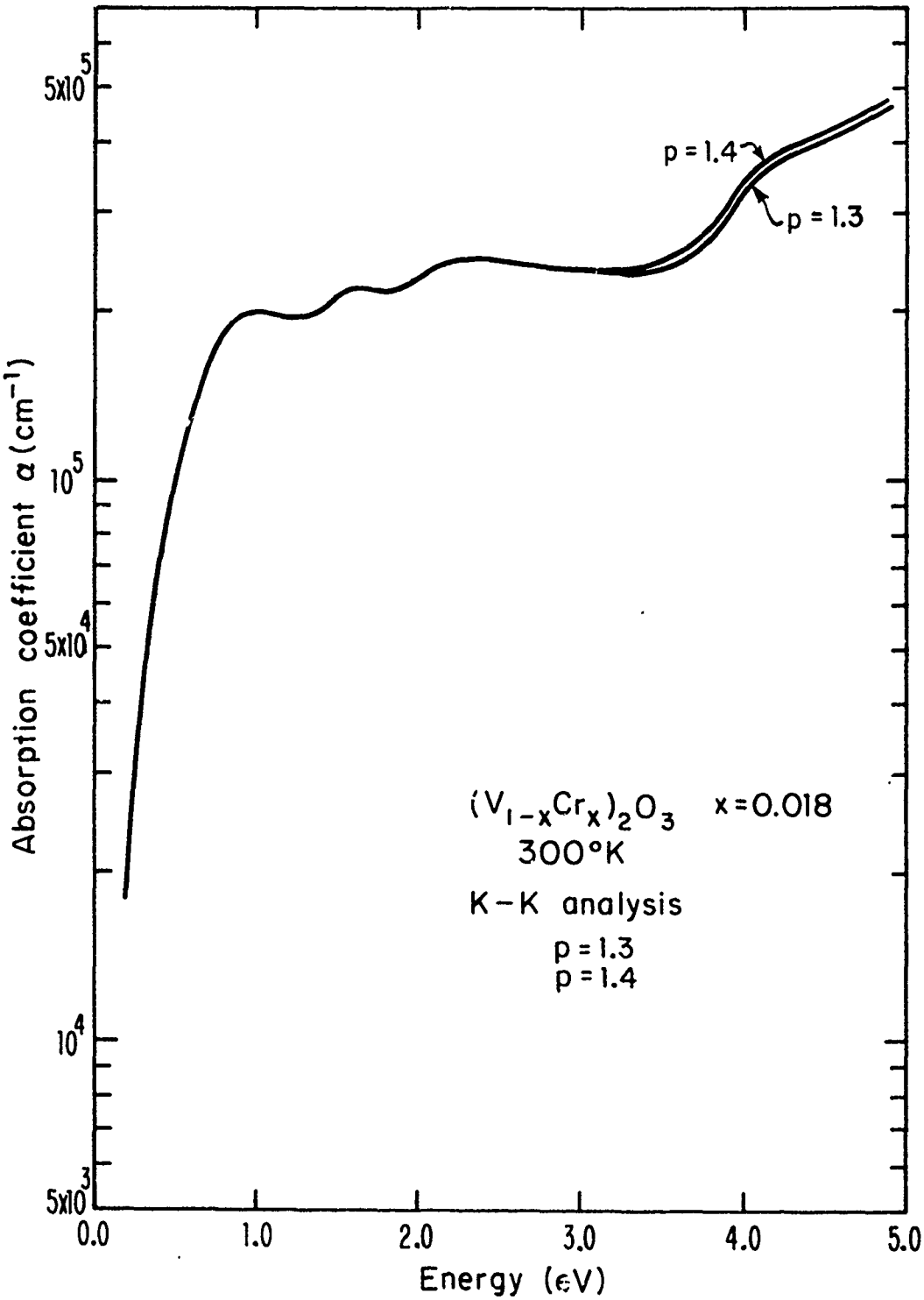

FIGURE IV-40 α curve, obtained from the Kramers-Kronig analysis of the reflectivity spectrum of $(V_{0.982}Cr_{0.018})_2O_3$.

240

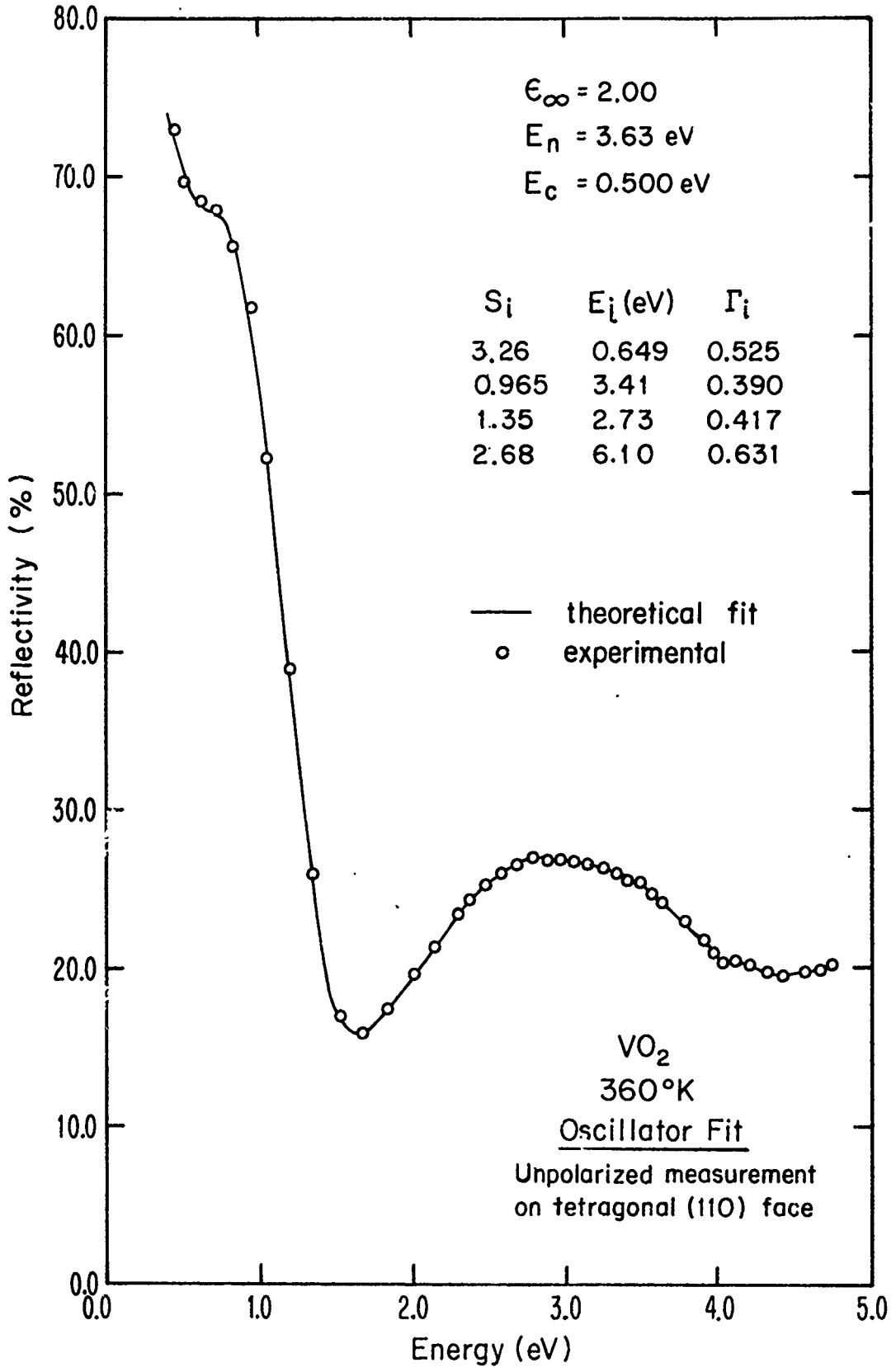

FIGURE IV-41 A theoretical fit to the experimental data of a VO_2 crystal (at 360°K) by the oscillator fit method.

241

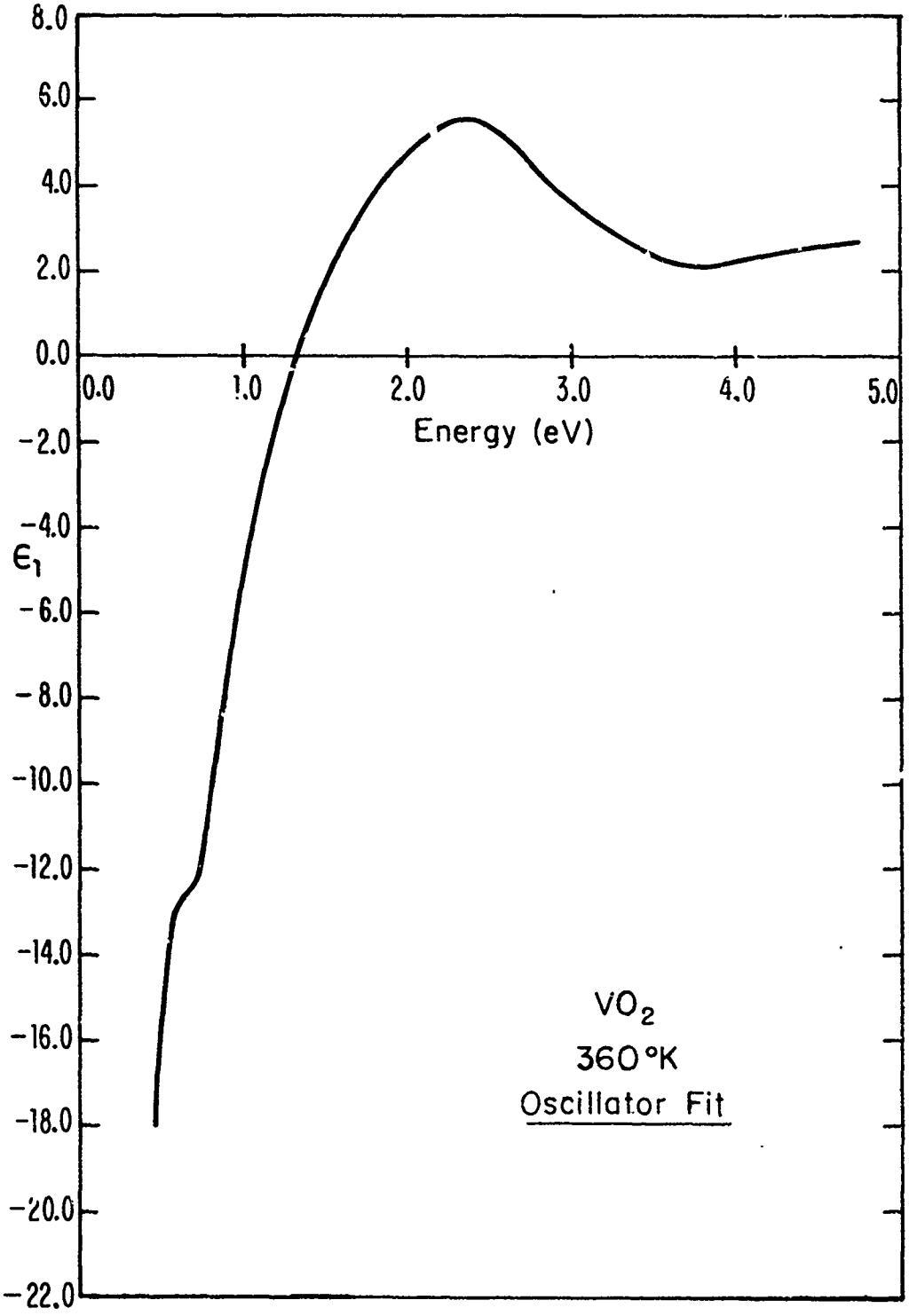

FIGURE IV-42 ϵ_1 curve of the VO_2 crystal, obtained from the fit shown in Fig. IV-41.

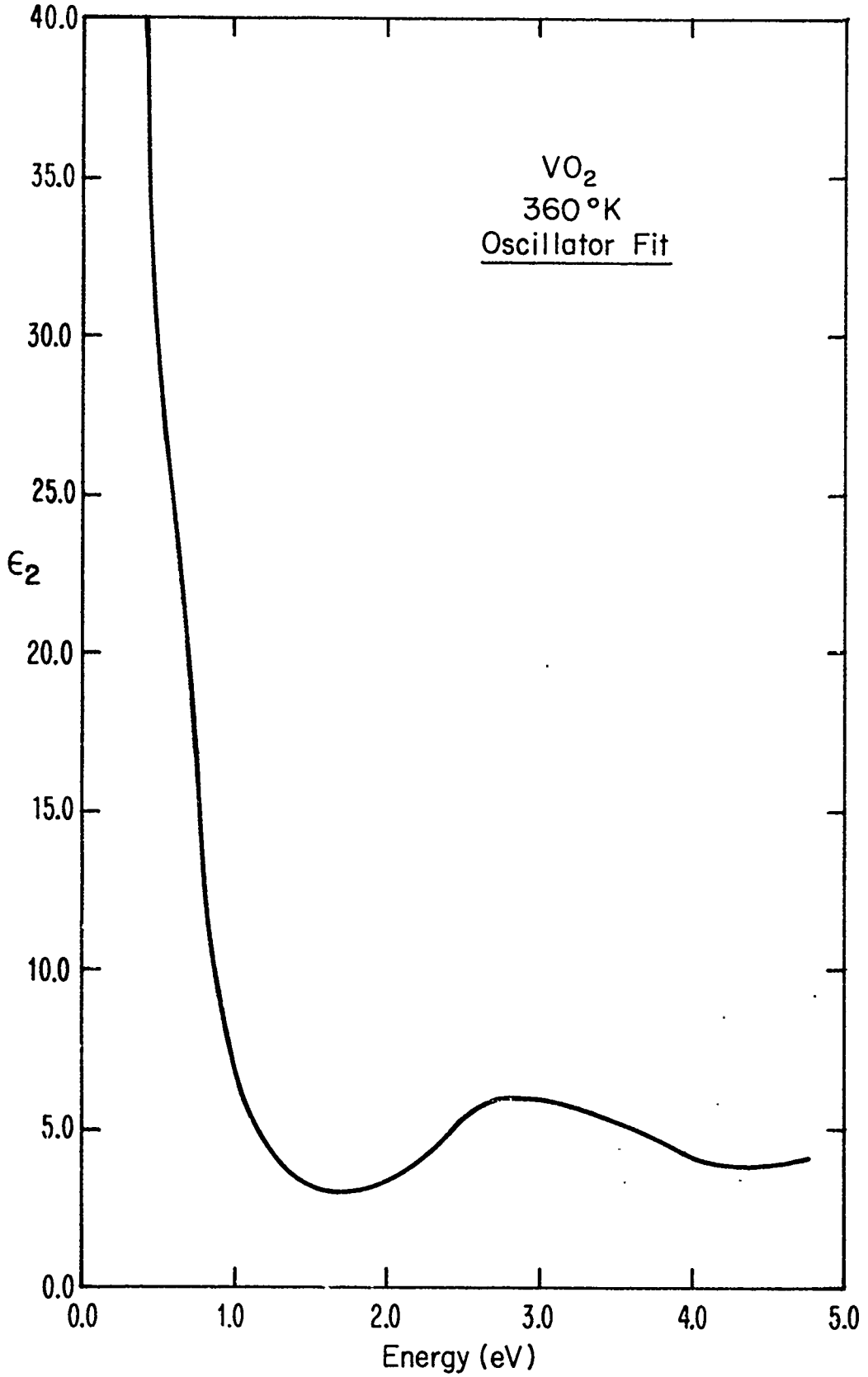

FIGURE IV-43 ϵ_2 curve of the VO_2 crystal, obtained from the fit shown in Fig. IV-41.

243

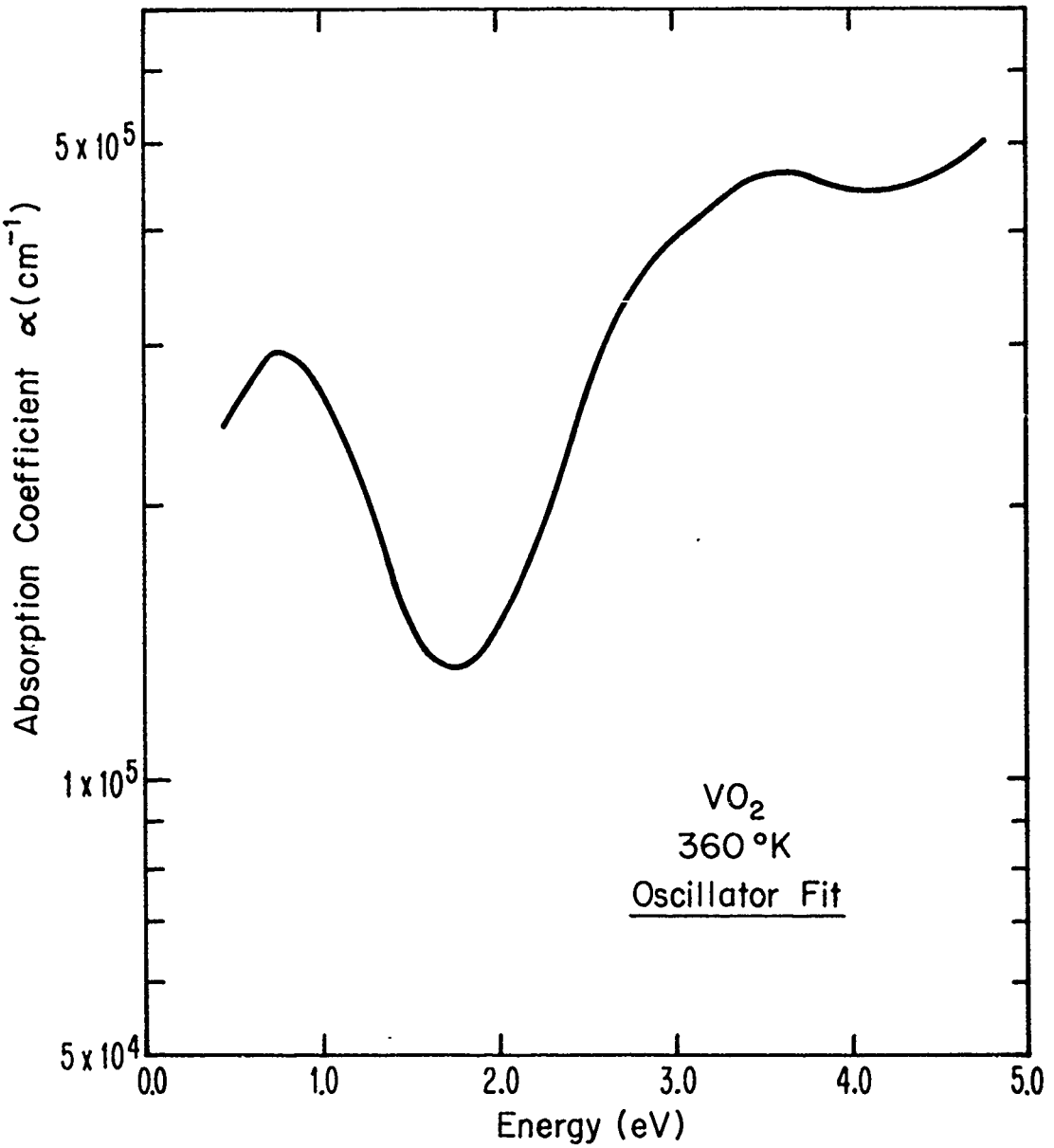

FIGURE IV-44 α curve of the VO_2 crystal, obtained from the fit shown in Fig. IV-41.

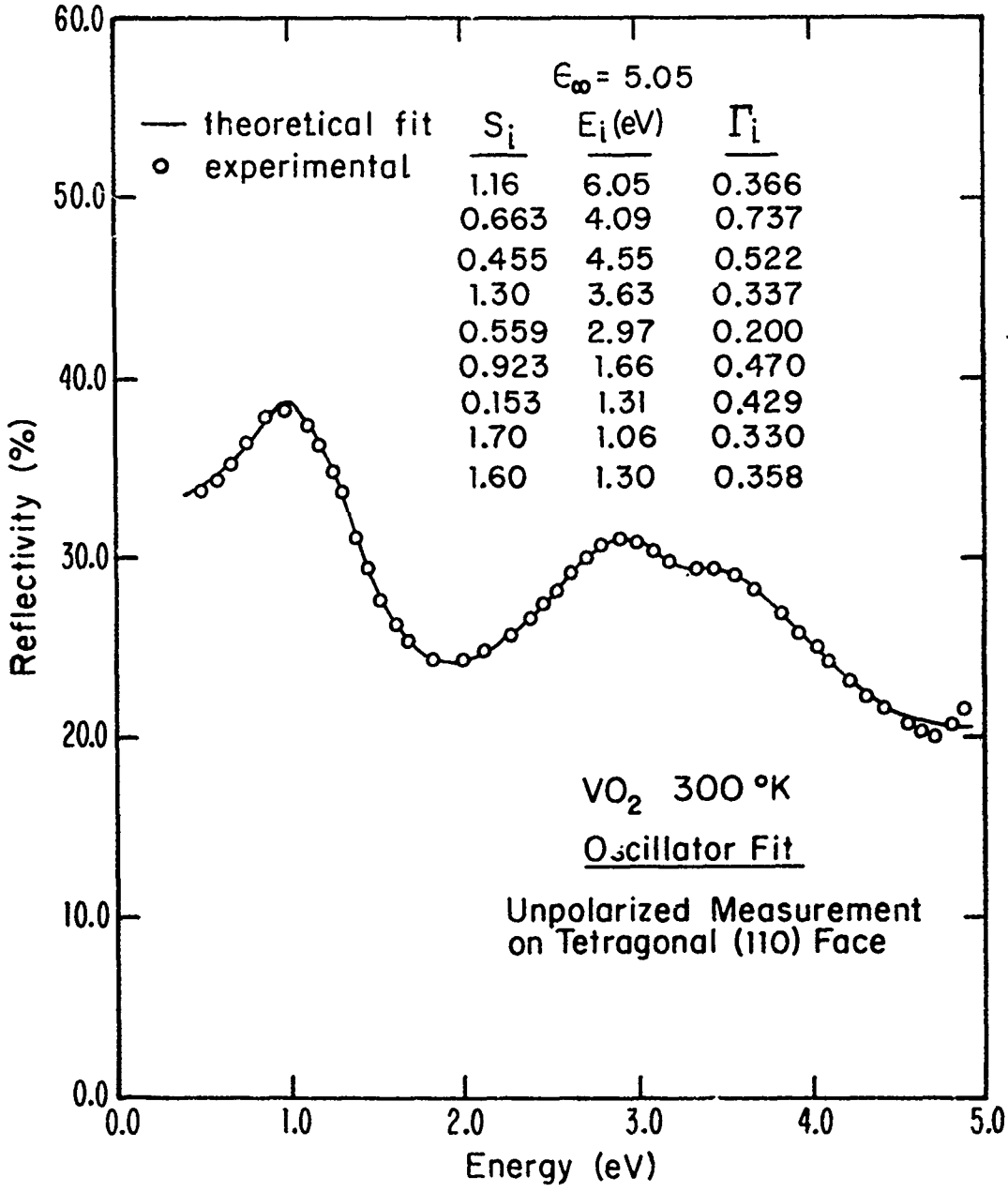

FIGURE IV-45 A theoretical fit to the experimental data of the VO_2 crystal (at 300°K) by the oscillator fit method.

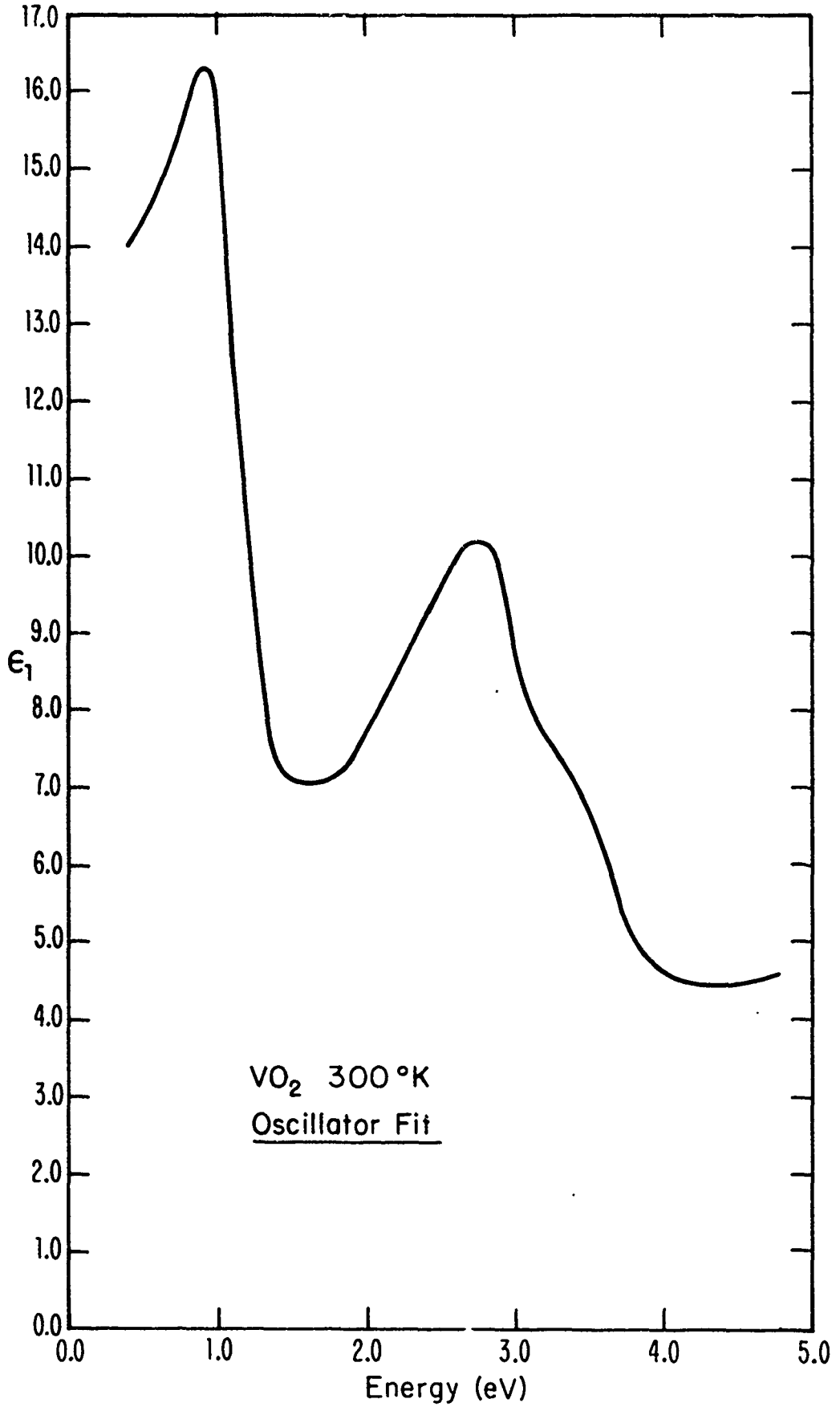

FIGURE IV-46 ϵ_1 curve of the VO_2 crystal obtained from the fit shown in Fig. IV-45.

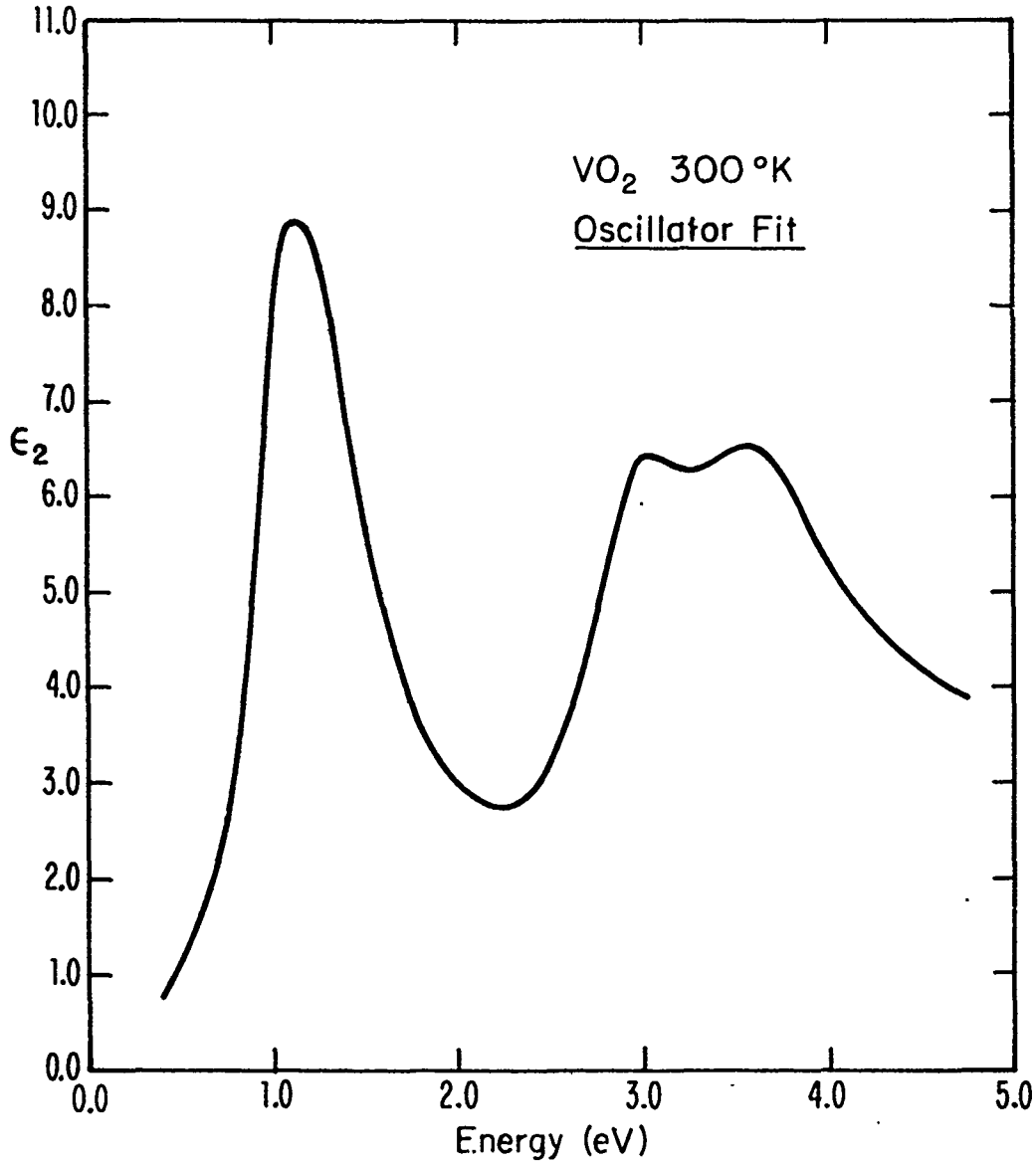

FIGURE IV-47 ϵ_2 curve of the VO_2 crystal obtained from the fit shown in Fig. IV-45.

247

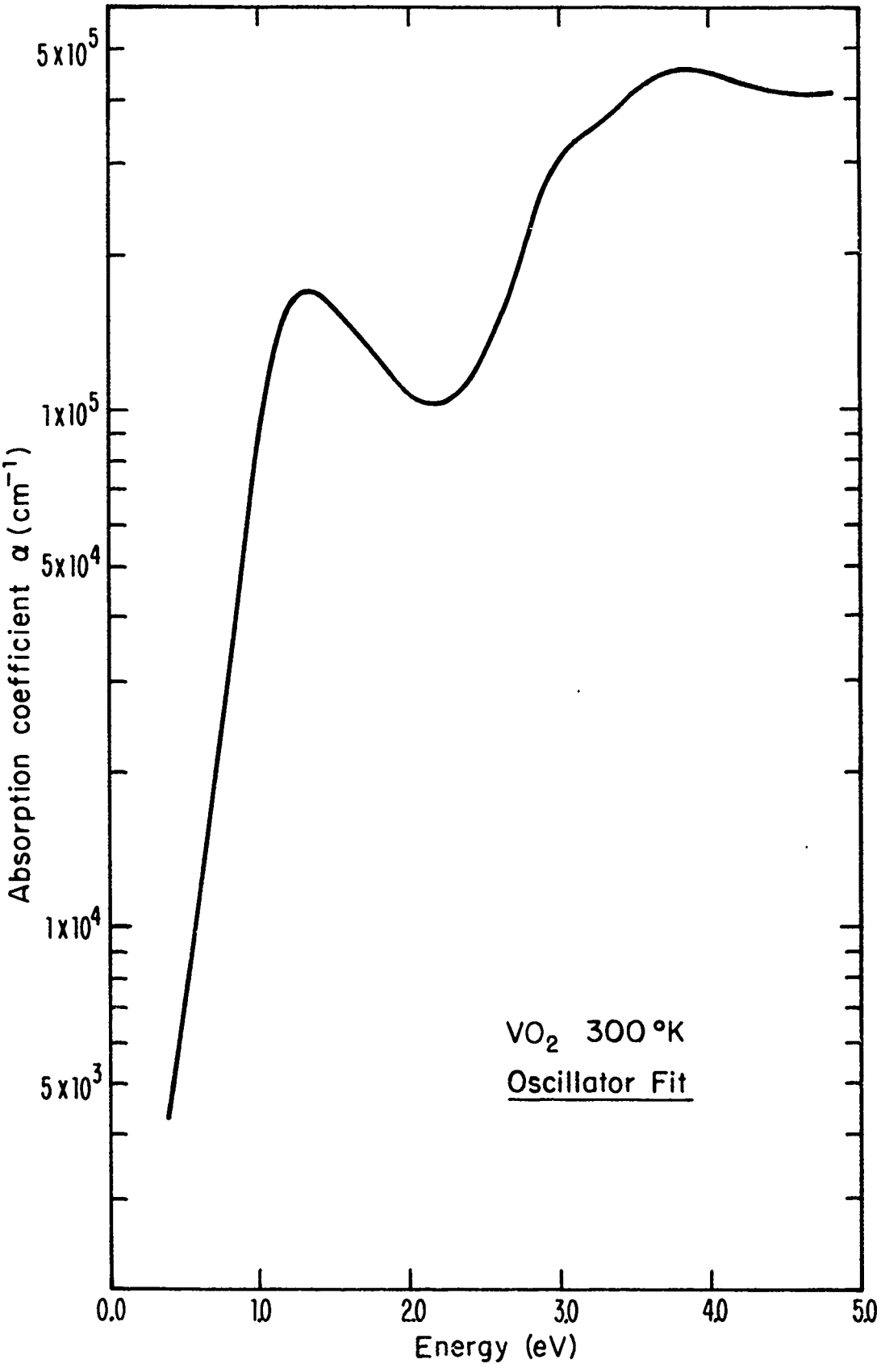

FIGURE IV-48 α curve of the VO_2 crystal obtained from the fit shown in Fig. IV-45.

248

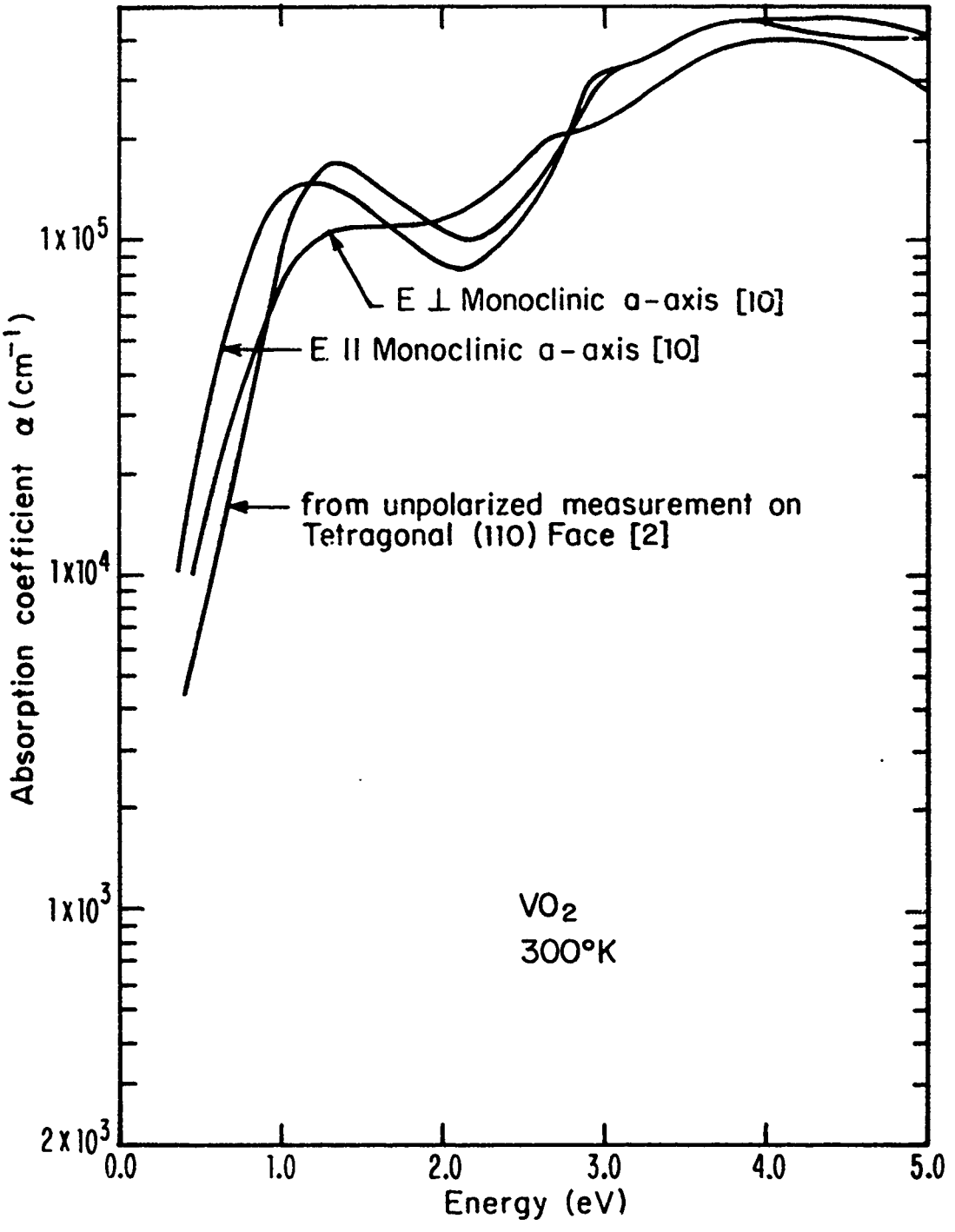

FIGURE IV-49 A comparison of the values of α obtained by fitting Ladd's data (2) with those reported by Barker et al. (10).

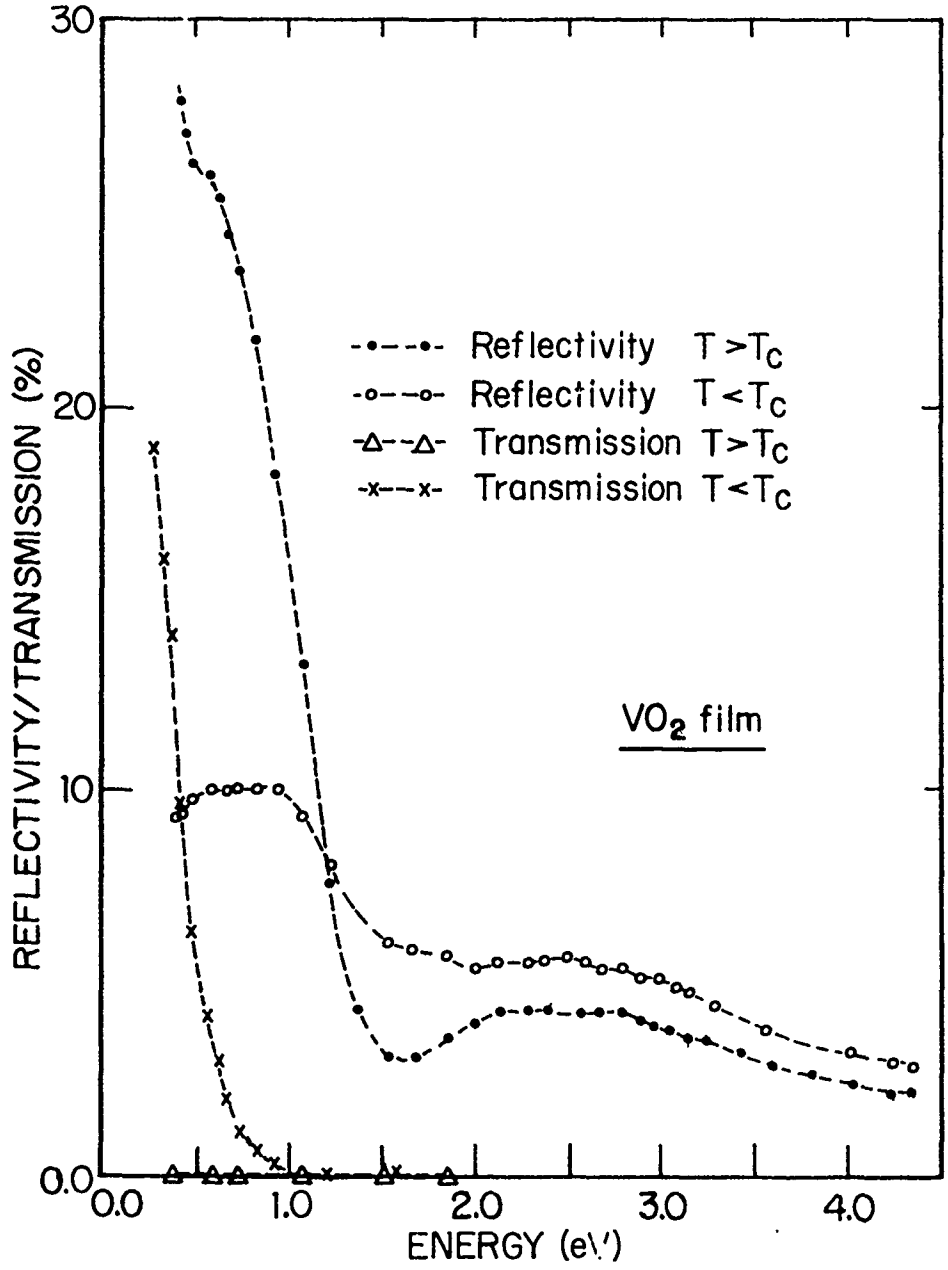

FIGURE IV-50 Apparent reflectivity and transmission of a VO_2 film grown by the vapor transport method, above (350°K) and below (300°K) the transition temperature.

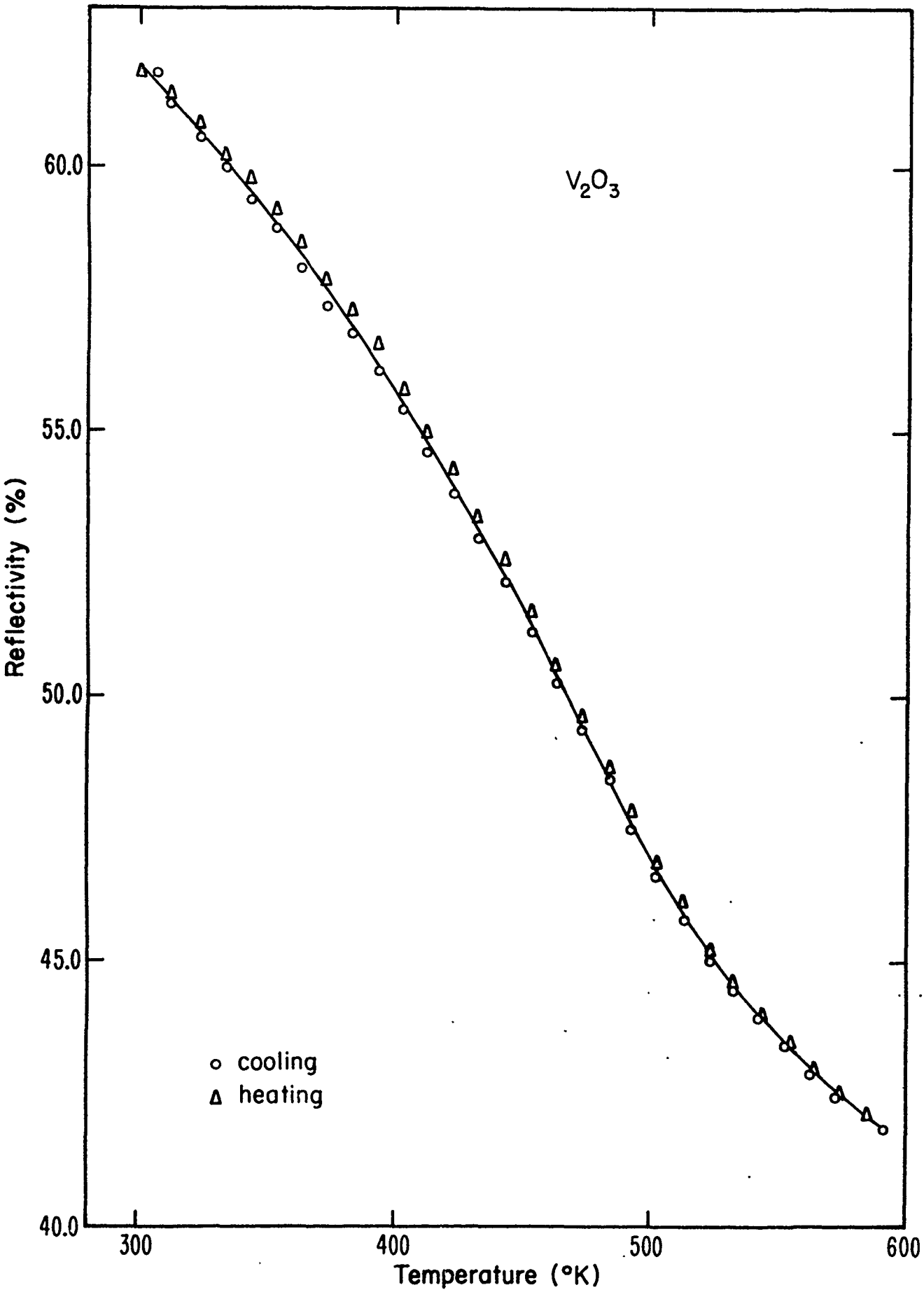

FIGURE IV-51 The reflectivity of a V_2O_3 crystal at 0.65 eV as a function of temperature.

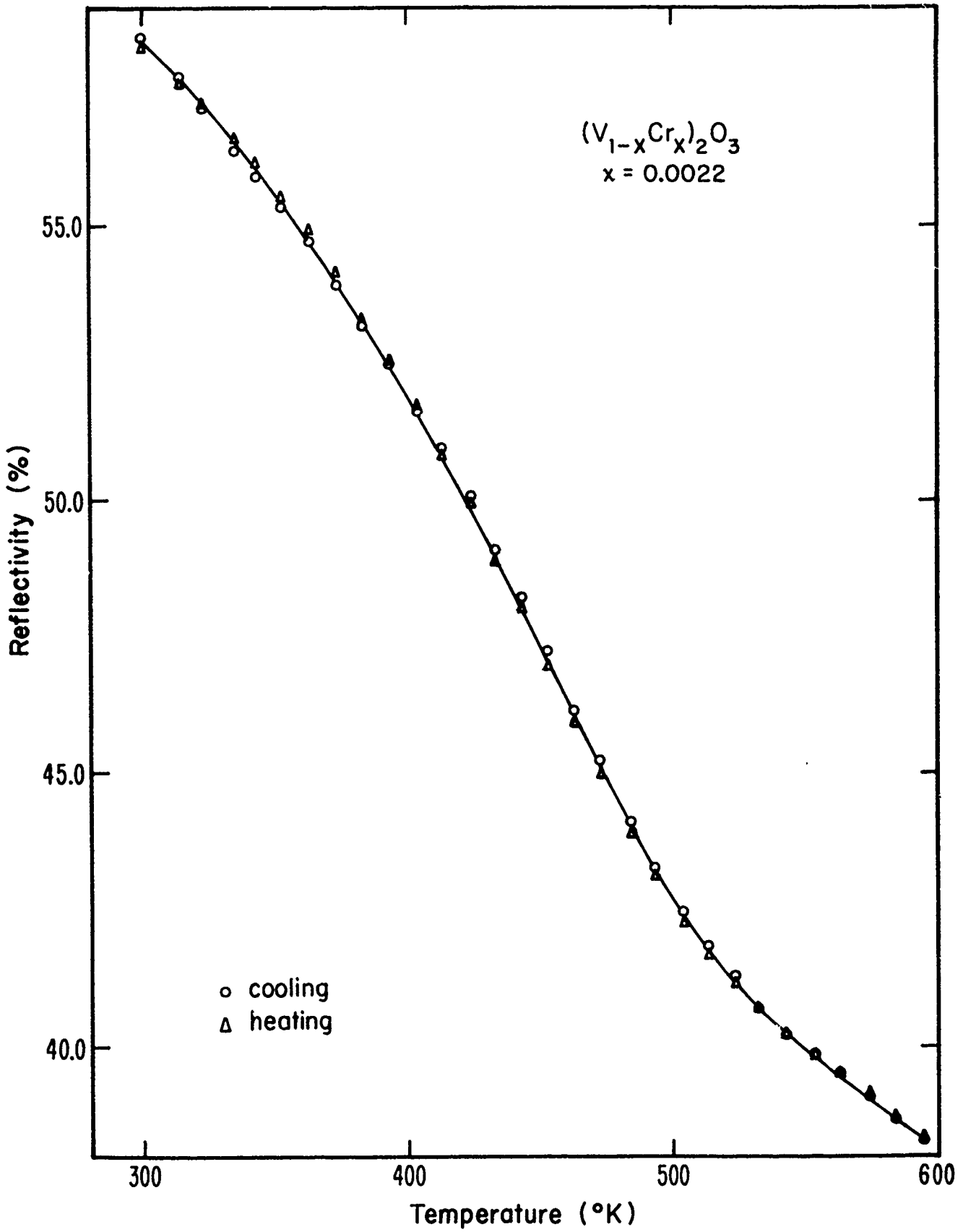

FIGURE IV-52 The reflectivity of a $(V_{1-x}Cr_x)_2O_3$ crystal (where x=0.0022) at 0.65eV as a function of temperature.

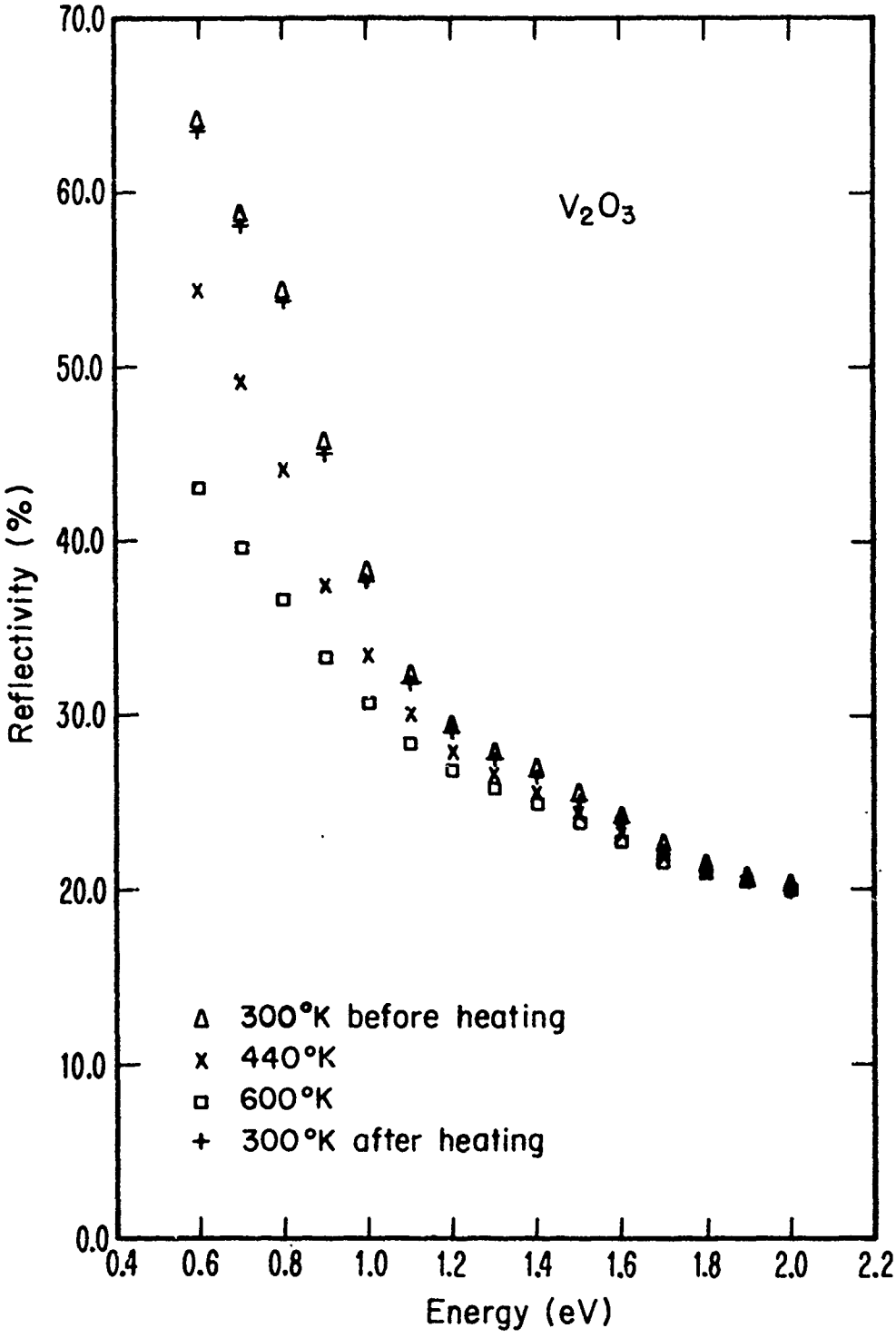

FIGURE IV-53 The reflectivity of a V_2O_3 crystal at different temperatures as a function of photon energy.

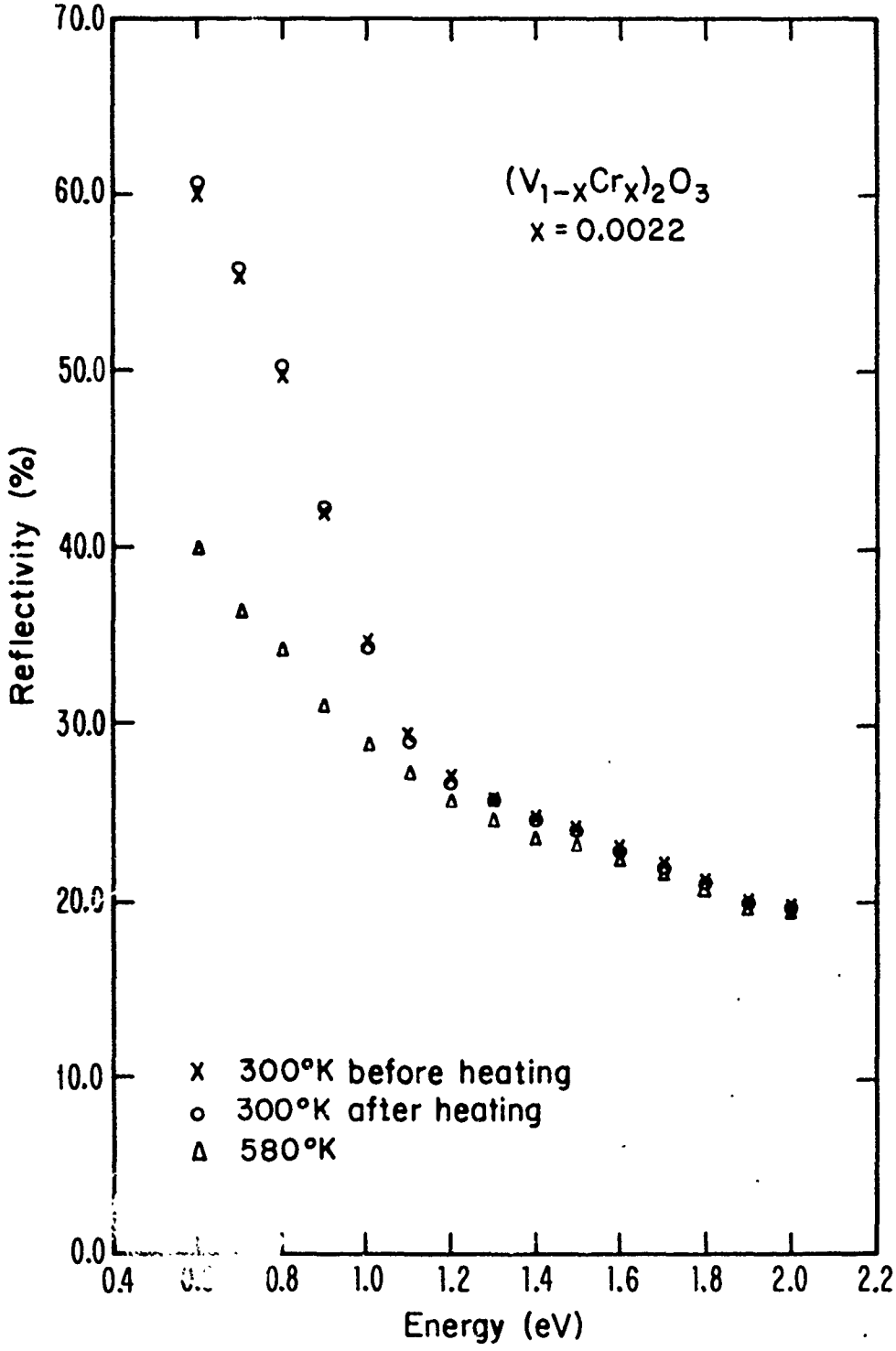

FIGURE IV-54 The reflectivity of a V_2O_3 crystal (where x=0.0022) at different temperatures as a function of photon energy.

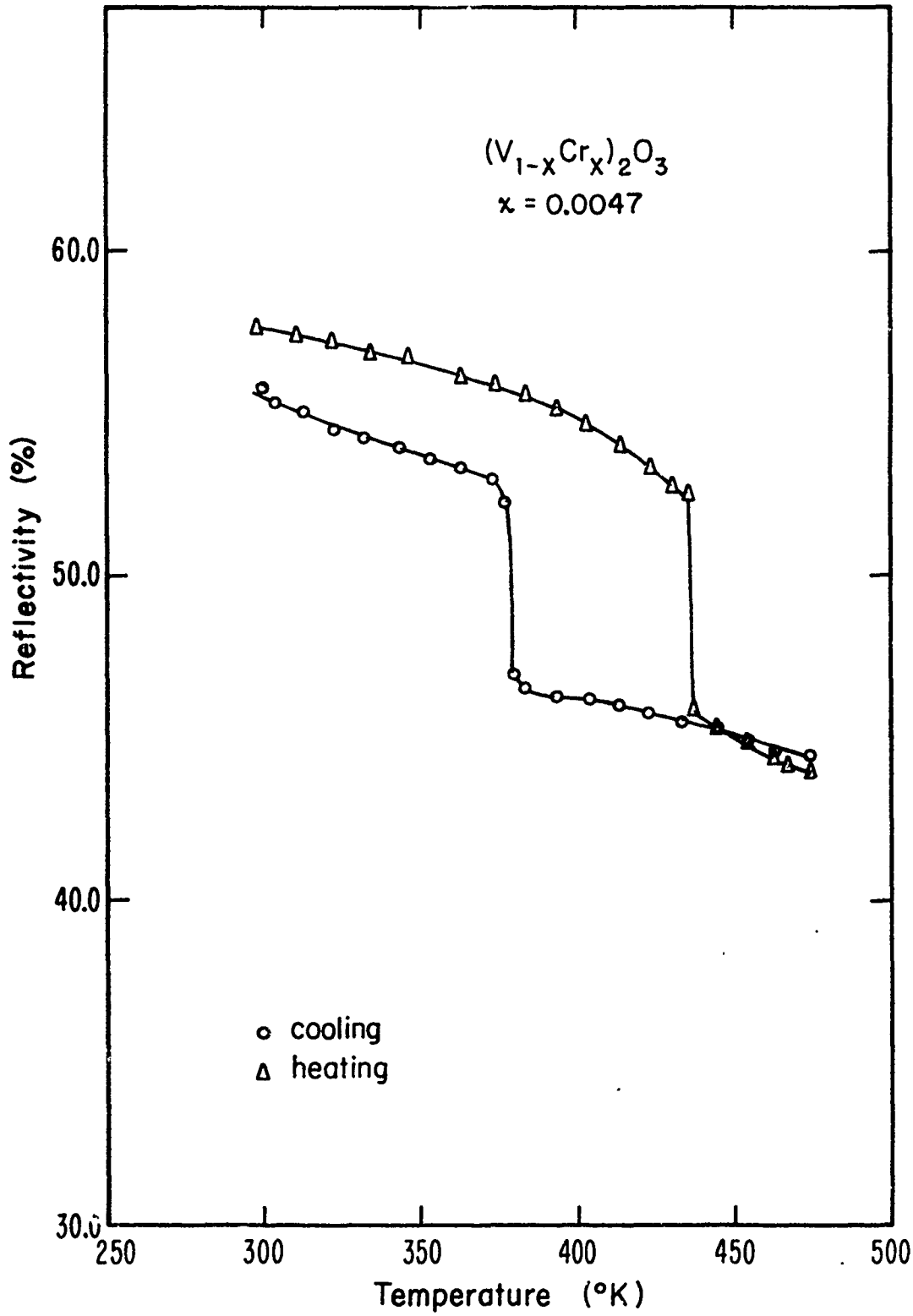

FIGURE IV-55 The reflectivity of a $(V_{1-x}Cr_x)_2O_3$ crystal (where x = 0.0047) at 0.65 eV as a function of temperature.

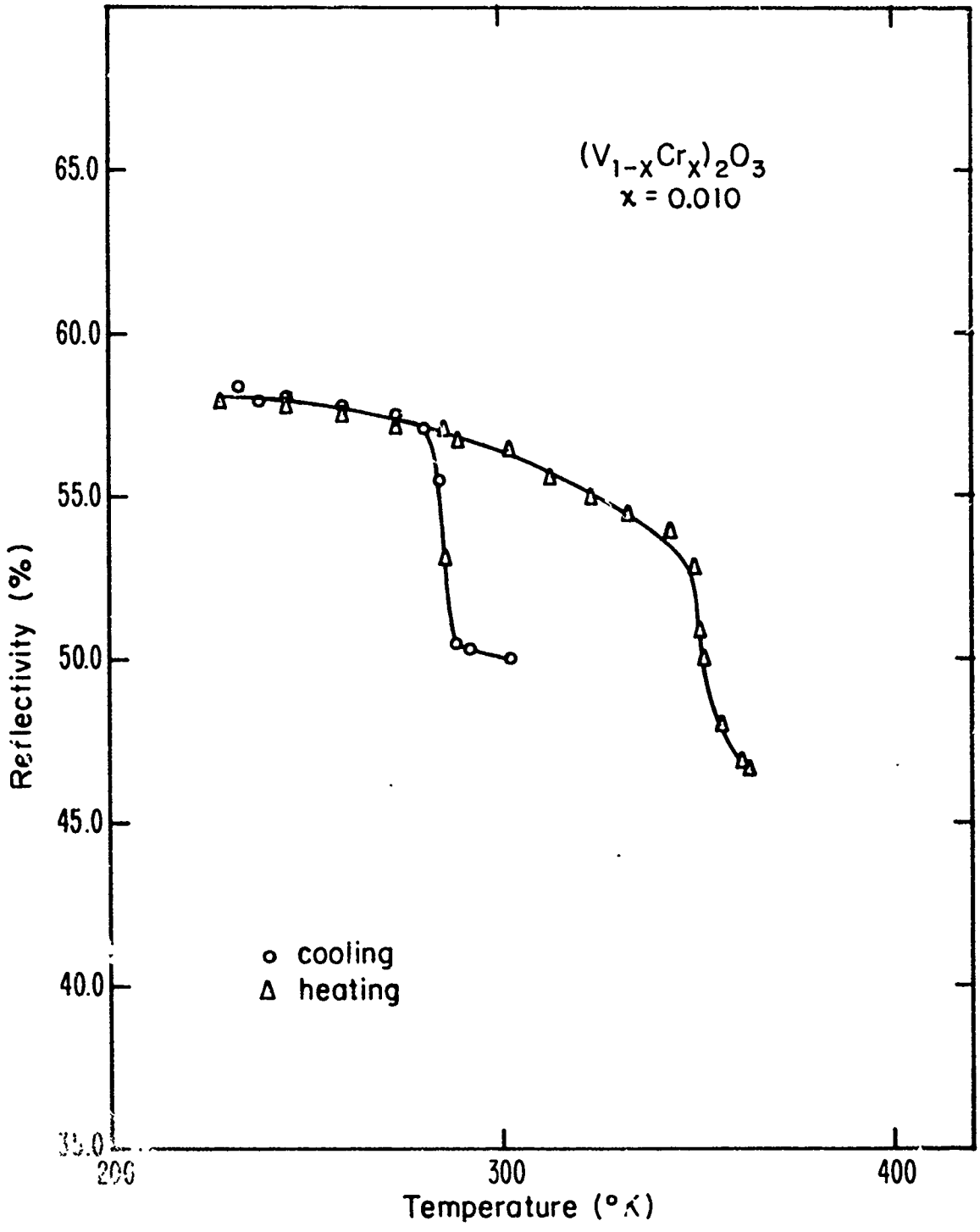

FIGURE IV-56 The reflectivity of a $(V_{1-x}Cr_x)_2O_3$ crystal (where x=0.010) at 0.65 eV as a function of temperatures.

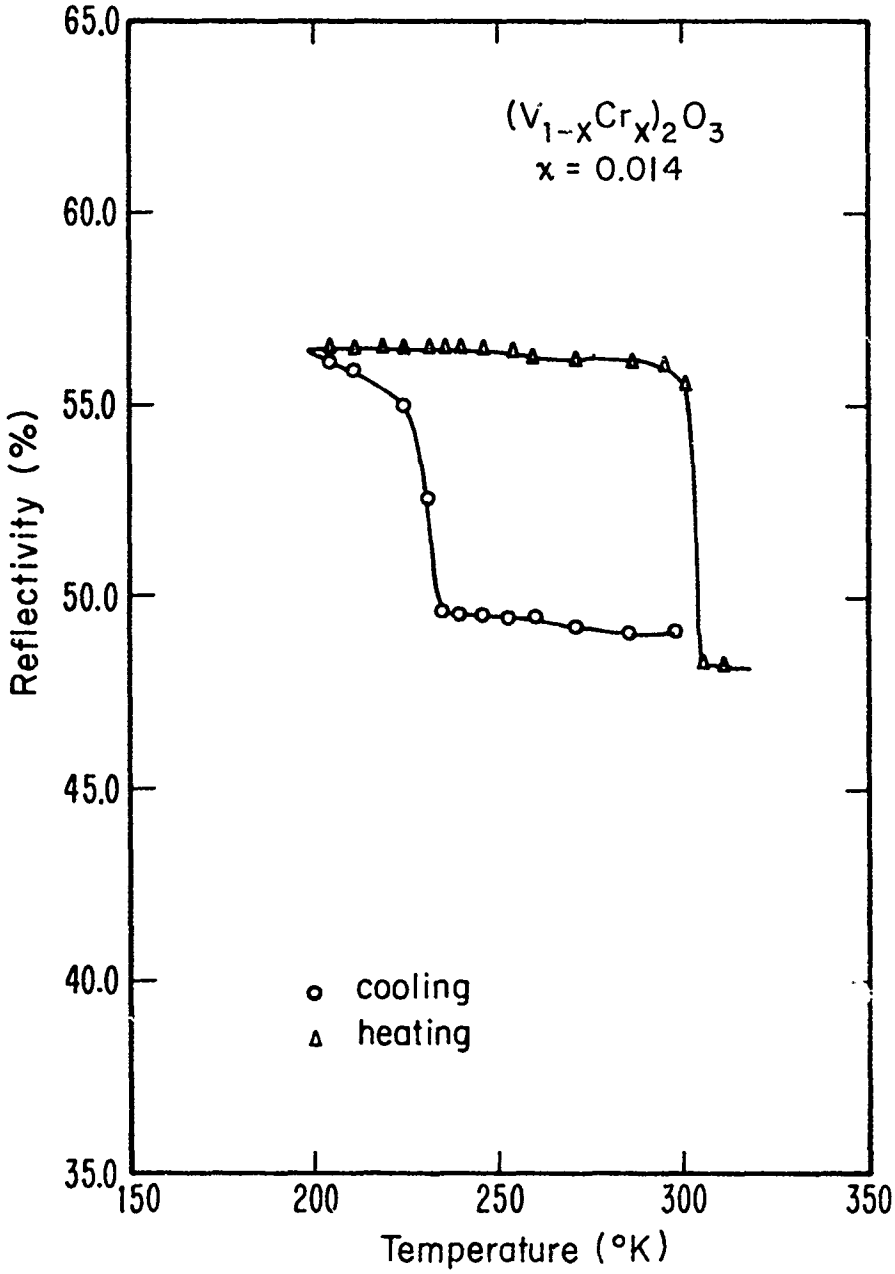

FIGURE IV-57 The reflectivity of a $(V_{1-x}Cr_x)_2O_3$ crystal (where x=0.014) at 0.65eV as a function of temperature.

257

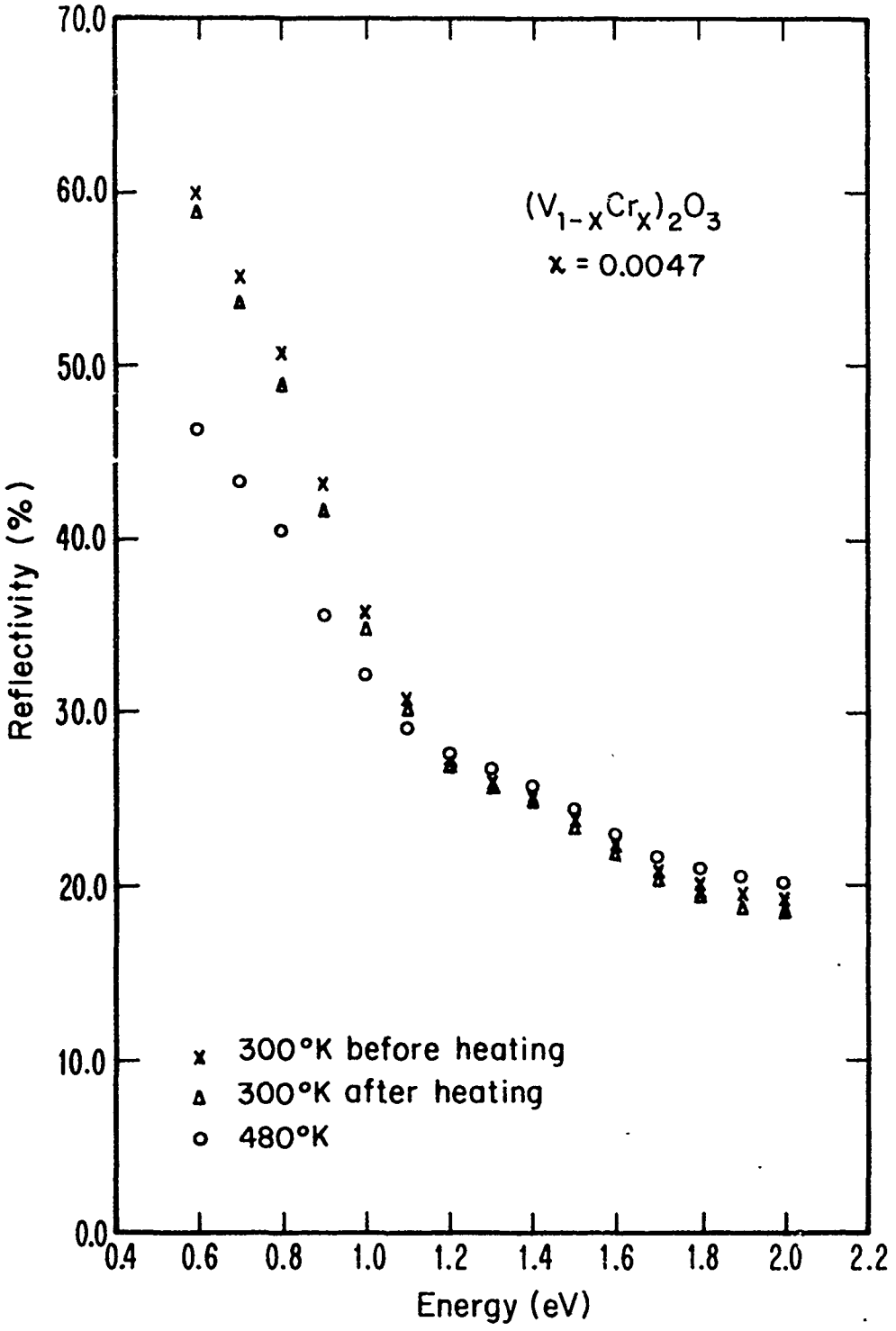

FIGURE IV-58 The reflectivity of a $(V_{1-x}Cr_x)_2O_3$ crystal (where x=0.0047) at different temperatures as a function of photon energy.

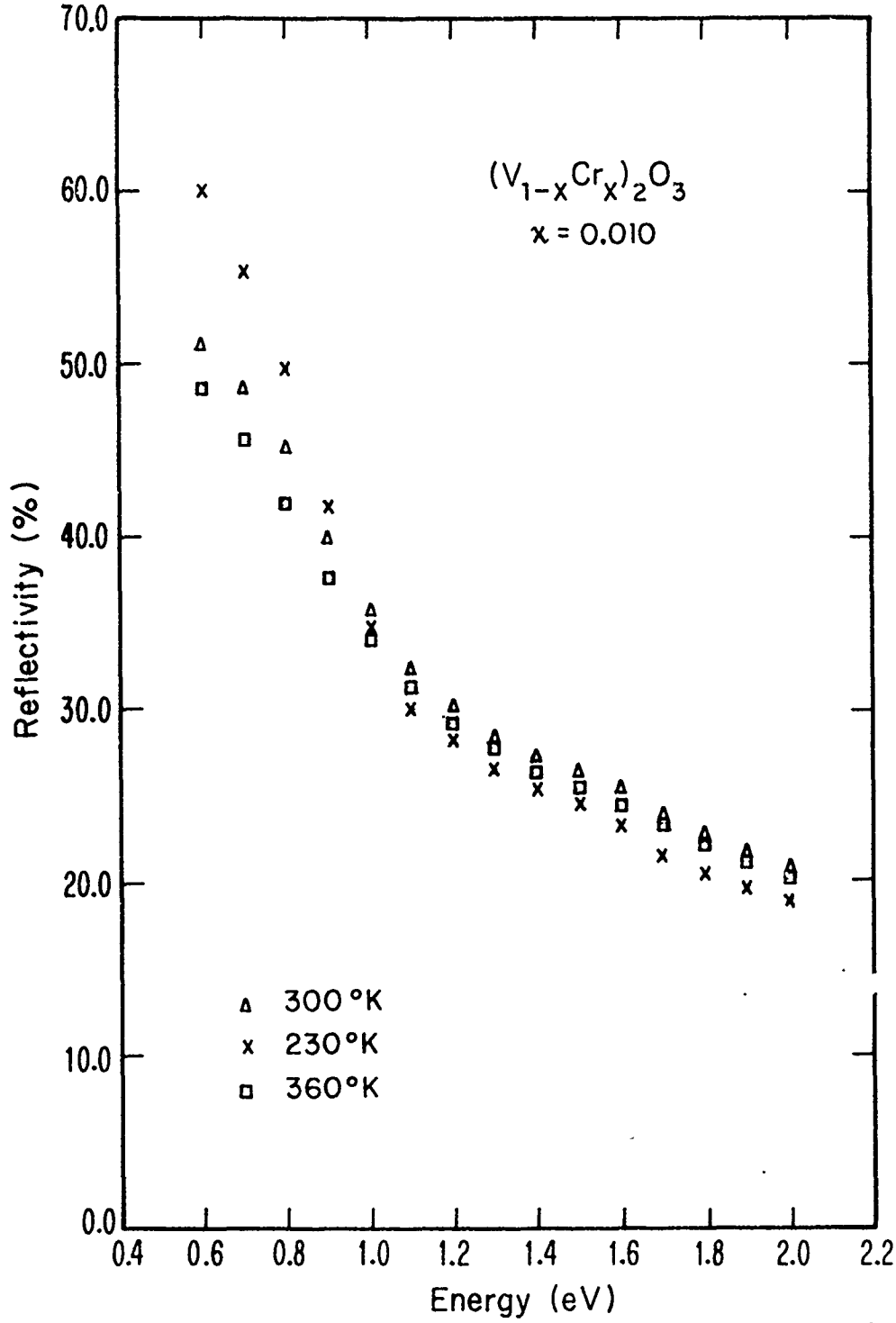

FIGURE IV-59 The reflectivity of a $(V_{1-x}Cr_x)_2O_3$ crystal (where x=0.010) at different temperatures as a function of photon energy.

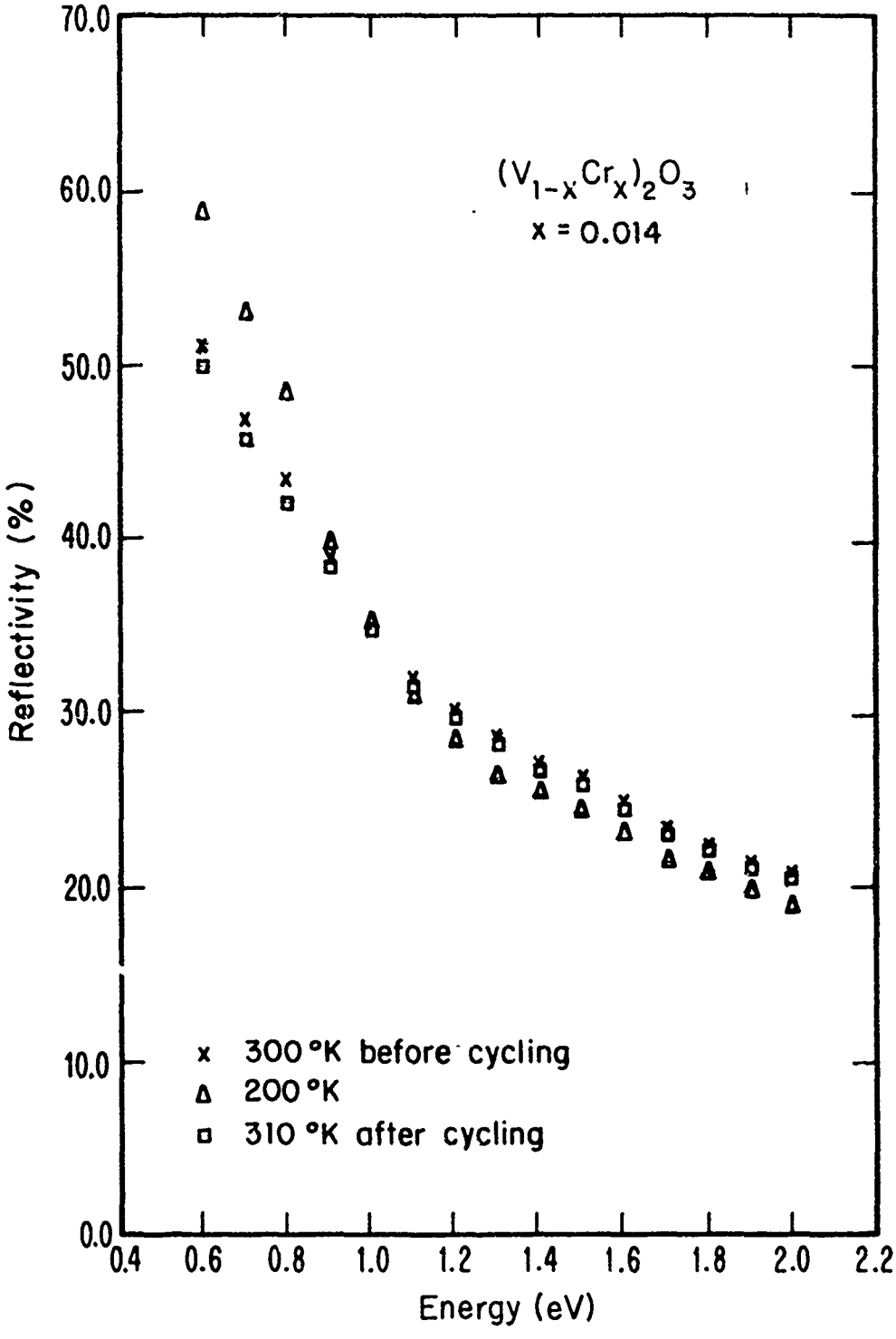

FIGURE IV-60 The reflectivity of a $(V_{1-x}Cr_x)_2O_3$ crystal where x=0.014) at different temperatures as a function of photon energy.

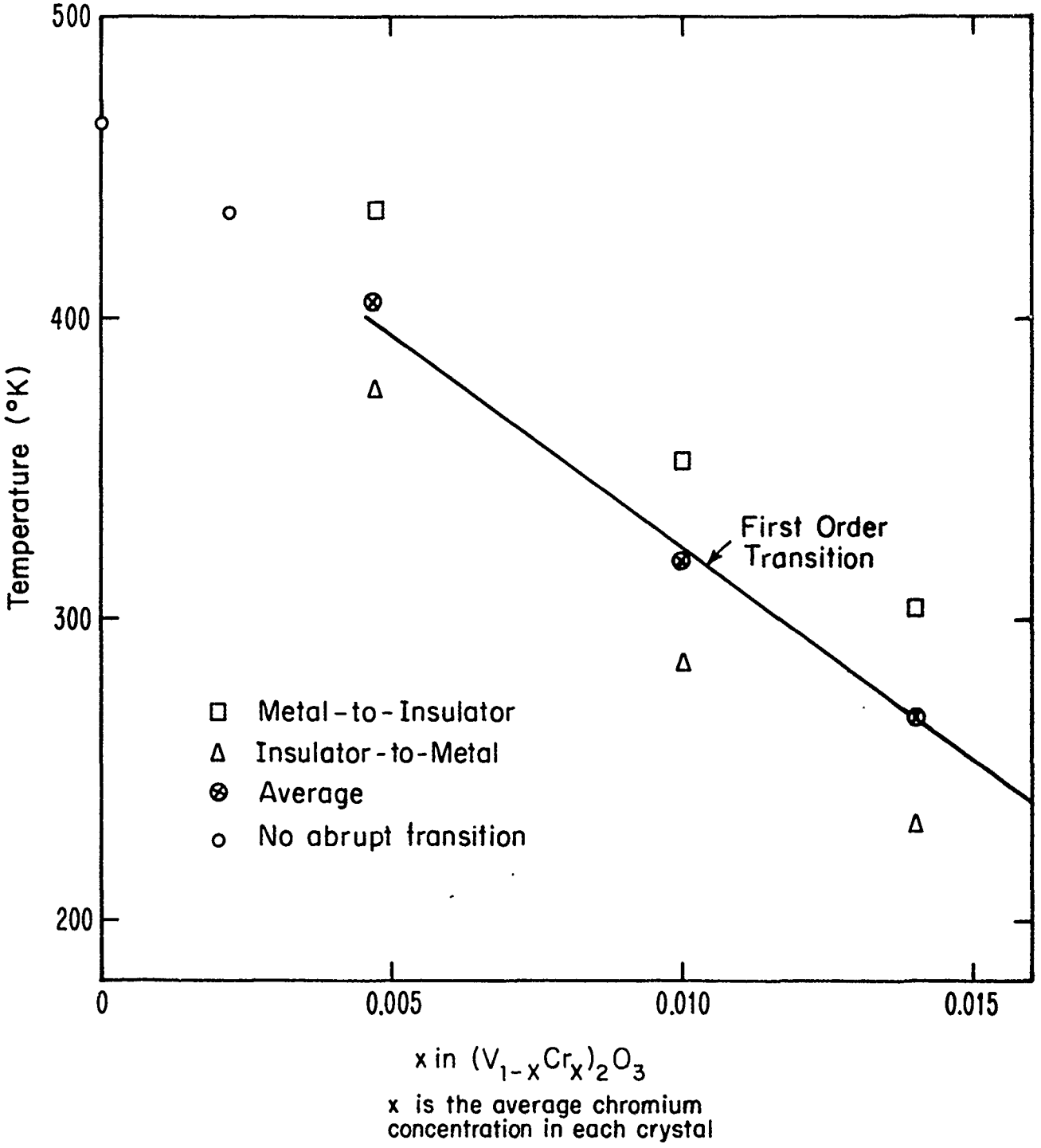

FIGURE IV-61 Transition temperatures observed in reflectivity measurements on $(V_{1-x}Cr_x)_2O_3$.

CHAPTER V

DISCUSSION AND CONCLUSIONS

Our investigation of both the methods of preparation and the properties of films and crystals of VO_2 and V_2O_3 and crystals of $(V_{1-x}Cr_x)_2O_3$ has been reported in Chapters II, III and IV. It has gained us new experimental results which have contributed to our understanding of the basic properties of these materials. In this chapter, we shall present a critical discussion of the implication of these results, especially those of our optical measurements.*

A. Discussion

1. Methods of Determining Optical Constants. In Chapters II and IV, we discussed the various methods of determining the optical constants of solids and presented our values of the constants of VO_2, V_2O_3 and $(V_{0.982}Cr_{0.018})_2O_3$ using these methods.

Among the methods used, the angular dependence method is apparently the most direct and accurate one for obtaining the optical constants of solids. It often proved difficult, however, to obtain a narrow collimated beam of sufficient intensity for our measurements on small crystals, unless a laser was used. Since we did not have lasers of wide spectral range at our disposal, this method was necessarily limited to obtaining optical constants at only a few photon energies, in our case, at 1.96 eV and 2.54 eV.

*Since detailed discussion on our preparation of these materials has already been presented in Chapter II, we will not comment further on it here.

In our attempt to obtain optical constants over a wide spectral range, we used two indirect methods: Kramers-Kronig analysis and the oscillator fit method. To obtain accurate optical results using the former technique, we found that we required an independently accurate determination of the optical constants at a few wavelengths in the spectral range of interest which allowed us to choose the appropriate parameters for our extrapolation procedure. In the latter method, there are two possible approaches to derive the optical constants from the reflectivity spectra: 1) Eq. (3-21b), which was used where the calculated values of n and k at 1.96 eV and 2.54 eV were constrained to approach those obtained from the angular dependence measurements; and 2) Eq. (3-21a), which was used where there were no constraints on n and k at 1.96 eV and 2.54 eV.

From the results reported in Chapter IV, we note that the optical constants derived from these two approaches of the oscillator fit method, while they did have minor differences, were, in general, quite similar to each other, provided, of course, that an adequate fit between the calculated and experimental reflectivity data was obtained, and that there were no large errors in the near-normal incidence reflectivity measurements. The fact that the constants were similar suggests that the oscillator fit method is less sensitive to the extrapolation uncertainties than the Kramers-Kronig analysis. Therefore, in instances where we have no independent knowledge of some of the values of the optical constants in the spectral range of interest, the oscillator fit method is preferable to the Kramers-Kronig analysis. On the other hand, there

are some minor differences in the values of the optical constants obtained from the two approaches of the oscillator fit method. The values of n and k at 1.96 eV and 2.54 eV obtained using Eq. (3-21a) are not as close to those obtained by the angular dependence method as those obtained using Eq. (3-21b). Therefore, to obtain accurate values of optical constants, it appears the better approach is to use Eq. (3-21b), where the values of the optical constants at certain frequencies are constrained to approach those obtained by the angular dependence method.

We also obtained the parameters of the free electron contribution directly from the oscillator fit analysis, and from these parameters, in turn, we obtained a rough notion of the values of the optical effective mass and the optical mobility of the conduction electrons in the metallic states of both VO_2 and V_2O_3. These were reported in Chapter IV.

The oscillator fit method does have a drawback. Judging from our results, we found that some fine structures in the optical constants were not so apparent when they were derived by the oscillator fit method as when they were derived by the Kramers-Kronig analysis, mainly because of the difficulties in fitting fine structures in reflectivity spectra by the oscillator fit method.

Finally, one of the advantages of the oscillator fit method over the Kramers-Kronig analysis, and in fact one of our main reasons for studying the oscillator fit method in the first place, is that it can provide us with the optical constants of thin transparent crystals and films.

Unfortunately, we concluded from the structural and transport studies that our films were not of sufficient quality that the data from them warranted such analysis.

We conclude that the oscillator fit method and the Kramers-Kronig analysis have their respective advantages and disadvantages, but they may be used to complement each other in arriving at the optimum description of the optical parameters.

2. VO_2. The nature of the low temperature insulating and high temperature metallic states of VO_2 has been discussed in detail by many, among them Ladd (1), Paul (2), and Hearn (3) of our laboratory. We will not repeat their arguments here, but simply describe some features of the insulating and metallic states of VO_2, which may be derived from our optical measurements. The optical constants obtained from the reflectivity spectra by the oscillator fit method show that in the metallic state there is free electron absorption in the infrared wavelength region, and structure in ϵ_2 at about 0.7 eV, 2.9 eV and 3.5 eV. If we assume a one-band model and suppose that each vanadium ion contributes one conduction electron, then from the values of the parameters E_n and E_c (see Chapter IV) obtained by the oscillator fit method, an optical effective mass of the conduction electrons of $3.3m_e$ (where m_e = free electron mass) and an optical mobility of ~ 0.7 cm^2/V-sec is obtained. The effective mass is not very large, and thus indicates that the bandwidth of the conduction band is probably not very narrow. The optical

mobility is low and this suggests that electron correlation effects and/or electron phonon interaction may be present.*

In the low temperature insulating state, the free electron absorption is replaced by the appearance of an absorption edge for photon energies less than 1 eV. Structures in ϵ_2 were observed at about 1.1 eV, 3.0 eV and 3.6 eV. The Hall mobility in the insulating state is low (~ 0.5 cm^2/sec) (5, 6) and its value is about the same order of magnitude as the values of the Hall mobility and optical mobility of the

---

*This can be illustrated by the following order of magnitude calculation. If we were to take a one non-degenerate band model and apply the theory of a free Fermi Gas, then we would obtain (4):

$$v_F = \left(\frac{\hbar}{m^*}\right)(3\pi^2 n_c)^{1/3} = 0.34 \times 10^8 \text{ cm/sec.}$$

where

v_F = carrier velocity at the Fermi surface,
n_c = carrier concentration = 3.15×10^{22} cm^{-3} (see Chapter IV)
m^* = effective mass = $3.3 m_e$ (carrier effective mass assumed to be the same as the optical effective mass).

Then the mean free path $\ell_F = v_F \tau_F$, where τ_F = relaxation time of the carriers at the Fermi surface. If we assume $\tau_F = \tau_c = 1.4 \times 10^{-15}$ sec (see Chapter IV), then $\ell_F = 4.4$°A, which is the same order of magnitude as the lattice constant of VO_2, indicating that the effects of electron correlation and/or electron-phonon interaction are probably important. In the above calculation, we have also made an approximation that all the electrons at the Fermi surface have the same effective mass and relaxation time.

conduction electrons in the metallic state (see Chapter IV), indicating that there is most likely no large change in mobility at the phase transition and that the abrupt changes of resistivity are probably caused by a large change in the number of charge carriers.

It is not clear whether the insulating and metallic states can indeed be explained in terms of a conventional band model. Even if they could, unless we have a detailed band calculation of VO_2, which is still unavailable, it would be very difficult to assign the structures in ϵ_2 to any particular optical transitions. Nonetheless, we will go ahead and interpret the structures in a conventional band scheme, keeping in mind that the interpretation will necessarily be sketchy and tentative.

In $SrTiO_3$, each titanium is surrounded by an octahedral configuration of six oxygen ions. Kahn and Leyendecker (7) did the energy band calculation for $SrTiO_3$ and found that the valence bands were derived primarily from the oxygen 2p orbitals, separated by approximately 3 eV from the conduction bands which arose primarily from the titanium 3d orbitals. This calculated band structure has been found to be in reasonable agreement with experimental evidence (Schooley et al., 8). Furthermore, Cardona and Harbeke (9) measured the reflectivity of TiO_2 where as in $SrTiO_3$, each titanium ion is surrounded by a similar (though slightly distorted in TiO_2) octahedral arrangement of oxygen ions. They found an optical transition at around 3 eV which they ascribed to a transition from the oxygen 2p valence band to a 3d conduction band. Since VO_2 crystal

symmetry is tetragonal and is very similar to $SrTiO_3$ and TiO_2, we would expect the band scheme in VO_2 in its metallic state to be very similar to that of TiO_2 and $SrTiO_3$, that is the valence bands should be primarily from oxygen 2p orbitals and separated approximately 3 eV from the conduction bands arising primarily from the vanadium 3d orbitals. The structures in ϵ_2 at 2.9 eV and 3.5 eV are, therefore, probably due to transitions from the 2p valence bands to the 3d conduction bands. The structure at 0.7 eV is probably a transition between the d bands.

The metallic conductivity of this high temperature state can be explained in the following manner. In the VO_2 high temperature state, each unit cell of the crystal contains two vanadium ions. Since each vanadium ion has five 3d orbitals, we have ten 3d bands in the solid. If we assume that the 3d band with the lowest energy is separated from the other nine d bands, then this band will be completely filled by the two extra d electrons, one associated with each vanadium ion, and we should have insulating behavior. Instead, we have metallic properties, and this suggests that the bottom band probably overlaps with one or more of the nine remaining bands. The amount of overlap is not known. Verleur et al. (10) presented arguments similar to ours for the band model, and suggested that the overlap was probably small, based on the Hall electron concentration (2×10^{21} cm^{-3}) they obtained using a one-band model. The Hall data reported by Rosevear (11), where the Hall electron concentration (1.2×10^{23} cm^{-3}) is about four times the maximum number of carriers allowed, also suggests multi-band conduction, and [illegible]el

of overlapping bands is thus quite reasonable. The amount of overlap is, however, unknown, and the large differences in the values of Hall electron concentrations suggest that it would be risky to try to derive the amount of band overlap from the Hall data.

Below 67°C, the crystal structure changes from tetragonal to monoclinic symmetry, and VO_2 becomes insulating. The mechanism or mechanisms that cause this first order transition are still not clear, nor are our optical measurements capable of identifying them. However, in a simple band interpretation, we should expect the band structure of VO_2 in the monoclinic phase to be similar to that of the tetragonal phase, since the monoclinic phase is only a slight distortion of the tetragonal phase. Hence, we expect the energy separation between the oxygen 2p bands and the vanadium 3d bands to remain nearly the same, but doubling the size of a unit cell (in monoclinic symmetry) will double the number of bands. There are twenty 3d bands (many of them should be degenerate) made up of the five 3d orbitals of each of the four vanadium ions per unit cell. Since insulating behavior is observed, two of these bands must be completely filled and separated from the other eighteen bands by a finite energy gap. This band scheme is substantiated by our optical measurements. In the insulating state, the structures in ϵ_2 near 3.0 eV remain essentially the same as in the metallic state, as expected. There is, indeed, an absorption edge for photon energy less than 1 eV, indicating an energy gap. Assuming that the metallic properties of VO_2 are caused by band overlap, this energy gap may arise

in either of two ways: 1) the change in lattice spacings associated with the monoclinic distortion may change the band structure in such a way as to remove the band overlap; and 2) whether or not the band overlap is removed by the change in lattice spacings, the reduced symmetry of the monoclinic crystal will open up new gaps in the energy vs wave vector curves. It is then conceivable that a discontinuity in the electrical resistivity can occur if the Fermi level lands in an absolute gap in the density of states versus energy curve. Whatever the reason, an absorption edge appears in the insulating state along with a sharp drop in conductivity. The above band model suggests that the change in conductivity should be primarily due to changes in the number of carriers with no large change in mobility across the phase transition, consistent with our finding that there is probably no large change of mobility across the phase transition. An interesting point about the absorption edge is that it is gradual and not as sharp as that in germanium and silicon. The absence of a definite threshold in the absorption coefficient α could be caused by several factors, such as non-stoichiometry or impurities. In summary, the optical properties of both the insulating and metallic states of VO_2 can be explained in terms of a conventional band picture, despite the fact that the effects of electron correlation and/or electron-phonon interaction may be important which may make interpretation in terms of a band picture not very appropriate.

3. V_2O_3. The general features of the optical reflectivity spectra of both the insulating and metallic states of V_2O_3 are quite similar to those of VO_2. Hence, in interpreting the spectra of V_2O_3, many of the arguments will be parallel to those for VO_2 presented above.

At room temperature, the reflectivity spectrum exhibits free electron absorption behavior. Using the oscillator fit method, we obtained values of the parameters E_n and Γ_c (see Chapter IV). By assuming that in a one-band model each vanadium ion contributes two conduction electrons, we obtained an optical effective mass of $9.1m_e$ and an optical mobility of $0.2 cm^2/V\text{-}sec$. The effective mass is not very large, indicating that the bandwidth of the conduction band is probably not very narrow. The low optical mobility may suggest that electron correlation and/or electron-phonon interaction effects are present.*

In the low temperature insulating state, the free electron absorption is replaced by the appearance of an absorption edge. The absorption coefficient α does not show any threshold; instead, it gradually

---

*As in VO_2, we performed the following order of magnitude calculation. Assuming a non-degenerate one band model,

$$v_F = \left(\frac{\hbar}{m^*}\right)(3\pi^2 n_c)^{1/3} = 1.7 \times 10^7 \text{ cm/sec}$$

where

v_F = carrier velocity at the Fermi surface,
n_c = carrier concentration = $2.84 \times 10^{22} cm^{-3}$,
m^* = optical effective mass = $9.1m_e$.

If we assume that $\tau_c = \tau_F = 9.8 \times 10^{-16}$ sec, then ℓ_F = mean free path of the conduction carriers at the Fermi surface, and $\ell_F = v_F \tau_F = 1.7$ Å. Despite the approximate nature of the calculation, the short mean free path does suggest that electron correlation effects and/or electron phonon interaction may be important.

decreases below 1.0 eV with a structure of $\sim$ 0.4 eV. The absence of a sharp absorption edge may be due to non-stoichiometry, sample impurities, etc. However, the absence of a sharp edge could very well be intrinsic, since this feature has been observed in films and crystals of both VO_2 and V_2O_3, prepared by various growth techniques.

The ϵ_2-vs-photon energy curves show structures at around 0.6 eV, 1.5 eV, 2.0-2.4 eV and 4.3 eV in the metallic state, and structures at around 0.4 eV, 0.9 eV, 1.5 eV, 2.0-2.4 eV and 4.3 eV in the insulating state. To interpret these structures in terms of band models would be very difficult since there has been no detailed band calculation of V_2O_3. Furthermore, our calculation of $\ell_F = 1.7$ Å suggests that effects of electron correlation and/or electron-phonon interaction may be important, and conventional band models may not be very appropriate in explaining the insulating and metallic states. Nevertheless, we will proceed to interpret the system in a conventional band scheme (a simple scheme, but the only one available), keeping in mind that such interpretation is by no means final.

In the metallic state, V_2O_3 has the corundum structure, and thus has four vanadium ions per unit cell. Since each vanadium ion has five 3d orbitals, we have twenty 3d bands in the solid. If we assume that the lowest four d bands are separated from the sixteen higher d bands, then the solid should be insulating since the four lowest d bands should be filled by eight extra d electrons, two associated with each vanadium ion. Instead, we have metallic conductivity, suggesting that the fourth

lowest band probably overlaps with one or more of the upper d bands. The amount of overlap is not known, but the fact that the Hall effect in the metallic state is positive suggests the existence of multi-band conduction. As in VO_2, oxygen 2p bands are below the 3d bands. In VO_2, the energy between the 2p bands and the lowest d band has been estimated to be ~ 3 eV. In V_2O_3, the Fermi level should be higher, since it is the fourth lowest d band that is supposed to overlap with the higher bands. The energy separation between the oxygen 2p bands and the Fermi level is therefore likely to be larger, and the structure in the ϵ_2 curve at 4.3 eV is assigned to this transition.

Ti_2O_3, like V_2O_3 at room temperature, has a corundum structure. Since it has only one outer d electron per titanium ion after all the bonding requirements are satisfied, we expect the two lowest d bands to be filled, and Ti_2O_3 should be insulating, which is indeed the case. Scouler and Raccah (12) measured the optical reflectivity of Ti_2O_3, and assigned the peak at 4.8 eV in the ϵ_2 curve to be from an optical transition from the oxygen 2p bands to an empty d band. It would, then, seem that, in V_2O_3, the energy separation between the 2p bands and the Fermi level should be larger than 4.3 eV. However, since vanadium is on the right of titanium in the periodic table, the vanadium ions will have larger ionic effective charges than the titanium ions; thus the 3d band should be closer to the 2p bands in V_2O_3 than in Ti_2O_3. Hence, we have two compensating effects in V_2O_3, and together with the possibility of difference in bandwidths in the 3d bands in V_2O_3 and Ti_2O_3, we feel our assignment is quite reasonable.

In the low temperature insulating state, V_2O_3 becomes insulating, and its crystal structure changes to monoclinic symmetry. The mechanism or mechanisms that cause this first order transition are still not clear, and our optical measurements cannot identify them. However, in a simple band interpretation, we expect the band structure of V_2O_3 in the monoclinic phase to be similar to that of the corundum phase since the monoclinic phase is only a slight distortion of the corundum phase. Hence, we expect the energy separation between the oxygen 2p bands and the vanadium 3d bands to remain nearly the same. Unlike VO_2, in the low temperature monoclinic phase, the number of vanadium ions per unit cell remains the same as in the corundum phase (four). Therefore, we still have twenty bands, many of them degenerate, made up of the 3d orbitals of each of the four vanadium ions per unit cell. Since insulating behavior is observed, four of these bands must be completely filled and separated from the other sixteen bands by a finite energy gap. This simple band scheme is consistent with our optical measurements. In the insulating state, the structures in ϵ_2 near 4.3 eV remains essentially the same as in the metallic state. There is, indeed, an absorption edge for photon energy less then 1 eV, indicating an energy gap. Since this energy gap is not sharp and there is an additional structure near about 0.4 eV, the exact assignment of the energy gap is difficult. The cause of this energy gap is also not clear; as discussed earlier in the case of VO_2, the energy gap observed in our optical measurements could arise in several ways: 1) the change in lattice spacings associated with the

monoclinic distortion may remove the band overlap, or 2) the reduced symmetry of the monoclinic crystal (the weak antiferromagnetism in the insulating states of V_2O_3 further reduces the symmetry) will open up new energy gaps in the energy vs wavevector curves. If the Fermi level lands in an absolute gap in the density of states vs energy curve, we can have a discontinuity in the electrical resistivity and an absorption edge in our optical measurements. For whatever reason, an absorption edge appears in the low temperature state along with a sharp drop in conductivity.

4. $(V_{0.982}Cr_{0.018})_2O_3$. The reflectivity spectrum of the $(V_{0.982}Cr_{0.018})_2O_3$ crystal at room temperature is very interesting. The structures in the ϵ_2 curve appear at about the same energies as in the metallic state of V_2O_3. McWhan, Remeika et al. (11, 12) suggested that the transition from a metal to an insulator on temperature increase might be of the Mott type, that is, the paramagnetic insulating state might be a Mott insulator where the electrons are localized. According to the phase diagram (13) shown in Chapter I, the $(V_{0.982}Cr_{0.018})_2O_3$ crystal should be in the paramagnetic insulating state at the temperature of our measurement (300°K). Thus, although the details of the reflectivity spectrum of a Mott insulator have not been worked out, it would appear that the density-of-states structure and the matrix elements for the optical transitions would — if the original assertion of McWhan et al. is correct, and in view of our results — have to remain essentially unaffected by the electronic correlations.

However, judging from the optical data above, it seems that the metal to insulator transition in a chromium doped crystal with increasing temperature could well be explained by a conventional band model. The rationale that, in V_2O_3, the metallic conductivity is probably the result of band overlap can also be applied to the explanation of the metallic state of a doped crystal. At the transition, the crystal becomes insulating and undergoes a volume change — a decrease of $\sim 2\%$ in volume. Tho gh the symmetry of the crystal remains the same, viz., corundum, the change of volume could very well remove the band overlap and result in the insulating properties. By this argument, we do not have to invoke the Mott theory. Furthermore, the above argument suggests that the optical properties of the insulating state are probably similar to those of the metallic state of V_2O_3 in the visible and ultraviolet regions, and further suggests that there should be an appearance of an absorption edge. Our optical measurements, reported earlier, did show, of course, that the optical properties of $(V_{0.982}Cr_{0.018})_2O_3$ in its paramagnetic insulating state were similar to those of the metallic state of V_2O_3, and that an absorption edge did appear in the insulating state of $(V_{0.982}Cr_{0.018})_2O_3$ for photon energy less than 1.0 eV. The absorption edge, as in the low temperature insulating state of V_2O_3 and VO_2, is gradual and not as sharp as in silicon and germanium. In summary, the optical properties of $(V_{0.982}Cr_{0.018})_2O_3$ in its insulating state can be explained in terms of a conventional band model, where the band structure is similar to that of the metallic state of V_2O_3, except in the former case, there is an

absorption edge in the infrared wavelength region. This absorption edge may be due to a removal of band overlap at the prescribed Mott transition. This is not to say that the insulating state of $(V_{0.982}Cr_{(.018)_2}O_3$ is not due to a highly correlated electron gas, only that our optical measurements do not require that explanation.

5. $(V_{1-x}Cr_x)_2O_3$. Our optical reflectivity studies confirmed the existence of two types of phase transition in the $(V_{1-x}Cr_x)_2O_3$ system: a first order transition and a higher order transition. We also noted sharp changes in reflectivity at the first order phase transition with large hysteresis (see Chapter IV). It is interesting that the first order transition from a metallic to an insulating state with increasing temperature occurs for x between about 0.005 and 0.015, the same region where there is the coexistence of both the metallic and insulating phases at room temperature.* A crystal with a chromium concentration in the aforesaid region will then have both insulating and metallic phases at room temperature. If the insulating phase is in the Mott insulating state, then the electrons in this phase should essentially be localized. The electrons in the metallic phase should, however, be itinerant, and they can conceivably go into the insulating phase, effectively screen out the excitons associated with the Mott insulating phase, and cause the insulating phase to go into the metallic phase. If the chromium doping concentration is evenly distributed across such a crystal, it would be difficult to imagine how such a coexistence of two phases could occur.

*This was confirmed by our x-ray diffraction measurements, reported in Chapter II.

Actually, if the insulating state is a Mott insulating state, in accordance with our above arguments, a coexistence of two phases would still be hard to explain, even if the chromium concentration is not evenly distributed. The actual distribution of the metallic and insulating phases and the local chromium concentration fluctuation, if any, in such a crystal are, however, not known, and experiments should be done to determine them. Experiments of this nature, more detailed suggestions of which will be presented later, can conceivably yield some insight into the nature of the transition.

6. Summary. Our optical studies show that the optical properties of VO_2, V_2O_3 and $(V_{1-x}Cr_x)_2O_3$ do not differ in nature from those of conventional solid state materials, and can be interpreted in terms of band models. Optical constants have been evaluated for these materials, all of which exhibited a gradual absorption edge in their insulating states. Approximate values of optical effective mass and optical mobility of the conduction electrons in the metallic states of V_2O_3 and VO_2 were obtained. The mean free paths of these conduction electrons have also been shown to be of the same order of magnitude as the lattice constants of the materials, indicating that perhaps electron correlation or polaron effects are important and that conventional band schemes may not be appropriate. Therefore, our explanation of the optical data in terms of a conventional band picture represents a simple, but the only available approach. Until detailed theoretical studies are done on these materials where effects of electron correlation and/or electron

phonon interaction may be important, further interpretation of the optical properties of such materials is difficult. Parallel to the need for theoretical studies is the need for experimental studies that will further increase our knowledge and understanding of the mechanism or mechanisms that cause the first order phase transitions in these materials.

B. Suggestions for Future Study

In our optical reflectivity studies, we noticed that there were no sharp structures in the optical spectra. Electroreflectance and electroabsorption in crystals and films of VO_2, V_2O_3 and $(V_{1-x}Cr_x)_2O_3$ might give us a better determination of the energy locations of the structures in the spectra.

Our measurements on the $(V_{0.982}Cr_{0.018})_2O_3$ in its paramagnetic insulating state indicated the optical properties of the state are similar to those of the metallic state of V_2O_3 in the visible and ultraviolet regions. Though we have not measured the optical properties of the metallic state of this doped crystal, we would expect that its optical properties should also be similar to those of the metallic state of V_2O_3. If the optical properties of the metallic and insulating states of this doped crystal are similar in the visible and ultraviolet regions, then the band structures of these two states on both sides of the prescribed Mott transition should be similar, which is consistent with the Mott theory. A Hall effect measurement on these two states would be very revealing. Let us assume that the metallic conductivity of this doped crystal is due to band overlap such that we have both electrons and holes at the Fermi level.

If the band structure does not change at the transition, and if the value of mobility of the electrons changes by about the same percentage as that of the mobility of the holes across the transition, then the Hall constant should remain the same across a Mott transition. The change in the Hall mobility will then be reflected in the change in electrical conductivity. The above argument rests on the fact that in a Mott transition, the charge carriers are itinerant in the metallic state and localized in the insulating state. Therefore, at the phase transition, the number of charge carriers should not change, but there will be a change of mobility, causing a change in electrical conductivity. Hence, if the Hall effect measurement shows a constant Hall coefficient across the transition, this will indicate the transition is consistent with the Mott mechanism. If, however, there is a change in Hall constant across the transition, then either of the following situations may have occurred; 1) the value of the mobility of the electrons changes by a different percentage from that of the mobility of the holes — the number of the respective charge carriers remains constant. In this case, the transition may still be a Mott transition, or 2) there is a change in the number of charge carriers at the transition and the phase transition is not a Mott transition. Though this Hall effect measurement is important, normally it is difficult to measure the change of mobility across the transition because of crystal cracking. However, we have a unique opportunity in the chromium doped crystals to measure the Hall mobility of the crystals in the ir - sulating state at room temperature, since at a properly selected doping

level, e.g., for x = 0.018, the crystal as grown is not cracked. A comparison of the value of the Hall mobility at room temperature of such a crystal with that of the Hall mobility at room temperature of V_2O_3, which should be very similar to that of the metallic state of such a crystal, but which as grown is not cracked at room temperature, should indicate whether there is a change in the Hall constant across the transition.

It has been suggested that the phase transition in VO_2 could be due to phonon softening in the crystal as it goes from its insulating to its metallic state (1, 2, 3). Velocity of sound, inelastic neutron diffraction and Raman scattering measurements on VO_2 might provide us with very useful information about the suggested effects. In fact Raman scattering studies on VO_2 have been done which show changes in the Raman modes across the phase transition (15), but these results are hard to interpret and further experiments need to be done. Similarly, Raman scattering, neutron scattering and velocity of sound experiments should be done on V_2O_3 and $(V_{1-x}Cr_x)_2O_3$ as phonon softening effects at the phase transitions in these materials could be very important.

We have discussed earlier that the metallic and insulating phases coexist for some chromium doping concentrations in the $(V_{1-x}Cr_x)_2O_3$ system. The coexistence of the two phases could be due to fluctuations of local chromium concentrations with separate regions of large and small chromium concentrations in such a crystal. X-ray small angle scattering experiments may be very useful in determining the the concentration and sizes of the separate regions, provided that the sizes of the separate regions are less than about 100 Å.*

*Small angle scattering experiments can only pick up fluctuations of sizes less than about 100 Å.

There is another experiment that should be done to examine further the nature of the postulated Mott transition in $(V_{1-x}Cr_x)_2O_3$ systems. As we have demonstrated in Chapter IV, crystals of $(V_{0.99}Cr_{0.01})_2O_3$ and $(V_{0.986}Cr_{0.014})_2O_3$ at room temperature are in their paramagnetic insulating state. When the temperature is raised above the room temperature, the reflectivity has been found to decrease slowly with increasing temperature. When the temperature is lowered from room temperature, the crystals undergo a phase transition from the insulating state to the metallic state at 280°K (for $(V_{0.99}Cr_{0.01})_2O_3$)and 232°K (for $(V_{0.986}Cr_{0.014})_2O_3$), with abrupt increases in reflectivity at 0.65 eV of about 7% (see Chapter IV). We are, therefore, presented with a unique opportunity to examine whether this particular transition is a thermal or an electronic one. Suppose at room temperature, an infrared laser, with photon energy at say ~ 0.65 eV, is incident on a crystal of chromium concentration $x \tilde{=} 0.010$, charge carriers would be excited in such a crystal, and if the insulating state at room temperature is indeed a Mott insulator, the newly generated carriers would start reducing the Coulomb attraction in the excitons, where the holes and electrons are bound together by the Coulomb interaction, until at a certain laser power (that is, at a certain carrier concentration), the excitons would break up and the insulator become metallic. The optical reflectivity should increase abruptly at the threshold laser power.*

*

N. B. The optical reflectivity can be monitored by another infrared laser or actually by the same laser that is used to excite the carriers.

The particular advantage of this system is that the heating effects of the laser could only cause the reflectivity to decrease. And a sudden increase in reflectivity of such a crystal with increasing laser power (as long as the surface of the crystal does not melt) cannot be due to thermal effects and necessarily has to be of an electronic nature. In contrast, in VO_2, an induced transition by laser power would not distinguish whether the transition is thermal or electronic in nature.* If we can indeed induce such an electronic transition in the abovementioned chromium doped crystal, we would be able to disprove all the theories that rely on thermal effects to explain the phase transition. It would still, however, be inadequate in proving that the transition is definitely a Mott transition, as other mechanisms such as the one suggested by Adler and Brooks (17), could have the same effect. Nevertheless, an electronic transition can have important device implications: the switching time of such a transition would be much faster than that of a thermal transition.

We have discussed in Chapter I that a Mott transition does not depend on crystal symmetry and thus may presumably occur in amorphous films. If any of the phase transitions in VO_2, V_2O_3 and $(V_{1-x}Cr_x)_2O_3$ are Mott transitions, then the amorphous films of such a material could still show the phase transition. Such an experiment has been done on amorphous films of VO_2 and V_2O_3 by Kennedy and Mackenzie (18) who found that the phase transitions of VO_2 and V_2O_3 were absent in the

*Such an experiment has been done on VO_2 and the phase transition induced by laser power (15).

amorphous films of these materials. Their experiments, however, were not very definitive, and further detailed studies must be done. In fact, there is yet another important experiment. Our experiments on sputtered V_2O_3 films showed that the films as grown did not exhibit the low temperature phase transition. After annealing, the phase transition occurred. Though this effect could be due to slight chemical changes that might occur during annealing, the possibility of effects of grain sizes on the nature of these phase transitions cannot be ignored. In fact, an interesting experiment would be to investigate just how the phase transitions in VO_2, V_2O_3, and $(V_{1-x}Cr_x)_2O_3$ are influenced by the grain sizes; such an experiment might reveal much information about the details of the mechanism or mechanisms of the phase transition.

Since Morin (19) focussed attention on the first order phase transition in crystals of VO_2 and V_2O_3, much intensive effort has been devoted, both experimentally and theoretically, to the understanding of these materials. We believe that the present work has contributed to the firm establishment of some of the optical parameters of these materials, and has also suggested useful approaches to a final resolution of the interesting problems involved.

REFERENCES

1. L. Ladd, Tech. Rept. No. HP-26, Gordon McKay Laboratory, Harvard University, 1971 (unpublished).

2. W. Paul, Mat. Res. Bull. 5, 691 (1970).

3. C.J. Hearn, to be published.

4. C. Kittel, "Introduction to Solid State Physics," 3rd Ed., p. 208, Wiley & Sons, 1966.

5. W. Rosevear and W. Paul, Bull. Am. Phys. Soc., Ser. II, 15, 316 (1970).

6. A.S. Barker, Jr., H.W. Verleur and H.J. Guggenheim, Phys. Rev. Lett. 17, 1286 (1966).

7. A.H. Kahn and A.J. Leyendecker, in Proceedings of the Seventh International Conference on Semiconductors, Paris, 1964, (Academic Press Inc., New York, 1964), p. 33.

8. J.F. Schooley, W.R. Hosler and M.L. Cohen, Phys. Rev. Lett. 12, 474 (1964).

9. M. Cardona and G. Harbeke, Phys. Rev. 137, A1467 (1965).

10. H.W. Verleur, A.S. Barker, Jr., and C.N. Berglund, Phys. Rev. 172, 172 (1968).

11. W. Rosevear and W. Paul, to be published.

12. W.J. Scouler and P.M. Raccah, Bull. Am. Phys. Soc., Ser. II, 15, 289 (1970).

13. D.B. McWhan and J.P. Remeika, Phys. Rev. B2, 3734 (1970).

14. A. Jayaraman, D.B. McWhan, J.P. Remeika and P.D. Dernier, Phys. Rev. B2, 3751 (1970).

15. Ramakant Srivastava and L.L. Chase, Phys. Rev. Lett. 27, 727 (1971).

16. W.R. Roach and I. Balberg, Solid State Comm. 9, 551 (1971).

17. D. Adler and H. Brooks, Phys. Rev. 155, 826 (1967).

18. T. N. Kennedy and J. D. Mackenzie, J. Non-Crystalline Solids, 1, 326 (1969).

19. R. J. Morin, Phys. Rev. Lett. 3, 34 (1959).

```
FORTRAN IV G LEVEL  20                MAIN              DATE = 72082        06/07/38            PAGE 0001

0001                IMPLICIT COMPLEX*16(F-G)
0002                DIMENSION U(300)
0003                DIMENSION E(300),R(300),THI(21),P(50),Y1(300),THA(300),
                   1          ON(300), OK(300),ALF(300),W(300),TRANS(300),
                   2          EO(300),ET(300)
0004                TH=5.5E-1
0005                ALF(1)=0.0
0006                L1=37
0007                L2=49
0008                EC(1)=0.0
0009                ET(1)=0.0
0010                CK(1)=0.0
0011                ON(1)=0.0
0012                TRANS(1)=0.0
0013                READ(5,1) D1
0014              1 FORMAT(E10.5)
0015                READ(5,2) E(1),R(1)
0016              2 FORMAT(2E10.5)
0017                DO 3 I=2,501
0018                READ(5,5) E(I), R(I)
0019              5 FORMAT(2E10.5)
0020                II=I-1
0021                IF (E(I) .EQ. -1.0) GO TO 7
0022                IF (D1 .EQ. 1.0) E(I)=1.23946/E(I)
0023              3 CONTINUE
0024              7 PMAX=R(I1)
0025                EMAX=E(I1)
0026                E(1)=0.0
0027                I2=I1-1
0028                DO 9 I=1,21
0029                READ(5,8) THI(I)
0030              8 FORMAT(E10.5)
0031                IF (THI(I) .EQ. -1.0) GO TO 10
0032              9 CONTINUE
0033             10 P(1)=1.0
0034                DO 200 I=2,40
0035            200 P(I)=P(I-1)+0.1
0036                PMAX=P(40)
0037                I4=1
0038             13 I3=0
0039             14 IF (P(I3) .EQ. PMAX) GO TO 45
0040                I3=I3+1
0041                WRITE(6,15) P(I3)
0042             15 FORMAT(1H1,5H P = , 1PE15.4///)
0043                WRITE(6,16)
0044             16 FORMAT(1H ,11H WAVELENGTH,2X,6HENERGY,1X,12HREFLECTIVITY,
                   1       4X,5HALPHA,6X,1HN,8X,1HK,8X,5HTHETA,8X,1HT,
                   2      10X,2HEO,8X,2HET,//)
0045                DO 42 J=2,500
0046                DO 21 I=1,500
0047                IF (E(I) .EQ. E(J)) GO TO 17
0048                Y1(I)=(ALOG(R(I))-ALOG(R(J)))/(E(J)**2-E(I)**2)
0049                GO TO 19
```

```
0050          17 Y1(I)=0.5*((ALOG(R(I-1))-ALOG(R(J)))/(E(J)**2-E(I-1)**2)
                1        +(ALOG(R(I+1))-ALOG(R(J)))/(E(J)**2-E(I+1)**2))
0051             Z1=Y1(J)
0052          19 IF (I .EQ. I1) GO TO 23
0053          21 CONTINUE
0054          23 DO 25 I=1,500
0055             Y1(I)=(Y1(I)+Y1(I+1))*(E(I+1)-E(I))*0.5
0056             IF (I .EQ. I2) GO TO 27
0057          25 CONTINUE
0058          27 THA(J)=0
0059             Y1(J-1)=Z1*(E(J)-E(J-1))
0060             Y1(J)=Z1*(E(J+1)-E(J))
0061             DO 29 I=1,500
0062             THA(J)=THA(J)+Y1(I)*E(J)/3.14159
0063             IF (I .EQ. I2) GO TO 31
0064          29 CONTINUE
0065          31 Y=ABS(EMAX-E(J))
0066             THA(J)=THA(J)+(1.0/6.2832)*ALOG(R(J)/RMAX)*ALOG((EMAX+E(J))/Y)
0067             Z=0.0
0068          32 DO 33 I=1,50
0069             Z=Z+1.0
0070             THA(J)=THA(J)+(P(I3)*((2.0*Z-1.0)**(-2))*(E(J)/EMAX)**(2*I-1))/
                1        3.14159
0071          33 CONTINUE
0072             ON(J)=(1.0-R(J))/(1.0+R(J)-2.0*SQRT(R(J))*COS(THA(J)))
0073             OK(J)=(2.0*SQRT(R(J))*SIN(THA(J)))/(1.0+R(J)-2.0*SQRT(R(J))*
                1       COS(THA(J)))
0074          41 IF (J .EQ. I2) GO TO 43
0075          42 CONTINUE
0076          43 IF ((0.95*THI(1)).LE.ON(L1).AND.ON(L1).LE.(1.05*THI(1))) GO TO
                147
0077             GO TO 14
0078          47 IF ((0.95*THI(2)).LE.OK(L1).AND.OK(L1).LE.(1.05*THI(2))) GO TO
                148
0079             GO TO 14
0080          48 IF ((0.95*THI(3)).LE.ON(L2).AND.ON(L2).LE.(1.05*THI(3))) GO TO
                149
0081             GO TO 14
0082          49 IF ((0.95*THI(4)).LE.OK(L2).AND.OK(L2).LE.(1.05*THI(4))) GO TO
                144
0083             GO TO 14
0084          44 DO 46 J=2,500
0085             W(J)=1.23946/E(J)
0086             ALF(J)=4.0*3.14159*OK(J)/W(J)
0087             U(J)=ATAN(2.0*OK(J)/((ON(J)*ON(J))+(OK(J)*OK(J))-1.0))
0088             TRANS(J)=(((1.0-R(J))**2)+(4.0*R(J)*SIN(U(J))*SIN(U(J))))*EXP(-
                1ALF(J)*TH)/(1.0-R(J)*R(J)*EXP(-2.0*ALF(J)*TH))
0089             EC(J)=ON(J)**2-OK(J)**2
0090             ET(J)=2*ON(J)*OK(J)
0091             I4=I4+1
0092             WRITE(6,35) W(J), E(J), R(J), ALF(J), ON(J), OK(J), THA(J),
                1            TRANS(J),EC(J), ET(J)
0093          35 FORMAT(1H ,1P10E10.2)
```

A-2

```
0094              IF (J.EQ.I2) GO TO 52
0095           46 CONTINUE
0096           52 CALL PRPLT(E,R,J)
0097              CALL PRPLT(E,ON,J)
0098              CALL PRPLT(E,CK,J)
0099              CALL PRPLT(E,EO,J)
0100              CALL PRPLT(E,ET,J)
0101              CALL PRPLT(E,TRANS,J)
0102              IF (I4.EQ.4) GO TO 45
0103              GO TO 14
0104           45 CALL EXIT
0105              END
```

```
FORTRAN IV G LEVEL  20                PRPLT              DATE = 72082          06/07/38              PAGE 0001

0001              SUBROUTINE PRPLT(X,Y,M)
0002              DIMENSION X(501), Y(501), YN(10), XN(10), LINE(101), ORD(6)
0003              REAL LINE
0004              DATA BLANK,XXX,PLUS,DOT,DASH/1H ,1HX,1H+,1H.,1H-/
0005              DATA MCNT/0/
0006              MCNT=MCNT+1
0007              IF (MCNT.EQ.8) MCNT=1
0008              YMIN=0.0
0009              YMAX=Y(1)
0010              XSTEP=X(2)-X(1)
0011              DO 2 I=2,M
0012              IF (Y(I) .GT. YMAX) YMAX=Y(I)
0013              IF (Y(I) .LT. YMIN) YMIN=Y(I)
0014              DELX=X(I)-X(I-1)
0015              IF (DELX .LT. XSTEP) XSTEP=DELX
0016            2 CONTINUE
0017              WRITE(6,106) MCNT
0018              WRITE(6,108) X(1), X(M), YMIN,YMAX
0019            4 YSCL=(YMAX-YMIN)/100.
0020              NLZ=ABS(YMIN)/YSCL+1.0
0021              IF (NLZ .EQ. 1) YMIN=0.0
0022           12 ORD(1)=YMIN
0023              DO 14 I=2,6
0024              A=I-1
0025           14 ORD(I)=YMIN+A*YSCL*20.0
0026              WRITE(6,100)
0027              WRITE(6,101) ORD
0028              N=0
0029              DO 30 J=1,10
0030              N=N+1
0031              LINE(N)=PLUS
0032              DO 30 I=1,9
0033              N=N+1
0034           30 LINE(N)=DOT
0035              LINE(101)=PLUS
0036              NYV=ABS(Y(1)-YMIN)/YSCL+1.0
0037              LINE(NYV)=XXX
0038              WRITE(6,102) X(1), LINE
0039              DO 36 I=1,101
0040           36 LINE(I)=BLANK
0041              LINE(NLZ)=DASH
0042              LINE(1)=DOT
0043              K=0
0044              NYV=1
0045              DO 40 I=2,M
0046              NLN=(X(I)-X(I-1))/XSTEP+0.5
0047              IF (NLN .LE. 1) GO TO 45
0048              NLN=NLN-1
0049              DO 42 J=1,NLN
0050              K=K+1
0051              IF (K .LT. 5) GO TO 41
0052              FAC=I+J
0053              XX=X(1)+FAC*XSTEP
```

```
0054              K=0
0055              WRITE (6,104) XX
0056              GO TO 42
0057           41 WRITE(6,102)
0058           42 CONTINUE
0059           45 K=K+1
0060              LINE(NYV)=BLANK
0061              LINE(NLZ)=DASH
0062              LINE(1)=DOT
0063              NYV=ABS(Y(I)-YMIN)/YSCL+1.0
0064              LINE(NYV)=XXX
0065              IF (K .LT. 5) GO TO 46
0066              K=0
0067              IF (NYV .NE. 1) LINE(1)=PLUS
0068              WRITE(6,103) X(I), LINE
0069              GO TO 40
0070           46 WRITE(6,105) LINE
0071           40 CONTINUE
0072              RETURN
0073          100 FORMAT(1H1,18X,'PLOT 1--R/ PLOT 2--ALPHA/ PLOT3--N/ PLOT 4--K/ ',
                 1       'PLOT 5--EO/ PLOT6--ET/  PLOT 7--TRANS')
0074          101 FORMAT(1HO,16X,E10.3,5(10X,E10.3),/)
0075          102 FORMAT(1H ,20X,1H.)
0076          103 FORMAT(1H ,8X,E10.3,2X,101A1)
0077          104 FORMAT(1H ,8X,E10.3,2X,1H+)
0078          105 FORMAT(1H ,20X,101A1)
0079          106 FORMAT(1H1,20(/),1HO,54X,'PLOT NO.',I3,/)
0080          108 FORMAT(1H ,20X,'DATA ON VARIABLES',/,1HO,25X,'XMIN = ',E15.8,/,
                 1       1H ,25X,'XMAX = ',E15.8,/1HO,25X,'YMIN = ',E15.8,/,1H ,
                 2       25X,'YMAX = ',E15.8)
0081              END
```

```
FORTRAN IV G LEVEL  20          MAIN            DATE = 72087      23/30/39          PAGE 0001

            C     THIS IS THE MAIN PROGRAM FOR PROVIDING THE NECESSARY DATA OF THE
            C     PARAMETER
0001              IMPLICIT COMPLEX*16(X-Z)
0002              EXTERNAL ORDER,CNTROD,SCHECK,SUBNAM
0003              DIMENSION W(130),WW(130),UU(130),U(130),VV(130),V(130)
0004              DIMENSION ALF(130)
0005              DIMENSION EO(130),ET(130)
0006              DIMENSION DLTVX(33,34),S(36),DCVX(33,36)
0007              COMMON U,UU,V,VV,W,WW,EO,ET,ALF
0008            4 FORMAT(F16.8)
0009            5 FORMAT(2E10.5)
0010          101 FORMAT(10I5)
0011          102 FORMAT(9E8.3)
0012          103 FORMAT(/16H EVALUATION NO =I5/)
0013          104 FORMAT(7E13.6)
0014          105 FORMAT(7E10.4)
0015          106 FORMAT (2X,6HENERGY,5X,5HEXP R/)
0016          107 FORMAT(20X,E18.9,5X,E18.9,5X,E18.9)
0017          108 FORMAT(9F7.3)
0018          109 FORMAT(15F5.2)
0019          110 FORMAT (/17HCONTROL VARIABLES/)
0020          304 FORMAT(/17X,6HENERGY,11X,5HEXP R,15X,6HTHEO R,14X,2HEO,18X,
                 12HET,18X,3HALF/)
0021          305 FORMAT(10X,E12.3,5X,E15.6,5X,E15.6,5X,E15.6,5X,E15.6,5X,E15.6)
0022              READ(5,101) NDIM,MAXNO,NDATA
0023              READ(5,105) ERROR,SUPLIM
0024              DO 300 I=1,NDIM
0025              DO 301 J=1,NDIM
0026          301 DLTVX(I,J)=0.0
0027          300 CONTINUE
0028              I=1
0029              J=1
0030          302 READ(5,5) DLTVX(I,J)
0031              I=I+1
0032              J=J+1
0033              IF(I-NDIM) 302,302,303
0034          303 IY=1
0035              DO 200 I=1,NDATA
0036              READ(5,5) W(I),U(I)
0037          200 CONTINUE
0038              WRITE (6,106)
0039              DO 201 I=1,NDATA
0040              WRITE (6,5) W(I),U(I)
0041          201 CONTINUE
0042           22 DO 111 I=1,NDIM
0043              READ (5,109) DCVX(I,1)
0044          111 CONTINUE
0045              WRITE (6,110)
0046              WRITE(6,101) NDIM,MAXNC,NDATA
0047              WRITE(6,104) ERROR,SUPLIM
0048              WRITE(6,102) (DCVX(I,1),I=1,NDIM)
0049              DO 203 J=1,NDIM
0050              WRITE(6,102) (DLTVX(I,J),I=1,NDIM)
```

```
0051          203 CONTINUE
0052              CALL JCFAN(NDIM,MAXNC,NDATA,ERROR,SUPLIM,DLTVX,DCVX,S,KK)
0053              WRITE(6,102) S(NDIM+2),(DCVX(I,NDIM+2),I=1,NDIM)
0054              NDIMM=NDIM+1
0055              WRITE(6,102) ((DCVX(I,J),I=1,NDIM),J=1,NDIMM)
0056              WRITE(6,102) (S(I),I=1,NDIMM)
0057              WRITE(6,103) KK
0058              WRITE (6,304)
0059              DO 33 I=1,NDATA
0060           33 WRITE(6,305) W(I),U(I),UU(I),EO(I),ET(I),ALF(I)
0061              IY=IY+1
0062              IF (IY-2) 22,43,43
0063           43 STOP
0064              END
```

```
0001            SUBROUTINE JCFAN(NDIM,MAXNO,NDATA,ERROR,SUPLIM,DLTVX,DCVX,S,KK)
0002            IMPLICIT COMPLEX*16(X-Z)
0003            DIMENSION W(130),WW(130),UU(130),U(130),VV(130),V(130)
0004            DIMENSION DLTVX(33,34),S(36),DCVX(33,36)
0005            DIMENSION C(34),CNTROX(33)
0006            DIMENSION ALF(130)
0007            DIMENSION EO(130),ET(130)
0008            COMMON U,UU,V,VV,W,WW,EO,ET,ALF
0009          111 FORMAT(/16H THIS IS SIMPLEX/)
0010          113 FORMAT(/16H ****WARNING****/)
0011          114 FORMAT(  50H INADEQUATE GIVEN MAX. NO FOR FUNCTION EVALUATION,)
0012          115 FORMAT(47H INCREASING THE MAXNO OR CHANGING THE STEP SIZE/)
              C     THIS IS THE SIMPLEX.
              C
0013            JMCHEN=1
0014            KCHEN=2
0015            ALPHO=1.0
0016            BETA=0.5
0017            GAMMA=2.0
0018            WRITE(6,111)
0019            GO TO 1
              C
              C     NO STATEMENTS FROM NOW ON CAN BE REMOVED EXCEPT YOU ARE CERTAINLY SURE
              C     WHAT TO DO.
              C
              C     SET UP THE INITIAL PATTERN
              C
              C     1) EVALUATION OF THE GIVEN INITIAL POINT
              C
0020          1 J=1
0021            KK=1
0022            CALL SUBNAM(NDIM,NDATA,J,SUPLIM,S,DCVX,KK)
0023            K=NDIM+JMCHEN
0024            KLT1=K-1
              C
              C     2) EVALUATION OF THE REMAINING POINTS OF THE INITIAL PATTERN
              C
0025            DO 3  J=2,K
0026            DO 2  I=1,NDIM
0027          2 DCVX(I,J)=DCVX(I,1)+DLTVX(I,J-1)
0028            CALL SUBNAM(NDIM,NDATA,J,SUPLIM,S,DCVX,KK)
0029          3 CONTINUE
0030          4 M=K
0031            ALPHA=ALPHO
              C
              C     ORDERING THE FUNCTION VALUES OF THE PATTERN
              C
0032            CALL ORDER(M,NDIM,S,DCVX)
              C
              C     DEFINING THE CENTROID TO OBTAIN THE FURTHER SEARCH
              C
0033            DO 5  I=1,KLT1
0034          5 C(I)=1.
```

```
0035              CALL CNTROD(NDIM,KLT1,C,CNTROX,DCVX)
                  C     REFLECTING OPERATION
                  C
                6 DO 7  I=1,NDIM
                7 DCVX(I,K+1)=CNTROX(I)+ALPHA*(CNTROX(I)-DCVX(I,K))
                  J=K+1
                  CALL SUBNAM(NDIM,NDATA,J,SUPLIM,S,DCVX,KK)
                  IF(KK-MAXNO) 9,9,36
                9 IF(S(K+1)-S(1))10,10,23
               10 DO 11 I=1,NDIM
               11 DCVX(I,K+2)=CNTROX(I)+GAMMA*(DCVX(I,K+1)-CNTROX(I))
                  J=K+2
                  CALL SUBNAM(NDIM,NDATA,J,SUPLIM,S,DCVX,KK)
                  IF(KK-MAXNO) 13,13,36
               13 IF(S(K+2)-S(1))14,14,21
               14 S(K)=S(K+2)
                  DO 15 L=1,NDIM
               15 DCVX(L,K)=DCVX(L,K+2)
                  GO TO 35
               21 S(K)=S(K+1)
                  DO 22 L=1,NDIM
               22 DCVX(L,K)=DCVX(L,K+1)
                  GO TO 35
               23 IF(S(K+1)-S(K-1))21,21,24
               24 IF(S(K+1)-S(K))25,25,27
               25 S(K)=S(K+1)
                  DO 26 I=1,NDIM
               26 DCVX(I,K)=DCVX(I,K+1)
                  C
                  C     CONTRACTING OPERATION
                  C
               27 DO 28 I=1,NDIM
               28 DCVX(I,K+1)=CNTROX(I)+BETA*(DCVX(I,K)-CNTROX(I))
                  J=K+1
                  CALL SUBNAM(NDIM,NDATA,J,SUPLIM,S,DCVX,KK)
                  IF(KK-MAXNO)29,29,36
               29 IF(S(K+1)-S(K))30,30,32
               30 S(K)=S(K+1)
                  DO 31 I=1,NDIM
               31 DCVX(I,K)=DCVX(I,K+1)
                  GO TO 35
                  C
                  C     SHRINKING THE PATTERN DUE TO A BAD CONTRACTION
                  C
               32 DO 34 J=2,K
                  DO 33 I=1,NDIM
               33 DCVX(I,J)=(DCVX(I,1)+DCVX(I,J))/2.
                  CALL SUBNAM(NDIM,NDATA,J,SUPLIM,S,DCVX,KK)
               34 CONTINUE
                  IF(KK-MAXNO)35,35,36
               35 CALL SCHECK(K,SUM,NDIM,S)
                  IF(SUM-ERROR)37,37,4
                  C     THE SEARCH IS INCOMPLETE ACCORDING TO THE GIVEN INADEQUATE MAXNO.
```

```
      C
0079     36 WRITE(6,113)
0080        WRITE(6,114)
0081        WRITE(6,115)
0082        GO TO 40
      C     THE SEARCH IS COMPLETED, RETURN TO THE MAIN PROGRAM AFTER EVALUATING
      C     THE CNTROD OF THE PATTERN.
0083     37 M=K
0084        CALL ORDER(M,NDIM,S,DCVX)
0085        DO 38 I=1,KLT1
0086     38 C(I)=1.
0087        CALL CNTROD(NDIM,KLT1,C,CNTROX,DCVX)
0088        DO 39 I=1,NDIM
0089     39 DCVX(I,K+1)=CNTROX(I)
0090        J=K+1
0091        CALL SUBNAM(NDIM,NDATA,J,SUPLIM,S,DCVX,KF)
0092     40 RETURN
0093        END
```

B-5

```
C
C     THIS SUBROUTINE SUBNAM SHOULD PROVIDED BY USER FOR OBTAINING THE
C
C     KCONT...A CONTROL NUMBER SET FOR OUTPUT. FOR EVERY KCONT NO. OF
C             FUNCTION EVALUATIONS THE COMPUTER WILL WRITE OUT THE DATA
C             ONCE.
C
C     ERR.....A FUNCTION VALUE SET FOR THE DATA TO BE WEITTEN OUT AS THE
C             COMPUTED FUNCTION VALUE DROPPED  A TENTH ORDER EACH TIME.
C     SOPT....THE BEST FUNCTION VALUE HAS BEEN FOUND AT EACH STAGE OF
C             COMPUTATION.
C
C     XOPT(I).THE CORRESPONDING ITH DECISION VARIABLE OF SOPT.
C
0001          SUBROUTINE SUBNAM(NDIM,NDATA,J,SUPLIM,S,DCVX,KK)
0002          IMPLICIT COMPLEX*16(X-Z)
0003          DIMENSION S(36),DCVX(33,36),X(33),XOPT(33)
0004          DIMENSION ZCT(130),ZCD(130),WO(130),WT(130),AOPT(130),Z4(130)
0005          DIMENSION Z5(130), Z6(130), ALF(130), TRANS(130), ON(130),OK(130)
0006          DIMENSION Z2(130),Z3(130), ZT(130),ZC(130),ZCO(130),Y(130)
0007          DIMENSION Z8(130)
0008          DIMENSION Z9(130)
0009          DIMENSION Z7(130)
0010          DIMENSION Z10(130)
0011          DIMENSION W(130),WW(130),UU(130),U(130),VV(130),V(130)
0012          DIMENSION WP(130),WR(130)
0013          DIMENSION EO(130),ET(130)
0014          DIMENSION WWW(130)
0015          COMMON U,UU,V,VV,W,WW,EC,ET,ALF
0016        1 FORMAT(31H THE OPTIMUN FUNCTION VALUE IS E13.6)
0017        2 FORMAT(6E13.6)
0018        3 FORMAT(10I4)
0019      107 FORMAT(10X,E12.3,5X,E15.6,5X,E15.6,5X,E15.6,5X,E15.6,5X,E15.6)
0020      303 FORMAT(/17X,6HENERGY,11X,5HEXP R,15X,6HTHEO R,14X,2HEO,18X,
             12HET,18X,3HALF/)
0021          AI=0.90
0022          AR=1.82
0023          BI=1.10
0024          BR=1.77
0025          I1=22
0026          I2=30
0027          IF(J-1)4,4,5
0028        4 KCONT=100
0029          ERR=10.
0030          GO TO 6
0031        5 KK=KK+1
0032          I=1
0033      300 IF(DCVX(I,J)-0.0) 16,16,301
0034      301 I=I+1
0035          IF(I-NDIM) 300,300,6
C
```

```
0036            6 DO 7  I=1,NDIM
0037              X(I)=DCVX(I,J)
0038            7 CONTINUE
0039              Z1=CMPLX(0.0,1.0)
0040              DO 200 I=1,NDATA
0041              Y(I)=W(I)
0042              Z2(I)=(X(2)*X(2))/(Y(I)*Y(I)+Z1*X(3)*Y(I))
0043              Z3(I)=X(4)/(1-(Y(I)*Y(I))/(X(5)*X(5))-((Z1*X(6)*Y(I))/X(5)))
0044              Z4(I)=X(7)/(1-((Y(I)*Y(I))/(X(8)*X(8)))-((Z1*X(9)*Y(I))/X(8)))
0045              Z5(I)=X(10)/(1-((Y(I)*Y(I))/(X(11)*X(11)))-((Z1*X(12)*Y(I))/X(11))
                 1)
0046              Z6(I)=X(13)/(1-((Y(I)*Y(I))/(X(14)*X(14)))-((Z1*X(15)*Y(I))/X(14))
                 1)
0047              Z7(I)=X(16)/(1-((Y(I)*Y(I))/(X(17)*X(17)))-((Z1*X(18)*Y(I))/X(17))
                 1)
0048              ZT(I)=X(1)-Z2(I)+Z3(I)+Z4(I)+Z5(I)+Z6(I)+Z7(I)
0049              SUM1=SUM1+(1.0-(U(I)/WW(I)))*(1.0-(U(I)/WW(I)))*1.0
0050              V(I)=REAL(ZT(I))
0051              VV(I)=AIMAG(ZT(I))
0052              ZC(I)=CDSQRT(ZT(I))
0053              WP(I)=AIMAG(ZC(I))
0054              WR(I)=REAL(ZC(I))
0055              ZCO(I)=ZC(I)-(1.0,0.0)
0056              ZCT(I)=ZC(I)+(1.0,0.0)
0057              ZCD(I)=ZCO(I)/ZCT(I)
0058              WO(I)=REAL(ZCD(I))
0059              WT(I)=AIMAG(ZCD(I))
0060              WWW(I)=1.24/W(I)
0061              ALF(I)=4.0*3.14159*WP(I)/WWW(I)
0062          200 WW(I)=WO(I)*WO(I)+WT(I)*WT(I)
0063              SUM1=0.0
0064              DO 201 I=1,NDATA
0065              SUM1=SUM1+(1.0-(U(I)/WW(I)))*(1.0-(U(I)/WW(I)))*4.0+(1.0-(AR/WR(I1
                 1)))*(1.0-(AR/WR(I1)))+(1.0-(AI/WP(I1)))*(1.0-(AI/WP(I1)))+(1.0-(BR
                2/WR(I2)))*(1.0-(BR/WR(I2)))+(1.0-(BI/WP(I2)))*(1.0-(BI/WP(I2)))
0066          201 CONTINUE
0067              T=SUM1
                C
                C     THE USER SHOULD PROVIDE A PART OF THIS SUBROUTINE FOR OBTAINING
                C     THE REQUIRED FUNCTION VALUE AT EACH VERTEX BETWEEN THIS COMMENT
                C     STATEMENT AND THE FOLLOWING STATEMENT IN WHICH T MEANS THE RE-
                C     QUIRED FUNCTION VALUE.
                C
                C
0068              S(J)=T
                C     STORAGE OF BETTER FUNCTION VALUE WITH THE CORRESPONDING INDEPEND-
                C     ENT AND DEPENDENT VARIABLES, IF NECESSARY.
0069              IF(J-1)9,9,11
0070            9 DO 10 I=1,NDIM
0071              ACPT(I)=REAL(X(I))
0072           10 CONTINUE
0073              DO 18 I=1,NDATA
0074              UU(I)=WW(I)
```

```
0075              EO(I)=V(I)
0076           18 ET(I)=VV(I)
0077              SOPT=T
0078              IF(J-1)102,102,12
0079           11 IF(S(1)-S(J))12,9,9
0080           12 IF(KK-5) 102,101,101
0081          101 IF(KK-KCONT) 14,13,13
0082           13 WRITE(6,1) SOPT
0083              WRITE(6,2) (AOPT(I),I=1,NDIM)
0084              WRITE(6,3) KK
0085              WRITE (6,303)
0086              DO 50 I=1,NDATA
0087           50 WRITE(6,107) W(I),U(I),UU(I),EO(I),ET(I),ALF(I)
0088              KCONT=KCONT+100
0089           14 IF (S(J)-ERR) 15,15,17
0090           15 WRITE (6,1) SOPT
0091              WRITE(6,2) (AOPT(I),I=1,NDIM)
0092              ERR=ERR*0.1
0093              GO TO 17
0094           16 S(J)=SUPLIM
0095              GO TO 17
0096          102 WRITE(6,1) SOPT
0097              WRITE(6,2) (AOPT(I),I=1,NDIM)
0098              WRITE (6,303)
0099              DO 19 I=1,NDATA
0100           19 WRITE(6,107) W(I),U(I),UU(I),EO(I),ET(I),ALF(I)
0101              WRITE (6,3) KK
0102           17 RETURN
0103              END
```

```
      C
      C
      C     THE SUBROUTINE FOR ORDERING THE FUNCTION VALUES OF THE PATTERN
      C
0001        SUBROUTINE ORDER(M,NDIM,S,DCVX)
0002        IMPLICIT COMPLEX*16(X-Z)
0003        DIMENSION W(130),WW(130),UU(130),U(130),VV(130),V(130)
0004        DIMENSION ALF(130)
0005        DIMENSION EO(130),ET(130)
0006        DIMENSION S(36),DCVX(33,36)
0007        COMMON U,UU,V,VV,W,WW,EO,ET,ALF
0008        K=M
0009        KLT1=K-1
0010        DO  5 I=1,KLT1
0011        M=M-1
0012        DO  4 J=1,M
0013        IF(S(M+1)-S(J))2,2,4
0014      2 A=S(M+1)
0015        S(M+1)=S(J)
0016        S(J)=A
0017        DO  3 L=1,NDIM
0018        B=DCVX(L,M+1)
0019        DCVX(L,M+1)=DCVX(L,J)
0020        DCVX(L,J)=B
0021      3 CONTINUE
0022      4 CONTINUE
0023      5 CONTINUE
0024        RETURN
0025        END
```

FORTRAN IV G LEVEL 20 MAIN DATE = 72082 23/30/39 PAGE 0001

```
      C
      C
      C     A NECESSARY PART OF THE WHOLE SEARCH DECK BUILT FOR OBTAINING THE
      C     CENTROID OF THE PATTERN EXCLUSIVE OF THE WORST POINT.
      C
0001        SUBROUTINE CNTROD(NDIM,KLT1,C,CNTROX,DCVX)
0002        IMPLICIT COMPLEX*16(X-Z)
0003        DIMENSION C(34),CNTROX(33),DCVX(33,36)
      C     SEARCHING FOR THE BETTER POINT OF THE SPACE
0004        DIMENSION W(130),WW(130),UU(130),U(130),VV(130),V(130)
0005        DIMENSION EO(130),ET(130)
0006        DIMENSION ALF(130)
0007        COMMON U,UU,V,VV,W,WW,EO,ET,ALF
0008        CSUM=0.
0009        DO 1  I=1,KLT1
0010      1 CSUM=CSUM+C(I)
0011        DC 3  I=1,NDIM
0012        AXIS=0.
0013        DO 2  J=1,KLT1
0014        CNTROX(I)=AXIS+C(J)*DCVX(I,J)
0015        AXIS=CNTROX(I)
0016      2 CONTINUE
0017        CNTROX(I)=CNTRCX(I)/CSUM
0018      3 CCNTINUE
0019        RETURN
0020        END
```

```
      C
      C     THE BUILT-IN SUBROUTINE FOR CHECKING WHETHER THE OPTIMUM POINT HAS
      C     BEEN ACHIEVED
      C     THE CRITERION USED IS SQRT(((AVG.(S)-S(J))**2/NDIM),J=1,K) .L.E.
      C     ERROR.
      C
0001        SUBROUTINE SCHECK(K,SUM,NDIM,S)
0002        IMPLICIT COMPLEX*16(X-Z)
0003        DIMENSION S(36)
0004        DIMENSION W(130),WW(130),UU(130),U(130),VV(130),V(130)
0005        DIMENSION EO(130),ET(130)
0006        DIMENSION ALF(130)
0007        COMMON U,UU,V,VV,W,WW,EO,ET,ALF
0008        SAVG=0.
0009        DO 1  L=1,K
0010      1 SAVG=S(L)+SAVG
0011        AK=K
0012        SAVG=SAVG/AK
0013        SUM=0.
0014        DO 2  L=1,K
0015      2 SUM=SUM+(S(L)-SAVG)*(S(L)-SAVG)
0016        ANDIM=NDIM
0017        SUM=SUM **0.5/ANDIM
0018        RETURN
0019        END
```

Director
Advanced Research Projects Agency
Attn: Technical Library
The Pentagon
Washington, D C 20301 [1]

(ARPA supported contractor
Advanced Research Projects Agency
Attn: Lt. Col. J. MacCallum
Lynn Building
Arlington, Virginia 20301 [1]

Office of Naval Research
Department of the Navy
Attn: Physics Branch
Washington, D C 20360 [1]

Naval Research Laboratory
Department of the Navy
Attn: Technical Library
Washington, D C 20390 [1]

Commanding Officer
Naval Weapons Center
Corona Laboratories
Corona, California 91720

Office of the Director of Defense
Research and Engineering
Information Office Library Branch
The Pentagon
Washington, D C 20301 [1]

U. S. Army Research Office
Box CM, Duke Station
Durham, North Carolina 27706 [1]

Defense Documentation Center
Cameron Station
Alexandria, Virginia 22314 [12]

Director, National Bureau of Standards
Attn: Technical Library
Washington, D C 20234

Commanding Officer
Office of Naval Research Branch Office
219 S. Dearborn Street
Chicago, Illinois 60604 [1]

San Francisco Area Office
Office of Naval Research
1076 Mission Street
San Francisco, California 94103 [1]

Air Force Office of Scientific Research
Department of the Air Force
Washington, D C 20333

Commanding Officer
Office of Naval Research Branch Office
1030 East Green Street
Pasadena, California 91101 [1]

Commanding Officer
Office of Naval Research Branch Office
495 Summer Street
Boston, Massachusetts 02210 [1]

Director
Naval Research Laboratory
Attn: Library, Code 2029 (ONRL)
Washington, D C 20390 [1]

Director
U. S. Army Engineering Research
and Development Laboratories
Fort Belvoir, Virginia 22060
Attn: Technical Documents Center

OOSR and U. Advisory Group on
Electron Devices
201 Varick Street
New York, New York 10014 [1]

New York Area Office
Office of Naval Research
207 W. 24th Street
New York, New York 10011 [1]

Air Force Weapons Laboratory
Technical Library
Kirtland Air Force Base
Albuquerque, New Mexico 87117

Air Force Avionics Laboratory
Air Force Systems Command
Technical Library
Wright-Patterson Air Force Base
Dayton, Ohio 45433

Air Force Cambridge Research Lab.
L. G. Hanscom Field
Technical Library
Cambridge, Massachusetts 02138

Navy Department Library
Technical Library
Connecticut Ave. at Van Ness N W
Washington, D C

Naval Weapons Center
Technical Library (Code 753)
China Lake, California 93555

Naval Training Device Center
Technical Library
Orlando, Florida 32813

Naval Research Laboratory
Underwater Sound Reference Division
Technical Library
P O Box 8337
Orlando, Florida 32806

Navy Underwater Sound Laboratory
Technical Library
Fort Trumbull
New London, Conn. 06320

Naval Ordnance Station
Technical Library
Indian Head, Maryland 20640

Naval Ship Engineering Center
Philadelphia Division
Technical Library
Philadelphia, Pennsylvania 19112

Department of the Navy
Bureau of Naval Personnel
Technical Library
Washington, D C 20370

Naval Postgraduate School
Technical Library (Code 0212)
Monterey, California 93940

Naval Missile Center
Technical Library (Code 5632.2)
Point Mugu, California 93040

Naval Ordnance Station
Technical Library
Louisville, Kentucky 40214

Naval Oceanographic Office
Technical Library (Code 1640)
Suitland, Maryland 20390

Naval Explosive Ordnance Disposal
Facility
Technical Library
Indian Head, Maryland 20640

Naval Electronics Laboratory Center
Technical Library
San Diego, California 92152

Naval Applied Science Laboratory
Technical Library (Code 2022)
Flushing and Washington Avenues
Brooklyn, New York 11251

Naval Undersea Warfare Center
Technical Library
3202 E. Foothill Boulevard
Pasadena, California 91107

Naval Weapons Laboratory
Technical Library
Dahlgren, Virginia 22448

Naval Ship Research and Development
Center
Central Library (Codes L42 and L43)
Washington, D C 20007

Naval Ordnance Laboratory White Oak
Technical Library
Silver Spring, Maryland 20910

Naval Avionics Facility
Technical Library
Indianapolis, Indiana 46218

Department of the Army
U S Army Electronics Command
Attn: AMSEL RD, E
Fort Monmouth, New Jersey 07703

J. Bardeen
Department of Physics
University of Illinois
Urbana, Illinois 61803

A. C. Beer
Battelle Memorial Institute
505 King Avenue
Columbus, Ohio 43201

J. M. Besson
Faculte des Sciences
Physique des Solides
Tour 13 - 2eme etage
4 Place St. Bernard
Paris
France

A. Bienenstock
Department of Materials Science
Stanford University
Stanford, California 94305

J. L. Birman
Department of Physics
New York University
University Heights
New York New York 10453

N. Bloembergen
Pierce Hall 210
Harvard University
Cambridge, Massachusetts 02138

A. S. Bradley
School of Chemistry
University of Leeds
Leeds ENGLAND

R. Brandwein
Physics Department
University of California
Los Angeles, California 90024

H. Brooks
Pierce Hall 217
Harvard University
Cambridge, Massachusetts 02138

E. Brown
Department of Physics
Rensselaer Polytechnic Institute
Troy, New York 12181

Prof. Ehud Burstein
University of Pennsylvania
Philadelphia, Pennsylvania 19104

J. Callaway
Department of Physics
Louisiana State University
Baton Rouge, Louisiana 70803

H. B. Callen
Department of Physics
University of Pennsylvania
Philadelphia, Pennsylvania 19104

Manuel Cardona
Max Planck Institut für
Festkörperforschung
7000 Stuttgart 1
Heisenbergstrasse 69
West Germany

M. Cohen
Institute for the Study of Metals
University of Chicago
Chicago, Illinois

E. M. Conwell
General Telephone and Electronics Labs
Bayside, New York 11360

M. DiMare
RCA Research Laboratory
Princeton, New Jersey 08540

Dept. of Scientific and Industrial
Research
National Engineering Laboratory
East Kilbride Glasgow
Scotland
Attn: Mr. J. F. Franklin

T. F. Deutsch
Research Division
Raytheon Company
28 Seyon Street
Waltham, Massachusetts 02154

H. G. Drickamer
Dept. of Chemistry and
Chemical Engineering
University of Illinois
Urbana, Illinois 61803

J. B. Dunlop
Department of Chemistry
University of Leeds
Leeds ENGLAND

Editorial Office
130 Pierce Hall
Harvard University
Cambridge, Massachusetts 02138

H. Ehrenreich
Pierce Hall 295 A
Harvard University
Cambridge, Massachusetts 02138

A. W. Ewald
Department of Physics
Northwestern University
Evanston, Illinois 60201

H. Y. Fan
Department of Physics
Purdue University
Lafayette, Indiana 47907

Johns Fenton
ITEK Corporation
60 Hampden Road
Lexington, Massachusetts

O. Feuer
General Electric Company
Research and Development Center
P O Box 1088
Schenectady, New York 12301

D. B. Fitchen
Dept. of Physics
Cornell University
Ithaca, New York 14850

E. U. Franck
Institut für Physikalische Chemie
Technische Hochschule
Karlsruhe
12 Englerstrasse
Germany

H. Frederikse
National Bureau of Standards
U S Department of Commerce
Washington, D C. 20234

H. Fritzsche
Institute for the Study of Metals
University of Chicago
5640 South Ellis Avenue
Chicago, Illinois 60637

M. Garbuny
Dept. of Materials Science
University of Southern California
Los Angeles, California 90007

C. H. Goodman
Materials Synthesis Department
Standard Telecommunication L t d.
London Road
Harlow, ENGLAND

Gordon McKay Library
Pierce Hall
Harvard University
Cambridge, Massachusetts 02136 [4]

P. Green
IBM Research Division
Monterey and Cottle Roads
San Jose, California 95114

S. Groves
M I T
Lincoln Laboratory
P O Box 73
Lexington, Massachusetts 02173

R. Hall
General Electric Research Lab
P O Box 1088
Schenectady, New York 12301

W. A. Harrison
Division of Applied Physics
Stanford University
Stanford, California 94305

M. Hercher
1 112 Research Building
Pennsylvania State University
University Park, Pennsylvania 16802

Frank Herman
IBM Research Division
San Jose, California 95114

C. Herring
J. Burton
Bell Telephone Laboratories
Murray Hill, New Jersey 07971

C. Hilsum
Ministry of Aviation
Royal Radar Establishment
St. Andrews Road
Great Malvern, Worcestershire
ENGLAND

R. Hoffman
Department of Physics
Case Institute of Technology
10900 Euclid Avenue
Cleveland, Ohio 44106

M. Holland
Research Division
Raytheon Company
Waltham, Massachusetts 02154

W. E. Howard
Thomas J. Watson Research Center
IBM
P O Box 218
Yorktown Heights, New York 10598

A. A. Ioffe
Bell Telephone Laboratories
Murray Hill, New Jersey 07971

A. Jayaraman
Bell Telephone Laboratories
Murray Hill, New Jersey 07971

B. I. Jones
Brun, Grad School of
Arts and Sciences
Harvard University
Cambridge Mass 02138

G. Jura
Department of Chemistry
University of California
Berkeley, California 94720

E. O. Kane
Bell Telephone Laboratories
Murray Hill, New Jersey 07971

G. Kennedy
Institute of Geophysics and Planetary
Physics
University of California
Los Angeles, California 90067

A. Lawson
Department of Physics
University of California
Riverside, California 92502

B. Lax
Director
National Magnet Laboratory
NW 14 5110
M I T
Cambridge, Massachusetts 02139

M. Lax
Bell Telephone Laboratories
Murray Hill, New Jersey 07971

D. Lazarus
Department of Physics
University of Illinois
Urbana, Illinois 61803

W. Low
The Hebrew University
Jerusalem, ISRAEL

R. Lucchesi
Thomas J. Watson Research Center
IBM
P O Box 218
Yorktown Heights, New York 10598

L. Merten
Room 303 South Building
National Bureau of Standards
Washington, D C 20234

Engineering Technical Reports
M I T Room 10 400
Cambridge, Massachusetts 02139

Massachusetts Institute of Technology
Lincoln Laboratory
P O Box 73
Lexington, Massachusetts 02173
Attn: Library

P. McElroy
Woods Hole Oceanographic Institute
Woods Hole, Massachusetts 02540

T. P. McLean
Royal Radar Establishment
Malvern, Worcestershire
ENGLAND

H. Meyer
Department of Physics
Duke University
Durham, North Carolina 27706

M. J. G. Meyer
Philips Research Laboratories
Eindhoven, NETHERLANDS

S. Minomura
Institute for Solid State Physics
University of Tokyo
Azabu Bldg/roku Chi-Mmoto-KU
Tokyo, JAPAN

E. W. Mitchell
J. J. Thomson Physical Laboratory
Whiteknights Park, Reading
ENGLAND

F. J. Morin
Associate Director
North American Aviation Science Center
1049 Camino Dos Rios
Thousand Oaks California 91360

G. Morton
RCA Laboratories
David Sarnoff Research Center
Princeton, New Jersey 08540

T. S. Moss
R. A. E.
Farnborough, Hants
ENGLAND

S. Mrowarski
Department of Physics
State University of New York
at Buffalo
Hochstetter Hall
Administration Road
Buffalo, New York 14214

M. M. Mochterich
Institute for the Study of Metals
University of Chicago
Chicago Illinois 60637

M. I. Nathan
Thomas J. Watson Research Center
IBM
P O Box 218
Yorktown Heights, New York 10598

R. Newman
Sperry Rand Research Laboratory
Sudbury, Massachusetts 01776

R. Parmenter
Physics Department
University of Arizona
Tucson, Arizona

M. S. Paterson
Department of Geophysics
Australian National University
Canberra, AUSTRALIA

W. Paul
Pierce Hall 209
Harvard University
Cambridge, Massachusetts 02138 [5]

G. Pearson
Stanford Electronics Laboratories
Stanford University
Stanford, California 94305

R. Keyes
Thomas J. Watson Research Center
IBM
P O Box 218
Yorktown Heights, New York 10598

C. Kittel
Department of Physics
University of California
Berkeley California 94720

L. Kleinman
Department of Physics
University of Texas
Austin Texas

J. Koehler
Department of Physics
University of Illinois
Urbana, Illinois 61803

W. Kohn
M. Dahl
Department of Physics
University of California
La Jolla, California 92038

B. Kramer
Bell Telephone Laboratories
Murray Hill, New Jersey 07971

L. Kravitz
General Electric Research Laboratory
P O Box 1088
Schenectady New York 12301

J. Krumhansl
Department of Physics
Cornell University
Ithaca New York 14850

Larry Ladd
RADC
Raytheon
130 2nd Avenue
Waltham, Mass 02154

P. Parmar
Pierce Hall 213 C
Harvard University
Cambridge, Massachusetts 02138

H. Philipp
General Electric Research Laboratory
P O Box 1088
Schenectady, New York 12301

Philips J. C.
Bell Telephone Laboratories
Murray Hill, New Jersey 07974

G. Pratt Jr.
Dept. of Electrical Engineering
M I T
Cambridge, Massachusetts 02139

R. H. Rediker
M I T
Lincoln Laboratory
P O Box 73
Lexington, Massachusetts 02173

Research Materials Information Center
Oak Ridge National Laboratory
P O Box X
Oak Ridge Tennessee 37831
Attn: Mr. T. F. Connolly

C. M. Roermann
Philips Research Laboratories
Eindhoven, NETHERLANDS

C. Rosei
4400 McKenzie Drive
Monroeville, Pennsylvania 15146

L. Roth
General Electric Research Laboratory
The Knolls
Schenectady New York 12301

A. L. Ruoff
Department of Physics
Cornell University
Ithaca, New York 14850

A. Sagar
Westinghouse Electric Corp.
Research and Development Center
Beulah Road
Churchill Boro
Pittsburgh, Pennsylvania 15235

S. Saito
Research Laboratories of Engineering
Materials
Tokyo Institute of Technology
Ookayama Meguro Ku
Tokyo, JAPAN

G. A. Samara
Sandia Corporation
Albuquerque, New Mexico 87115

Dr. W. W. Scanlon
USNOL
White Oak
Silver Spring, Maryland 20910

J. E. Schirber
Sandia Corporation
Albuquerque New Mexico 87115

Bernard O. Seraphin
Optical Sciences Center
University of Arizona
Tucson, Ariz. 85721

T. Sharkhnel
Geology Department
Harvard University
Cambridge, Massachusetts 02138

B. J. Shaluh
Department of Physics
Purdue University
Lafayette, Indiana 47907

A. C. Smith
Dept. of Electrical Engineering
10-079
M I T
Cambridge, Massachusetts 02139

R. Smoluchowski
Solid State and Materials Program
University of Chicago
Princeton, New Jersey 08540

W. Spitzer
Electronics Science Laboratory
School of Engineering
University of Southern California
University Park
Los Angeles, California 90017

C. A. Swenson
Department of Physics
Iowa State University
Ames, Iowa 50010

D. G. Thomas
Bell Telephone Laboratories
Murray Hill, New Jersey 07971

C. C. Tsuei
Department of Physics
University of Arizona
Tucson, Arizona

B. Vodar
LP 30
Bellevue FRANCE

W. C. Walker
Department of Physics
University of California
Santa Barbara, California 93018

E. Weber
President
Polytechnic Institute of Brooklyn
333 Jay Street
Brooklyn, New York 11201

G. B. Wright
ONR - Physics Program
Code 421
Arlington, Virginia 22217

A. B. Yelle
Physics and Chemistry of Solids
Sub-Dept. of the Cavendish Laboratory
Free School Lane
Cambridge, ENGLAND

R. Zallen
Xerox Corporation
Research Laboratories
100 Phillips Road
Bldg. 114
Webster, New York

N. J. Zeiger
M I T
Lincoln Laboratory
P O Box 73
Lexington, Massachusetts 02173

ARPA DISTRIBUTION LIST

Dr. Frank R Arnow
Consultant
Airborne Instruments Laboratory
Melville, Long Island, New York 11746

Dr. O. C Simpson
Director, Solid State Sciences Division
Argonne National Laboratory
9700 South Cass Avenue
Argonne, Illinois 60440

Dr. Douglas S Billington
Director, Solid State Division
Oak Ridge National Laboratory
Post Office Box X
Oak Ridge, Tennessee 37381

Gordon MacKay Library (2 cys)
Harvard University
Cambridge, Massachusetts 02138
Attn: Technical Reports Collection

Brown University (2 cys)
Providence, Rhode Island 02912
Attn Coordinator of Research

University of Chicago (2 cys)
Chicago, Illinois 61401
Attn Division of the Physical Sciences

Cornell University (2 cys)
Ithaca, New York 14850
Attn Center for Materials Research

University of Illinois (2 cys)
Urbana, Illinois 61801
Attn: Materials Research Laboratory

University of Maryland (2 cys)
College Park, Maryland 20742
Attn: Center for Materials Research

Massachusetts Institute of
Technology (2 cys)
Cambridge, Massachusetts 02139
Attn: Center for Materials Science
and Engineering

University of North Carolina (2 cys)
Chapel Hill, North Carolina 27514
Attn: Director, Materials Research
Center

Northwestern University (2 cys)
Evanston, Illinois 60201
Attn Materials Research Center

University of Pennsylvania (2 cys)
Philadelphia, Pennsylvania 19104
Attn. Laboratory for Research on
the Structure of Matter

Purdue University (2 cys)
Lafayette, Indiana 47907
Attn. Professor Honig

Stanford University (2 cys)
Stanford, California 94305
Attn Center for Materials Research

Dr A Sesin
Institute for Materials Research
University of Utah
Salt Lake City, Utah 84112

Dean S E Wiberley
Dean of Faculty
Rensselaer Polytechnic Institute
Troy, New York 12180

Professor H E Rorschach, Jr.
Chairman, Department of Physics
Rice University
Houston, Texas 77001

Professor James I Mueller
Department of Mining, Metallurgy
and Ceramic Engineering
University of Washington
Seattle, Washington 98105

Materials Research Laboratory
Pennsylvania State University
University Park, Pennsylvania 16802
Attn Prof Rustum Roy (2 cys)

Dr. H. Kreitler (Code AA)
Chief Scientist
Naval Air Development Center
Johnsville, Warminster, Pennsylvania
18974

Mr. Thomas Monahan Code 901
Assistant Technical Director of Programs
Naval Applied Science Laboratory
Brooklyn, New York 11251

Mr. W L. Williams
Head, Materials Laboratory
Naval Ship Research and
Development Laboratory
Annapolis, Maryland 21402

Dr Graham W Marks
Code 0403
Naval Undersea Research
and Development Center
San Diego, California 92132

Mr. Dwight Lyman
Code 2064
Naval Underwater Sound Laboratory
New London, Connecticut 06320

Mr M. L. Pittman
Code M134
San Francisco Bay Naval Shipyard
Vallejo, California 94592

Naval Mine Defense Laboratory
Attn Technical Library Branch
Panama City, Florida 32402

Mr. A R Willner
Head, Personnel Protection
Concepts Branch, Code 187
Naval Ship Research and
Development Center
Washington, D. C 20007

Mr. F S Williams (Code MAM)
Naval Air Development Center
Johnsville, Warminster, Pa 18974

Mr. J M Bowen (Code MA-1)
Technical Director
Naval Air Development Center
Johnsville, Warminster, Pa 18974

Naval Underwater Weapons Research
and Engineering Station
Attn. Technical Library
Newport, Rhode Island 02840

Mr. W F Burhart
Technical Director
Naval Civil Engineering Laboratory
Port Hueneme, California 93041

Defense Documentation Center (12 cys)
Cameron Station
Alexandria, Virginia 22314

Dr Howard Eisel
Physics Section, Room 307
National Science Foundation
Washington, D C 20550

National Materials Advisory
Board (2 cys)
2101 Constitution Avenue, N W
Washington, D C. 20418

Dr Israel Warshaw
Division of Engineering
National Science Foundation
Washington, D C 20550

Dr. Albert Lightbody
U S Naval Ordnance Laboratory
Chief, Chemistry Research Department
White Oak, Silver Spring, Maryland 20901

Mr. Winston H Duckworth
Defense Ceramic Information Center
Battelle Memorial Institute
505 King Avenue
Columbus, Ohio 43201

Commanding General
Natick Laboratories
Attn: Scientific Director
Natick, Massachusetts 01762

Commanding Officer
Harry Diamond Laboratories
Attn. R and D Supervisor
Washington, D C 20438

Commanding General
U S Army Electronics Command
Attn Institute for Exploratory Research
Electronic Parts and Materials Div
Fort Monmouth, New Jersey 07703

Commanding Officer
Picatinny Arsenal
Attn Feltman Research Laboratories
Dover, New Jersey 07801

Scientific Director
Medical-Bio Mechanical
Research Labs.
Walter Reed Army Medical Center
Washington, D C 20012

Commanding Officer
Rock Island Arsenal
Attn. Director of Laboratories
Rock Island, Illinois 61202

Commanding Officer
Watervliet Arsenal
Attn Chief, Research and Engineering
Division
Watervliet, New York 12189

Chief of Research and Development
Department of the Army
Attn Army Research Office (CRDPES)
Chemistry and Materials Branch
Physical Sciences Division
Washington, D C 20310

Commanding General
U S Army Missile Command
Attn. Director, Research and
Development
Redstone Arsenal, Alabama 35809

Commanding General
U S. Army Tank Automotive
Center
Attn: Research and Engineering
Directorate
Warren, Michigan 48090

Commanding Officer
U.S Army Engineer R and D Labs
Attn: Chief, Materials Branch
Technical Service Department
Ft Belvoir, Virginia 22060

Commanding Officer
U S Army Transportation Research
Command
Attn. Physical Sciences Group
Ft. Eustis, Virginia 23604

Commanding Officer
Frankford Arsenal
Attn: Pitman-Dunn Laboratories
Philadelphia, Pennsylvania 19137

Commanding General
U S Army Chemical R and D Laboratories
Attn. Technical Director
Edgewood Arsenal, Maryland 21010

Commanding Officer
U S Army Research Office-Durham
Attn Chief Scientist
Box CM, Duke Station
Durham, North Carolina 27706

Dr D F Bleil
Associate Technical Director
and Head, Research
U S Naval Ordnance Laboratory
White Oak, Silver Spring, Maryland 20910

Dr. Hugh Hunter
Head, Research Department
Naval Ordnance Test Station
China Lake, California 93555

Mr Bernard Smith
Technical Director
Naval Weapons Laboratory
Dahlgren, Virginia 22448

Dr Leo Brewer
Director, Inorganic Materials
Research Division
Lawrence Radiation Laboratory
University of California
Berkeley, California 94720

Dr Donald K Stevens
Assistant Director for
Metallurgy and Materials Programs
Division of Research
U S Atomic Energy Commission
Washington, D C. 20545

Dr. R Haasen, Director
Ames Laboratory
U S Atomic Energy Commission
P.O Box 1129, Station A
Ames, Iowa 50010

Dr John H. Frye, Director
Metallurgy Division
Oak Ridge National Laboratory
P O Box X
Oak Ridge, Tennessee 37381

Dr H H. Chiswik
Assistant Director
Metallurgy Division
Argonne National Laboratory
9700 South Cass Avenue
Argonne, Illinois 60440

Dr David H Gurinsky
Head, Metallurgy Division
Brookhaven National Laboratory
Upton, Long Island, New York 11973

Dr. George H. Vineyard, Assoc
Director
Brookhaven National Laboratory
Upton, Long Island, New York 11973

Dr J J. Cadwell
Reactor and Fuels Laboratory
Battelle Northwest
P O Box 999
Richland, Washington 99352

Dr. R D Fowler
CMF Division
Los Alamos Scientific Laboratory
P O Box 1663
Los Alamos, New Mexico 87544

Dr R R Nash
Chief, Materials Sciences Branch
Division of Research - Code RRS
Office of Advanced Research and Technology
NASA Headquarters
Washington, D. C 20546

Dr. R. A Lad
Chief, Chemical Physics Branch
Nuclear Reactor Division
NASA Lewis Research Center
Cleveland, Ohio 44135

Dr. Charles A. Hermach
Chief, Materials Research Branch
Vehicle Environment Division
NASA Ames Research Center
Moffett Field, California 94035

Dr H E Frankel
Chief, Materials and Development Section
Spacecraft Systems and Projects Division
NASA Goddard Space Flight Center
Greenbelt, Maryland 20771

Dr. W Crawford Dunlap
Code DE
Transportation Systems Center
55 Broadway
Cambridge, Mass 02142

Headquarters, USAF (AFRSTC)
Washington, D C 20330

Dr S Katzoff
Assistant Chief
Applied Materials and
Physics Division
NASA Langley Research Center
Langley Station
Hampton, Virginia 23365

Dr R L. Johnston
Head, Spacecraft Materials Section
Structure and Mechanics Division
NASA Manned Spacecraft Center
Houston, Texas 77058

Dr W R Lucas
Chief, Materials Division
Propulsion and Vehicle
Engineering Laboratory
NASA George C Marshall
Space Flight Center
Huntsville, Alabama 35812

Mr H E Martens
Chief, Materials Research Section
Engineering Mechanics Division
Jet Propulsion Laboratory
4800 Oak Grove Drive
Pasadena, California 91103

RCA Research Laboratories
Princeton, New Jersey 08540
Attn. Dr Fred Rost

Westinghouse Electric Corporation
Beulah Road
Churchill Borough, P O Box 10864
Pittsburgh, Pennsylvania 15236
Attn. Dr Kossowsky

National Bureau of Standards (2 cys)
Washington, D C. 20234
Attn. Dr. Alan Franklin, 31305

Naval Research Laboratory
Washington, D C 20390
Attn Dr James Schulman (2 cys)
Attn Dr. George Rado (1 cy)

Hq. Office of Aerospace Research (RROS)
1400 Wilson Boulevard
Arlington, Virginia 22209

Hq. Air Force Office of Scientific
Research (SRP)
1400 Wilson Boulevard
Arlington, Virginia 22209

Hq Air Force Office of Scientific
Research (SRE)
1400 Wilson Boulevard
Arlington, Virginia 22209

Hq. Air Force Systems Command (SCT)
Andrews Air Force Base
Washington, D C. 20331

Director of Laboratories, AFSC
Andrews Air Force Base
Washington, D C 20331

Air Force Materials Laboratory (MAS)
Wright-Patterson Air Force Base,
Ohio 45433

Air Force Materials Laboratory (MAAM)
Wright-Patterson Air Force Base,
Ohio 45433

Aerospace Research Laboratories (ARD)
Wright-Patterson Air Force Base,
Ohio 45433

Chief Scientist
Air Force Cambridge Research Labs
L. G Hanscom Field
Bedford, Massachusetts 01731

Chief Scientist
The Frank J Seiler Research Lab
USAF Academy, Colorado 80840

Commanding Officer
Army Material and Mechanics Research
Center
Watertown, Massachusetts 02172
Attn: Chief Scientist

Commanding Officer
U S. Army Ballistic Research
Laboratories
Attn: Chief, Solid Mechanics
Branch (AMXBR-TA)
Aberdeen Proving Ground,
Maryland 21005

Dr Alfred A Wolf
Associate Technical Director
for Research
Naval Ship Research and
Development Center
Annapolis, Maryland 21402

Dr Robb M Thomson
Chairman, Department of
Materials Science
State University of New York
Stony Brook, New York 11790

Dr Alan Tetelman
Head, Materials Division
Department of Engineering
University of California
Los Angeles, California 90024

Documents Acquisitionist
Lincoln Laboratory/MIT
Lexington, Massachusetts 02173

Office of Naval Research
Department of the Navy
Washington, D C 20360
Attn Code 419 (1 cy)
Attn Code 439 (1 cy)
Attn: Code 421 (2 cys)
Attn: Code 425 (1 cy)

Naval Supply Systems Command
Department of the Navy
Washington, D. C 20360
Attn. Code 042 (1 cy)
Attn: Code 0421 (1 cy)

Naval Ship Systems Command
Department of the Navy
Washington, D. C 20360
Attn: Code 031

Dr. Victor Zachay
Inorganic Materials Research Div.
Lawrence Radiation Laboratory
University of California
Berkeley, California 94720

Dr. John J Brogan
5 Research Drive
Ann Arbor, Michigan 48103